

Dissertation  
submitted to the  
Combined Faculties for the Natural Sciences and for Mathematics  
of the Ruperto-Carola University of Heidelberg, Germany  
for the degree of  
Doctor of Natural Sciences

Put forward by

**M.Sc. Christian Helmut Simon**

born in Wiesbaden, Germany

Oral examination: February 9, 2021



INVESTIGATIONS OF RATE AND MULTI-HIT CAPABILITY OF MULTI-GAP  
RESISTIVE PLATE CHAMBERS

Referees: Prof. Dr. Norbert Herrmann  
Prof. Dr. Hans-Christian Schultz-Coulon



## ZUSAMMENFASSUNG

Der Einsatz von MRPC-Detektoren (Multi-gap Resistive Plate Chamber) für Flugzeitmessungen (TOF) an zukünftigen Hochratenexperimenten mit Schwerionenkollisionen wie CBM (Compressed Baryonic Matter) bei FAIR wird sowohl durch anspruchsvolle Teilchenfluss- als auch Mehrfachtrefferbedingungen auf der Zähleroberfläche eingeschränkt. Zur Mitte der  $120\text{ m}^2$  großen TOF-Wand von CBM hin werden bei Kollisionen von Goldkernen mit 10 MHz und 11 A GeV (SIS100) Flüsse von bis zu  $25\text{ kHz/cm}^2$  durch Detektoren mit niederohmigem Spezialglas verarbeitet. Im Randbereich finden aus Kostengründen Zähler mit Normalglas Verwendung. In dieser Arbeit werden Ergebnisse aus einer Teststrahlzeit für entsprechende Prototypen, die in einer Mehrfachtrefferumgebung bei moderaten Teilchenflüssen von  $1\text{--}2\text{ kHz/cm}^2$  am CERN/SPS gewonnen wurden, systematisch auf Raten- und Interferenzeffekte auf die Zählerleistung untersucht. Zur Beschreibung in Simulationen wird eine neuartige Parametrisierung der Antwortfunktion von MRPCs eingeführt, die sowohl den Einfluss einer anhaltenden Bestrahlung auf das Detektionsvermögen in der Zeit als auch die Verzerrung rekonstruierter Treffer durch interferierende induzierte Signale modelliert. Damit wird eine beabsichtigte qualitative Übereinstimmung zwischen realen und simulierten Beobachtungen erzielt. Während lediglich der Normalglaszähler eine erwartete ratenbedingte Leistungsminderung aufweist, wird die Auswertung der Reaktion beider Prototypen mittels Korrelationen auf benachbarten Detektoren durch Mehrfachtreffereffekte beträchtlich erschwert. Das neue Reaktionsmodell bietet eine verlässliche Simulationsreferenz für weitere diesbezügliche Untersuchungen.

## ABSTRACT

The application of multi-gap resistive plate chambers (MRPC) for time-of-flight (TOF) measurements in future high-rate heavy-ion-collision experiments like CBM (Compressed Baryonic Matter) at FAIR is constrained by both challenging particle-flux and multi-hit conditions on the counter surface. Towards the center of the  $120\text{ m}^2$  TOF wall of CBM, fluxes of up to  $25\text{ kHz/cm}^2$  in gold-on-gold collisions at 10 MHz and 11 A GeV (SIS100) are handled by detectors with special low-resistive glass. At the periphery, common-glass counters are used for cost reasons. In this work, test-beam results for corresponding prototypes obtained in a multi-hit environment under moderate particle fluxes of  $1\text{--}2\text{ kHz/cm}^2$  at CERN/SPS are systematically analyzed for rate and interference effects on counter performance. For a reproduction in simulations, a novel parametrization of the MRPC response function is introduced which models both the impact of sustained irradiation on detection capability in time and the distortion of reconstructed hits by interfering induced signals. An envisaged qualitative agreement is achieved between real and simulated observations. While only the common-glass counter shows an expected performance degradation due to rate, the response evaluation of both prototypes via correlations on adjacent detectors is significantly complicated by multi-hit effects. The new response model provides a reliable simulation reference for further investigations on this matter.



To Whom it concerns.



## ACKNOWLEDGMENTS

First and foremost, I am indebted to my supervisor Prof. Dr. Norbert Herrmann who accepted me as his PhD student and continuously made available his support on an exceptionally long research journey through experimental nuclear physics. Owing to his sound advice and everlasting patience alone, convergence of this comprehensive project could finally be achieved. Despite his versatile occupation as lecturer, research group leader, and spokesperson of the CBM Collaboration, he takes on a pioneering role in TOF software development for data calibration and analysis which proved beneficial also to this work.

For his willingness to act as second referee of the present dissertation, I would like to cordially thank Prof. Dr. Hans-Christian Schultz-Coulon. Regarding completion of my examination committee, I owe my deepest gratitude to my additional examiners Prof. Dr. Peter Fischer and Prof. Dr. Jörg Jäckel who, by their generous flexibility, made possible a rather uncomplicated scheduling of the examination date.

During the entire course of my doctoral research, Dr. Ingo Deppner has been a reliable mentor and a highly frequented addressee for physics- and life-related questions. Particularly, I would like to thank him and Dr. Pierre-Alain Loizeau who is an inexhaustible mine of computing knowledge for supporting my work. In view of a smooth and fruitful cooperation on setting up and thoroughly testing a TrbNet-based DAQ system for various beam-time activities, I would like to commend Jochen Frühauf, Dr. Jan Michel, and Cahit Uğur.

Within the local working group in Heidelberg, many former and current colleagues have accompanied and alleviated the maturation process of this project, both by providing valuable professional input and by contributing to a nonchalant office climate. To restrict a lengthy list to long-term companions only, I would like to mention—in alphabetical order—Adeel Akram, Erjin Bao, Dr. Dongdong Hu, Dennis Sauter, Philipp Weidenkaff, Dr. Yapeng Zhang, and Dr. Victoria Zinyuk. Actually, it has been a pleasure to go to work every morning.

Beyond words is the unconditional support by my parents which they have made available in numerous ways, especially in the final stage of writing. Their sympathetic attitude and encouragement from the beginning to the end of this work have been worth their respective weight in gold. Hence, I would like to express my heartfelt gratitude and, in the same breath, sincerely apologize for undoubtedly many worries that I have been the cause of.

To family members and friends in general, I would like to give thanks for always being around for some rare but edifying off-campus amusement. I have very much appreciated living in a wholesome social environment.



## TABLE OF CONTENTS

<b>LIST OF TABLES</b>	<b>xiii</b>
<b>LIST OF FIGURES</b>	<b>xv</b>
<b>CHAPTER 1 INTRODUCTION</b>	<b>1</b>
<b>CHAPTER 2 THE CBM EXPERIMENT AT FAIR</b>	<b>13</b>
2.1 Physics observables and detection instruments . . . . .	14
2.2 Data acquisition and online event selection . . . . .	19
2.3 Simulation and reconstruction in CbmRoot . . . . .	23
2.4 Time-of-flight measurements with resistive plate chambers . . . . .	26
2.4.1 The time-of-flight method . . . . .	26
2.4.2 Multi-gap resistive plate chambers . . . . .	29
2.4.3 A large-area time-of-flight wall for CBM . . . . .	34
<b>CHAPTER 3 MRPC PROTOTYPE TESTS WITH HEAVY IONS</b>	<b>39</b>
3.1 Test-beam setup at CERN/SPS in March 2015 . . . . .	40
3.1.1 Detection instruments and geometry . . . . .	40
3.1.2 Particle flux and spill structure . . . . .	46
3.1.3 Monte Carlo estimate of experimental conditions . . . . .	47
3.2 Dual detector readout with TrbNet . . . . .	53
3.2.1 Digitization of MRPC signals using FPGA-TDCs . . . . .	53
3.2.2 The centrally controlled trigger and readout process . . . . .	54
3.2.3 Bandwidth limitations and event yields . . . . .	58
3.3 Raw-data calibration and hit building . . . . .	62
<b>CHAPTER 4 DETECTOR RESPONSE PARAMETRIZATION</b>	<b>73</b>
4.1 Modeling assumptions and procedure . . . . .	74
4.1.1 Signal generation and calibration of simulated data . . . . .	74
4.1.2 Cluster residuals and resolutions . . . . .	79
4.1.3 Response dependence on a static working coefficient . . . . .	85
4.1.4 Parameter adjustment and model limitations . . . . .	87
4.2 Memorization of local E-field breakdown and recovery . . . . .	90
4.3 Implementation in a time-based simulation framework . . . . .	96
4.3.1 Signal interference handling . . . . .	96
4.3.2 Multithreading and parallelization . . . . .	100
4.3.3 Applicability for full-featured test-beam simulations . . . . .	102
<b>CHAPTER 5 RESULTS</b>	<b>107</b>
5.1 Event selection and hit matching in data analysis . . . . .	108
5.2 Track-interference bias on detector response . . . . .	116

5.3	Rate effects under continuous irradiation . . . . .	125
5.4	Perspectives with the mCBM experiment at GSI/SIS18 . . . . .	129
<b>CHAPTER 6 SUMMARY</b>		<b>133</b>
<b>APPENDICES</b>		<b>139</b>
APPENDIX A	CURRICULUM VITAE . . . . .	141
APPENDIX B	LIST OF PUBLICATIONS . . . . .	143
<b>REFERENCES</b>		<b>147</b>

## LIST OF TABLES

Table 1.1:	Threshold energies for strangeness production processes in proton–proton collisions. . . . .	5
Table 2.1:	Design aspects of MRPCs composing the TOF wall of the CBM experiment. . . . .	35
Table 3.1:	Technical design aspects and operating conditions of MRPC prototypes studied at CERN/SPS. . . . .	41
Table 3.2:	Counter positioning and trigger geometry of the MRPCs tested at CERN/SPS. . . . .	44
Table 3.3:	Monte Carlo event properties of the collision scenario at CERN/SPS. .	51
Table 3.4:	Disabled cells and signal propagation velocities in counter calibration.	67
Table 4.1:	Constraints and free parameters for counter response modeling. . . . .	88
Table 4.2:	Control parameters for particle memorization during digitization. . . .	93
Table 4.3:	Computational limits for particle-flux simulations with an active particle memory. . . . .	102
Table 4.4:	Comparison of digitization times between runs with an active and with an inactive particle memory. . . . .	105
Table 5.1:	Ranges for peak fitting of selector and DUT-matching residuals. . . .	110
Table 5.2:	Exemplary $\chi^2$ -weights and scaling factors obtained for counter 9-0-0. .	112
Table 5.3:	Numerical response evaluation of counters 9-0-0 and 7-0-0 in selector events with a single cluster on the Sel2 counter. . . . .	121



## LIST OF FIGURES

Figure 1.1:	Theoretically predicted phases and phase boundaries of strongly interacting matter. . . . .	1
Figure 1.2:	Measured QCD phase diagram and center-of-mass-energy dependence of temperature and baryon chemical potential according to a thermal hadronization model. . . . .	4
Figure 1.3:	Hadron yields measured by the HADES experiment in Ar + KCl collisions at $\sqrt{s_{NN}} = 2.61$ GeV. . . . .	5
Figure 1.4:	Experimentally observed strangeness enhancement at low center-of-mass energies modeled by PHSD. . . . .	6
Figure 1.5:	Omega (anti-)baryon yield per event and production yield per day in the CBM experiment as a function of energy expected with and without partonic degrees of freedom in a transport calculation. . . . .	7
Figure 1.6:	Expected yields from a thermal-model treatment of hypernuclei and (doubly) anti-kaonic nuclear clusters as functions of center-of-mass energy. . . . .	8
Figure 1.7:	Maximum interaction rates at (planned) heavy-ion experiments operating between 1 and 40 GeV in $\sqrt{s_{NN}}$ . . . . .	10
Figure 2.1:	Overview of the planned FAIR facility. . . . .	13
Figure 2.2:	Model of the experimental setup in the future CBM cave comprising the HADES spectrometer and the CBM experiment. . . . .	15
Figure 2.3:	Sketch of the self-triggered readout concept of the CBM experiment. . . . .	20
Figure 2.4:	The timeslice data structure of the CBM experiment on which four-dimensional track and event reconstruction is performed. . . . .	22
Figure 2.5:	Dielectron setup of the CBM experiment implemented in the TGeo geometry modeler. . . . .	24
Figure 2.6:	Simulation, digitization, and reconstruction steps in CbmRoot. . . . .	25
Figure 2.7:	Phase space populated by primary pions, kaons, and protons in fixed-target gold-on-gold collisions at $p_{\text{beam}} = 10$ A GeV/c. . . . .	26
Figure 2.8:	Squared particle masses of primary pions, kaons, and protons as a function of laboratory momentum assuming different time resolutions of the TOF system. . . . .	28

Figure 2.9: Squared-mass slices of primary pions, kaons, and protons at $p = 3 \text{ GeV}/c$ assuming different time resolutions of the TOF system. . . .	28
Figure 2.10: Particle flux through the CBM TOF wall at a beam–target interaction rate of 10 MHz. . . . .	29
Figure 2.11: Construction and working principle of an MRPC. . . . .	31
Figure 2.12: Measured MRPC performance as a function of particle flux for different resistive materials. . . . .	33
Figure 2.13: Conceptual design view of the CBM Time-of-Flight wall. . . . .	34
Figure 2.14: Analog processing of an MRPC signal including preamplification and discrimination. . . . .	37
Figure 3.1: Photographic documentation of the test-beam setup at CERN/SPS. . .	40
Figure 3.2: Photographic documentation of detector and readout components of the setup at CERN/SPS. . . . .	42
Figure 3.3: Test-beam setup at CERN/SPS implemented in the TGeo geometry modeler. . . . .	43
Figure 3.4: Sketch of global and local coordinate systems for test-beam analysis. . . . .	45
Figure 3.5: Particle-flux estimate on plastic scintillators enframing the MRPC setup. . . . .	47
Figure 3.6: Spill quality at CERN/SPS monitored with time stamps of detector raw data. . . . .	48
Figure 3.7: Production processes of externally and internally created particles detected by counter 3-0-0. . . . .	49
Figure 3.8: Phase space, particle type, and creation process of Monte Carlo selector tracks in the simulated CERN/SPS setup. . . . .	50
Figure 3.9: Monte Carlo track flux, occupancy, and multi-track probability across the surface of counter 3-0-0. . . . .	52
Figure 3.10: Sketch of the TrbNet-based data acquisition network implemented at CERN/SPS. . . . .	55
Figure 3.11: Comparison of event building with a periodically and with a physics-triggered TrbNet. . . . .	57
Figure 3.12: Readout-system behavior close to and beyond data-uplink saturation. . . . .	59
Figure 3.13: Trigger and data rates obtained both with a periodical and with a physics trigger. . . . .	61

Figure 3.14: Fine-time and offset calibration of TDC raw data. . . . .	63
Figure 3.15: Time and position corrections of detector cells. . . . .	65
Figure 3.16: Translation of cell top/bottom time differences into local coordinates. . . . .	66
Figure 3.17: Correlations in time and position between signals on neighboring cells as a basis for cluster building. . . . .	68
Figure 3.18: Original and scaled time-over-threshold spectra of counter 9-0-0. . . . .	70
Figure 3.19: Cluster-size distributions of counter 9-0-0. . . . .	71
Figure 3.20: Illustrations of cluster building from cell hits and time walk. . . . .	71
Figure 3.21: Velocity and time-walk correction of the time residual between position- matched MRPC clusters. . . . .	72
Figure 4.1: Simulated cluster-size distributions of counter 9-0-0. . . . .	77
Figure 4.2: Original and scaled simulated time-over-threshold spectra of counter 9-0-0. . . . .	78
Figure 4.3: Simulated cell position spectra and offsets for counter 9-0-0. . . . .	80
Figure 4.4: Impact of time-walk corrections on position and time residuals in sim- ulations. . . . .	80
Figure 4.5: Dependence of simulated cluster residuals of counter 9-0-0 on cluster size. . . . .	82
Figure 4.6: Simulated cluster residuals of counter 9-0-0. . . . .	84
Figure 4.7: Application of the chi-square formalism to the simulated response function of counter 9-0-0. . . . .	85
Figure 4.8: Simulated detector response observables of counter 9-0-0 as a function of a static working coefficient. . . . .	86
Figure 4.9: Examples of bias on the simulated response function of counter 9-0-0. . . . .	89
Figure 4.10: Simulated particle-flux scan on a $1\text{ cm}^2$ spot of counter 9-0-0 for low- resistive and for common glass. . . . .	92
Figure 4.11: Spot-response simulation of efficiency degradation in time on counter 9-0-0 for selected particle fluxes. . . . .	94
Figure 4.12: Single-track full-area illumination of counters 9-0-0 and 7-0-0 in the CERN/SPS setup with $3\text{ GeV}/c$ muons at $1\text{ kHz}/\text{cm}^2$ . . . . .	95
Figure 4.13: Interference handling in time-based simulations. . . . .	98

Figure 4.14: Impact of response interference between simulated tracks on cluster residuals of counter 9-0-0. . . . .	99
Figure 4.15: Benchmark of utilizing multiple threads for particle-memory computation. . . . .	100
Figure 4.16: Parallel processing of time-based simulations featuring counters with an active particle memory. . . . .	103
Figure 4.17: Digi production time stamps for the CERN/SPS setup as a function of simulation time. . . . .	104
Figure 5.1: Event selection and hit matching based on a $\chi^2$ -formalism. . . . .	109
Figure 5.2: Calibration of $\chi^2$ -distributions by fitting a scaling factor to their respective weights. . . . .	111
Figure 5.3: Goodness of fit as a function of $\chi^2$ -limit for selector and DUT-matching $\chi^2$ -distributions. . . . .	113
Figure 5.4: Residual peak sigmas of experimental and simulated counters as functions of the selector $\chi^2$ -limit. . . . .	114
Figure 5.5: Dependence of counter efficiency on selector and DUT-matching $\chi^2$ -limits. . . . .	115
Figure 5.6: Mean cluster multiplicities in experimental and simulated selector events as functions of an upper MUL limit on the Sel2 counter. . . . .	117
Figure 5.7: Experimental and simulated DUT-matching residuals of counter 9-0-0 with different multiplicity limits on the Sel2 counter. . . . .	118
Figure 5.8: Experimental and simulated DUT-matching residuals of counter 7-0-0 with different multiplicity limits on the Sel2 counter. . . . .	119
Figure 5.9: Multiplicity scan of experimental and simulated response observables of counter 9-0-0. . . . .	120
Figure 5.10: Multiplicity scan of experimental and simulated response observables of counter 7-0-0. . . . .	123
Figure 5.11: Dependence of matching purity on a MUL limit on the Sel2 counter. . . . .	124
Figure 5.12: Nearest-neighbor acceptance of clusters on DUT counters 9-0-0 and 7-0-0 as a function of event time in spill. . . . .	126
Figure 5.13: Behavior of experimental and simulated response observables of counter 9-0-0 as a function of event time in spill. . . . .	127
Figure 5.14: Behavior of experimental and simulated response observables of counter 7-0-0 as a function of event time in spill. . . . .	128

Figure 5.15: Depiction of the mCBM setup in March 2019 by photograph and with  
the TGeo geometry modeler. . . . . 130



# CHAPTER 1

## INTRODUCTION

At temperatures and densities reflecting the conditions on the Earth’s surface, the constituents of nuclear matter—quarks, antiquarks, and gluons (altogether also referred to as partons)—exist in three-quark (baryons) and quark–antiquark (mesons) bound states. The former are omnipresent as nucleons (protons and neutrons) of atomic nuclei and the latter are produced e.g. when cosmic rays collide with atmospheric atoms. States of free quarks have not been observed at such conditions—a phenomenon known as “confinement” in the quantum field theory of the strong interaction, quantum chromodynamics (QCD). Hadrons (a collective term for baryons and mesons) with equal total angular momentum  $J$  but opposite parity  $P$  are not found to exist in degenerate states but rather differ significantly in mass like the  $\rho$  ( $J^P = 1^-$ ) and the  $a_1$  ( $J^P = 1^+$ ) mesons. This is attributed to a spontaneous breaking of chiral symmetry by a non-zero chiral quark condensate that the vacuum is filled with at low temperatures and densities [1]. Confinement and (spontaneous) chiral symmetry breaking do—according to theoretical predictions and experimental findings—not constrain strongly interacting matter at high temperatures  $T$  and/or high baryon densities/baryon chemical potentials  $\mu_B$ . Figure 1.1 sketches different theoretically predicted phases of nuclear matter in a  $(T, \mu_B)$  phase diagram. Their exact properties and positions on the phase diagram are as much de-

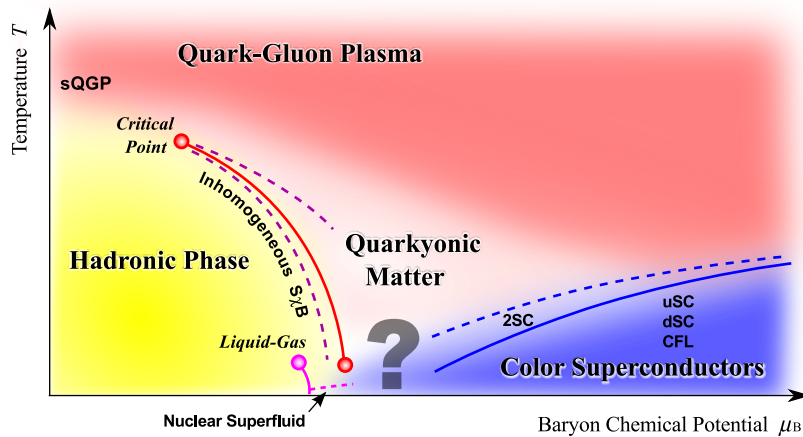


Figure 1.1: Theoretically predicted phases and phase boundaries of strongly interacting matter in a sketched  $(T, \mu_B)$  phase diagram. A plasma of free quarks and gluons is expected to be created if nuclear matter in the hadronic phase is heated up sufficiently [2]. With increasing baryon chemical potential, an intermediate chirally symmetric, yet confined phase named quarkyonic matter might be entered [3]. Cold nuclear matter at very high baryon chemical potentials could possibly exhibit properties of color superconductivity [4]. Figure adapted from [5].

bated as the true nature of the boundaries between them which could, for instance, be cross-overs or (first-order) phase transitions with critical endpoints.

Due to the limited theoretical accessibility of the phase diagram at high baryon chemical potentials [5], experimental and theoretical efforts in exploring the properties of strongly interacting matter at extreme conditions are mutually dependent. In fact, progress in understanding the baryon-dense sector of the phase diagram is mainly driven by experimental results serving as input to various models which take over where first-principle calculations of (lattice) QCD cease to work. Experimentally, a significant share of the phase diagram is accessible by colliding two nuclei at ultra-relativistic energies. In particular, the cross-over between hadronic and partonic matter, the predicted first-order phase transition between the hadronic and the quarkyonic phase, and its critical endpoint towards lower  $\mu_B$  could be created in the hot and dense collision zone (“fireball”) of two heavy ions penetrating each other. Which area of the phase diagram is traversed in a heavy-ion collision depends on the size of the colliding system, on how central the two nuclei hit each other, and on the incident kinetic energy of the nuclei.

By means of heavy-ion collisions, astrophysical conditions can be created in the laboratory for fractions of a second ( $\sim 10^{-22}$  s). When the Large Hadron Collider (LHC) at CERN generates center-of-mass energies of  $\sqrt{s_{NN}} = 5.02$  TeV in a system of two nucleons colliding in accelerated Pb nuclei, the dedicated heavy-ion experiment ALICE [6] can record signatures of a quark–gluon plasma formation, the expected state of matter in the universe shortly after the Big Bang. Also, at top energies (up to  $\sqrt{s_{NN}} = 200$  GeV in gold-on-gold collisions) of the Relativistic Heavy Ion Collider (RHIC) at Brookhaven National Laboratory, conditions dominating the early universe can be mapped e.g. by the STAR experiment [7]. With decreasing center-of-mass energies the properties of astrophysical objects like neutron stars [8] might become accessible in the laboratory. The SIS100 accelerator of the future Facility for Antiproton and Ion Research (FAIR) [9] delivers gold-ion beams for fixed-target operation of the planned Compressed Baryonic Matter (CBM) experiment [10] in the energy range of  $\sqrt{s_{NN}} = 2.7 - 4.9$  GeV which leads to very baryon-dense collision zones approaching anticipated neutron star core densities. An optional SIS300 accelerator upgrade might extend the energy range for gold-on-gold collisions available at FAIR up to 8.9 GeV in  $\sqrt{s_{NN}}$ .

Conclusions about the processes and conditions in a collision fireball can only be drawn from reaction products measured by spectrometers like ALICE, STAR, and CBM which are able to identify particles emerging from the hot and dense zone as well as their subsequent decay products. A quantitative characterization of complex collision scenarios with thermodynamic variables is provided by a thermal model [11] which is well established in the field. Assuming the system to be in thermal equilibrium when inelastic collisions between reaction products cease (so-called “chemical freeze-out”), a grand-canonical formalism can be applied to describe particle production from a thermal source constrained by conservation laws regarding baryon number, charge (isospin), and strangeness if only the “light” up ( $u$ ), down ( $d$ ), and strange ( $s$ ) quarks are taken into account. The logarithm of the grand-canonical partition function of a non-interacting hadron gas at chemical freeze-out can be written as the sum of logarithms of individual

hadronic partition functions,

$$\ln Z^{\text{GC}}(T, V, \vec{\mu}) = \sum_i \ln Z_i^{\text{GC}}(T, V, \vec{\mu}). \quad (1.1)$$

The model comprises five parameters in total—the fireball temperature  $T$ , its volume  $V$ , and the chemical potentials  $\vec{\mu} = (\mu_{\text{B}}, \mu_{\text{S}}, \mu_{\text{I}_3})$  related to the aforementioned conservation laws—three of which ( $V$ ,  $\mu_{\text{S}}$ , and  $\mu_{\text{I}_3}$ ) are fixed by baryon number conservation,

$$V \sum_i n_i B_i = Z + N, \quad (1.2)$$

charge (isospin) conservation,

$$V \sum_i n_i I_{3,i} = \frac{Z - N}{2}, \quad (1.3)$$

and strangeness conservation,

$$V \sum_i n_i S_i = 0, \quad (1.4)$$

where  $n_i$  denotes the density of particle state  $i$ ,  $B_i$  its baryon number,  $S_i$  its strangeness,  $I_{3,i}$  the third component of its isospin vector, and  $Z/N$  the summed up proton/neutron numbers of the colliding nuclei. By deriving the grand potential with respect to the total chemical potential  $\mu_i$  of particle species  $i$ ,

$$\mu_i = B_i \mu_{\text{B}} + S_i \mu_{\text{S}} + I_{3,i} \mu_{\text{I}_3}, \quad (1.5)$$

the average particle density  $n_i$  can be expressed as

$$n_i = -\frac{T}{V} \frac{\partial \ln Z_i^{\text{GC}}}{\partial \mu_i} = \frac{g_i}{2\pi^2} \int_0^\infty dp \frac{p^2}{\exp[(\varepsilon_i - \mu_i)/T] \pm 1}, \quad (1.6)$$

with the single-particle energy  $\varepsilon_i = \sqrt{p^2 + m_i^2}$ , the spin–isospin degeneracy factor  $g_i$ , and the ( $\pm$ ) sign referring to fermions/bosons.

By fitting the remaining two free parameters— $T$  and  $\mu_{\text{B}}$ —to particle yield ratios [12] measured in heavy-ion collisions with a given center-of-mass energy, one can—under the assumption of the system globally being in thermal equilibrium—mark the frozen-out collision zone on a  $(T, \mu_{\text{B}})$  phase diagram (cf. Fig. 1.2, left plot). The agreement between the measured temperature at low baryon chemical potential and the theoretical prediction concerning a cross-over between phases as well as temperature saturation at  $\sqrt{s_{\text{NN}}} \sim 10$  GeV (cf. Fig. 1.2, upper right plot) might indicate properties of a new phase during the fireball evolution. The energy dependence of the extracted baryon chemical potentials hints at the highest baryon densities being produced if center-of-mass energies are low (cf. Fig. 1.2, lower right plot).

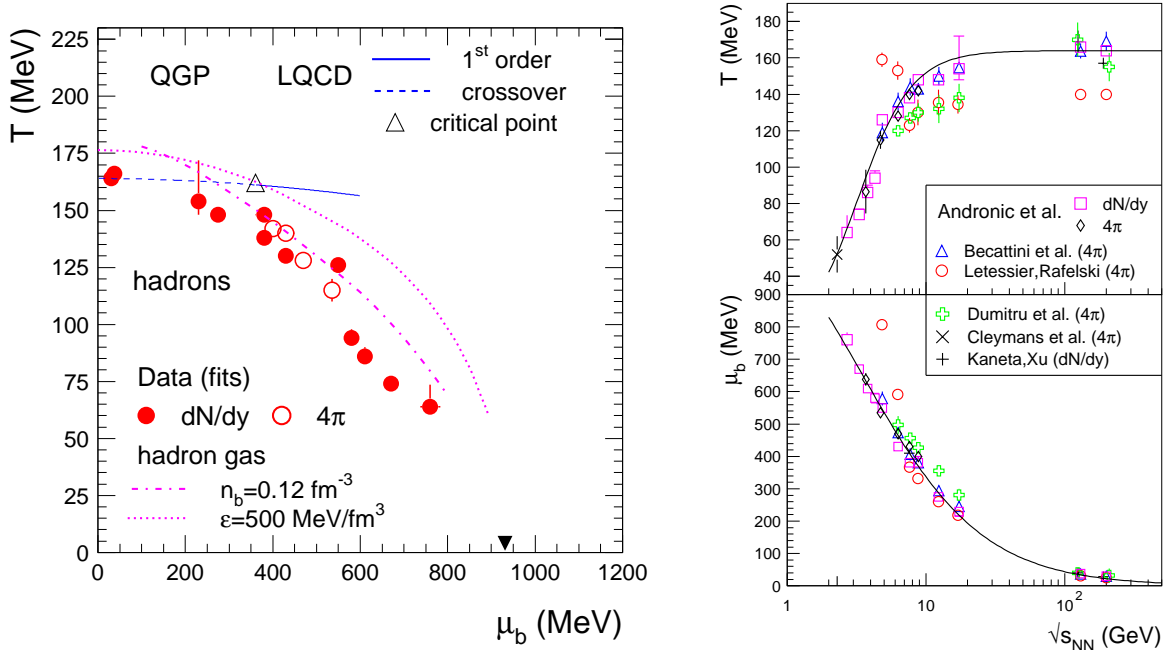


Figure 1.2: Experimentally assessed regions of the QCD phase diagram in  $(T, \mu_B)$  dimensions assuming global thermal equilibration of the hot and dense zone created in a heavy-ion collision upon hadronization. Theoretical predictions concerning a cross-over, a critical point, and a first-order phase transition from hadronic to partonic matter are marked in blue (left plot). Measured and thermally fitted chemical freeze-out temperature  $T$  and baryon chemical potential  $\mu_B$  as a function of center-of-mass energy in a nucleon–nucleon collision. The temperature curve saturates at about 160 MeV (right plot). Figures taken from [12].

Of particular interest when studying compressed baryonic matter is the role of strangeness, i.e. of hadrons containing strange or anti-strange quarks. On the quark mass scale, strange quarks of about  $100 \text{ MeV}/c^2$  in bare quark mass are relatively light compared to the heavy charm ( $c$ ), bottom ( $b$ ), and top ( $t$ ) quarks. Thus, they become accessible in heavy-ion collisions in the center-of-mass energy range of a few GeV where the collision zone is expected to be particularly dense. Before the two heavy ions collide, the system does not contain any strangeness as nucleons are bound states of up and down quarks only (cf. Eq. (1.4)). Consequently, any reaction product containing  $s$  or  $\bar{s}$  quarks must have undergone a strangeness production process in the hot and dense zone of the collision. The threshold center-of-mass energies for producing strange hadrons in proton–proton collisions are listed in Tab. 1.1.

In systems of two colliding accelerated protons,  $\Xi^-$  ( $dss$ ) baryons cannot be produced below a threshold center-of-mass energy of  $\sqrt{s_{NN}} = 3.25 \text{ GeV}$ . In heavy-ion collisions at  $\sqrt{s_{NN}}$  below the threshold value, the  $\Xi^-$  baryon can—owing to the baryon-dense environment—result from strangeness exchange reactions [13] in a multi-step process

Table 1.1: Threshold energies for different strangeness production processes in proton–proton collisions in the center of mass (middle column) and in the rest frame of one proton (right column).

reaction	$\sqrt{s_{\text{NN}}}$ (GeV)	$T_{\text{lab}}$ (A GeV)
$pp \rightarrow K^+ \Lambda p$	2.55	1.6
$pp \rightarrow K^+ K^- pp$	2.86	2.5
$pp \rightarrow K^+ K^+ \Xi^- p$	3.25	3.7
$pp \rightarrow K^+ K^+ K^+ \Omega^- n$	4.09	7.0
$pp \rightarrow \Lambda \bar{\Lambda} pp$	4.11	7.1
$pp \rightarrow \Xi^- \bar{\Xi}^+ pp$	4.52	9.0
$pp \rightarrow \Omega^- \bar{\Omega}^+ pp$	5.22	12.7

where e.g. first two  $\Lambda$  hyperons ( $uds$ ) are produced in a p–p collision which then transform into  $\Xi^- p$ . The  $\Xi^-$  yield per event in Ar + KCl collisions at SIS18 energies ( $\sqrt{s_{\text{NN}}} = 2.61$  GeV) is in disagreement with thermal-model fits (cf. Fig. 1.3). In fact, an enhancement of approximately a factor of 15 compared to the yield expected from a thermo-statistical model is reported [14]. This observation requires confirmation but might indicate that the production of (multi-)strange hadrons at sub-threshold energies enters chemical equilibrium on a different time scale than the bulk of hadrons.

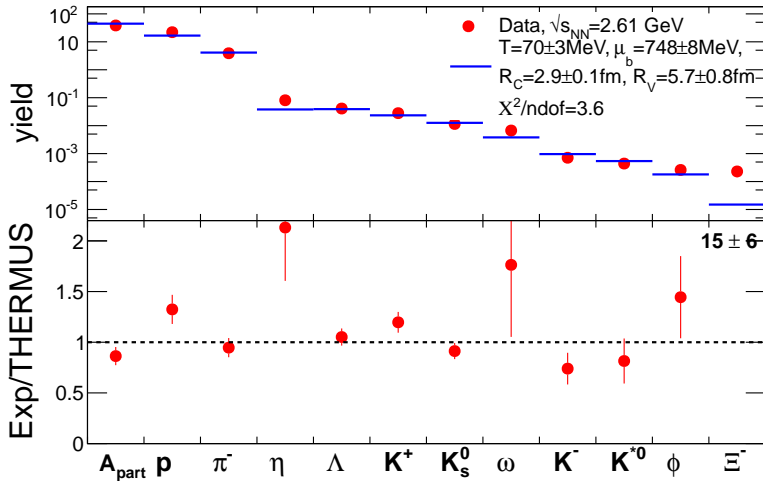


Figure 1.3: Hadron yields measured by the HADES experiment in Ar + KCl collisions at  $\sqrt{s_{\text{NN}}} = 2.61$  GeV (upper half; red dots). The horizontal blue lines result from a thermal-model fit to the data with the THERMUS package [15] (v3.0). Ratios between experimental and fitted values are given in the lower half. Figure taken from [14].

Theoretical efforts to link the experimentally observed strangeness enhancement at  $\sqrt{s_{\text{NN}}} < 10$  GeV to the role of growing partonic degrees of freedom in the compressed collision zone with increasing collision energy have in particular focused on the kink structure in the  $K^+/\pi^+$  yield ratio measured by the NA49 Collaboration at the Super Proton Synchrotron (SPS) at CERN [16]. Microscopic transport model calculations applied to the data that describe dynamically the full evolution of the fireball comprising transitions to a deconfined and/or chirally symmetric quark matter (cf. Fig. 1.4) suggest that the enhancement could be due to a partially restored chiral symmetry, rather than to the onset of deconfinement [17].

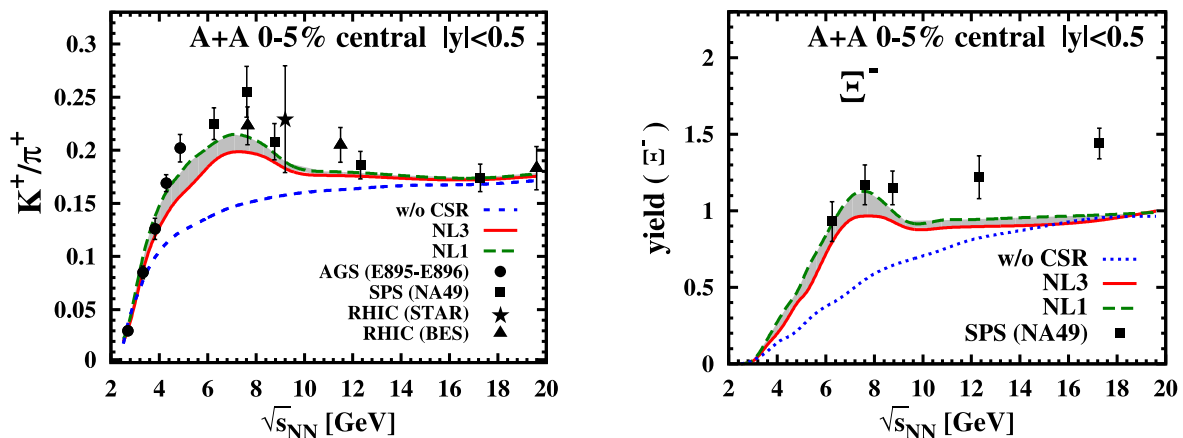


Figure 1.4: Reproduction of the pronounced kink structure in the  $K^+/\pi^+$  yield ratio measured at  $\sqrt{s_{\text{NN}}} < 10$  GeV within the PHSD model [18, 19] by including effects of chiral symmetry restoration (CSR) in the hot and dense collision zone (left plot). Prediction (due to the scarcity of data, in particular at low  $\sqrt{s_{\text{NN}}}$ ) of a similar enhancement and decline mechanism in an energy scan of the  $\Xi^-$  baryon yield (right plot). The red curve assumes a stiff nuclear equation of state (larger nuclear compression modulus) while the green curve assumes a soft EOS. Figures taken from [17].

Although there are data available with sufficient statistics for the  $K^+/\pi^+$  yield ratio in the SIS100 energy range (cf. Fig. 1.4, left plot), the experimental situation for  $\Xi^-$  yields in this range is still terra incognita (cf. Fig. 1.4, right plot). For  $\Omega$  ( $sss$ ) and anti- $\Omega$  ( $\bar{s}\bar{s}\bar{s}$ ) baryons, no data exist at all below beam kinetic energies of  $T_{\text{lab}} = 40$  A GeV [20] which corresponds to  $\sqrt{s_{\text{NN}}} = 8.9$  GeV. Measuring their yields for the first time at SIS100 energies with sufficient statistics would allow for investigating the anticipated impact of starting deconfinement and chiral symmetry restoration on multi-strange antibaryon production in a compressed baryonic environment (cf. Fig. 1.5). For  $\bar{\Omega}^+$  production in the dense collision zone, the excess yield resulting from partonic degrees of freedom in a PHSD transport simulation is much more pronounced than in the  $\Omega^-$  case. Although both the threshold energies for direct  $\bar{\Omega}^+$  production in primary p-p collisions (cf. Tab. 1.1) and for multi-step sub-threshold production via  $\bar{\Xi}^+ K^+ \rightarrow \bar{\Omega}^+ \pi^+$  are higher than for  $\Omega^-$  (sub-threshold production via  $\Lambda \Xi^- \rightarrow \Omega^- n$  and  $\Xi^- K^- \rightarrow \Omega^- \pi^-$ ),

allowing for partonic degrees of freedom in the transport simulation hints at almost balanced  $\Omega$  and anti- $\Omega$  production also at SIS100 energies (compare Fig. 1.5, left plot, to Fig. 1.5, right plot). The statistical-only error bars are (if visible at all) rather small and do not take into account systematic uncertainties of the transport approach. However, the discrepancies between expected  $\bar{\Omega}^+$  yields from pure hadronic processes (HSD) and from partially partonic mechanisms (PHSD)—in particular at SIS100 energies—of up to two orders of magnitude suggest with emphasis measuring  $\Omega$  (anti-)baryons in baryon-dense environments.

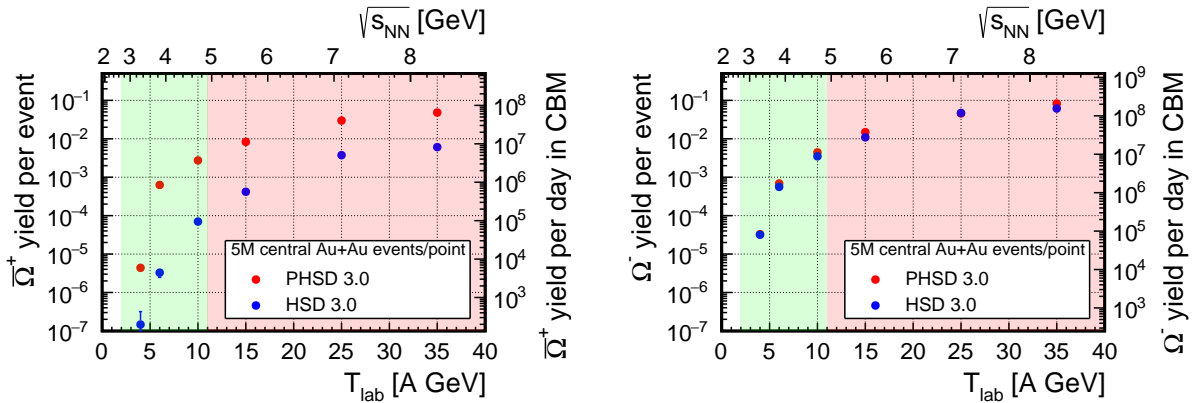


Figure 1.5: Predicted excess yield (red dots compared to blue dots) due to partonic degrees of freedom in the fireball evolution within the (P)HSD 3.0 transport model of  $\bar{\Omega}^+$  (left plot) and  $\Omega^-$  (right plot) baryons per event in the kinetic beam energy range corresponding to  $1.88 \text{ GeV} < \sqrt{s_{\text{NN}}} < 8.87 \text{ GeV}$ . A coarse estimate of the production yield within 24 hours of continuous CBM operation at design interaction rates of 10 MHz is indicated by the right-hand ordinates (for details see text). The green-shaded area marks the SIS100 energy range while the red-shaded area could be explored by SIS300 beams. Plots taken from [21] showing transport simulation results from [22].

Accumulating sufficient statistics in multi-strange (anti-)baryon measurements at sub-threshold energies requires high interaction (collision) rates and imposes challenging constraints on the data acquisition (DAQ) system due to complex event topologies and signatures of such rare probes. A hierarchical trigger system with first-level hardware triggers is not feasible for an  $\Omega$  physics program where  $\bar{\Omega}^+$  mostly decays into  $\bar{\Lambda}K^+$  with  $\bar{\Lambda}$  further decaying into  $\bar{p}\pi^+$  which does not show a characteristic trigger signature in the detector like a high transverse momentum (the CMS experiment at LHC, for instance, triggers on high- $p_T$  leptons to identify Higgs events [23]). The physics cases of (double- $\Lambda$ ) hypernuclei [24] and anti-kaonic nuclear clusters [25] at SIS100 energies impose similar constraints on experiments. Hypernuclei which are bound states of nucleons ( $p, n$ ) and hyperons ( $\Lambda, \Xi, \Omega$ ) extend the table of nuclides into a third strangeness dimension. In baryon-dense heavy-ion reactions, they can be produced via coalescence of hyperons (in particular  $\Lambda$ ) with nucleons or light nuclei. They decay weakly into charged hadrons, e.g.  ${}^6_{\Lambda\Lambda}\text{He} \rightarrow {}^5_{\Lambda}\text{He} + p + \pi^-$ ,  ${}^5_{\Lambda}\text{He} \rightarrow {}^4\text{He} + p + \pi^-$ . Notationally, the

superscript denotes the number of baryons and the subscript depicts the hyperons that compose the hypernucleus. The element symbol is specified by the number of protons. Data for double- $\Lambda$  hypernuclei are very scarce due to the low production cross section, even in the SIS100 energy range where the expected yields are maximal (cf. Fig. 1.6, left plot). A high-rate experiment therefore has a substantial discovery potential with respect to these rare probes. In the sector of deeply bound anti-kaonic clusters due to the attractive  $K^-N$  interaction, indications of  $ppK^-$  bound states via their strong  $\Lambda p$  decay channel (with consequent  $\Lambda \rightarrow p\pi^-$  decay) have been reported [25] (and references therein). However, no experimental signature of larger bound anti-kaonic systems like the predicted  $ppnK^-$  (decaying into  $\Lambda d$ ) and  $ppK^-K^-$  (decaying into  $\Lambda\Lambda$ ) states [26] has been observed yet. According to thermal model predictions (cf. Fig. 1.6, right plot), doubly anti-kaonic cluster production shows a maximum within or close to the SIS100 energy range. Yields per event (concerning the normalization: one expects about 4  $\Lambda$  hyperons at  $\sqrt{s_{\text{NN}}} = 3.3$  GeV and about 50 at  $\sqrt{s_{\text{NN}}} = 8.9$  GeV in central Pb+Pb collisions [20]) are low but not out of reach for a dedicated high-rate experiment.

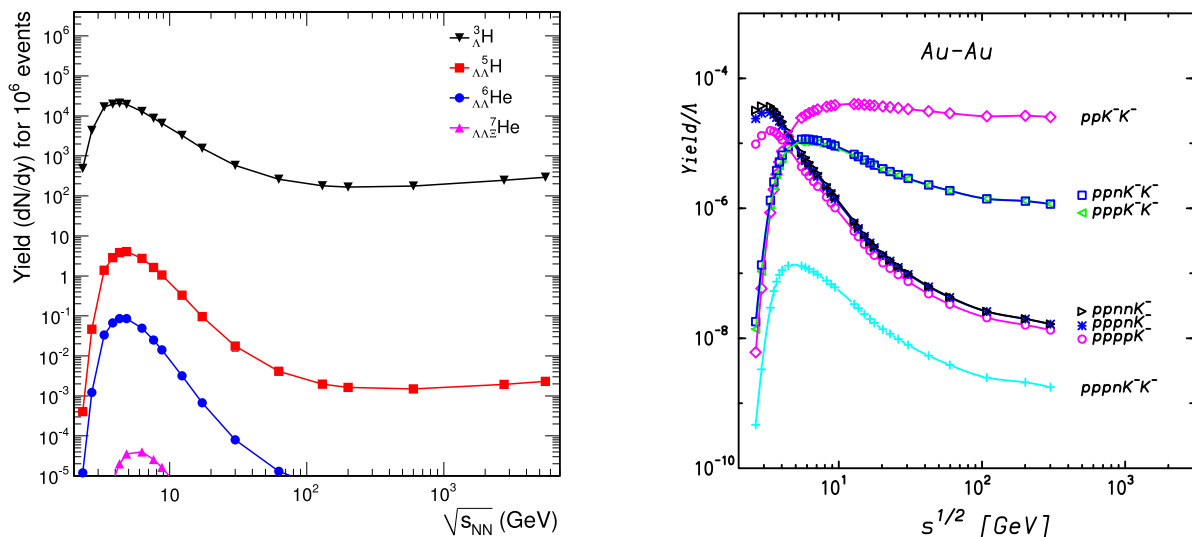


Figure 1.6: Production yields from one million events calculated with a thermal model for selected (double-) $\Lambda$  hypernuclei in central Au+Au or Pb+Pb collisions at mid-rapidity as a function of collision energy (left plot, adapted from [27]). Thermal-model yields per  $\Lambda$  hyperon of theoretically predicted (doubly) anti-kaonic clusters in Au+Au collisions as a function of collision energy (right plot, adapted from [28]).

The CBM experiment at FAIR is (not exclusively) designed for high-statistics measurements of rare probes via their decays into charged hadrons, i.e. pions, kaons, protons, and their respective antiparticle. To circumvent unavoidable trigger latency in a centrally controlled data acquisition system, the front-end digitization electronics in CBM send their data upon availability—without an explicit readout request—to a computing farm where data streams are scanned on the fly (online) for signatures of rare probes or other observables currently under study. Promising time intervals in the data streams

are then written to disk for further offline inspection and physics analysis. This way, data acquisition at the detector level is not put on hold while high-level trigger decisions are taken in the back end. The online selection of interesting events requires a partial reconstruction of reaction products on the computing farm. For  $\bar{\Omega}^+$  measurements, one would e.g. try to identify data time intervals that contain  $K^+$  mesons according to the primary decay channel. The two independent measurements that are at least necessary for particle identification of charged hadrons in CBM are made by a silicon tracking system (STS) residing in a magnetic dipole field which provides momentum and charge information and by a time-of-flight (TOF) wall that contributes the particle's time of flight along its reconstructed track.

To accumulate sufficient statistics for rare probes, CBM is designed to run at interaction rates of up to 10 MHz of gold-on-gold collisions which result from gold-ion beam intensities of the SIS100 accelerator on the order of 1 GHz impinging on a gold target foil right in front of the CBM spectrometer that has a 1 % interaction probability with the beam. Given the branching ratio of 0.68 for  $\Omega \rightarrow \Lambda K$  [29], assuming a downscale factor of 10 % from central collisions to the entire range of impact parameters, and anticipating total acceptance and reconstruction efficiencies of 2.3 % for  $\bar{\Omega}^+$  and 4.3 % for  $\Omega^-$  [30], the estimated production yields in one day of beam-on-target time (ignoring the duty cycle of the accelerator) are indicated by the right-hand ordinates of Fig. 1.5. At  $T_{\text{lab}} = 10 \text{ A GeV}$  (4.7 GeV center-of-mass energy), about  $3.7 \times 10^6$   $\bar{\Omega}^+$  and  $1.1 \times 10^7$   $\Omega^-$  baryons are expected per day in CBM according to PHSD calculations. For (double- $\Lambda$ ) hypernuclei at  $T_{\text{lab}} = 10 \text{ A GeV}$  (cf. Fig. 1.6, left plot), the expected yields per one week of beam-on-target time amount to 3000 for  ${}^5_{\Lambda\Lambda}\text{H}$  and 60 for  ${}^6_{\Lambda\Lambda}\text{He}$  assuming a branching ratio of 10 % for two sequential weak decays and an efficiency of 1 % [31]. Although CBM is not the only (planned) experiment operating in the SIS100 energy range, its design interaction rate is unique worldwide (cf. Fig. 1.7). Any rare observable to be possibly measured in the fixed-target program of STAR would require an additional factor of 5000 of beam-on-target time to collect the same amount of statistics as CBM would do for this measurement. In terms of distilling the impact of partonic degrees of freedom on  $\Omega$  baryon production in this energy range and of producing double- $\Lambda$  hypernuclei at highest baryon densities, there is currently no experimental alternative to CBM.

While the online event-selection algorithms on the computing farm filter the incoming data streams and only allow a fraction of all data to be stored permanently, the detector system of CBM is data agnostic and needs to cope continuously with the combined high collision rate and high particle multiplicity per collision at SIS100 energies. The TOF wall which is conceptualized as an array of multi-gap resistive plate chambers (MRPCs) faces particle fluxes between  $1 \text{ kHz/cm}^2$  at the periphery up to several tens of  $\text{kHz/cm}^2$  close to the beam pipe [33]. MRPCs utilize as underlying physical detection process the acceleration and multiplication of electrons in a uniform electric field applied to gas-filled gaps between several resistive glass plates. A small initial number of primary electrons is stripped off from gas molecules which are ionized by charged incident particles and develops into an avalanche of secondary charges. The consequential accumulation of electrons and gas ions on opposing glass plates causes a local breakdown of the electric field in the affected gaps degrading the detector response function if external irradiation

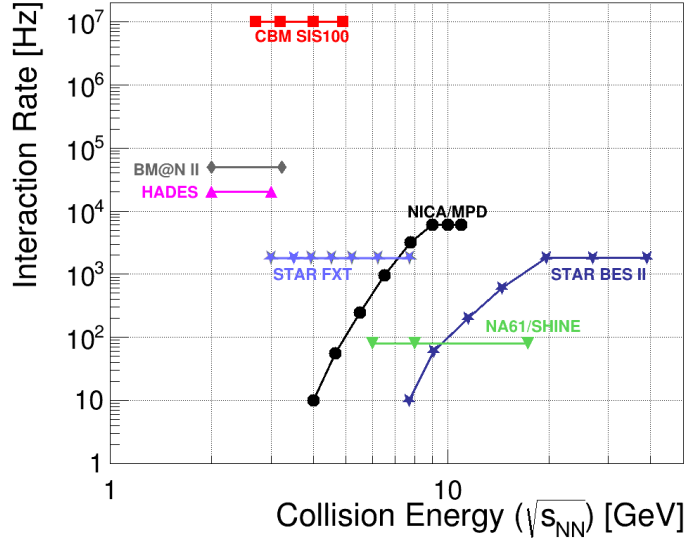


Figure 1.7: Maximum interaction rates at (planned) heavy-ion experiments operating between 1 and 40 GeV in  $\sqrt{s_{NN}}$ . HADES, BM@N II, CBM SIS100, STAR FXT, and NA61/SHINE are experiments with fixed-target operation while NICA/MPD and STAR BES II record head-on collisions of two accelerated heavy-ion beams. Figure adapted from [31] regarding the extent of the STAR fixed-target program [32].

continues. On a relaxation time scale proportional to the resistivity of the employed glass, the E-field in the gaps is recovered by dissipation of these charges via the external high-voltage power supply which allows for compensating bulk currents through the glass. Owing to the multi-hit scenario created on counter surfaces by large projectile and target nuclei colliding at beam kinetic energies of up to 11 A GeV, multiple signals may be induced on a single readout cell by different avalanche processes. Signal interference merges information of individual track passages through the detection volume and leads to distortions of residuals in time and position against a reference measurement which impacts the matching of correlated hits on different stations in a setup. Besides assessing efficiency and resolving capacity of MRPC prototypes in a laboratory environment with cosmic rays [34], it is therefore crucial to examine their performance under constraints that resemble operating conditions during CBM production runs. Such efforts in on-site prototype testing at particle accelerators need to be accompanied by response simulations in software to get the full picture of the rate and multi-hit capability of devices under test.

## Outline

The work summarized in this dissertation is a substantial contribution to the research and development done by the CBM-TOF working group on MRPC prototypes intended to be mass-produced for and operated at SIS100 energies at FAIR, with a focus on rate

and hit-multiplicity aspects concerning the evaluation of detector performance which are systematically investigated in experimental and simulated collision data for the first time in a synoptic fashion. In Chap. 2, the CBM experiment at FAIR is introduced, emphasizing in particular its TOF subsystem and the MRPC detector technology involved. Chapter 3 concentrates on describing a particular test beam conducted at CERN/SPS in February/March 2015 which is embedded in a series of prototype tests to which this work contributed primarily with the set-up and operation of a data acquisition system in both hardware and software. For instance, corresponding algorithms were designed for the calibration and synchronization of raw data. In the selected test beam, a prototype equipped with special low-resistive glass, aiming at a high rate capability by short recovery times for the electric field in the gaps, and a counter composed of common glass plates were exposed to moderate flux conditions in a multi-hit environment. This experimental scenario which is assessed in detail by a dedicated Monte Carlo study facilitates a direct comparison of the respective response behavior, providing two reference cases for simulations. The latter are based on a novel parametrization of the MRPC response function, presented in Chap. 4, which features a sensitivity to both incident particle flux and track multiplicity on the counter surface, implementing the time-based digitization strategy of CBM for the TOF subsystem. An existing event-based solution lacks this functionality and is replaced by a closer description of the physical reality. Results obtained for real and virtual prototypes are compared in Chap. 5 with regard to performance and matching quality as a function of both average hit multiplicities in the setup and irradiation time. At the end of the chapter, an application of the developed response model at the ongoing “mini”-CBM (mCBM) experiment [35] is discussed. A summary of the entire work is given in Chap. 6.



## CHAPTER 2

### THE CBM EXPERIMENT AT FAIR

The international accelerator Facility for Antiproton and Ion Research (FAIR) [9] will be operational on the GSI site near Darmstadt, Germany, in 2025. Upgraded existing GSI infrastructure—the heavy-ion high-current linear accelerator UNILAC and the SIS18 synchrotron—serves as pre-accelerator and injector to the SIS100 synchrotron of FAIR with a bending power (magnetic rigidity) of 100 Tm. Civil construction plans include also an option for additionally building a more powerful SIS300 synchrotron. The SIS100 accelerator is designed to deliver high-intensity heavy-ion (Au up to  $T_{\text{lab}} = 11 \text{ A GeV}$  or  $\sqrt{s_{\text{NN}}} = 4.9 \text{ GeV}$ ) and proton (up to  $T_{\text{lab}} = 29 \text{ GeV}$  or  $\sqrt{s_{\text{NN}}} = 7.6 \text{ GeV}$ ) primary beams and secondary radioactive and antiproton beams to various experiments. FAIR comprises four scientific pillars (cf. Fig. 2.1): experimental setups for atomic and plasma physics (APPA), an antiproton storage ring for hadron physics at the PANDA experiment, a fragment separator for studying the structure of exotic nuclei with the NUSTAR detectors, and a heavy-ion program to explore the properties of compressed baryonic matter (CBM). An overview of the latter is given in this chapter.

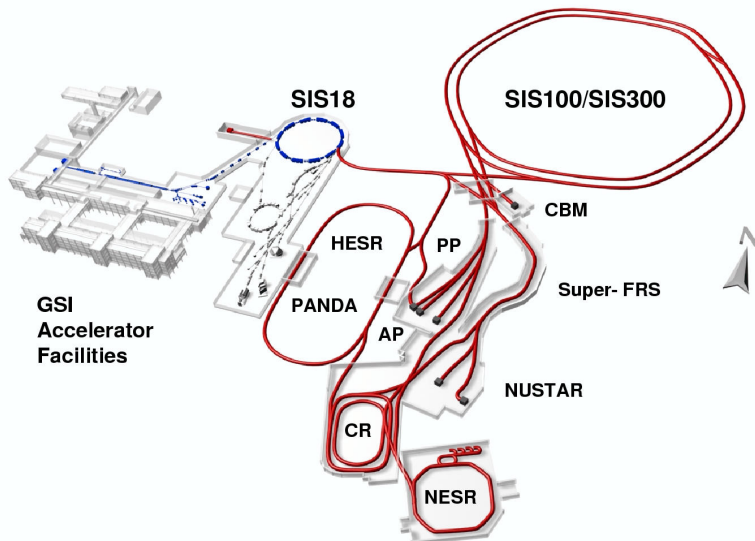


Figure 2.1: Overview of the planned FAIR facility showing existing GSI beam lines in blue and future FAIR beam lines in red. Experiments and accelerators/beam storage rings are labeled in black. Figure taken from [36].

Section 2.1 briefly introduces the physics cases to be studied in the CBM experiment and describes the detector subsystems built for particle identification. The novel free-

streaming readout paradigm of CBM is sketched in Sec. 2.2. Section 2.3 addresses the software framework CbmRoot which serves as development platform for the algorithms outlined in chapters 3, 4, and 5. In Sec. 2.4, the time-of-flight (TOF) subdetector and the underlying multi-gap resistive plate chamber (MRPC) technology are discussed.

## 2.1 Physics observables and detection instruments

The design of the CBM spectrometer is optimized for measuring the most relevant probes of high-density QCD matter in the SIS100 energy range with unprecedented accuracy. Apart from the significance of observables related to strangeness—multi-strange (anti-)baryons, (double- $\Lambda$ ) hypernuclei, deeply-bound strange objects, etc.—for understanding the evolution of the collision fireball (cf. Chap. 1), the importance of measuring dileptons (pairs of a lepton and an antilepton), particles carrying open or hidden charm, event-by-event fluctuations of conserved quantities, and the collective flow of hadrons from the collision zone has constrained the detector layout [31].

Dileptons ( $e^+e^-$  and  $\mu^+\mu^-$ ) are penetrating probes of the baryon-dense collision zone due to their ignorance of the strongly interacting medium which they are produced in. They originate either from virtual photons that are radiated by the fireball during its entire evolution or from dileptonic decays of low-mass vector mesons ( $\rho$ ,  $\omega$ ,  $\phi$ ) in the medium. The latter mechanism allows for studying the in-medium properties of vector mesons—in particular the spectral function of the  $\rho$  meson—which might unveil a partial restoration of chiral symmetry in the hot and dense zone. Charm can be studied at SIS100 energies both above (in proton-induced reactions) and below (in heavy-ion reactions) the kinetic production threshold. Hadrons containing charm quarks are assumed to be formed in the initial stage of the collision. The relative yields of charmonium, i.e. the  $J/\psi$  meson ( $c\bar{c}$ ), and open-charm states like  $D^+$  ( $c\bar{d}$ ),  $D^-$  ( $d\bar{c}$ ),  $D^0$  ( $c\bar{u}$ ), and  $\bar{D}^0$  ( $u\bar{c}$ ) are sensitive to partonic degrees of freedom which lead to charmonium suppression in the medium. Applying a thermal model, higher-order moments of event-by-event fluctuations of baryon number, strangeness, and electric charge in certain regions of phase space are expected to be influenced by a possible critical endpoint in the phase diagram if conditions during the fireball evolution are appropriate. The dependence of the excess kurtosis times the squared standard deviation,  $\kappa\sigma^2$ , of the net-proton multiplicity distribution on collision energy is considered a promising observable with this respect. The pressure gradient created in the early fireball drives a collective flow of final-state hadrons with regard to the reaction plane that is spanned by the beam axis and the impact parameter vector which connects the centers of the colliding nuclei. Its anisotropic components, the directed (in-plane) flow of strength  $v_1$  and the elliptic (out-of-plane) flow of strength  $v_2$ , are dependent on the nuclear equation of state (EOS) and thus carry information on its properties in the dense medium.

All probes sketched above have in common that either no related data exist at all in the SIS100 energy range or available statistics are insufficient for a comprehensive physics picture. The CBM apparatus (cf. Fig. 2.2) will contribute new discoveries and fill existing gaps by the interplay of its detector subsystems.

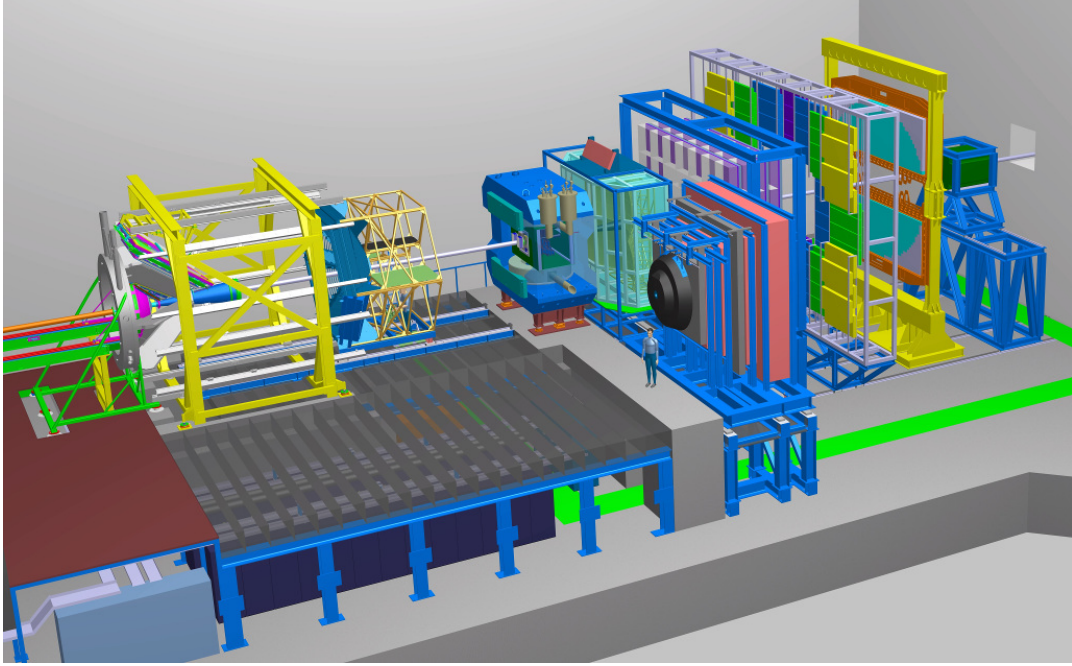


Figure 2.2: Model of the experimental setup in the future CBM cave comprising the HADES spectrometer and the CBM experiment. The beam enters the cave from the left-hand side. HADES is located on the dark-colored platform on the left while CBM components start on the grey-colored concrete block in the center. A superconducting dipole magnet houses the target, a micro-vertex detector (MVD), and a silicon tracking system (STS). Further downstream, a ring-imaging Cherenkov (RICH) detector is located that can be replaced by muon chambers (MuCh). Behind the RICH detector, a transition radiation detector (TRD), a time-of-flight (TOF) wall, an electromagnetic calorimeter (ECAL), and a projectile spectator detector (PSD) complete the setup. Figure provided by the CBM Collaboration.

### Superconducting dipole magnet

The H-type dipole magnet [37, 38] generates in its gap of 1 m along the beam axis a vertical magnetic field with a bending power of 1 Tm. This is necessary for precise momentum determination ( $\Delta p/p < 1\%$ ) of charged particles bent in the magnetic field with the Micro-Vertex Detector and the Silicon Tracking System both residing in the gap of the magnet. It comprises two circular superconducting coils in two separate cryostats. The maximum stored energy amounts to 5.15 MJ at an operating current of 686 A.

### Micro-vertex detector (MVD)

Measuring open charm at SIS100 energies requires determining the secondary decay vertices of  $D$  mesons with extremely high precision. Identifying a vertex of  $D$  mesons hadronically decaying into pions and kaons, e.g.  $D^+ \rightarrow K^- \pi^+ \pi^+$  or  $D^0 \rightarrow K^- \pi^- \pi^+ \pi^+$ ,

is complicated by background from pions and kaons which are promptly emitted from the collision zone, in particular if  $D$  meson multiplicities are low as in the SIS100 case. In addition, the mean free paths of  $D^{+/-}$  ( $c\tau = 311.8 \mu\text{m}$ ) and  $D^0$  ( $c\tau = 122.9 \mu\text{m}$ ) in the laboratory at  $\gamma = 1$  are by two orders of magnitude smaller than for  $\Lambda$  ( $c\tau = 7.89 \text{ cm}$ ),  $\Xi$  ( $c\tau = 4.91 \text{ cm}$ ), and  $\Omega$  ( $c\tau = 2.46 \text{ cm}$ ) hyperons. The dedicated Micro-Vertex Detector (MVD) [39] consists of four layers of highly granular CMOS monolithic active pixel sensors (MAPS) which are positioned between 5 and 20 cm downstream in the gap of the dipole magnet inside the vacuum vessel of the target. The vacuum condition and the very low material budget per sensor ( $50 \mu\text{m}$  thickness) are supposed to reduce multiple scattering of the decay products in the detector. Decay vertices of  $D$  mesons can be resolved with an uncertainty of only  $50 \mu\text{m}$  along the beam axis. Information from the MVD can also improve the tracking capability of the Silicon Tracking System at  $p < 0.5 \text{ GeV}/c$ . Due to the limited readout speed of the MAPS technology which would lead to a pile-up of events at high beam–target interaction rates and radiation tolerance constraints in close vicinity to the target, the MVD is the only subsystem that will be operated at 300 kHz instead of 10 MHz which is the design value for CBM.

### Silicon tracking system (STS)

Momentum determination of primary and secondary heavy-ion collision products is a key to particle identification (PID). An arrangement of several parallel tracking layers capable of performing high-resolution two-coordinate measurements of traversing charged particles which are bent in a magnetic dipole field further allows for geometrical track reconstruction. This, in turn, enables a purely topological reconstruction of short-lived reaction products such as hyperons by relying only on track information of their hadronic daughter particles without a priori identifying their species. The physics program of CBM which aims at measuring rare probes by their decay products at sustained interaction rates of 10 MHz is instrumentally based on its Silicon Tracking System (STS) [40, 41]. The eight tracking stations of the STS reside in the gap of the magnet right behind the MVD but outside the target vacuum. They comprise in total about 1200 highly segmented double-sided silicon micro-strip sensors of  $300 \mu\text{m}$  thickness. The STS covers polar angles  $\theta$  with respect to the beam axis between  $2.5$  and  $25^\circ$  for the entire azimuthal angle ( $\phi$ ) range, thus constraining the (large) share of reaction phase space accessible to CBM. It is designed for efficient track reconstruction ( $\varepsilon > 95\%$ ) and precise momentum determination ( $\Delta p/p < 1\%$ ) of charged particles at momenta above  $1 \text{ GeV}/c$ . Charged track multiplicities of about 350 are faced by the STS in central Au+Au collisions at  $T_{\text{lab}} = 8 \text{ A GeV}$ . For rare probes with very low yields per event like  $\Omega$  baryons, the combinatorial background of the topological invariant-mass reconstruction can be reduced by PID information provided by an additional time-of-flight measurement.

## Ring-imaging Cherenkov (RICH) detector

The identification of dielectronic decay products (electron–positron pairs) of low-mass vector mesons like  $\rho$  and  $\omega$  to beyond charmonium ( $J/\psi$ ) is one pillar of the dilepton program of CBM. Electrons can be identified by means of Cherenkov radiation in e.g. a  $\text{CO}_2$  radiator gas up to a few  $\text{GeV}/c$  in momentum where the Cherenkov light produced by pions starts to become increasingly indistinguishable from the electronic production (momentum threshold:  $4.65 \text{ GeV}/c$ ). In CBM, the Ring-Imaging Cherenkov (RICH) [42, 43] detector achieves pion suppression factors of above 100 for momenta up to  $8 \text{ GeV}/c$  and is the main dielectron identification tool by matching extrapolated charged particle tracks from the STS to Cherenkov rings originating from reflected and focused Cherenkov radiation. The detector is located behind the dipole magnet and consists of a  $1.7 \text{ m}$  long  $\text{CO}_2$  gas vessel, two segmented spherical-glass focusing mirrors divided into two halves above and below the beam pipe, and two photodetector planes registering the emitted UV light with multi-anode photomultiplier tubes. The Cherenkov rings appearing in the photodetector planes are expected to be formed by about 20 detected photons.

## Muon chambers (MuCh)

The second pillar of the dilepton program of CBM are the measurement of charmonium via its decay into  $\mu^+\mu^-$  pairs and complementary measurements of the dimuonic decay channels of low-mass vector mesons. The latter contributes to a better understanding of the physical and combinatorial background of lepton pairs due to its fundamentally different sources in the dielectronic and dimuonic channels. Owing to their high penetrating power in matter, muon detection systems commonly feature hadron absorber plates behind which only (high-momentum) muons are supposed to not have been significantly absorbed. The amount of absorber material can be adjusted to the intended measurement campaign. Muons originating from a  $J/\psi$  decay would not be considerably suppressed behind an integrated  $250 \text{ cm}$  of iron while low-momentum muons from an  $\omega$  meson decay would get absorbed by a factor of 10. For low-mass vector meson measurements at low beam energies, decay muons can be identified with much less absorber material. The definition of a muon is thus momentum dependent. The Muon Chamber (MuCh) [44, 45] detector of CBM is a compact structure of four alternating absorber and tracking stations. It can replace the RICH detector right behind the magnet for muon measurements. Each tracking station consists of three layers of detector chambers, the first two stations being composed of gas electron multipliers (GEM) and the latter two being made of straw tube detectors. Adding and removing absorber material depending on the observable under study is mechanically possible despite of the compact construction necessary to reduce the muon background from the weak decays of pions and kaons. As an additional tracking station the transition radiation detector can be used.

## Transition radiation detector (TRD)

Hypernuclei decay i.a. into doubly charged nuclear fragments ( ${}^4\text{He}$  and  $d$ ) which cannot be separated by the Time-of-Flight system alone if PID information is needed in addition to the decay topology reconstructed based on STS data. Measuring the specific energy loss of these particles would improve the reconstruction capability of CBM with respect to hypernuclei. Electron identification by the RICH detector is limited in momentum due to the onset of pionic Cherenkov radiation. Both issues are addressed by the Transition Radiation Detector (TRD) [46, 47] positioned behind the RICH detector and in front of the Time-of-Flight wall. The TRD station consists of four detector layers which are composed of individual detector modules each comprising a radiator and a Xe/CO<sub>2</sub> based multi-wire proportional chamber (MWPC). Only electrons above 1 GeV/c in momentum produce soft X-ray photons in the radiator which are detected in the MWPC in addition to the particle's energy loss due to ionization in the gas. The signature that electrons leave in the TRD is thus unique. Providing an electron transition radiation efficiency of 90 % and a pion suppression factor of 10–20, the TRD improves the quality of dielectron measurements in CBM. It also serves as an intermediate tracking station which positively contributes to matching STS tracks with hits in the Time-of-Flight wall.

## Time-of-flight (TOF) wall

Pions, kaons, and protons (particles and antiparticles) which are either direct probes of the collision zone or “long-lived” daughter particles of rare probes such as hyperons can be unambiguously identified by their mass and their charge. If the momentum is known, the particle mass can be calculated from its velocity which, in turn, requires knowledge of the time difference between a particle's production and its detection and of the associated trajectory length. To separate  $\pi$ ,  $K$ , and  $p$  up to a few GeV/c in momentum, the resolution of the time-of-flight measurement is the limiting factor. The Time-of-Flight (TOF) [48, 49] wall of the CBM experiment in combination with an appropriate start detector solution serves this purpose. A system time resolution of better than 80 ps and a detection efficiency of above 95 % make it the backbone of hadron identification in CBM. It not only enables PID of primary pions, kaons, and protons emitted from the collision zone but also substantially reduces combinatorial background in invariant-mass spectra of hyperons generated from STS track information. The worse the signal over background ratio of rare probes, the more important an independent time-of-flight measurement becomes, as for  $\bar{\Omega}^+ \rightarrow \bar{\Lambda}K^+$  and  $\Omega^- \rightarrow \Lambda K^-$ . The wall covers an active area of about 120 m<sup>2</sup> and is positioned at 6 m downstream the beam line. Large-area multi-gap resistive plate chambers (MRPCs) varying in size with a high rate capability are used as detection technology. The TOF system is described in more detail in Sec. 2.4.

## Electromagnetic calorimeter (ECAL)

Direct photons which are produced in the early stage of the collision carrying undisturbed information of the conditions at production time through the fireball can be detected by electromagnetic showers in lead absorber plates. This argument extends to the measurement of the (semi-)photonic decay channels of  $\pi^0 \rightarrow \gamma\gamma$ ,  $\eta \rightarrow \gamma\gamma$ , and  $\omega \rightarrow \pi^0\gamma$  which is necessary for counter-checking the contribution of the corresponding Dalitz decays—e.g.  $\pi^0 \rightarrow \gamma e^+e^-$ —to dielectron measurements. In CBM, the Electromagnetic Calorimeter (ECAL) [50] measures photons by the energy deposited in a “shashlik”-type stack of lead absorber plates interspaced with scintillator tiles as active material. Wavelength-shifting fibers penetrate the stack orthogonally to transport the visible light produced in the scintillation material from the radiated shower energy to photomultipliers. The 1088 “shashlik” stacks of dimensions  $6 \times 6 \text{ cm}^2$  are grouped in two rectangular blocks above and below the beam pipe which can be rearranged to accommodate different experimental conditions.

## Projectile spectator detector (PSD)

The analysis of event-by-event fluctuations crucially depends on precise knowledge of the centrality class of the event, i.e. how central the projectile nucleus hit the target nucleus. Collective flow of hadrons can only be studied quantitatively if the reaction plane can be well defined. Both event characteristics are linked to the number of projectile nucleons that do not participate in the collision (spectators) and can be deduced from the energy distribution of projectile fragments and forward going particles moving close to the beam axis. The Projectile Spectator Detector (PSD) [51, 52] designed as a compensating hadronic calorimeter performs the determination of collision centrality classes with an uncertainty of better than 10 % and resolves the reaction plane angle with a worst-case accuracy of  $40^\circ$ . In total, the PSD comprises 44 modules each made of 60 lead/scintillator sandwiches of transverse dimensions  $20 \times 20 \text{ cm}^2$ . Scintillation light is collected by fiber tiles which are read out by micro-pixel avalanche photodiodes (MAPD).

## 2.2 Data acquisition and online event selection

Identifying candidate events that might contain rare probes like open charm or multi-strange baryons at continuous beam–target interaction rates of 10 MHz does not only impose challenging requirements on the individual subsystems of CBM, e.g. a high rate capability and—in the same time—a high radiation tolerance, but also necessitates a novel readout paradigm concerning each subsystem and the entire apparatus. Trigger patterns for rare-probe detection cannot be implemented straightforwardly in hardware as a significant share of detector raw data needs to be processed, including track reconstruction, to find signatures of  $D$  meson or  $\Omega$  baryon decay topologies in the data. The subsystems in CBM thus push all digitized detector response messages autonomously

towards a high-performance computing farm which serves as a first-level event selector (FLES) [53]. In fact, no low-level event filtering is done prior to this stage.

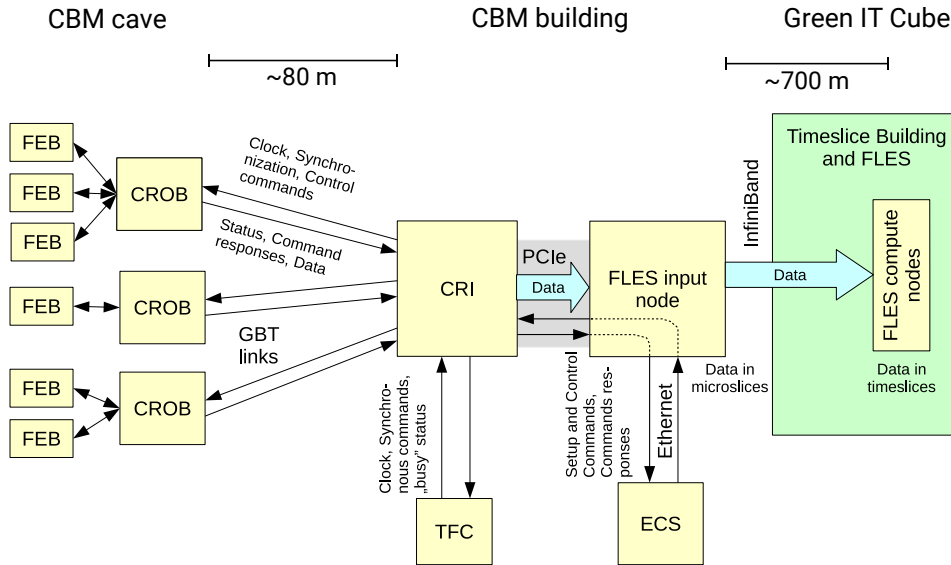


Figure 2.3: Sketch of the self-triggered readout concept of the CBM experiment. Numerous front-end boards (FEB) hosting the front-end digitization electronics push any available raw data to a layer of (common) readout boards (CROB) which, in turn, concentrate many electrical input connections into single optical data uplinks towards the common readout interface (CRI) layer. The CRI boards serve as gateway to the FLES network. The latter consists of input and compute nodes. A Timing and Fast Control (TFC) system keeps the entire readout chain in synchronization while the Experiment Control System (ECS) implements configuration access and readout of control registers. Details are explained in the text. For simplification, the sketch focusses on the data flow of only a few FEBs via CROBs to a single CRI board residing—together with others—in one of many FLES input nodes. Figure adapted from [54].

The data flow from the detector subsystems to the FLES is sketched in Fig. 2.3. All analog detector signals exceeding some detection threshold are digitized by the subsystem-specific front-end electronics (FEE) integrated into front-end boards (FEB) which are mounted in close vicinity to the detection instruments. In a self-triggered manner, i.e. without any readout request, these data are pushed upon availability to an aggregation layer of readout boards (CROB) via electrical connections. The CROB layer [55] is data agnostic and concentrates several electrical FEB inputs into a single optical output for data transport ( $\sim 80$  m) from the CBM cave underground to the ground level of the CBM building. In the absence of a global readout trigger signal that would associate raw data with an event, the detector information needs to be synchronized across all

subsystems to preserve the physical correlation of data in time for the FLES algorithms to reconstruct events both in time and space. The time stamps that are generated by the front-end electronics along with detector response messages thus need to be derived from a common reference clock signal which is provided by the Timing and Fast Control (TFC) system [56]. The value of a time stamp corresponds to the number of reference clock cycles the digitization electronics have counted at the point in time when digitization takes place. A system-wide synchronous reset of these clock-cycle counters is triggered by critical low-latency synchronization messages generated by the TFC system. Both the reference clock signal and synchronization messages are transported to the front-end layer via downlinks of the CRI boards which receive the aggregated data streams from the front-end electronics. The Common Readout Interface is the first stage in the readout chain which explicitly reads the time stamps of incoming data to partition them into data containers representing a fixed time interval of about  $1\ \mu\text{s}$ . These “microslices” of data contain an index which is incremented synchronously throughout all CRI boards in CBM which allows for matching data between different (parts of) subsystems. Depending on the experimental snapshot which is represented by a microslice, its size is—in contrast to its duration—variable. The CRI boards are intended to be plugged into the FLES input nodes located in the CBM building. They forward the system clock signal and synchronization commands from the TFC system to the front-end layer and send and receive slow-control commands (setting of FEE configuration registers, reading of FEE status registers) issued by the Experiment Control System (ECS).

Via an optical fiber connection of 700 m, the FLES input nodes form a high-throughput InfiniBand network with the FLES compute nodes that are located in the Green IT Cube of FAIR, a six-story high-performance computing center. The purpose of this network and of the inter-node data management software FLESnet operating on it is the encapsulation of a series of microslice containers originating from different detector subsystems into a self-contained “timeslice” (cf. Fig. 2.4, left) of data that can be independently processed by event-reconstruction algorithms on a single FLES compute node. Each compute node processes data from a different timeslice, with some overlap in time to account for physical events possibly split by a timeslice border. At beam–target interaction rates of 10 MHz in the SIS100 energy range, the raw data rate in the FLES is estimated to be on the order of 100 GB/s [49]. Even if such a high sustained rate could be permanently stored for offline analysis, it would not be very efficient given the low multiplicities of rare probes that CBM addresses. Huge amounts of data would need to be filtered in search of rare-probe signatures and mostly be discarded in the end. CBM is designed to perform this operation online prior to permanent storage. Depending on the physics observable under study, a certain share of raw data, mostly from the STS for track reconstruction, possibly extended to data from a PID detector like TOF, i.e. a subset of timeslice components is inspected online on the FLES compute nodes to estimate by partial event reconstruction if the data under study are a promising candidate for a detailed offline analysis. By applying this online data reduction scheme, CBM aims at a final data archival rate of 1 GB/s only.

The tracking algorithms devoted to online event selection need to be efficient, fast, and optimized for vectorized and parallel computations, utilizing modern many-core

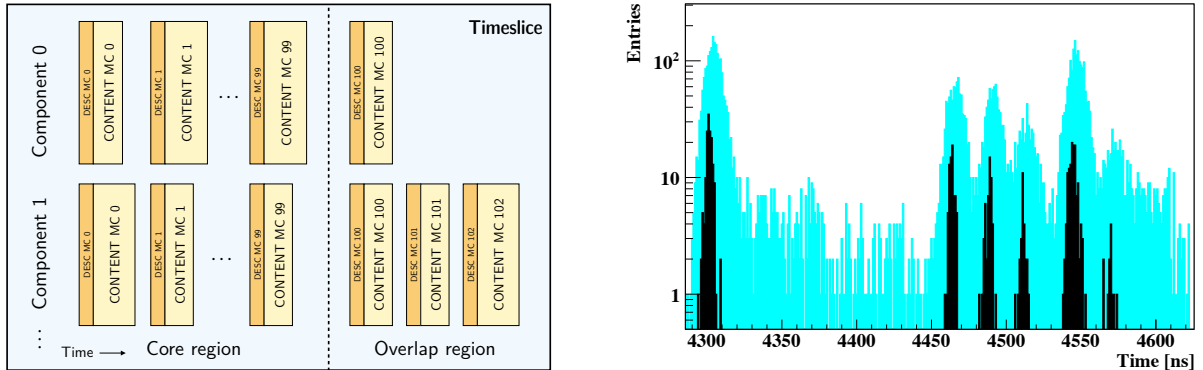


Figure 2.4: A fixed amount of consecutive microslices (here: MC for micro-container) from different components (usually a part of a detector subsystem) of the experiment form a timeslice container consisting of a core and an overlap region in case of event splitting across borders (left plot, taken from [57]). Simulated four-dimensional track reconstruction (black bars) from detector hit information (cyan bars) within a timeslice at 10 MHz interaction rate distributing time intervals between events exponentially (right plot, taken from [58]).

CPU/GPU computing architecture. The FLES software package [58] which meets these demands requires as input a geometric description of the tracking detector and hits of charged particles intersecting the geometry. A prerequisite is that the latter are built, also online, from detector raw data which depends on an efficient online calibration of the digital detector response. First, a track-finding stage based on a Cellular Automaton (CA) groups detector hits into tracks in time and space [59] which are then fitted by a Kalman Filter (KF) to precisely estimate the track parameters. A good track-fit quality helps reducing the combinatorial background of invariant-mass spectra of topologically reconstructed short-lived particles.

After fitting, tracks are combined into clusters which fill a series of non-empty histogram bins in time (cf. Fig. 2.4, right) and can thus be identified as tracks belonging to the same physical event. This histogram method does not allow for disentangling event overlaps which occur in 22% of cases at collision rates of  $r = 10$  MHz, assuming an exponentially distributed time between two consecutive collisions,

$$f(t) dt = e^{-rt} r dt, \quad (2.1)$$

and a time distribution of hits from a single event in the detector of 25 ns. Instead, the different primary vertices of overlapping events (four-dimensional interaction points) would need to be determined by extrapolating fitted tracks to the target zone, followed by a multi-vertex analysis. Identifying event structures in the time distribution of raw data directly [60] is also possible but much more susceptible to background from delta electrons produced in the target and detector noise due to the lack of correlation introduced by tracking.

After event building from particles that leave tracks in the detector, the KF Particle

Finder package reconstructs short-lived particles, i.e. the rare probes of interest which decay ahead of the tracking stations, from the tracks of their long-lived daughter particles. Ultimately, events of interest are selected based on the trigger signatures found during online reconstruction and written to disk. If the information about the event topology reconstructed from STS tracks alone is not sufficient to take a trigger decision, track following and propagation methods to PID instruments further downstream using STS tracks as seeds [61] need to be run online at additional computational cost.

### 2.3 Simulation and reconstruction in CbmRoot

A feasibility study of the online event-selection strategy developed by CBM is a synergy of hardware and software aspects. On the hardware side, prototypical high-throughput readout-chain components need to be tested under realistic in-beam conditions. Concerning software, it is necessary to realistically simulate a free-streaming data flow from the front-end digitizers to the computing farm in order to design online reconstruction algorithms to be run on the FLES. As most heavy-ion experiments of the past could rely on hardware-triggered events as input to their reconstruction and analysis frameworks, CBM is required to implement—building upon familiar event-by-event processing—a data-handling concept as well as algorithms that operate on containers representing fixed time intervals, i.e. timeslices.

The standard framework for future FAIR experiments comprising simulation, reconstruction, and data-analysis functionality, FairRoot [62], makes use of existing event-based infrastructure provided by ROOT [63]. CbmRoot, in turn, inherits from FairRoot and implements experiment-specific data classes. The entire code is compiled into shared libraries which are loaded on demand by the ROOT executable which processes user-supplied configuration macros for specific purposes. At the heart of a FairRoot run, the run manager class governs initialization and execution of a hierarchy of tasks (implementations of ROOT’s TTask class) each of which processes the output data of the preceding task and generates input data for its successor. All tasks are sequentially executed by the run manager to transform a set of initial data classes (e.g. detector raw data) to the desired output format (e.g. tracks). If several such sets of data (events) are available, the run manager repeatedly calls the sequence of registered tasks, once for each event. All data of the same type produced by a task within the scope of one event reside in a TClonesArray entry of a TTree branch, utilizing functionality of ROOT. Branches declared persistent are serialized and streamed into a ROOT output file which might serve as input to a subsequent FairRoot run.

As the TClonesArray container is indifferent to being considered an event or a timeslice, the consequential starting point for time-based data handling is re-interpreting it as the latter [64]. However, nuclear collision seeds produced by microscopic transport codes like UrQMD [65, 66] or PHSD [18, 19] for a simulation are propagated through a virtual description of the detector geometry (cf. Fig. 2.5) by Monte Carlo (MC) transport engines [67] event by event. Primary particles from the collision zone are pushed onto an event stack and then—in reverse order—transported with a defined step size through

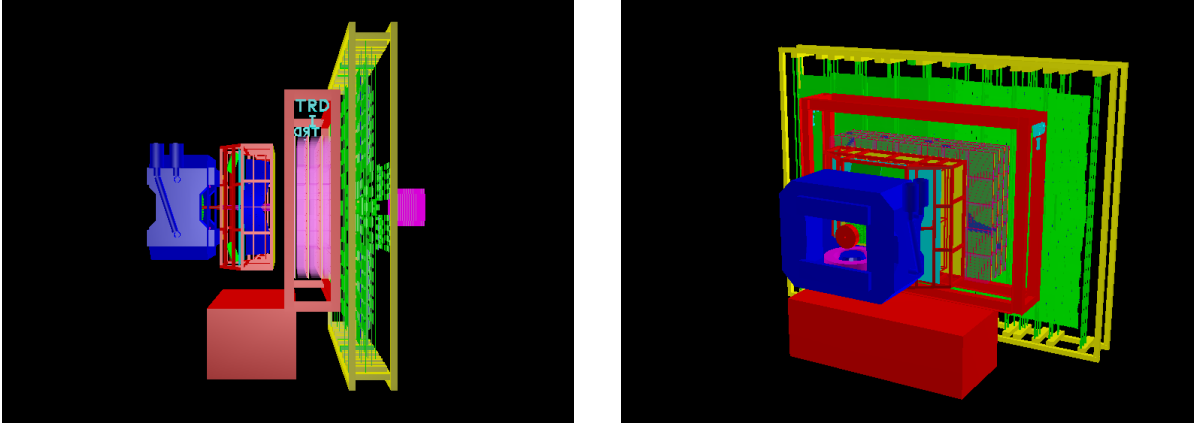


Figure 2.5: Side view of the dielectron setup of the CBM experiment comprising, from left to right, the dipole magnet housing MVD and STS, the RICH detector, TRD, TOF, and PSD (left image). Angled view of the same setup (right image). The ECAL is not included in both cases. Geometry definitions are directly made in ROOT utilizing the TGeo geometry modeler [68].

“passive” and “active” detector material. Intersections with the latter can be saved as Monte Carlo points in a different TClonesArray for each subsystem participating in the simulation. For each step, the MC engine takes into account possible decays into secondary particles and interactions with the traversed material (energy loss, Coulomb multiple scattering, etc.).

The (digital) response of the detector to these MC tracks needs to be saved in timeslices to model data production in the real experiment. Timeslices, though, can contain multiple events. Consequently, an event-based input needs to be transformed asynchronously into a time-based output, i.e. the run manager must not issue a write request to the TClonesArray buffers when all tasks have been executed for the current input event but only if the output timeslice can actually be closed. Figure 2.6 shows the different stages in the time-based simulation of the CBM experiment. The output of the MC simulation is event-based which serves as input to the digitization stage. Here, the assignment of MC points to events is removed by placing points according to the sampled start time of their original events (cf. Eq. (2.1)) onto a continuous, sorted time axis. This leads to an overlap of events in case time intervals between them are small; fast particles from an event with a later start time are delivered to the digitizer algorithms for detector response calculations before slow particles from an event with an earlier start time, like in the real experimental situation. The digitizer classes buffer the response evoked by a certain particle until it can be safely assumed that the impact of any following particle would not interfere with it. Upon time-stamping, non-interfering detector messages are passed to the timeslice output buffer which is written to file when it is guaranteed that no further digital response messages that would belong to the current timeslice by their respective time stamps could still emerge from the digitization buffers which handle response interference. The time-based digitization scheme of the TOF subsystem

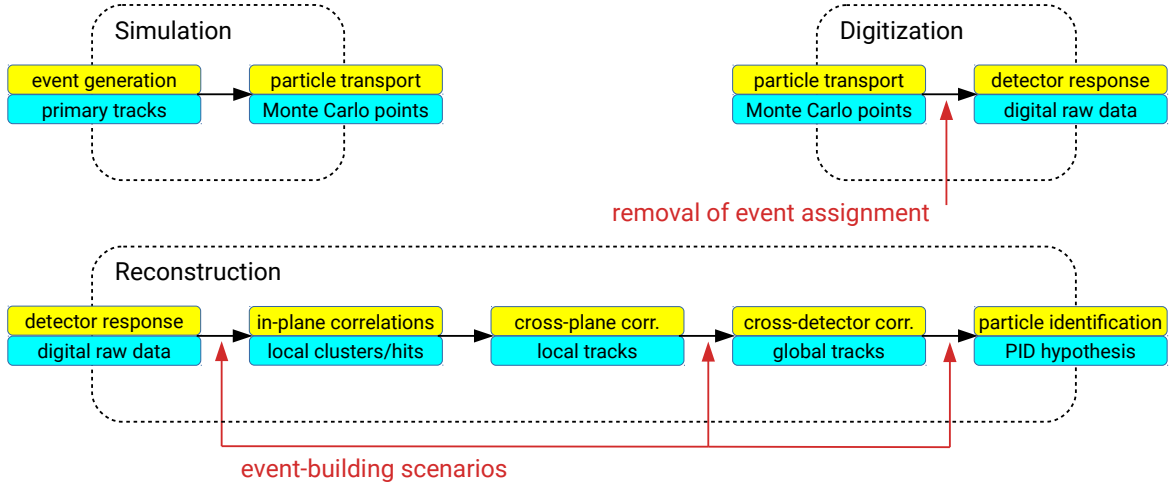


Figure 2.6: The simulation, digitization, and reconstruction chain as currently implemented in CbmRoot. The simulation is based on nuclear collision seeds which define an event. Prior to digitization, the event assignment is removed to allow for response interference handling across overlapping events. The time-based data are then reconstructed step by step by algorithms operating on timeslice instead of event containers until event structures are recovered using digitization or tracking information.

is described in detail in Chap. 4.

Timeslices are, in a subsequent reconstruction run of CbmRoot, input to cluster-, hit-, and track-finding algorithms which operate on an entire timeslice [69]. At some point in the reconstruction chain, the original event structures need to be retrieved from time-based data objects which can e.g. be done based on accumulation structures of these objects in time displayed by histograms. At latest the physics analysis of identified particles requires events to be separated again because the characterization of individual event properties (collision centrality, reaction plane angle) is a basis for understanding the collision dynamics and the relative yields of particle species.

The ROOT-based data processing is intrinsically non-parallel, i.e. does not make use of multi-core computing architecture as available in the FLES. Tasks are executed one after another by the run manager. To develop reconstruction algorithms that are supposed to run online on free data streams, a single-threaded, single-process software environment is insufficient. The FairMQ [70] approach aims at running independent tasks (e.g. cluster finding in STS and TOF) in parallel in separate processes. Internally, these parallel processes can also be multithreaded. Data are exchanged between processes utilizing message queues (MQ).

## 2.4 Time-of-flight measurements with resistive plate chambers

### 2.4.1 The time-of-flight method

From the curvature of a trajectory in the magnetic dipole field measured by the STS the momentum and the charge sign of a particle can be deduced but its species cannot be identified without an additional, independent measurement. For the rare-probe program of CBM, the identification of abundant charged hadrons ( $\pi^+$ ,  $K^+$ ,  $p$ , and their antiparticles) in a large share of reaction phase space is essential. Figure 2.7 shows the phase space spanned by lab rapidity and by the ratio of transverse momentum over mass accessible to prompt pions, kaons, and protons at upper-end SIS100 energies.

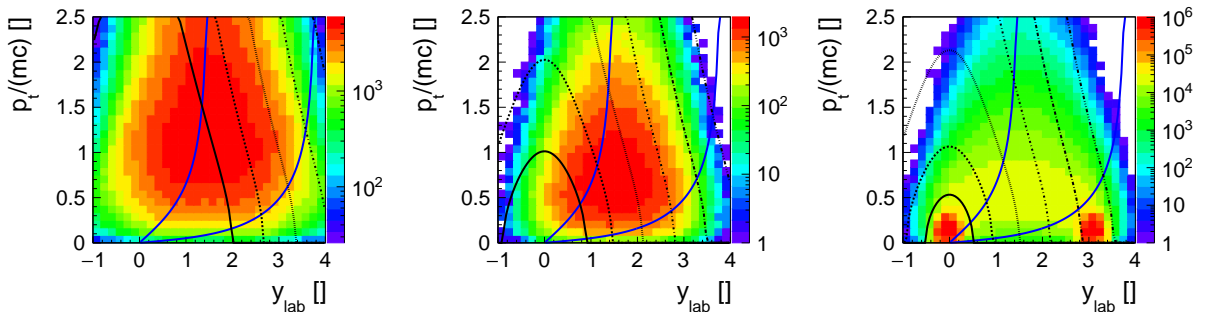


Figure 2.7: Phase space populated by (positively charged) primary pions (left plot), kaons (middle plot), and protons (right plot) originating from 100,000 UrQMD collisions of gold nuclei at  $p_{\text{beam}} = 10$  A GeV/c with minimum centrality bias. The black lines indicate constant total laboratory momentum (from left to right: 0.5, 1.0, 2.0, 4.0, 8.0, and 16.0 GeV/c) while the blue lines represent the geometrical acceptance of the STS, between  $2.5$  (right line) and  $25^\circ$  (left line) in polar angle.

In particular, the particle identification concept needs to be capable of cleanly separating pions from kaons which is challenging due to their similar masses ( $0.140 \text{ GeV}/c^2$  and  $0.494 \text{ GeV}/c^2$ , respectively) on the hadronic mass scale. To disentangle kaons from pions at mid-rapidity (here:  $y_0 = 1.53$ ), the separation power of the PID method for this case should cover the momentum range up to 3–4 GeV/c. This can be achieved by the time-of-flight method [71] which makes use of the relativistic relation between the (squared) particle mass  $m$ , its momentum  $p$ , its trajectory length  $L$ , and its time of flight  $t$ ,

$$m^2 = \frac{p^2}{c^2} \left( \frac{c^2 t^2}{L^2} - 1 \right). \quad (2.2)$$

The relative uncertainty of the squared mass measurement, assuming Gaussian errors of individual contributions,

$$\frac{\sigma_{m^2}}{m^2} = 2 \sqrt{\left( \frac{\sigma_p}{p} \right)^2 + (1 + (\beta\gamma)^2)^2 \left( \left( \frac{\sigma_t}{t} \right)^2 + \left( \frac{\sigma_L}{L} \right)^2 \right)}, \quad (2.3)$$

is by a factor of about 13 ( $\beta\gamma \sim 3.5$  for minimum ionizing particles) more susceptible to errors in determining the time of flight and the track length than to errors in momentum. Usually, the bottleneck is the resolution of the time of flight which consists of a start time and a stop time measurement.

Solving Eq. (2.2) for  $t$  and considering the limit  $p \gg mc$  leads to the expression

$$|t_1 - t_2| = \frac{Lc}{2p^2} |m_1^2 - m_2^2| \quad (2.4)$$

for the absolute difference in time of flight between two different particle species at a given momentum and trajectory length. The separation power with respect to the TOF measurement is then given by

$$n_{\sigma_t} = \frac{|t_1 - t_2|}{\sigma_t} = \frac{Lc}{2p^2 \sigma_t} |m_1^2 - m_2^2|. \quad (2.5)$$

Assuming the TOF error to be the dominating contribution to the squared-mass uncertainty (cf. Eq. (2.3)) and expressing  $\sigma_t$  in Eq. (2.5) by  $\sigma_{m^2}$  only depending on  $\sigma_t$ ,

$$\sigma_{m^2} = \frac{2p^2}{Lc\beta} \sigma_t, \quad (2.6)$$

one obtains a relation between the absolute difference of two squared particle masses, the required TOF separation power, and the squared-mass resolution,

$$|m_1^2 - m_2^2| = \beta n_{\sigma_t} \sigma_{m^2}. \quad (2.7)$$

In the relativistic limit ( $\beta \rightarrow 1$ ), the widths of squared particle-mass distributions should be similar across particle species and only depend on momentum and trajectory length (cf. Eq. (2.6)). A TOF separation power of  $n_{\sigma_t} = 3$  would, for instance, be achieved if the 1.5-sigma lines of two neighboring squared-mass distributions just crossed each other. Figure 2.8 shows an idealized PID scenario utilizing the separation-power formalism of Eq. (2.7) based on simulated Monte Carlo data. The intersection points of the red PID gate lines indicate the limiting momenta above which the required separation power does not hold anymore, i.e. the squared-mass branch of one particle species becomes increasingly contaminated by its neighbor(s). The limiting momenta depend strongly on the system time resolution  $\sigma_t$ , decreasing for  $\pi/K$  separation from about 4.3 GeV/c at  $\sigma_t = 50$  ps to 3.5 GeV/c at  $\sigma_t = 80$  ps to 3.1 GeV/c at  $\sigma_t = 100$  ps.

According to Eq. (2.6), larger distances between production vertex and detection point lead to narrower  $m^2$ -distributions and thus improve the PID capability. On the other hand, the limited mean free path of K mesons in the laboratory ( $\gamma c\tau = 8.4$  m at  $p = 1$  GeV/c) places additional constraints on the positioning of a TOF system with respect to the target. In the end, the position needs to be optimal for the physics observable under study. The bend towards higher  $m^2$ -values observable in the proton branch at low momenta is due to energy loss in the material between target and TOF wall and needs to be corrected for in the final experiment. At higher momenta, the distribution

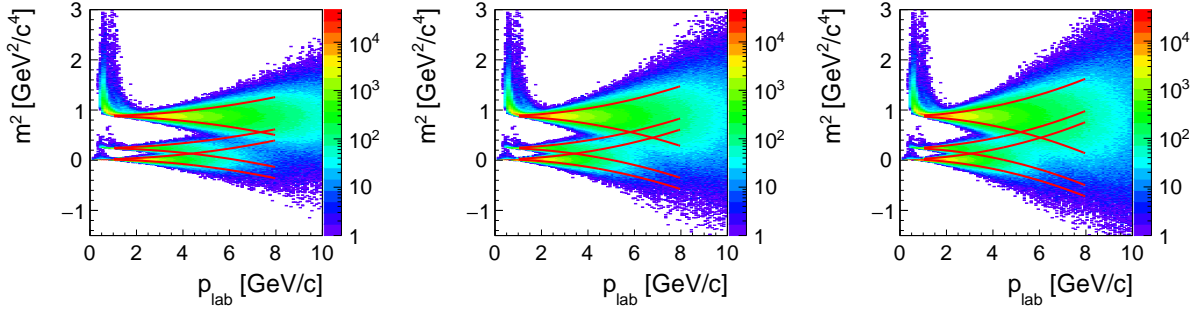


Figure 2.8: Squared particle masses of primary pions, kaons, and protons as a function of laboratory momentum obtained from the MC sample described in Fig. 2.7. The momentum is the initial value from the production vertex. Exact time-of-flight and trajectory-length information is provided by the MC track propagator. When a trajectory intersects an active geometric volume of the TOF wall (positioned at  $6 \text{ m} < L < 7 \text{ m}$  from the target, cf. Fig. 2.5), the time is stopped. For realistic trajectories, four passages through STS tracking planes are requested per track. TOF values are smeared with Gaussian resolutions of 50 ps (left plot), 80 ps (middle plot), and 100 ps (right plot). The red lines correspond to second-order polynomial fits to the  $1.5\text{-}\sigma$  values extracted from the sum of three equal- $\sigma$  Gaussian fit functions which are centered about the true squared masses of the particles in every squared-mass slice along the momentum axis.

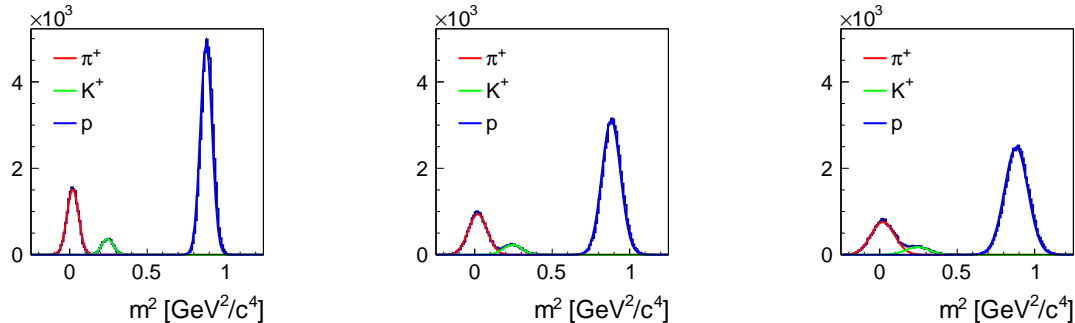


Figure 2.9: Squared-mass slices of primary pions, kaons, and protons at  $p = 3 \text{ GeV}/c$  extracted from the plots in Fig. 2.8. The colored curves represent the individual Gaussian contributions of each particle species to the summed Gaussian function which has been fitted to each squared-mass slice.

of protons can be described by a Gaussian function as in the case of pions and kaons. Figure 2.9 demonstrates the feasibility of the described PID method, at least in the limit of an ideal detector. In the running experiment, the white area in Fig. 2.8 will be covered with background resulting—among others—from track-to-hit mismatches between the STS and TOF subsystems. On the Monte Carlo level, the affiliation of a TOF point with a given primary track is known. In Fig. 2.9, one can see how the kaon peak merges with the pion peak as the simulated system time resolution worsens. At  $\sigma_t = 100 \text{ ps}$ ,

it could already be difficult to separate kaons from pions up to 3 GeV/c in momentum with  $n_{\sigma_t} = 3$  if the detector response were realistic.

For completeness, it shall be pointed out that separating particle species via PID gates on an  $m^2(p)$ -plot is one particular implementation of the time-of-flight method. In the ALICE experiment, for instance, different approaches are combined [72].

### 2.4.2 Multi-gap resistive plate chambers

A detector technology suitable for charged-hadron identification via time of flight in CBM needs not only to allow for precise time measurements (on the order of 80 ps for the entire timing system) as shown in the previous subsection. In addition, it must be scalable to a large detection area to cover the geometrical acceptance of the STS taking into account the trajectory bending in the magnetic field at distances between 6 and 10 m from the target as required for hadron separation up to a few GeV/c in momentum. Lastly, the response function of the detector should sustain a high detection efficiency even at nominal beam–target interaction rates of 10 MHz which exposes the TOF wall to particle fluxes from a few tens of kHz/cm<sup>2</sup> in the inner zone (even above 100 kHz/cm<sup>2</sup> in the immediate vicinity of the beam pipe) to below 1 kHz/cm<sup>2</sup> at the periphery (cf. Fig. 2.10). Currently, only (large-area) multi-gap resistive place chambers (MRPCs) meet the challenging technological demands of the TOF system at an affordable cost

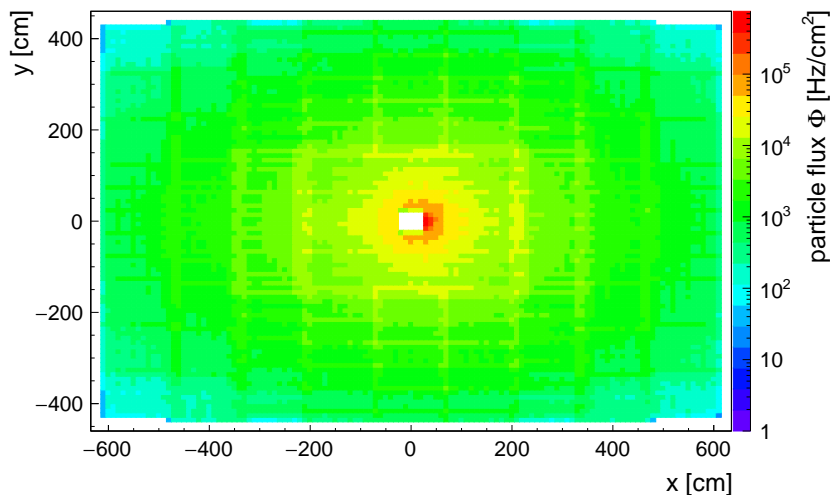


Figure 2.10: Particle flux through the CBM TOF wall positioned between 6 and 7 m from the target at a beam–target interaction rate of 10 MHz in cave coordinates  $xy$ , integrated in  $z$  over the entire support frame. Due to the staggered and partially tilted placement of active detector volumes within the frame, the particle flux extrapolated from 100,000 Au+Au events at  $p_{\text{beam}} = 10$  GeV/c with minimum centrality bias only approximately corresponds to the actual flux. Structures visible on the flux plot result from detector volumes overlapping in  $xy$ .

and provide sufficient design flexibility to adapt to the strongly varying flux conditions across the wall. Conceptual details of the TOF wall are given in Sec. 2.4.3.

Multi-gap resistive plate chambers [73] utilize the ionization of gas molecules by traversing charged particles in an electric field as primary detection process. Electrons stripped off from their atoms are accelerated towards the anode and ionize further molecules. Subsequently, secondary ionization electrons repeat this procedure which leads to a rapid multiplication of electrons developing into a Townsend avalanche containing on the order of  $10^7$  electrons. The probability for an avalanche to consist of  $n + 1$  electrons at a distance of  $x + dx$  from the primary ionization point provided that it comprises  $n$  electrons at  $x$  is given by  $n\alpha dx$  wherein the Townsend coefficient  $\alpha$  states the number of secondary electron-ion pairs created per unit length in the gaseous medium depending on the applied electric field [74]. Similarly, the reattachment of electrons to positively charged ions during avalanche formation is described by the attachment coefficient  $\eta$ . Combining both differential detachment and attachment processes in a single formula and integrating over position yields the expression

$$N = N_0 e^{(\alpha - \eta)x} \quad (2.8)$$

for the average number of avalanche electrons at a distance of  $x$  to the primary ionization cluster containing  $N_0$  electrons. For a gas mixture typically used in MRPCs of 85% 1,1,1,2-tetrafluoroethane ( $C_2H_2F_4$ ), 10% sulfur hexafluoride ( $SF_6$ ), and 5% isobutane ( $C_4H_{10}$ ) under atmospheric pressure at room temperature in an electric field of 100 kV/cm ( $\alpha - \eta \sim 113/\text{mm}$  [74]), an average avalanche would—according to the simplified approach described by Eq. (2.8)—consist of  $10^8$  electrons after growing for a distance of only 160  $\mu\text{m}$ .

An MRPC is composed of a stack of rectangular resistive plates made of materials ranging from ceramics to common glass (cf. Fig. 2.11(a)). To the external surfaces of the outer plates a high voltage is applied which creates a strong uniform electric field in the gaps between the resistive plates. The inner plates are electrically floating and separated from each other by 100 to 300  $\mu\text{m}$  using appropriate spacers like fishing line. These small gap widths allow for a very large gas gain (high electric field) without forming streamer discharges in the gaps by stopping the avalanche growth early enough. The onset of the latter occurs at above  $10^8$  avalanche electrons [76], known as the Raether limit, and involves the production of a large amount of charge which deteriorates the detector performance (see below). In addition, strong space-charge effects due to the high charge density in the narrow gaps limit the number of electrons in the avalanche.

Signal induction on the readout electrodes which are adjacent to but isolated from the high-voltage layers (cf. Fig. 2.11(a)) by moving avalanche electrons in any gap starts immediately after primary ionization and is not hampered by the presence of the resistive plates which are transparent for fast induced signals. The current signal induced by electrons is much bigger than the corresponding signals induced by positively and negatively charged ions in the avalanche due to the high drift velocity of electrons in the gap. For the above gas mixture in an electric field of 100 kV/cm, electron drift velocities of  $v_{\text{drift}} \sim 200 \mu\text{m}/\text{ns}$  are achieved [74] which results in signal formation times of

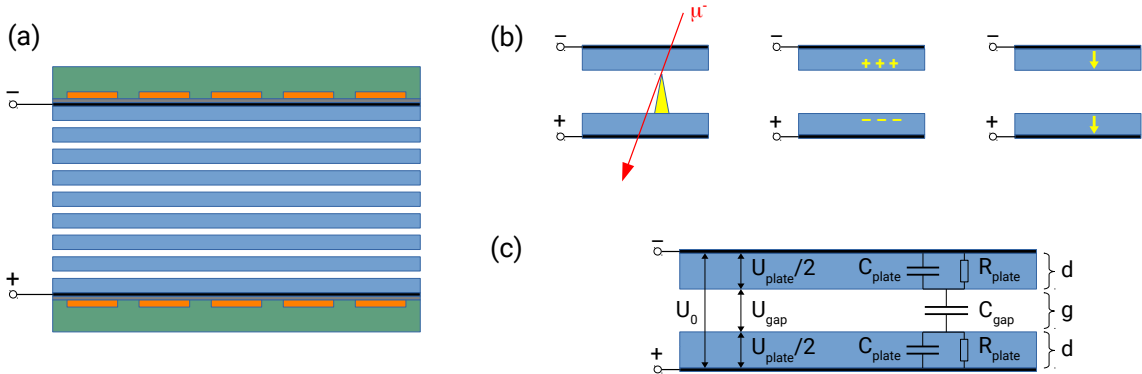


Figure 2.11: Subfigure (a): Profile of the structural components of an MRPC which consists of a stack of resistive plates (blue) separated by gas gaps. To the outer plates a high voltage is applied (black). Opposing printed circuit boards (green) with readout electrodes (orange) are isolated from the high-voltage electrodes. Subfigure (b): Positive and negative avalanche charges accumulate on the resistive plates and are compensated for by bulk currents through the plates. Subfigure (c): Notation used in the text to describe a single gap as a planar capacitor with two dielectrics, adapted from [75].

about 1 ns in a single gap. A primary relativistic particle orthogonally penetrating the resistive plate stack (assuming 8 gaps of  $200\ \mu\text{m}$  width with 7 plates of  $500\ \mu\text{m}$  thickness in between) would require about 20 ps to traverse all gaps which indicates that the final signal is constituted by all avalanches triggered by the primary. On the signal formation time scale of 1 ns, avalanches in different gas gaps start simultaneously and—in effect—fluctuations in growth of individual avalanches which impose a limit on the time resolution of the detector are reduced by averaging.

The analytical approach to the detector physics of (M)RPCs described in [74] provides an order-of-magnitude formula for the time resolution of a single-gap RPC,

$$\sigma_t = \frac{\pi}{\sqrt{6}(\alpha - \eta)v_{\text{drift}}}, \quad (2.9)$$

which yields  $\sigma_t = 57\ \text{ps}$  for the numbers stated above. As the timing response also depends on the crossing point of the signal with a discriminator threshold, the statistically expected  $1/\sqrt{n}$  improvement of Eq. (2.9) for a multi-gap RPC is not entirely realized. Regarding the signal formation and discrimination as  $n$  independent time measurements, the largest signal due to an avalanche triggered close to the top of one gap determines the (earliest) threshold crossing time. The average of  $n$  measurements of the earliest signal time has a larger uncertainty than just the average of  $n$  time measurements.

To filter detector noise which is uncorrelated with the passage of a primary charged particle, the discrimination threshold—among other factors—limits the detection efficiency  $\varepsilon$  of the MRPC. Assuming a detectable avalanche to be created in a single gap with probability  $\varepsilon_{\text{gap}}$ , the total efficiency of an  $n$ -gap RPC behaves like

$$\varepsilon = 1 - (1 - \varepsilon_{\text{gap}})^n \quad (2.10)$$

if each gap is treated as a separate detection instrument which is only approximately the case because all avalanches created in the stack contribute to the same induced signal. Even if none of the individual gap avalanches produced a signal that would exceed the discrimination threshold, the superposition could still be large enough. In the simplified picture given by Eq. (2.10), individual gap efficiencies of  $\varepsilon_{\text{gap}} \sim 31\%$  result in a total detector efficiency of about 95% for  $n = 8$ .

When an avalanche is triggered in a gas gap, electrons and ions drift to opposing resistive plates and accumulate on the surfaces (cf. Fig. 2.11(b)). This process can be modeled for a single gap with a resistive and capacitive network ([75] and references therein) as sketched in Fig. 2.11(c). The area on both resistive plates which is later on charged up by the avalanche forms a capacitor cell of capacitance  $C_{\text{gap}}$  to which initially the full high voltage of the detector is applied. When charges accumulate on the capacitor electrodes following avalanche formation, i.e. on the resistive plates, the capacitor is rapidly “discharged” and a share of its voltage is transferred to the adjacent plates. Consequently, the electric field is locally reduced negatively impacting the detector response function for subsequent traversing particles. Depending on the amount of charge deposited on the resistive plates, the detector can develop a dead spot because the electric field in the gap becomes so low that the growth of another avalanche is strongly inhibited and the resulting signal cannot pass the discrimination threshold anymore. Via the external high-voltage source, the surface charges on the plates are drained creating bulk currents through the plates. This leads to a restoration of the voltage/electric field in the gas gap and happens on a relaxation time scale of [75]

$$\tau = 2R_{\text{plate}} \left( \frac{1}{2}C_{\text{plate}} + C_{\text{gap}} \right) = \rho \epsilon_0 \left( \epsilon_r + \frac{2d}{g} \right), \quad (2.11)$$

wherein  $R_{\text{plate}}$  denotes the resistance of the plate,  $C_{\text{plate}}$  its capacity,  $C_{\text{gap}}$  the capacity of the gap capacitor,  $\rho$  the resistivity of the plate,  $\epsilon_0$  the vacuum permittivity,  $\epsilon_r$  the relative permittivity of the plate material, and  $d/g$  the ratio of plate thickness over gap width (cf. also Fig. 2.11(c)). For identical detector configurations (retaining the  $d/g = 5/2$  ratio used above and assuming a glass permittivity of  $\epsilon_r = 7$ ), relaxation times range from  $\mathcal{O}(10\text{ms})$  to  $\mathcal{O}(10\text{s})$  for typical resistivities between  $10^{10}\Omega\text{cm}$  and  $10^{13}\Omega\text{cm}$ . The lower the plate resistivity  $\rho$ , the sooner the MRPC locally recovers from the passage of a particle.

Usually, MRPCs in a running experiment are not irradiated in a single spot but flood-illuminated over the entire detector surface. When irradiation with a constant particle flux  $\Phi$  sets in suddenly, the time constant given in Eq. (2.11) influences how fast the detector enters a stationary situation [77] which is characterized by a constant average current  $\bar{I}$  through all resistive plates to balance the flow of positive and negative avalanche charges into the plates. This current is a mechanism of self-regulation which keeps the gas gains, i.e. the voltage drops, equal throughout all gaps. The current increases with increasing  $\Phi$  but enters saturation as the MRPC’s capability to neutralize charges between consecutive avalanches in the same location gets exhausted. The smaller the voltage drop between resistive plates becomes, the less charge can be created by new avalanches, which in turn limits the increase of the current. This is yet another

manifestation of self-regulation which is at work in MRPCs. Following the simplified one-gap treatment depicted in Fig. 2.11(c), one can express the mean voltage drop in the gas gap after the MRPC has adjusted to a certain flux condition by [75]

$$\begin{aligned}\bar{U}_{\text{gap}} &= U_0 - 2\bar{U}_{\text{plate}}/2 \\ &= U_0 - 2R_{\text{plate}}\bar{I} \\ &= U_0 - 2\rho d\Phi\bar{q}_{\text{aval}},\end{aligned}\tag{2.12}$$

wherein  $\bar{q}_{\text{aval}}$  is the average charge created by an avalanche under the given stationary conditions.

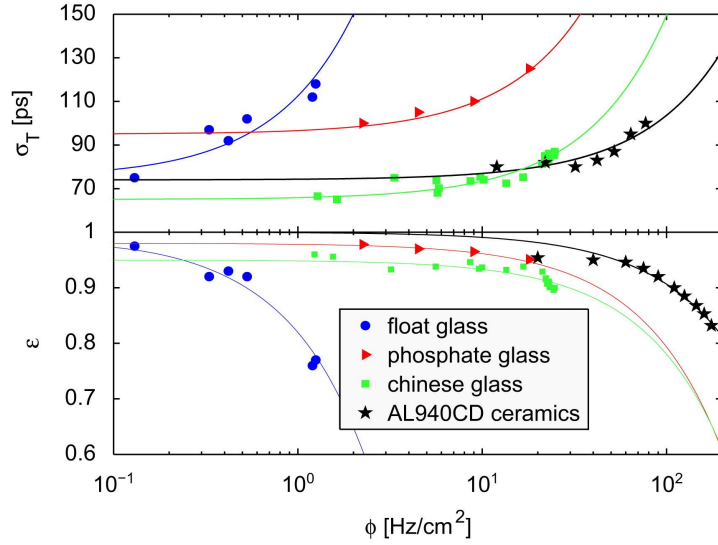


Figure 2.12: Measured time resolutions and efficiencies as a function of particle flux for four types of MRPCs built with different resistive materials. Resistivities range from  $\sim 10^9 \Omega\text{cm}$  for ceramic electrodes to  $\sim 10^{10} \Omega\text{cm}$  for Chinese silicate glass and phosphate glass to  $\sim 10^{13} \Omega\text{cm}$  for common glass. First-order polynomials according to Eqs. (2.13) and (2.14) are fitted to the data. Figure taken from [33].

Treating the MRPC response function in this ohmic direct-current limit—referred to as the DC model [78]—allows for a simple description of the experimentally observed rate capability of detectors equipped with plates of different resistivity  $\rho$ . Both the time resolution  $\sigma_t$  and the efficiency  $\varepsilon$  can be shown [33] to linearly deteriorate as a function of particle flux  $\Phi$  (cf. Fig. 2.12). The average charge created per (detected) avalanche is not subject to significant change with  $\Phi$  in the first-order approximations

$$\sigma_t = \sigma_{t,0} + K_t \rho d \Phi \bar{q}_{\text{aval}} \quad \text{and} \tag{2.13}$$

$$\varepsilon = \varepsilon_0 - K_\varepsilon \rho d \Phi \bar{q}_{\text{aval}}, \tag{2.14}$$

positive constants  $K_t$  and  $K_\varepsilon$  depending on the multi-gap structure. Figure 2.12 demonstrates a good agreement between the above relations and data obtained in actual detector tests.

When MRPCs composing the TOF system of CBM are exposed to sustained particle fluxes according to Fig. 2.10 in the running experiment, the rate effects described in this subsection become visible in the data. For exploiting the full PID capability of the TOF wall, it is necessary to characterize and to possibly correct for these effects. In Chap. 4, a response model is introduced which facilitates investigating both the transient and the stationary performance of MRPCs simulated in CbmRoot.

### 2.4.3 A large-area time-of-flight wall for CBM

The time-of-flight system of CBM is designed as an array of MRPCs (in the following often referred to as “counters”) which are contained in gas-tight aluminum boxes (“modules”) that are arranged in staggered columns according to Fig. 2.13. The placement of counters within modules and the placement of modules on the  $\sim 120\text{ m}^2$  wall allow for some overlap between active detector areas to avoid edge effects and to geometrically cover the solid angle of the STS without acceptance holes. Counter and module designs

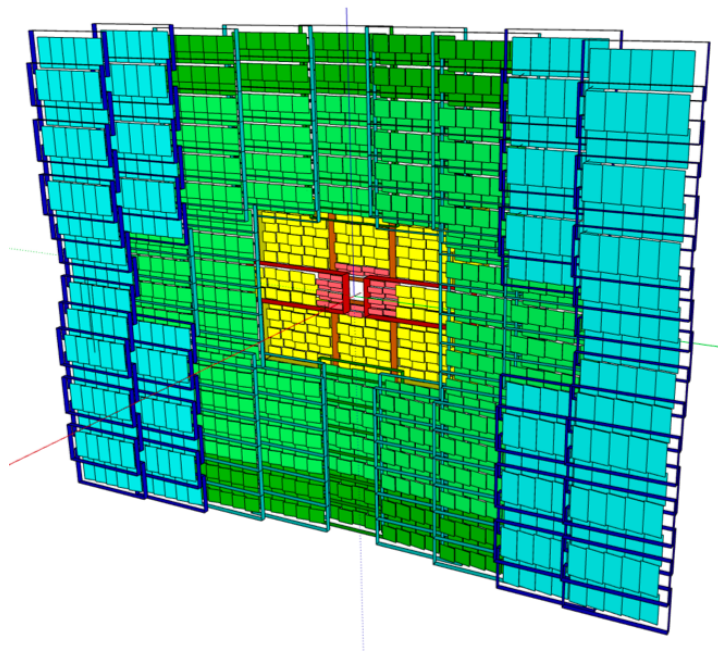


Figure 2.13: Conceptual design of the TOF wall as presented in the Technical Design Report [49]. Different colors indicate different architectures of MRPCs which are positioned inside gas-tight aluminum boxes (here transparent) of various dimensions. The light blue and dark green counters contain common glass as resistive material while the rest is equipped with low-resistive glass.

are adapted to the strongly varying hit density and flux conditions (cf. Fig. 2.10) across the wall. This concerns both the choice of resistive plate material and the dimensions of the readout electrodes (“cells”) on which signal induction occurs (cf. Fig. 2.11(a)). To-

wards the beam pipe where two particles are more likely to traverse the detector closely in time and space, much higher cell granularities are required than at the periphery of the wall. An interference of two or more signals induced by different primary particles on the same cell complicates the matching of STS tracks with (distorted) TOF hits. An occupancy criterion of  $< 5\%$  for each readout cell in the TOF system serves as a point of orientation for this design aspect. The counter size consequently shrinks with the size of the printed circuit board (PCB) into which the readout electrodes are integrated.

Table 2.1: Differences in design of MRPCs constituting different regions of the TOF wall as proposed in [49]. Naming conventions and specifications given in this table represent a provisional point of reference for counter design and have partially been subject to modifications.

	MRPC1	MRPC2	MRPC3a	MRPC3b	MRPC4
color in Fig. 2.13	red	yellow	light green	dark green	light blue
resistive plates [#]	12	12	9	9	9
resistivity $\rho$ [ $\Omega\text{cm}$ ]	$\mathcal{O}(10^{10})$	$\mathcal{O}(10^{10})$	$\mathcal{O}(10^{10})$	$\mathcal{O}(10^{12})$	$\mathcal{O}(10^{12})$
plate thickness $d$ [ $\mu\text{m}$ ]	700	700	700	500	500
plate surface [ $\text{mm}^2$ ]	$320 \times 100$	$320 \times 200$	$330 \times 280$	$330 \times 280$	$330 \times 540$
gas gaps [#]	10	10	8	8	8
gap width $g$ [ $\mu\text{m}$ ]	140	140	220	220	220
readout cells [#]	64	64	32	32	32
cell length [mm]	100	200	270	270	530
cell width [mm]	2.18	2.18	7	7	7
cell spacing [mm]	2.54	2.54	3	3	3
cell pitch [mm]	4.72	4.72	10	10	10
cell granularity [ $\text{cm}^2$ ]	4.7	9.4	27	27	53
active area [ $\text{mm}^2$ ]	$302 \times 100$	$302 \times 200$	$320 \times 270$	$320 \times 270$	$320 \times 530$

Table 2.1 summarizes the different MRPC designs for the outer TOF wall (MRPC3a, MRPC3b, and MRPC4) where particle fluxes are assumed to not exceed  $8 \text{ kHz}/\text{cm}^2$  and the inner TOF wall (MRPC1 and MRPC2) where fluxes range from  $8$  to  $25 \text{ kHz}/\text{cm}^2$  [48]. Except for the MRPC3a design which relies on low-resistive silicate glass developed in China [79] (therefore sometimes referred to as “Chinese” glass), the outer wall is equipped with common glass. The inner wall, in contrast, is entirely based on low-resistive glass plates due to the higher flux constraints. Regarding cell granularity, the difference between the innermost MRPC1 counters and the outermost MRPC4 counters corresponds to an order of magnitude. Architecture-wise, MRPC1 and MRPC2 are constructed in a double-stack configuration, i.e. an intermediate layer of high-voltage electrodes would effectively divide the single stack shown in Fig. 2.11(a) into two stacks adjacent to each other. This halves the high voltage which needs to be applied to create

the same electric field (two stacks of plates with half the size of a single stack) but results in a higher material need.

The readout cells of all counter designs in Tab. 2.1 are shaped like strips being expanded much more in one planar dimension than in the other one (length  $\gg$  width). For the inner TOF wall, an alternative MRPC design based on pad-shaped readout cells has been discussed during research and development (R&D) [48] and is considered a backup. The readout PCB in this case comprises 24 pad cells of dimensions  $2 \times 2 \text{ cm}^2$  with 2 mm interspace. Signals induced on pad cells are typically read out from the center of the pad. In comparison to strip cells which are read out on both narrow edges, pad cells by design yield a worse spatial and temporal resolution. In the limiting case of one cell (pad or strip) delivering a measurable signal for a traversing primary particle, the discretization error of the position measurement in both planar coordinates—assuming the cell to be read out in the center—is given by

$$\begin{aligned} \sigma_x^2 = \langle (x_{\text{true}} - x_{\text{meas}})^2 \rangle &= \int_a^b \left( x' - \left( \frac{a+b}{2} \right) \right)^2 \frac{dx'}{b-a} \\ &= \frac{1}{12} (b-a)^2, \end{aligned} \quad (2.15)$$

wherein  $a$  and  $b$  represent the extension of a one-dimensional discretization cell. The spatial resolution of a pad cell is limited by Eq. (2.15) in both dimensions while for a strip cell which is read out on both ends only the position resolution across the cell is dimension over  $\sqrt{12}$ . Along a strip cell, the position of signal induction can be estimated more precisely by comparing the signal propagation times along the electrode to both readout points at its ends. Also, the time of signal induction can be measured more accurately if two independent measurements are available. The total readout channel count of the TOF system would be slightly reduced from 110,000 to 100,000 if the inner wall were composed of pad-MRPCs.

Signal readout is unified for all strip-MRPCs in Tab. 2.1 and fully differential, i.e. readout cells flanking the resistive plate stack on top and bottom (cf. Fig. 2.11(a)) pick up the same signal with opposite polarity and transmit it to a preamplification/discrimination stage for further analog processing. Common-mode noise influencing the signal between sender and receiver can be filtered out this way because external electromagnetic interference shows identical polarity on both transmission lines and gets eliminated by subtraction—in contrast to the oppositely polarized signal. The preamplification/discrimination chip PADI [80] (cf. Fig. 2.14) first amplifies the low-amplitude MRPC signal and then discriminates it according to a configurable threshold. The threshold value needs to be chosen with care to eliminate detector noise on the one hand and to not eliminate small signals from traversing primary particles on the other hand. As PADI is a leading-edge discriminator, its time response function is susceptible to amplitude variations of incoming signals. The resulting time-walk effect spoils the detector resolution and can be corrected for using the time a signal spent above discrimination threshold (cf. Sec. 3.3). For this reason, the rectangular output pulses of PADI not only carry the signal time-stamp information with their leading edge but also transport the time-over-threshold information which corresponds to the distance

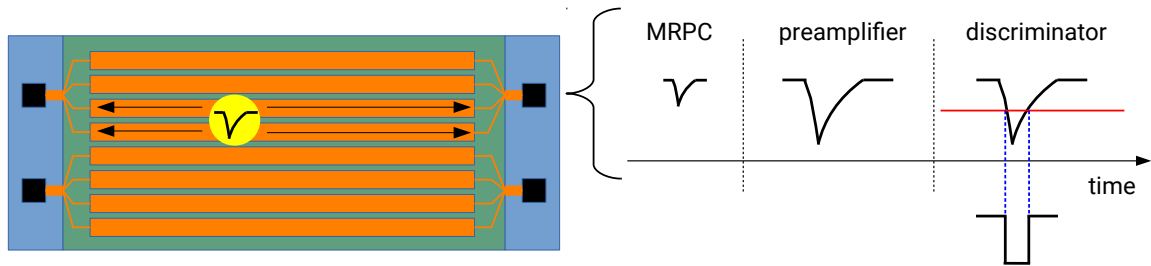


Figure 2.14: An avalanche induces a measurable signal on multiple readout cells which propagates along the cells in two directions to an integrated preamplification and discrimination circuit (black squares). Although signal induction is not restricted to the immediate vicinity of the avalanche in the readout plane, in effect a limited number of cells picks up a signal which surpasses the detection threshold. Following this argument, the yellow spot marks the “area of effect” of an avalanche. Finally, a rectangular pulse is output which corresponds in width to the time over discrimination threshold of the amplified MRPC signal. Every cell end is connected to its individual readout channel.

between leading and trailing edge. PADI output pulses are digitized by a time-to-digital converter (TDC) named GET4 (GSI event-driven TDC with 4 channels) [81]. According to the self-triggered readout paradigm of CBM (cf. Sec. 2.2), the GET4 chip does not wait for a readout request to transmit data but pushes them to the concentrating stage upon availability. To avoid continuously recording data originating from detector noise or reflected signals, a lot of effort was put in the design of the analog part of the readout chain. A very important aspect is the matching of the readout-cell impedance to the  $100\ \Omega$  input impedance of PADI. An alternative readout chain comprising PADI ASICs (application-specific integrated circuit) and FPGA-TDCs (field-programmable gate array) which was used in prototype tests is introduced in Chap. 3.

Measuring the arrival times of charged particles at the TOF wall needs to be complemented by a reconstruction of the collision time  $T_0$  to obtain an actual time of flight. If for PID purposes a system time resolution of at least 80 ps is required and the MRPC array contributes approximately 60 ps, the  $T_0$ -reference must be determined with an uncertainty of less than 50 ps. As the TOF method always requires a start time and a stop time, the  $T_0$ -reconstruction efficiency should be close to 100 %. Depending on beam parameters and collision systems, feasibility studies have been carried out [49] for different  $T_0$ -approaches. A pure software ansatz derives the collision time from the arrival time of the fastest particles at the TOF wall itself. While this strategy does not involve any additional detector equipment, it is less efficient for more peripheral collisions with low particle multiplicities/statistics. Additional timing information provided by beam fragments moving close to the beam pipe can extend the applicability of the software approach to larger impact parameters. For this purpose, a forward zone of MRPCs located in the  $1.2 \times 1.2\ \text{m}^2$  hole in the inner TOF wall (cf. Fig. 2.13) could be placed around the beam pipe [82]. Due to anticipated flux conditions of up to  $200\ \text{kHz}/\text{cm}^2$  in this region,

$\text{Si}_3\text{N}_4/\text{SiC}$  ceramics ( $\rho \sim 10^9 \Omega\text{cm}$ ) are considered as resistive plate material. Individual MRPCs for the proposed Beam Fragmentation  $T_0$  Counter (BFTC) have a triple-stack structure with a surface of  $2 \times 2 \text{ cm}^2$  and two gas gaps of  $250 \mu\text{m}$  per stack. A third option for collision-time reconstruction is an explicit diamond start detector placed in beam ahead of the target in the vacuum of the beam pipe. Despite of the low material budget of  $300 \mu\text{m}$  and  $50 \mu\text{m}$ , respectively, for detecting beams of protons/light nuclei and heavy ions, the interaction probability of the beam with the start detector still amounts to  $0.4\%$  which can—at high beam intensities—impose a significant additional load on the CBM experiment. In this scenario, the foregoing methods are preferable.

## CHAPTER 3

### MRPC PROTOTYPE TESTS WITH HEAVY IONS

During research and development (R&D) of MRPC prototypes adapted in design to the different flux regions of the future CBM time-of-flight wall (cf. Tab. 2.1), the TOF working group conducted numerous irradiation tests at various test-beam facilities. Full-surface illuminations of large-area counters are feasible only with collision secondaries of accelerated heavy ions impinging on a fixed target which is mounted downstream of the test setup, allowing for higher intensities to be achieved than with two colliding ion beams. In 2014 and in 2015, two such test-beam experiments were carried out each year, first at GSI/SIS18 (in April and in October 2014) and then at CERN/SPS (in February/March and in November 2015), with different prototypes participating and under varying experimental conditions, depending on the relative positioning of counters in the setup and on available ion species and beam intensities [83–89]. For successful data taking, a reliable data acquisition (DAQ) system is essential which was realized with conventionally hardware-triggered FPGA (field-programmable gate array) boards of the TRB3 (trigger and readout board) family [90]—customized to the needs of CBM TOF—in the aforementioned test-beam campaign, representing an important focus of this work. A stable version of the novel self-(respectively software-)triggered DAQ concept of the future CBM experiment (cf. Fig. 2.3) which is gradually completed in the ongoing mCBM experiment (see Sec. 5.4) was not available for counter readout at the time. The hardware-triggered readout chain implemented for test-beam measurements at GSI and CERN continues to be used for quality control (QC) in mass production of MRPC3a [91] and MRPC3b [92] final counter designs with cosmic irradiation. The first production badges of these counter types are deployed for end-cap time-of-flight (eTOF) measurements in the STAR experiment during phase II of the Beam Energy Scan (BES-II) at BNL/RHIC [93] and constitute the mTOF subsystem of the mCBM experiment at GSI/SIS18 [35], both activities being part of the intermediary FAIR Phase-0 research program towards Day-1 experiments at the completed FAIR facility.

In this chapter, the counter setup installed for the data-taking period at CERN/SPS in March 2015 and the particle-flux and multi-hit conditions which it was exposed to are described in detail in Sec. 3.1. The latter are estimated by means of a dedicated Monte Carlo study developed in this work. Corresponding experimental data are suited for a comparison with simulated results presented in Chap. 5. The dual operation of the DAQ chain based on a both periodically and physics-triggered TrbNet [94] (the communication protocol implemented between FPGAs) is outlined in Sec. 3.2. Finally, Sec. 3.3 covers the calibration of raw detector messages and the reconstruction of correlations between them in time and space, a process called cluster building. Within the scope of this work, a particular effort was made concerning the synchronization of prototype data measured by 512 individual readout channels which were distributed over 20 time-to-digital converters (TDCs).

## 3.1 Test-beam setup at CERN/SPS in March 2015

### 3.1.1 Detection instruments and geometry

Registered as test-beam users at CERN under the abbreviation RE21/CBM (Recognized Experiment) since 2011, CBM TOF and TRD working groups successfully applied for participation—for a seven-day period—in a beam momentum scan of  $\text{Ar}^{18+}$  ions on a scandium fixed target conducted by the NA61/SHINE experiment [95] in the CERN North Area (NA) between February and April 2015. From Thursday, February 26, 08:00 a.m. to Thursday, March 5, 08:00 a.m. collision data from 13 and 19 A GeV/c argon ions accelerated by the SPS impinging on a variable-size lead target were taken in a dedicated concrete cave—shown in Fig. 3.1—on the H4 beam line which runs parallel to the H2 beam line at which NA61/SHINE is located.

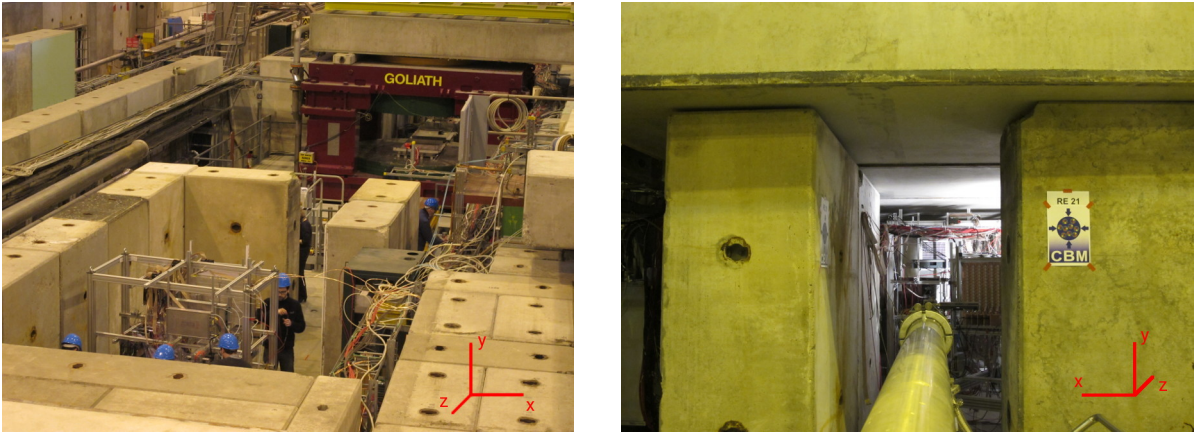


Figure 3.1: Aerial view of the test-beam setup installation in the PPE134 (Particle Physics Experiment) zone of EHN1 (Experimental Hall North) at CERN in a dedicated concrete cave (dimensions: 2.6–4.2 m wide (x), 2.4 m high (y), and 8.0 m long (z)) downstream the GOLIATH dipole magnet (left image). The beam enters the roofed cave through a beam pipe under vacuum at 1.26 m above the cave floor and—upon exiting the beam pipe—hits a lead target (not visible) to produce a spray of collision secondaries to irradiate the setup (right image). Photographs by courtesy of D. Emschermann.

The construction of a temporary CBM cave in the PPE134 zone from shielding concrete against collision products was necessary to operate the test-beam setup under particle fluxes on the order of  $\text{kHz}/\text{cm}^2$  which would not be possible in an open experimental hall due to radiation protection. Different counters under test were mounted in their respective aluminum gas boxes on an aluminum frame (cf. Fig. 3.1, left image), arranged in an upper branch more distant to the beam ( $z$ -)axis (exposed to smaller particle fluxes) and in a lower branch closer to the axis (exposed to higher particle fluxes). Results obtained for counters on the lower branch, exclusively equipped with low-resistive glass, are published in [84]. This work focuses on the upper branch of the setup, consisting of four

counters positioned in line, the outer ones serving as event selectors and reference for analyzing performance of the inner two, the first of which features a low-resistive glass stack and the second of which is built with common glass plates. This architectural difference between two adjacent counters allows for studying the impact of glass resistivity on detector response under—apart from counter positions in the setup—identical experimental conditions. In the order of mounting along the beam axis, design specifications and operating parameters of these counters are provided in Tab. 3.1.

Table 3.1: Technical design aspects and operating conditions of MRPC prototypes irradiated at CERN/SPS which are under investigation in this study.

counter	3-0-0 (HD-P2)	9-0-0 (THU)	7-0-0 (USTC)	4-0-0 (HD-P5)
glass type	low-resistive	low-resistive	common	low-resistive
glass thickness [mm]	0.7	0.7	0.33	1.0
configuration	single stack	double stack	double stack	single stack
gas gaps [#]	8	$2 \times 4$	$2 \times 5$	6
gap width [ $\mu\text{m}$ ]	220	250	220	220
readout cells [#]	32	24	16	16
cell length [cm]	27	27	27	4
cell pitch [mm]	$7 + 3$	$7 + 3$	$17 + 3$	$7.6 + 1.8$
active area [ $\text{cm}^2$ ]	$32 \times 27$	$24 \times 27$	$32 \times 27$	$15.04 \times 4$
high voltage [kV]	$\pm 11.5$	$\pm 5.5$	$\pm 5.0$	$\pm 8.5$
PADI threshold [mV]	200	190	200	220
PADI version	6	6	7	6

Some of these counters were studied in test-beam scenarios at GSI in 2014 already [83, 85] and—to a smaller or a greater degree—refurbished for the argon test beam at CERN. Two of them were designed and constructed at Heidelberg University in Germany (HD; prototypes P2 [96] and P5), one of them at Tsinghua University (THU) in Beijing, China, and the remaining one at the University of Science and Technology of China (USTC) in Hefei. The three-digit counter identifier reflects the module type followed by the module index followed by the counter index. As only one module of each type with a single counter inside was installed in the CERN setup, the latter digits equal zero. In the following, counters are referred to by their respective identifier. Operating voltages and discrimination thresholds given in Tab. 3.1 were determined with respect to optimal performance and stability for individual counters by dedicated high-voltage and threshold scans in the course of the beam time and used in (relatively) high-statistics runs selected for data analysis. Counters in their respective boxes were flushed with a gas mixture of 85 % 1,1,1,2-tetrafluoroethane ( $\text{C}_2\text{H}_2\text{F}_4$ ), 10 % sulfur hexafluoride ( $\text{SF}_6$ ), and 5 % isobutane ( $\text{C}_4\text{H}_{10}$ ) under atmospheric pressure. The gas box of counter 9-0-0

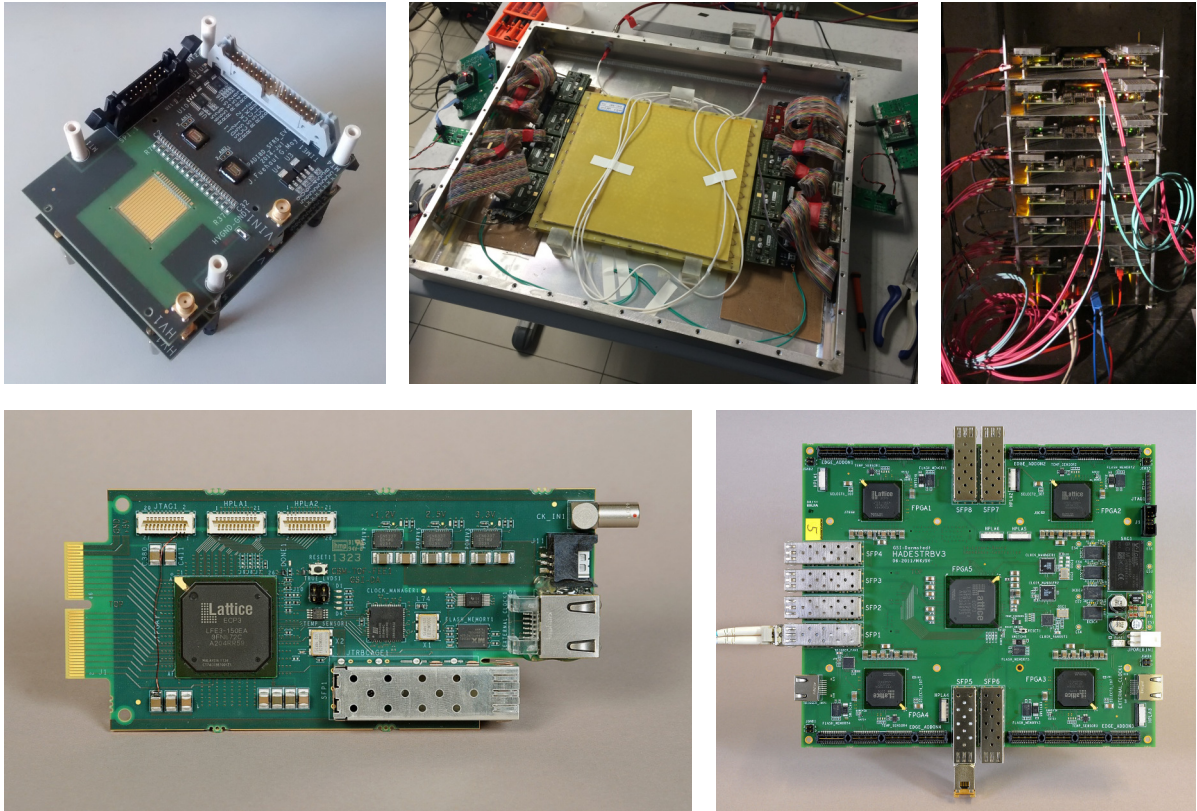


Figure 3.2: Double-diamond detector located below the golden electrode layer on two stacked PCBs (printed circuit board), respectively, equipped with two PADI-8D chips each (top left image). Open gas-tight aluminum box of counter 9-0-0 displaying the yellowish honeycomb support structure of the glass stack and two lines of PADI-6 add-on PCBs on opposing readout sides (top middle image). Stack of TRB3 data concentrators (top and bottom right images) cabled for operating a TrbNet DAQ network between FPGAs of the LatticeECP3 family (black packages) to read out a series of front-end TDC cards (bottom left image) digitizing PADI output signals. Photographs provided by GSI and by courtesy of Y. Wang (top middle) and D. Emschermann (top right).

without the top aluminum cover is shown in Fig. 3.2.

Three and one centimeters ahead of the lead target, respectively, a double-diamond detector is installed as a beam reference counter a signal on which is required for any positive physics-trigger decision to be taken by the DAQ system. Additionally, it provides a stable time reference for offset and velocity corrections in raw-data calibration (cf. Sec. 3.3) and—due to a lack of detector noise in the absence of beam—facilitates the estimation of event times in an ongoing spill of particles extracted from the accelerator with respect to the beginning of the spill (cf. Sec. 5.3). As time residuals between MR-PCs are considered in data analysis, the detector is not needed for  $T_0$ -determination. The device used at CERN is the second version of a prototypical focal-plane detector for the Super-FRS (Superconducting FRagment Separator) at FAIR [97, 98], contribut-

ing time-of-flight information to the identification of exotic nuclear fragments which are studied by NUSTAR. Both readout PCBs of the double-detector contain a pcCVD (polycrystalline chemical vapor deposition) diamond of dimensions  $20\text{ mm} \times 20\text{ mm} \times 0.3\text{ mm}$  with Cr/Au layers deposited on each side by photolithography serving as electrodes, the top side being segmented into 16 readout cells (pitch:  $1\text{ mm} + 0.15\text{ mm}$ , length:  $18\text{ mm}$ ) and the bottom side acting as a planar ground pad ( $18.25\text{ mm} \times 18\text{ mm}$ ). Cell orientation is horizontal on the first layer and vertical on the second layer. To not overload the DAQ system with diamond data at beam intensities on the order of  $10^7\text{ Hz}$  (cf. Sec. 3.1.2), no focusing effort was made to center the beam on the diamonds. Instead, the detector was positioned 1 cm above the nominal beam height and operated with the maximum available discrimination threshold for PADI-8D ( $-600\text{ mV}$ ).

For an independent estimation of particle fluxes in the setup, two Bicron BC-408 plastic scintillators of  $xyz$ -dimensions  $8\text{ cm} \times 2\text{ cm} \times 1\text{ cm}$  and  $11\text{ cm} \times 4\text{ cm} \times 2\text{ cm}$ , respectively, are positioned in front of (smaller unit) and behind (larger unit) the line of MRPCs (cf. Fig. 3.3). Two H2431-50 photomultiplier tube (PMT) assemblies each are attached to scintillator edges on the longitudinal axis for generating measurable electrical signals from scintillation light.

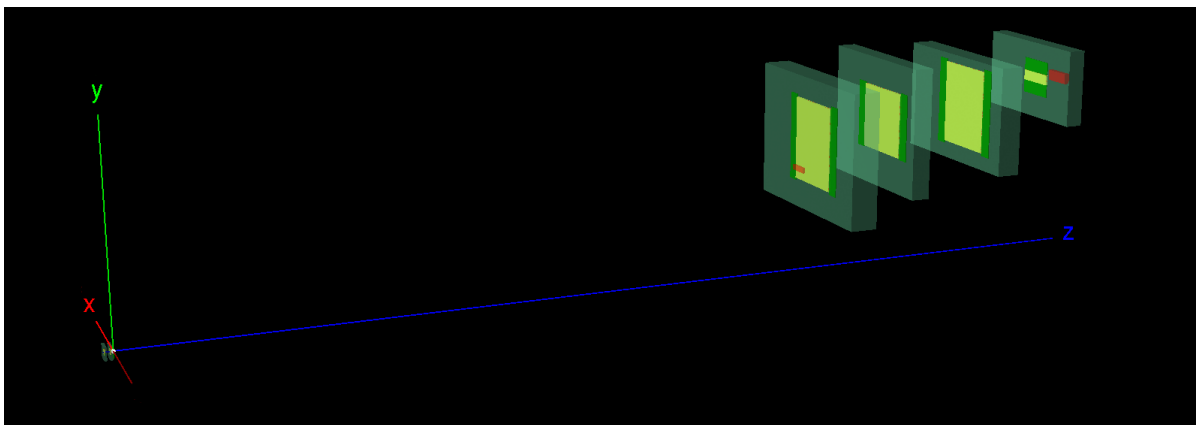


Figure 3.3: Visualization of the simplified test-beam setup described with TGeo volumes in ROOT (cf. Tab. 3.2). While the beam moves along the  $z$ -axis, it first crosses the double-diamond detector right ahead of the point of origin on which the target is centered. Reaction secondaries propagating through the setup eventually penetrate the glass stack of an MRPC (yellow) or a plastic scintillator (red). MRPC gas boxes (transparent teal) additionally contain rectangular readout PCBs (green).

For data analysis and simulations, component geometries of detection instruments in the setup are—in a greatly simplified fashion—implemented in ROOT with the TGeo geometry modeler (cf. Fig. 3.3). The entire setup is described with rectangular mother volumes containing rectangular daughter volumes of different size and material, the top volume in the hierarchy being a virtual cave filled with air composed of 78% nitrogen ( $\text{N}_2$ ), 21% oxygen ( $\text{O}_2$ ), and 1% argon ( $\text{Ar}$ ), given in molar proportions. In this cave volume, MRPC modules are placed according to actual positions at the experimen-

Table 3.2: Geometrical constraints of the MRPC test-beam setup complementing Tab. 3.1 with respect to counter positioning and projected detection areas under test with all four counters triggered by straight-line particle tracks (4xTRG). A TGeo visualization is provided in Fig. 3.3. (Side note: On grounds of historically grown geometric descriptions of counters in software, TGeo active areas might negligibly deviate from the technical values stated in Tab. 3.1.)

counter	3-0-0	9-0-0	7-0-0	4-0-0
cell orientation	horizontal	horizontal	horizontal	vertical
TGeo active area [cm <sup>2</sup> ]	32 × 26.9	25 × 26.7	32 × 27	15.04 × 4
	860.8	667.5	864.0	60.2
counter $x$ -center [cm]	0.0	2.8	−0.4	3.1
counter $y$ -center [cm]	48.9	55.0	58.2	66.8
counter $z$ -center [cm]	265.9	297.5	332.3	367.4
shortest time of flight [ns]	9.0	10.1	11.2	12.5
4xTRG projection area [cm <sup>2</sup> ]	10.9 × 2.9	12.2 × 3.2	13.6 × 3.6	15.04 × 4
	31.6	39.0	49.0	60.2
cells in projection area	14, 15, 16	9, 10, 11, 12	8, 9	0–15

tal site, slightly readjusted during data analysis based on measured spatial correlations between counters. The outer volume of an MRPC module is a hollow gas box of module-dependent dimensions made of elemental aluminum with wall thicknesses of 0.1 cm along cave- $y$  and cave- $z$  (beam axis) and of 0.5 cm along cave- $x$  where the feed-through of electrical counter signals occurs in reality. The gas box is filled with a passive gas volume (85 % C<sub>2</sub>H<sub>2</sub>F<sub>4</sub>, 10 % SF<sub>6</sub>, and 5 % C<sub>4</sub>H<sub>10</sub>) which serves as mother volume to a stack of soda–lime–silica (common) glass plates (used in ROOT also for counters with low-resistive glass), composed of 73.5 % silicon dioxide (SiO<sub>2</sub>), 15.9 % sodium oxide (Na<sub>2</sub>O), and 10.6 % calcium oxide (CaO), interspaced with active gas-gap volumes. The dimensions of the gas gaps determine the active counter area (cf. Tab. 3.2). Counters with a double-stack configuration are modeled as single stacks, preserving the total number of gas gaps but omitting the readout plane (and a glass plate) in the middle. Attached to opposing sides of the glass stack, either along cave- $x$  or along cave- $y$  depending on the respective orientation of readout cells, two volumes of elemental carbon representing front-end electronic boards equipped with PADI chips contribute some additional material budget. As pick-up electrodes carrying readout cells above and below the glass stack are not implemented, the counter volume is logically divided into the corresponding number of strip-shaped cells, taking the pitch between real cells as the width of immediately adjacent virtual cells. The double-diamond detector is virtualized as two small MRPC modules with active areas of 2 cm × 2 cm, respectively, each logically segmented into 16 readout cells. Situated ahead of the target, the detector does—except for some

rare combinations of scattering processes—not add material budget to trajectories of collision secondaries from the target volume which irradiate the counter setup. Treating it as an MRPC in software allows for modeling its response function (cf. Chap. 4) in the same way. A more accurate description is not required for data analysis in this work which concentrates on residuals between MRPCs. Finally, the two plastic scintillators in the setup are implemented as two blocks of hydrocarbon with an H/C atomic ratio of 1, positioned in the virtual cave in front of counter 3-0-0 and behind counter 4-0-0.

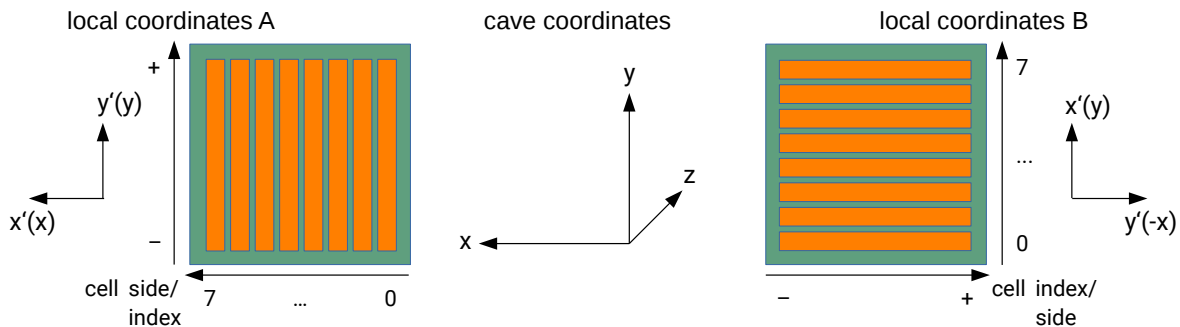


Figure 3.4: Comparison of cave and local counter coordinate systems for vertical (A; left drawing) and horizontal (B; right drawing) cell orientations. While local cell indexing in both cases runs along global  $x$ - (A) or global  $y$ -coordinates (B), respectively, the cell end marked with a plus sign is directed towards negative global  $x$  in case B (towards positive global  $y$  in case A in contrast) as the latter orientation (B) results from a clock-wise rotation by  $90^\circ$  of the former (A). The point of origin of local coordinates is the center of the glass stack. Note that in the TGeo representation—in contrast to this sketch aiming at a clear and simple view—no gaps exist between virtual cells, the cell width corresponding to the cell pitch.

The total active detection volume, i.e. the entirety of gas gaps interspaced with glass plates, is centered about the point of origin in  $xyz$  of the local coordinate frame of the counter. The volume in the middle of this stack which is either a glass plate (if the number of gaps is even) or a gas gap (in case of an odd gap number) contains the local origin in  $z$  and serves as a reference plane for coordinate transformations between the local counter frame and the global cave frame (cf. Fig. 3.4). To any hit reconstructed on the counter, a local  $z$ -coordinate of 0 is assigned. If the readout cell indexed with  $i$  fires, the reconstructed hit is positioned at the (pitch) center of cell  $i$  on the  $x$ -axis of the local coordinate system,

$$x_{\text{center}}(i) = (i - N_{\text{cells}}/2 + 1/2) x_{\text{pitch}}, \quad (3.1)$$

i.e. logical cells with pitch  $x_{\text{pitch}}$  are indexed along local  $x$ , starting from cell 0 in the lower negative  $x$ -range and ending with cell  $N_{\text{cells}} - 1$  in the upper positive  $x$ -range, constrained by the extension of the active area in this dimension. Reversely, the spatial passage of a simulated Monte Carlo track through the active counter volume—an average

over positions in all gas gaps involved—is interpreted in local  $x$  as a hit on cell

$$i(x) = \lfloor x/x_{\text{pitch}} + N_{\text{cells}}/2 \rfloor. \quad (3.2)$$

Hit coordinates in local  $y$  are derived from half the difference of digitized signal arrival times on opposing cell ends,

$$y = 1/2 (t^- - t^+) v_{\text{signal}}, \quad (3.3)$$

multiplied with the measured propagation velocity  $v_{\text{signal}}$  of signals on the pick-up electrodes. Signal induction closer to the cell end marked negative in Fig. 3.4 results in a negative local  $y$ -coordinate for the corresponding hit ( $t^- < t^+$ ) while a positive local  $y$ -coordinate results from a signal generated closer to the positive cell end ( $t^- > t^+$ ).

### 3.1.2 Particle flux and spill structure

To assess the high-rate performance of counters in a test-beam environment, a homogeneous flux—especially in time—of particles on the respective surfaces over a sustained period of a few seconds is a desired condition concerning reproducibility of measured results both in subsequent experiments and in simulations with mathematical models that are not limited to a very specific scenario. As the argon test beam at CERN/SPS in early 2015 marked the beginning of efforts by the CBM-TOF working group to test detector prototypes under the highest possible load at this location, details regarding the available beam intensity in the dedicated concrete cave (cf. Fig. 3.1) and the temporal homogeneity of the beam in spill had to be learned during this beam time. Originally, incident particle fluxes from the beam colliding with a variable-size lead target of up to 25 kHz/cm<sup>2</sup> were aimed at to evaluate the full potential of prototypes for the inner TOF wall (cf. Sec. 2.4.3) which were mounted in the lower branch of the setup. Due to constraints imposed by radiation protection, however, the setup could not be operated under stable conditions above 2.3 kHz/cm<sup>2</sup> in the upper branch (5.5 kHz/cm<sup>2</sup> in the lower branch), deduced from rate measurements with plastic scintillators, i.e. strongly depending on their respective position. In Fig. 3.5, the particle flux on the two scintillators in front of and behind the upper line of counters (cf. Fig. 3.3) is shown during a stable run with final operating parameters in the evening of March 4. Remarkably, the three flux patterns in both plots which each represent an accelerator spill all start with a huge spike, at least three times higher in flux than the subsequent regular spill, provided that PMTs were able to follow, i.e. no saturation occurred. Owing to the intentionally small readout frequency of scaler registers for diamond, MRPC, and PMT signals on a set of VULOM (VME Universal Logic Module) boards by an MBS (Multi Branch System) [99] running in parallel to the main TrbNet-based DAQ system, the width of the initial spike in beam intensity and the microscopic intensity structure of the regular spill are not resolved in Fig. 3.5.

With a periodically triggered TrbNet readout, the distribution of digital detector messages (“digis”) on a continuous experiment time axis shows the SPS spill structure (and

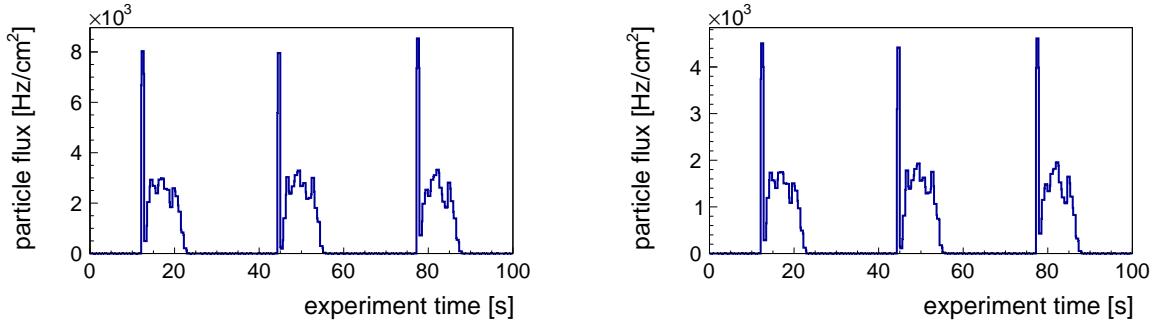


Figure 3.5: Particle flux as a function of experiment time on the two plastic scintillators in front of (left plot) and behind (right plot) the MRPC setup estimated from the logical AND signals of opposing photomultiplier tubes, respectively, as counted by dedicated scaler registers which are periodically read out at a frequency of 1.49 Hz (i.e. every 0.67 s).

its deviation from an ideal trapezoidal shape) during the test beam in much greater detail (cf. Fig. 3.6). In the flat-top stage of the magnetic cycle of the SPS which here lasts for 9.6 s, argon ions are slow-extracted from the accelerator over several million synchrotron turns [100] forming the spill of beam particles that here recurs every 32.4 s, the duration of an SPS super cycle. During spill break at the H4 beam line on which the MRPC test setup is installed, other experiments are served by the accelerator. Both numbers confirmed with digi time stamps are multiples of the CERN/PS basic period of 1.2 s. In the meantime, spill inhomogeneities resulting from initial and random intensity spikes as well as from 50 Hz intensity oscillations have been systematically investigated and also mitigated to a large extent [101–103]. However, they are present in the data analyzed in this work and have a significant impact on results (cf. Chap. 5).

The beam intensity in the spill “plateau”—calling it such with due care—is estimated from the reproduction of average plateau fluxes on the two plastic scintillators, amounting to 2.3 kHz/cm<sup>2</sup> on the front scintillator and to 1.4 kHz/cm<sup>2</sup> on the one in the back, with a Monte Carlo simulation. If the mean external track flux per event on both scintillators as determined with 1,000,000 minimum-bias Ar on Pb collisions, produced with UrQMD, in a 3 mm lead target is multiplied by intensity values of 21.5 MHz and 25.9 MHz, respectively, and by a 4 % geometric interaction probability between projectile and target nuclei, the measured fluxes can be reproduced individually. In the following, the mean value of these two numbers, 23.7 MHz, serves as input beam intensity to a MC estimation of track multiplicities and fluxes on the four counters in the test setup.

### 3.1.3 Monte Carlo estimate of experimental conditions

When a charged particle track crosses the boundary of an MRPC gas gap in the TGeo tracking geometry, its entry point—in space and time—into the active volume and the subsequent energy loss while step-wise propagating through the gap is registered as a Monte Carlo point in the CbmRoot simulation framework. The number of MC points

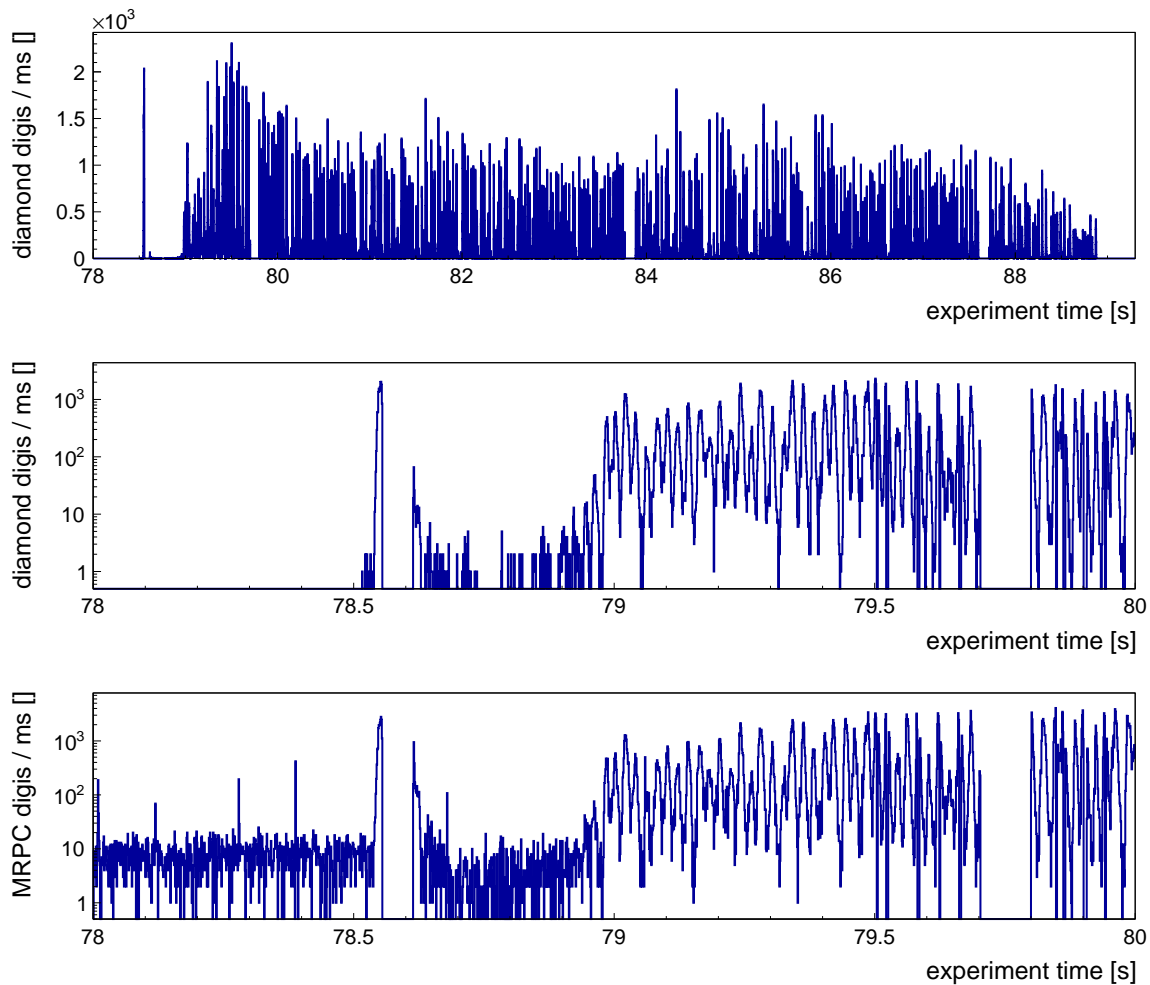


Figure 3.6: Typical spill structure and length during the test beam at SPS visualized by digital diamond-detector messages per ms experiment time (upper plot). Zoomed view of the spill start showing a roughly 100 ms wide initial spike of—due to fragmentary recording—unknown intensity less than 0.5 s ahead of the actual spill (lower two plots; cf. Fig. 3.5). A subspill intensity pattern of 50 Hz is clearly visible. The double-diamond detector does not show any off-spill noise (middle plot) in contrast to counter 9-0-0, for instance (lower plot). Holes appearing on the experiment time axis result from data loss in the readout system and in the event builder, respectively.

per counter produced for a track can amount to the total number of gaps if a track traverses the entire counter volume from top to bottom or even be limited to 1 if, for instance, a daughter track is created during propagation of a mother track through the glass plate in front of the last gap in the stack. Also, if a track decays in the counter volume or is kinetically stopped, the number of MC points is smaller than the gap number. In the Monte Carlo formalism, a track is considered geometrically detected by a counter if any corresponding MC point exists. As a level of detail at which entry

points and energy losses are stored for individual gas gaps is not required for simulation purposes in this work, a single MC point per track per counter is created based on average coordinates in position and time and on accumulated energy loss in all gaps crossed. Regarding particle flux on a counter surface, external tracks originating outside the respective module, i.e. the gas-box volume, need to be distinguished from internal tracks which result from interactions of an external track with module material or from particle decays inside the module. The former are counted towards (external) particle flux, the latter are considered part of the detector response. External tracks—whether charged or uncharged—are taken into account only once, independent of the number of internal descendants, even if no direct MC point exists for them, as long as at least one MC point is created for an internal daughter track. For the first station in the line of MRPCs, counter 3-0-0, creation mechanisms of both the external and the internal particle cocktail leaving traces in the detector are summarized in Fig. 3.7.

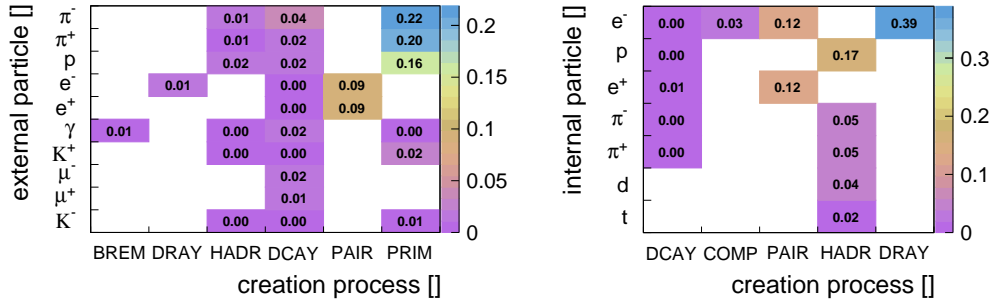


Figure 3.7: Production processes of externally (left plot) and internally (right plot) created particles which traverse an active detector volume of counter 3-0-0. The former set—in contrast to the latter—comprises also uncharged tracks a charged descendant of which is detected. External particles are created either in the target (86.8%) or in air (12.8%) while internal particles usually originate from a glass plate (85.9%) or from the aluminum box (12.6%). Normalized contributions up to a limit of 0.5% are not shown. Process names are abbreviated in the following way: bremsstrahlung (BREM), Compton scattering (COMP), particle decay (DCAY), delta-ray production (DRAY), hadronic interaction (HADR), pair production (PAIR), and collision-seed primaries (PRIM).

A share of internal tracks from counter 3-0-0 contributes to the respective external particle flux on the three rear modules. Actually, each module in the row successively adds rate to subsequent modules, mainly by interactions in the aluminum box or the soda–lime–silica glass stack which have similar material properties. The main source of electron–positron pairs created either in the target material or inside module aluminum or glass, respectively, are decay gammas from primary  $\pi^0 \rightarrow \gamma\gamma$ . Due to the short lifetime of neutral pions ( $c\tau = 0.2 \mu\text{m}$  at  $p = 1 \text{ GeV}/c$ ), these decays happen exclusively in the  $d_z = 3 \text{ mm}$  thick lead target wherein a photon with sufficiently high energy has a chance of

$$P(0 \leq Z \leq d_z) = 1 - \exp\left[-\frac{7}{9} \frac{\rho}{X_0} d_z\right] \quad (3.4)$$

to engage in pair production,  $Z$  being a random position variable,  $\rho$  the material density, and  $X_0$  its radiation length. In numbers (material properties taken from [29]), 34 % of  $\pi^0$ -decay gammas are converted into an  $e^+e^-$ -pair in the target while surviving gammas irradiating the line of modules have a probability to interact accordingly of 0.9 % in every 1 mm aluminum wall and of 0.5 % in every 0.7 mm glass plate in the line of counters—material contributions which sum up towards the rear end of the setup. The predominant creation mechanism of internal particles is delta-ray production in the glass stack.

Events relevant to data analysis are those in which a combination of counters responded to a straight-line track, ideally originating from the target volume. In the first stage of MRPC data calibration against a stable time reference, as provided by the diamond detector, only the respective counter needs to have fired (which is reflected by a set of independent trigger conditions between the diamond and individual counters in the DAQ system). When calibrating on and finally analyzing correlations between selector counters and detectors under test, the entire line of counters is required to be triggered. In the following, Monte Carlo events corresponding to the former case (any counter is hit) are labeled with 1xTRG (abbr. for trigger) and events qualifying for the latter case, comprising a target track crossing all four counters, are denoted with 4xTRG. The respective counter areas which can geometrically be traversed by straight-line 4xTRG selector tracks match with the projections of the small reference counter 4-0-0 (located in the back) towards the point of origin onto the respective counter planes (cf. Tab. 3.2). This spatial corridor is reflected in the narrow phase-space acceptance of selector particles (cf. Fig. 3.8). Among selector tracks, also a significant share of electron–positron pairs (20 %) can be found with trajectories that deviate—on average—more from the straight-line ideal than trajectories of selector bulk hadrons (pions, kaons, and protons) because of deflections arising from multiple Coulomb scattering with nuclei in the tracking material.

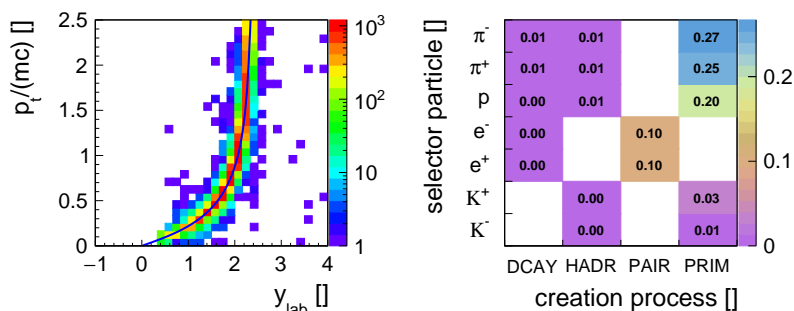


Figure 3.8: Phase space populated by Monte Carlo selector tracks which originate from the target volume and traverse all four counters (4xTRG) in the setup. The blue curve corresponds to the  $10.3^\circ$  central polar angle of the last counter in line (left plot; cf. Fig. 2.7). Particle type and creation mechanism of selector tracks in the target (right plot; for abbreviations see caption of Fig. 3.7). Normalized contributions up to a limit of 0.5 % are not shown.

Table 3.3: Monte Carlo track multiplicities (MUL), fluxes, and cell occupancies on the four MRPCs in the setup under various aspects. Note that the sum of mean external and internal charged track multiplicities slightly exceeds the mean multiplicity of Monte Carlo points as an external track triggering a response in an MRPC module by descendants might not have traversed an active detection volume itself.

counter	3-0-0	9-0-0	7-0-0	4-0-0
external charged track MUL	1.592	1.030	1.197	0.068
external uncharged track MUL	0.058	0.038	0.032	0.003
total external track MUL	1.650	1.068	1.229	0.071
total external track flux [kHz/cm <sup>2</sup> ]	1.817	1.517	1.348	1.119
total external track MUL (1xTRG)	3.040	1.968	2.264	0.131
total external track MUL (4xTRG)	4.821	3.526	3.897	1.145
selector track MUL (4xTRG)	0.045	0.045	0.045	0.045
internal charged track MUL	0.354	0.221	0.177	0.014
internal/external track MUL ratio [%]	17.7	17.1	12.7	16.5
Monte Carlo point MUL	1.938	1.246	1.369	0.082
Monte Carlo point flux [kHz/cm <sup>2</sup> ]	2.135	1.770	1.502	1.290
readout-cell occupancy [%]	4.8	4.1	6.8	0.4
readout-cell occupancy (1xTRG) [%]	8.9	7.6	12.5	0.8
readout-cell multi-track prob. [%]	6.3	7.1	11.6	2.7

Track multiplicities on counters vary depending on the trigger condition, i.e. the event-selection criterion, in place. Table 3.3 summarizes mean multiplicities of different track types. The argon-on-lead test beam analyzed in this work is a multi-track (multi-hit) scenario with an interfering counter response to individual tracks. In 4xTRG events, the average external track multiplicity on large-area prototypes is greater than 3 which necessitates a dedicated evaluation of multi-hit effects during data analysis (cf. Sec. 5.2). Mean particle fluxes on the counters vary depending on the respective position in the setup, ranging from 1.8 kHz/cm<sup>2</sup> on 3-0-0 in the front to 1.1 kHz/cm<sup>2</sup> on 4-0-0 in the back. For six external tracks, about one internal (charged) track is created in a module, varying with material budget. The extraordinary behavior of counter 7-0-0 is linked to its construction with thin glass plates (0.33 mm in thickness compared to 0.7 mm and 1.0 mm, respectively). Concerning simulations with an active particle memory (cf. Sec. 4.2), the total number of Monte Carlo points to be expected in the run—whether of external or of internal origin—is an important quantity for estimating computation times.

Data rates to be transported by a triggered DAQ system can be anticipated—and the readout be configured accordingly—with reliable numbers on trigger frequency and on readout-cell occupancy which—on a Monte Carlo level—corresponds to the share of events (under a given trigger condition) in which the volume of a virtual cell is traversed

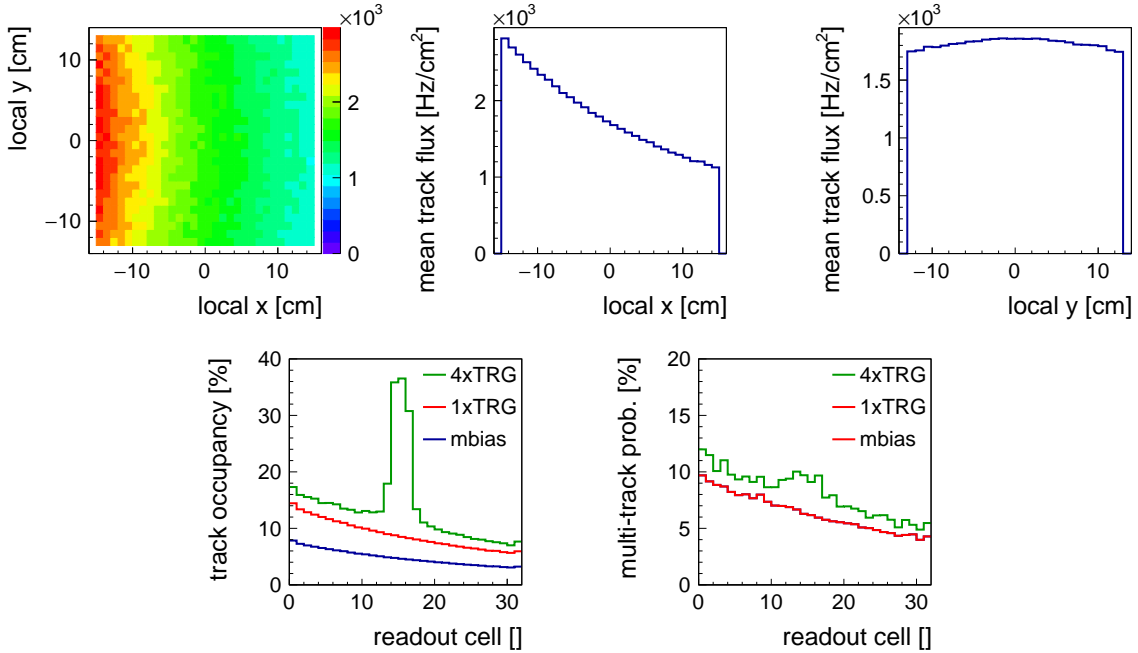


Figure 3.9: Mean flux of external—i.e. produced outside the respective gas box—Monte Carlo tracks from 1,000,000 minimum-bias argon-on-lead collisions at  $p_{\text{beam}} = 19 \text{ A GeV}/c$  leaving either directly or by secondary particles a trace in an active volume of counter 3-0-0, distributed over the counter surface (top left plot), projected onto the local  $x$ -axis (top middle plot), and projected onto the local  $y$ -axis (top right plot). Marginal bins are cropped not to display edge effects. Share of events in which readout cells of 3-0-0 are geometrically “occupied” (bottom left plot) by track traversal (normalized either to the entire set of UrQMD input collisions (mbias) or to subsets in which any (1xTRG) or all (4xTRG) counters in line are triggered by a—in the latter case target—MC track. Probability of an occupied cell to be traversed by multiple tracks (bottom right plot).

by an external track, determined from position averages of the external (if available) and all internal MC points of the respective track genealogy. Assuming that a collision event triggers any measurable response in the MRPC setup (1xTRG), occupancies of about 10% need to be coped with in the present case, depending on counter position and cell geometry. The impact of signal induction on multiple readout cells by a single primary particle traversing the counter on readout-cell occupancy is subject to a full response simulation including digitization. For the final CBM time-of-flight wall, an upper occupancy limit of 5% is pursued (cf. Sec. 2.4.3). Related to occupancy but more relevant to interference studies than to predictions of DAQ data load is the multi-track probability, i.e. the chance of a readout cell to be hit by multiple tracks within the same event. The preceding considerations are a posteriori knowledge gained while attempting to reconstruct the experimental results from the CERN/SPS setup with simulations. In fact, an adaptation of the DAQ system according to insights obtained from a priori

estimates of occupancies etc. would have been strictly constrained by the limited availability of readout-chain components and by the system stability in view of challenging spill conditions (cf. Sec. 3.2). Thus, a strategy was embarked on to achieve the most stable data output with the electronics at hand.

Owing to the positioning of modules parallel to the  $xy$ -plane of the cave at different distances to the beam axis, the average quantities stated in Tab. 3.3 correspond to integral values of strongly position-dependent distributions which is illustrated for counter 3-0-0 in Fig. 3.9. In the closest vicinity to the beam axis, i.e. on cell 0 situated in the negative local  $x$ -range, particle fluxes in the center approach  $3\text{ kHz/cm}^2$ , dropping to about  $1\text{ kHz/cm}^2$  on the upper counter end. As the counter is centered about cave- $x$  (local  $y$ ), the flux pattern along this axis is symmetric in contrast to cave- $y$  (local  $x$ ). Requiring a selector track to be present in an event (4xTRG), readout cells which this track can pass through geometrically (cf. Tab. 3.2) show an increased occupancy.

Given an estimated beam intensity of  $23.7\text{ MHz}$  (CBM:  $1\text{ GHz}$ ), a probability of  $4\%$  (CBM:  $1\%$ ) for a beam nucleus to collide with a target nucleus, and a resulting collision rate of  $948\text{ kHz}$  (CBM:  $10\text{ MHz}$ ), the question of possible event overlaps in time arises. Making use of Eq. (2.1), collisions in general overlap in a  $25\text{ ns}$  event-time window in  $2.3\%$  of the cases while this number is reduced to  $1.3\%$  if only detectable 1xTRG events are considered. In the data analysis, no specific effort is dedicated to identifying occurrences of event mixing.

## 3.2 Dual detector readout with TrbNet

### 3.2.1 Digitization of MRPC signals using FPGA-TDCs

Upon preamplification and discrimination of analog MRPC signals by PADI chips soldered onto readout boards which are—in most cases—directly connected to counter cell ends in the gas box (cf. Fig. 2.14), the resulting rectangular pulses which are routed out of the module need to be digitized. Both signal edges carry information about the arrival/discrimination time (leading edge) and the charge content/time over threshold (trailing edge minus leading edge) of the original detector signal. Digitization is the process of converting the analog PADI signal to a digital detector message (“digi”) consisting of a time stamp and a time-over-threshold (ToT) value. For comparability with messages from other counters, signal edges need to be measured against a common experiment clock which allows for placing digi time stamps on a contiguous time axis. This measurement is conducted in a TDC (time-to-digital converter) to which a periodical clock signal is fed. At CERN/SPS, an FPGA-TDC implemented on a LatticeECP3 (cf. Fig. 3.2) was employed for this task [104] (version 2.1.2) which provides 32 input channels for leading-/trailing-edge digitization of 32 input signals. Internally, each TDC channel features a so-called tapped delay line (TDL) where the actual digitization is carried out against the  $200\text{ MHz}$  experiment clock (with a period of  $5\text{ ns}$ ) provided by the CLOSY clock system [105]. In a simplified representation, a series of delay elements realized with architecture-dependent logic blocks of the FPGA is connected to a hit

register of D flip-flops each equipped with a data input D, an edge-sensitive clock input C, and an output Q. When an input signal propagates through a delay element, the binary logic level at the D-input of the connected flip-flop changes which repeatedly occurs in subsequent delay elements until the state of the entire hit register, i.e. the series of output states Q reflecting the respective input states D, is latched by the simultaneous arrival of the next rising edge of the 200 MHz clock signal at all C-inputs. The pattern of logic levels 0 and 1 read from the hit register expresses the arrival time difference between the input signal and the clock signal at the TDL in terms of delay elements the signal propagated through before the clock signal arrived. By this means, a coarse-time measurement with the 5 ns granularity of the clock period is complemented by a fine-time interpolation with delay elements. As signal delays caused by individual elements of the delay line are not uniform and also depend on operating temperature of the FPGA, the fine-time measurement needs to be calibrated (cf. Sec. 3.3). The 11-bit coarse-time counter implemented in each TDC channel covers a time interval of  $10.24 \mu\text{s}$  (called an epoch) and is extended by a single 28-bit epoch counter in the TDC—serving all channels—which is incremented when its own coarse counter overflows. The calibration software needs to keep track of overflows in the epoch counter occurring every 2748.8 s. Coarse- and (10-bit) fine-time information along with the channel index and the signal edge type (leading or trailing) form a 4-byte time word which is stored for every measurement in a 128-word channel ring buffer, together with a 4-byte epoch word if and only if the epoch counter has been incremented since the previous measurement. In total, 12 bytes of hit data are generated for a signal edge pair not split between two subsequent epochs. The ring buffer has a capacity to safely store data from about 40 input signals, digitized in different TDC epochs, leaving some margin for buffer overflow handling. To measure leading- and trailing-edge arrival times of the input signal in a single TDL given a TDC channel dead time of about 20 ns while the hit register is read out and the hit data stored in the ring buffer, the input signal is artificially stretched. For this reason, ToT values measured by the TDC do not directly correspond to the width of PADI output signals (cf. Sec. 3.3).

### 3.2.2 The centrally controlled trigger and readout process

While the FPGA-TDC autonomously digitizes signal-edge arrival times and stores the corresponding data in ring buffers, it does not automatically push the data towards the back end as the self-triggered GET4 chip [81]—the default TDC solution for CBM TOF—would do. Instead, it requires to be embedded in a data-pull architecture which fetches data from the TDC front end. Such a conventional trigger system based on the TrbNet protocol [94] (details in [106]) with a central controller sending trigger and readout requests to and receiving data from front-end nodes was operated at CERN/SPS (cf. Fig. 3.10). The central TrbNet controller, the Central Trigger System (CTS) [107], implemented on the central FPGA of a (master) TRB3 board (cf. Fig. 3.2) communicates via optical (off-board) and electrical (on-board) connections with TDC endpoints which are placed either on peripheral FPGAs of a (master/slave) TRB3 board or on customized

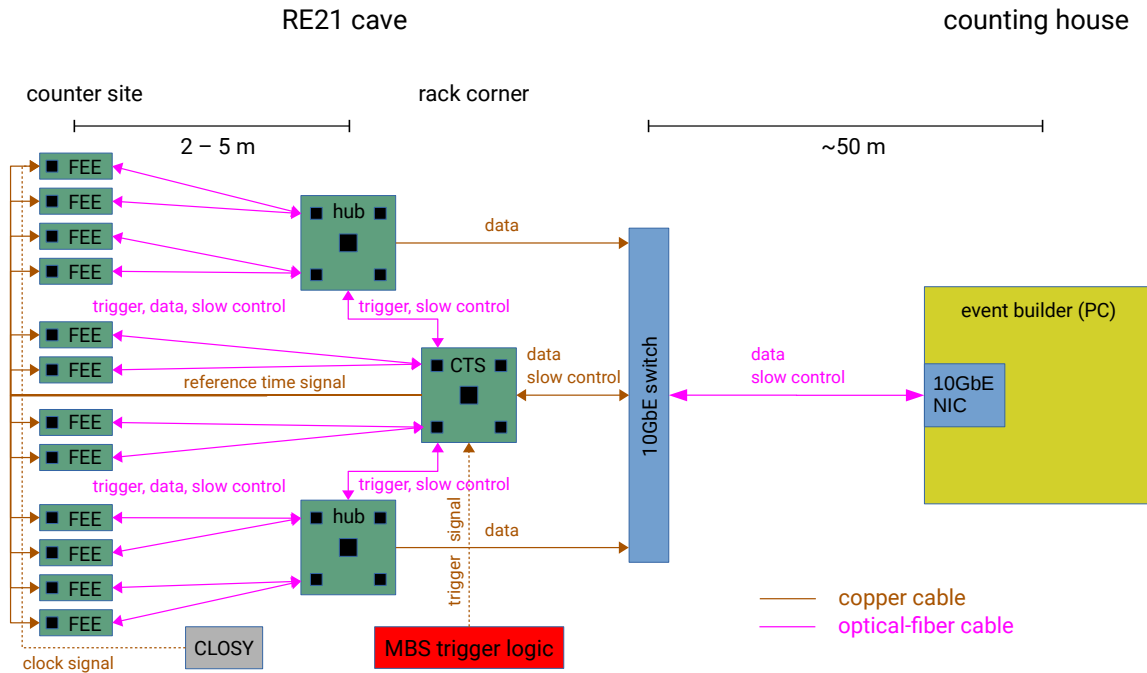


Figure 3.10: Sketch of the TrbNet-based data acquisition implemented at CERN/SPS. Upon reception of an external trigger signal by the MBS trigger logic, the Central Trigger System (CTS) first sends a reference time signal to the FEE-TDCs—mounted close to the detectors and synchronized by the clock system CLOSYS—which marks the upper end of the trigger window for TDC channel-buffer readout (cf. Fig. 3.11, right plot). Then, via central and peripheral TrbNet hubs, the CTS sends a trigger packet to the TDC endpoints and stays in busy state (ignoring any further external or internal trigger input) until it receives a busy-release packet from all endpoints indicating standby for another trigger cycle. In a separate readout process, the data stored in the FEE subsubevent buffers are requested to be sent towards the CTS and—on the first central FPGA of a TRB3 board which the FEE data packets arrive at—merged into subevents and bridged from TrbNet to Gigabit Ethernet (GbE). Several GbE data uplinks transmitting subevent data are combined into a single 10 Gigabit Ethernet (10GbE) connection by a dedicated switch. Via optical-fiber cable, the data are transported from the cave to the counting house and the final event is constructed from associated subevents by event-building software running on the DAQ PC from which slow-control messages can be sent to all TrbNet nodes via the CTS.

front-end cards in the vicinity of the detectors which were exclusively used as TDCs at CERN/SPS. Slave TRB3 boards without a CTS running on their respective central FPGA serve as hubs forwarding requests from the CTS and responses by endpoints on one of three logical TrbNet channels: a trigger channel to collect and tag front-end data for readout, a readout channel for data transport, and a slow-control channel for configuration—all realized on one physical link. FEE-TDC (front-end electronics) cards

are integrated into the DAQ network via peripheral and central hubs on master and slave TRB3 boards. Round-trip times of packets in this (rather small) star-topology network at CERN/SPS amount to about  $5\ \mu\text{s}$  which—ignoring preparation times for event data in the TDC endpoints—imposes a limit of 200 kHz on theoretically achievable trigger rates. Actually, delays originating from network latency in a centrally controlled DAQ system disqualify its deployment in the CBM experiment from a technical point of view. A trigger decision by the CTS is taken either periodically with respect to an internal pulser signal recurring at a fixed frequency or depending on coincidences in time between trigger signals obtained from individual counters responding to physical events. Hence, a dual readout strategy is pursued. The periodical readout of front-end buffers in the former case could be regarded as a mockup of a self-triggered data acquisition in an intrinsically triggered framework. Physics triggers result from coincident firing of any diamond channel (the logical OR of signals from all channels) and of any group of four neighboring MRPC cells on both ends (which are read out by the same two four-channel PADI chips). In total, 7 trigger signals derived from AND circuits between 7 MRPCs in the setup (including three counters in the lower branch) and the rear plane 5-1-0 of the double-diamond detector (the front plane, 5-0-0, is not considered) are generated by an external VULOM trigger logic and injected into the trigger logic of the CTS. Upon detecting a rising edge in a trigger input module—either from a periodical pulser or from an external trigger signal—the associated trigger channel is activated and a new TrbNet trigger process is started (cf. Fig. 3.10) if the previous one has been completed. First, the CTS sends a differential reference time signal to all TDC endpoints via direct electrical connections outside TrbNet of varying lengths depending on the position of the respective TDC card in the setup. Splitting is provided by dedicated trigger distribution boards. The rising edge of this signal is measured by a reference channel which every TDC features in addition to its 32 input channels. Concerning synchronization of clock (coarse) counters among different TDCs, a system-wide counter reset can be issued on DAQ startup upon arrival of the first reference time signal at each TDC to correct for time offsets, apart from shifts attributed to different trigger cable lengths. The same procedure can be performed in calibration software with digitized reference time stamps (cf. Sec. 3.3). In the TrbNet trigger process, the arrival of the reference signal starts the readout of channel ring buffers into the subsubevent buffer of the TDC endpoint, a 4096-word (16 kiB) FIFO with sufficient storage capacity for data from 32 completely filled 128-word channel ring buffers. While in self-triggered mockup operation all data residing in the ring buffers are read out, only a small fraction of data with time stamps falling into a trigger window (cf. Fig. 3.11, right plot) defined with respect to the reference time stamp is transferred to the subsubevent buffer if the system is driven by physics triggers. As the generation of trigger signals from combinations of detectors and the broadcast of the reference time signal by the CTS upon a positive trigger evaluation are delayed regarding the arrival time of counter signals at the TDC, the reference coarse-time stamp (including epoch information) is compared backwards in time against the coarse-time stamps of time-sorted channel data in the ring buffers. Channel signals which were digitized prior to an adjustable time difference to the reference signal, i.e. which do not fit into the trigger-window range, are discarded.

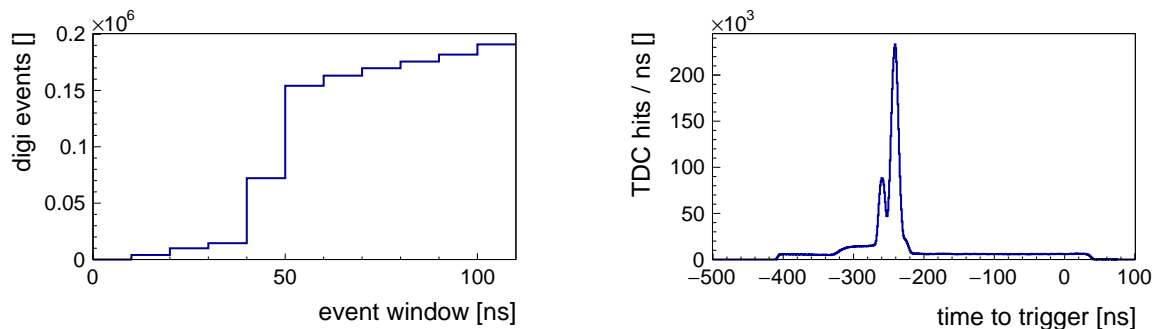


Figure 3.11: Exemplary event building in software from (calibrated) digital detector messages distributed in time in ascending order if TrbNet is triggered periodically, i.e. not linked to any correlation of physical signals in a combination of trigger detectors (left plot). With an increasing temporal size of the event window always starting with a diamond digi, an “event step” appears when—depending on the synchronization between TDCs—digi pairs from additional detectors required to be present fall into the window as well (here: 3-0-0 and 4-0-0). If the readout system is driven by (a coincidence matrix of) physics triggers instead (right plot), all detector signals digitized by the TDC (raw TDC hits) up to an adjustable point in time (here:  $-400$  ns) prior to the arrival time of the trigger signal at the TDC (which is delayed due to trigger-logic latency) are considered to belong to the same physical event. Normally, no further event building in software is necessary in this case. The double-peak structure indicates a superposition of different trigger conditions.

In the meantime, a TrbNet trigger packet has been prepared by the CTS and sent over the DAQ network including an event tag which the data from the ongoing (or already completed) transfer between channel ring buffers and subsubevent buffer in the TDC endpoint is marked with. When this data transfer is finished and the tagged subsubevent data are available for readout from the buffer, the endpoint replies to the CTS trigger packet with a busy-release packet, signaling readiness for reception of a subsequent trigger request. The CTS, in turn, waits for the arrival of busy-release packets from all TDC endpoints in the system before pushing a token with the current event tag into the readout queue and switching from busy to idle state, ready to process trigger input signals which are ignored while the CTS is busy. Readout operations on the corresponding channel of TrbNet are executed by the CTS asynchronously to trigger processes although they depend on the availability of a token in the readout queue. TrbNet does not suspend all trigger requests until the data from a single trigger and readout process have been extracted from the system as the TDC endpoint buffers can—under normal operating conditions with an active trigger window—store data of many subsubevents. Even in the unlikely case of all TDC channels (including the reference channel) firing in an event in physics-triggered mode, the resulting subsubevent of size 392 B ( $32 \times 12 \text{ B} + 1 \times 8 \text{ B}$ ) is rather small compared to a FIFO capacity of 16 kiB. When the TDC endpoint receives a readout request by the CTS, it sends the corresponding

subsubevent data in its buffer via TrbNet towards the central controller. On the first central hub which the TDC data packets arrive at (whether on the CTS FPGA itself or on the central hub of a slave TRB3 board), subsubevent data from all connected TDC downlinks are combined into a single subevent which is extracted from the ongoing readout process and filled into a subevent buffer. Data residing in the subevent FIFO are—by further encapsulation—prepared for transmission via Gigabit Ethernet (GbE) to the PC serving as event builder, i.e. combining subevents received from different TRB3 boards and writing the final event data to disk in a list-mode format. At CERN/SPS, the DABC (Data Acquisition Backbone Core) framework [108] (version 2.7.1) was used for this purpose.

### 3.2.3 Bandwidth limitations and event yields

The bottleneck for data transport in the DAQ system are the GbE uplinks towards the event builder. If several TDC endpoints are connected to a single TRB3 data concentrator, they need to share the same uplink which transmits 8-bit data words at a rate of 125 MHz (net bit rate: 1 Gbit/s). However, this technical bandwidth cannot be fully exploited due to idle time introduced by Ethernet frame construction between transmission of consecutive frames, limiting the achievable net bit rate to about 100 MB/s (800 Mbit/s) [109]. On links between TrbNet nodes, however, 16-bit data words are exchanged at a rate of 100 MHz (net bit rate: 1.6 Gbit/s), i.e. even a single TDC endpoint can saturate the GbE uplink if the channel data load is sufficiently high. Owing to the interdependence of trigger and readout processes in a centrally controlled setup, the most heavily loaded component puts the entire system on hold. In physics-triggered operation with a trigger window in place selecting only a small share of TDC channel data for readout, it is rather unlikely to reach the GbE bandwidth limit.

The situation for a self-triggered mockup, though, is different. When the reference time signal arrives at the TDC endpoints, the readout of all channel data generated from signals of heavy-ion collision secondaries on the connected detectors since the previous trigger is started. Here, depending on collision rates in conjunction with readout-cell occupancy, data uplink capacities of the DAQ system can be exhausted more easily. Applying a periodical trigger frequency which takes into account estimated channel hit rates and limited ring-buffer sizes not to risk buffered data to be overwritten by subsequent hits due to too large readout intervals does not ensure loss-free data taking alone, if data transmission speed is a limiting factor. Referring, as an illustrative example, to (idealized) Monte Carlo calculations in Sec. 3.1.3, TDC channel hit rates of about 50 kHz can be inferred from a theoretical event rate of 515 kHz under 1xTRG conditions with a single readout cell being occupied in 10 % of these cases on average. Assuming equal hit distances in time of 20  $\mu$ s—placing hits in different TDC epochs—the minimum readout frequency for a ring buffer filled with a maximum of 40 hits amounts to 1.25 kHz. For the argon test beam, different trigger frequencies of 10 and 20 kHz were used to keep fill levels of subsubevent buffers at moderate values. Even higher trigger rates might have stressed the event-building software on the DAQ PC beyond processing

capability. Disregarding the additional overhead which a more frequent system readout is accompanied by, the data rate to be conveyed periodically stays constant. The combined data volume in all  $32 + 1$  TDC channels to be transported out of the system within the  $800 \mu\text{s}$  maximum readout interval, ignoring protocol overhead, is  $15.368 \text{ kB}$  then. In the same time interval, the Gigabit Ethernet module can transmit  $80 \text{ kB}$  of data ( $100 \text{ kB}$  in theory). From this estimate, it seems reasonable to connect up to 5 TDC endpoints to a central data hub. At CERN/SPS, a total of 5 TRB3 boards (a master with a CTS and four slaves) was deployed for transport of data from up to 4 TDC downlinks each. From the accumulated channel count of  $640$  ( $20 \text{ cards} \times 32 \text{ channels}$ ),  $512$  TDC channels were connected to readout cells on diamond and MRPC detectors. However, due to the huge intensity fluctuations in the spill of argon ions extracted from SPS (cf. Fig. 3.6), GbE uplink capabilities were actually overstrained during copious  $50 \text{ Hz}$  subspills, taking a microscopic perspective (cf. Fig. 3.12). In the end, data-rate estimations based on beam-intensity averages are only meaningful if the macroscopic picture can be adapted to individual trigger and readout processes.

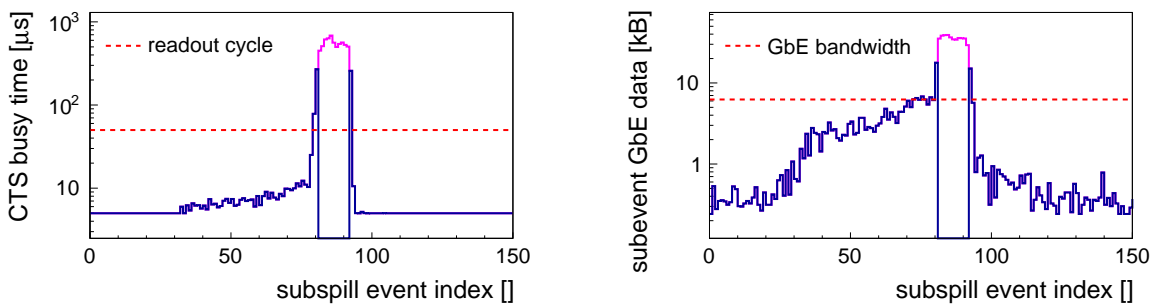


Figure 3.12: Mutual dependence between the evolution of the CTS busy time (left plot) and the evolution of the subevent size assembled by a TRB3 central hub (right plot) as a function of event index in an exemplary subspill (cf. Fig. 3.6). If the subevent data to be transported via GbE approaches the (theoretical) GbE bandwidth limit of  $6.25 \text{ kB}$  in a readout cycle of  $50 \mu\text{s}$ , full subevent buffers in the most heavily loaded central TrbNet hub exert back pressure on all front-end subsubevent buffers which in turn cannot dispatch their data. Eventually, the most heavily loaded front-end endpoint does not send a busy-release packet to the CTS in time for the next  $20 \text{ kHz}$  trigger to be accepted. If a periodical trigger cycle is skipped, the amount of data to be dispatched with the subsequent readout request by the CTS is—assuming constant load—doubled. In the end, if more TDC raw data are generated than can be transported through the GbE bottleneck for a sustained period of time, TDC channel ring buffers are partially (or even fully) overwritten (magenta curves), rendering data useless for analysis. Such events are nevertheless recorded as the integrity of TrbNet header data is not affected by the overflow of front-end buffers.

Confronted with the situation described in Fig. 3.12, a re-cabling of the setup aiming at a smaller number of TDC cards per TRB3 board—reading out the diamond-detector

and the four MRPCs in the upper setup only—would have been a logical step to take for mitigation of data loss resulting from overwritten channel buffers. Theoretically, the load of 7 TDCs (1 TDC for 16 single-ended cells of diamond detector 5-1-0, 2 TDCs for 32 double-ended cells of counter 3-0-0, 2 TDCs for 24 double-ended cells of counter 9-0-0, 1 TDC for 16 double-ended cells of counter 7-0-0, and 1 TDC for 16 double-ended cells of counter 4-0-0) could have been distributed to 5 data hubs to increase the recorded amount of usable event data. Practically, however, such mending efforts were impossible to undertake in the ongoing test beam. On Wednesday evening, March 4, between 07:27:03 and 08:09:09 p.m. (total duration: 00:42:06 hours), the self-triggered TrbNet mockup was operated to continuously record collision data from 43 accelerator spills—with interruptions for changing readout frequencies and trying different configurations for data transport (sending multiple subevents in a single UDP datagram and using larger Ethernet jumbo frames to increase throughput). Following event building from time-calibrated detector digis in CbmRoot (cf. Fig. 3.11, left plot), not to be confused with the composition of DAQ events from multiple subevent streams by DABC, about 11.5 M physical events could be extracted from the recorded mockup data, scanning—in software—a 75 ns event window, opened by the time stamp of a 5-1-0 diamond digi, for an additional digi pair on counter 3-0-0 (which geometrically shadows almost the entire rear part of the setup; cf. Tab. 3.2). Complementing the dual readout strategy at CERN/SPS, a physics-triggered run was conducted—with interruptions due to maintenance work at the parallel TRD setup in the cave—under similar experimental conditions on Thursday morning, March 5, between 00:47:00 and 05:49:36 a.m. (total duration: 05:02:36 hours), yielding 6.4 M events distributed over 383 spills which were rebuilt in software for a better comparability with mockup data and to dispose of potentially multiple diamond hits in the TDC trigger window. Both runs were fully calibrated and analyzed with virtually identical results but only the physics-triggered run is further considered in this work as it contains—despite a smaller overall event number—more statistics for the small counter 4-0-0 in the back, owing to the weighted mix of trigger combinations generating the original DAQ event sample, which is needed as a reference counter for data analysis.

Monitoring of conditions and occurrences in the experimental zone took place from a safe distance in a counting house. The system status was shown on various live displays for particle fluxes on scintillators (cf. Sec. 3.1.2) and counters, for TDC channel rates, for basic correlations between counters computed online in CbmRoot, etc. Selected differences between self-triggered mockup and physics-triggered regular operation of TrbNet are depicted in Fig. 3.13, visible on CTS and DABC monitors, respectively, during beam time.

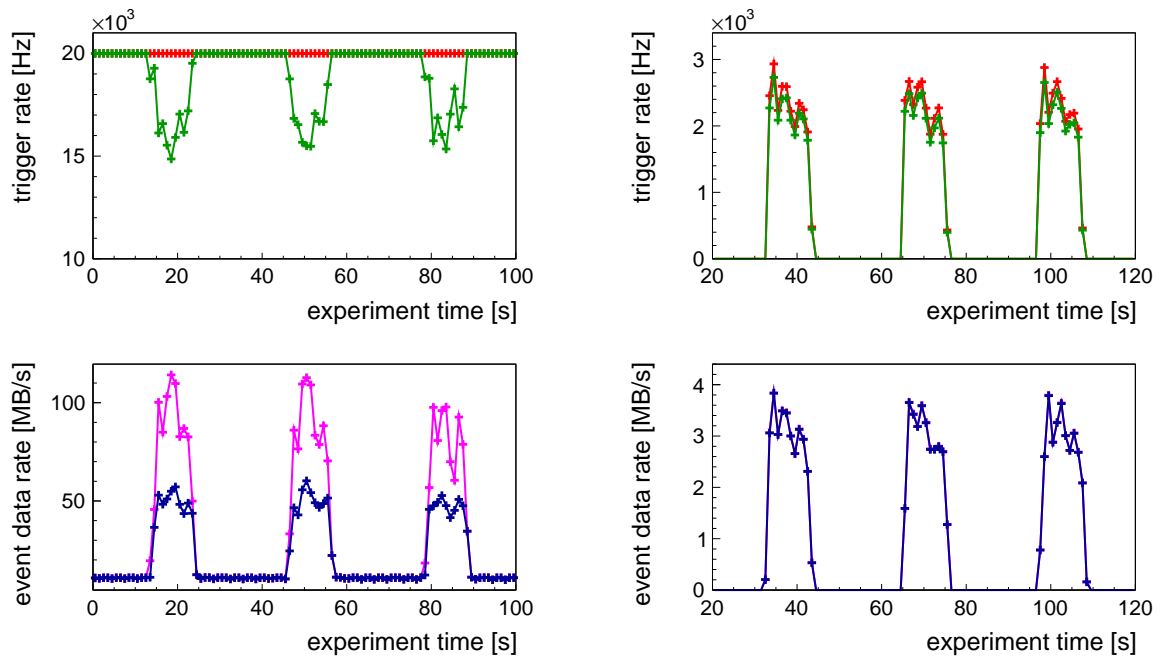


Figure 3.13: Comparison of trigger and event data rates as a function of experiment time obtained with a 20 kHz periodical pulser trigger (left column) and with a physics trigger based on coincident detector signals (right column) recorded under similar experimental conditions. In spill, the rate of accepted trigger signals (green curve) drops below the rate of available trigger signals (red curve) as the front-end readout process cannot permanently be completed within the  $50\ \mu\text{s}$  trigger-cycle window due to a too high event data load (top left plot). As a direct consequence, front-end buffers are partially overwritten leaving only a fraction (blue curve) of recorded event data (magenta curve) for data analysis (bottom left plot). With an input physics-trigger rate throttled by the MBS trigger logic for reasons of DAQ system stability, the corresponding curves in the right column differ much less from each other.

### 3.3 Raw-data calibration and hit building

Hit data read out from TDC channels during data acquisition contain coarse- (epoch included) and fine-time information reflecting subsequent arrival times of both input signal edges at the delay line with respect to the experiment clock. In order to convert TDC hit data to a digital detector message (“digi”), the final raw-data format in Cbm-Root, values of coarse- and fine-time counters need to be translated into time stamps. Regarding coarse time, the corresponding counter value is multiplied with the system clock period of 5 ns and counter overflows are kept track of. The spectrum of occupied fine-time bins obtained for all hits in a TDC channel reflects the arrival-time differences between input signals and the clock signal which samples the delay line, with a minimum of 0 ns attributed to the lower end of the spectrum (lower edge of bin  $b_{\min}$ ) and a maximum of 5 ns (a clock period) ascribed to the upper end (upper edge of bin  $b_{\max}$ ). An obvious translation method between fine-time bin  $i$  and a distance in time to the next rising edge of the clock signal is a linear interpolation between bin centers,

$$\text{ft}(i) = \frac{\tau_{\text{clk}}}{b_{\max} - b_{\min} + 1} \left( i - (b_{\min} - 1) - \frac{1}{2} \right), \quad (3.5)$$

$\tau_{\text{clk}}$  referring to the clock period. However, fluctuations in relative frequencies of fine-time bins (cf. Fig. 3.14, left plot) caused by varying lengths of individual delay elements (so-called non-linearities) should be accounted for to utilize the full resolving capacity of the TDC [104]. With sufficient statistics available for a TDC channel, an interpolation respecting relative frequencies  $n_k$  of  $N$  occupied fine-time bins,

$$\text{ft}(i) = \tau_{\text{clk}} \left( \sum_{k=1}^i n_k - \frac{1}{2} n_i \right) / \sum_{k=1}^N n_k, \quad (3.6)$$

yields better time resolutions between reference channels of TDCs 1–19 and of TDC 0, respectively, the latter of which specifies the common experiment time axis all measured time stamps are to be arranged on (cf. Fig. 3.14, middle plot).

Concerning the significantly worse time resolution obtained for TDC 13 digitizing cell signals from the front diamond detector 5-0-0 (not considered hereafter), some additional jitter might have been introduced on the reference time signal by cabling. As Gaussian sigmas of time-difference spectra between measurements of the same signal by two different TDCs are plotted, single-TDC resolutions can be derived by dividing the given numbers by the square root of two. A time-difference resolution of 20 ps corresponds to a single-TDC resolution of 14 ps. If coarse counters across TDCs are not reset simultaneously on system startup, a time-offset correction with respect to TDC 0 can be performed based on reference-channel information prior to further calibration steps (cf. Fig. 3.14, right plot). It is more a matter of convenience than of necessity, though, as signal propagation offsets due to routing differences between counter cells to a TDC and between neighboring TDC channels on the same FPGA need to be corrected for in a later iteration anyway. Now, a digi featuring a (continuous) time stamp and a time over threshold (ToT) can be generated from a leading-/trailing-edge TDC measurement

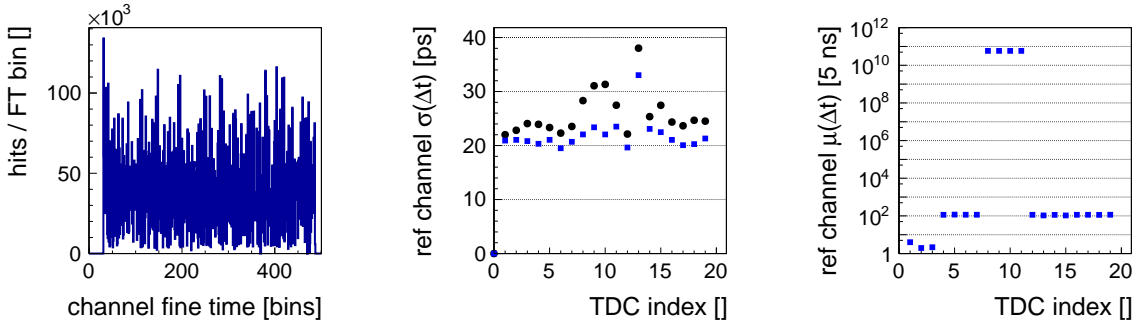


Figure 3.14: Non-linearity of TDC fine-time interpolation by the tapped-delay-line (TDL) method in an exemplary TDC channel (left plot). Gaussian sigmas of time-difference spectra between the reference channel of every TDC in the setup against reference TDC 0 (middle plot). The black circles are obtained with a linear interpolation between all occupied fine-time bins (cf. Eq. (3.5)) while the blue squares result from an estimation of actual fine-time bin widths based on relative bin occupancy (cf. Eq. (3.6)). Gaussian mean shifts between reference-channel coarse counters result from latency in the DAQ network if a global coarse-counter reset is issued via TrbNet slow control and—concerning TDCs 8–11—from individual power cycling not followed by a common reset (right plot).

and—with an addressing scheme extending the three-digit counter identifier by a cell index and a cell-side index (0 for negative local  $y$ , 1 for positive)—be traced back to its geometric origin in the test-beam setup.

Position and time of a particle hit on the counter surface are reconstructed from the index of the cell on which the signal was induced (local  $x$ ; cf. Eq. (3.1)), from the difference between time stamps on opposing cell ends (local  $y$ ; cf. Eq. (3.3)), and from the average of time stamps minus half the signal propagation time along the full cell of length  $s$ ,

$$t = 1/2 (t^- + t^+) - 1/2 s/v_{\text{signal}}. \quad (3.7)$$

Measured time stamps  $t^-$  and  $t^+$  depend on position  $y_0$  and time  $t_0$  of the induction “spot” on the cell and on the aforementioned signal propagation times to the delay line in the TDC which vary from cell to cell, labeled with  $c^-$  and  $c^+$  in the following. Actually, the latter quantities are functions of the signal amplitude, i.e. the time over threshold, as larger signals are discriminated and digitized earlier in time than smaller signals which is discussed later in this section. Ignoring uncertainties of the induction process and measurement resolutions, digitized signals on opposing cell ends would be time-stamped according to

$$\begin{aligned} t^- &= t_0 + (s/2 + y_0) / v_{\text{signal}} + c^- \quad \text{and} \\ t^+ &= t_0 + (s/2 - y_0) / v_{\text{signal}} + c^+, \end{aligned} \quad (3.8)$$

with unknowns  $c^-$  and  $c^+$  to be determined from residuals between reconstructed cell hits and a reference. Inserting these expressions into Eqs. (3.3) and (3.7), residuals in  $y$

and in  $t$  are obtained presuming ideal knowledge of hit position and time on the cell,

$$\begin{aligned} r_y &:= y_{\text{hit}} - y_0 = 1/2 (c^- - c^+) v_{\text{signal}} \quad \text{and} \\ r_t &:= t_{\text{hit}} - t_0 = 1/2 (c^- + c^+). \end{aligned} \quad (3.9)$$

Outside of a Monte Carlo simulation,  $y_0$  and  $t_0$  are not known. To determine routing offsets  $c^-$  and  $c^+$  for experimental data, these reference values need to be extracted from the data itself, in addition to the signal velocity  $v_{\text{signal}}$ . Starting from the mere time-difference spectrum  $d_t$  between signals on opposing cell ends due to a lack of knowledge on  $v_{\text{signal}}$ ,

$$d_t := 1/2 (t^- - t^+), \quad (3.10)$$

offsets can be constrained by requiring the  $d_t$ -spectrum to be centered about zero which does not necessarily imply shifting the mean value of  $d_t$  to the point of origin as the spectrum—depending on the irradiation profile on the cell—might not be axially symmetric. The deviation of the measured average  $d_t$  from the mean value of a centered  $d_t$ -spectrum,

$$\langle d_t \rangle_{\text{hit}} - \langle d_t \rangle_{\text{central}} = 1/2 (\langle c^- \rangle - \langle c^+ \rangle), \quad (3.11)$$

directly corresponds to half the time difference between mean values of  $c^-$  and  $c^+$ , angle brackets here denoting integration over ToT-dependencies of the two propagation-time offsets. The second boundary condition required for an unambiguous determination of these quantities is given by an alignment of the reconstructed hit time on the cell to a reference time measured within the same event,

$$\langle t_{\text{hit}} - t_0 \rangle = 1/2 (\langle c^- \rangle + \langle c^+ \rangle). \quad (3.12)$$

As an arrangement of hit times on the experiment time axis according to physical time-of-flight information between different stations—which could be obtained from a Monte Carlo simulation (cf. Tab. 3.2 for the shortest TOF values between target and counters)—is not needed for the  $\chi^2$ -analysis of residuals conducted later in this work (cf. Chap. 5), no extrapolation of the reference time towards the physical hit time on the cell to calibrate is performed. In the first calibration instance, the reference time is provided by diamond detector 5-1-0 in each event. As a result, calibrated hits on all cells in the setup occur—on average—simultaneous to the time stamp of the diamond measurement. Combining Eqs. (3.11) and (3.12) allows for calculating mean propagation-time offsets at both cell ends according to

$$\begin{aligned} \langle c^- \rangle &= \langle t_{\text{hit}} - t_0 \rangle + \langle d_t \rangle_{\text{hit}} - \langle d_t \rangle_{\text{central}} \quad \text{and} \\ \langle c^+ \rangle &= \langle t_{\text{hit}} - t_0 \rangle - \langle d_t \rangle_{\text{hit}} + \langle d_t \rangle_{\text{central}}. \end{aligned} \quad (3.13)$$

Concerning reconstruction of hit position and time on diamond cells which are read out on a single end only, a fixed position along the cell of  $y_0$  can be freely assigned (zero in this case) which enters the calculation of hit times from a single digi time stamp,

$$t = t^- - (1/2 s + y_0)/v_{\text{signal}}. \quad (3.14)$$

Also, this leaves a single offset parameter  $c^-$  to be determined for temporal alignment of diamond cells against an MRPC reference cell. Due to the position spread of beam-ion hits along the 1.8 cm long diamond cells which is not accounted for by a single-ended readout, some additional jitter is introduced to the time residual between the diamond and counters in the setup. Since these residuals are considered for calibration only and not for performance evaluation during analysis (done exclusively between MRPCs), this effect is not of any relevance.

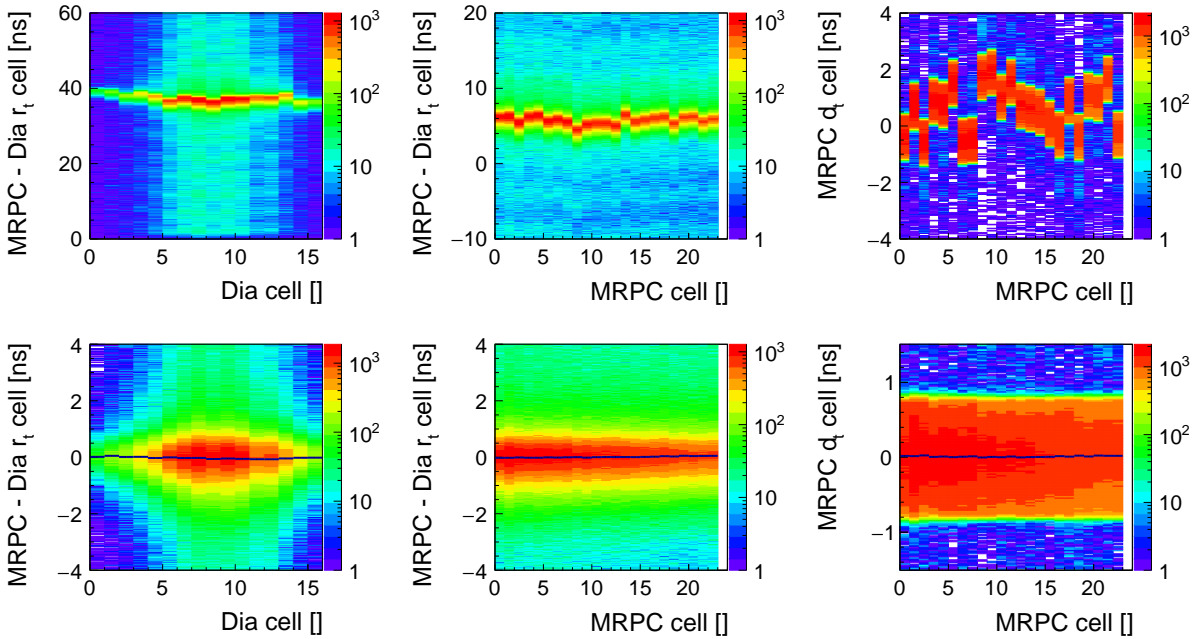


Figure 3.15: Cell-based time and position offsets after TDC calibration (upper row) and after corrections (lower row). Cell time residuals of diamond detector 5-1-0 against an MRPC reference cell of counter 3-0-0 (left column). Cell time residuals of counter 9-0-0 against a calibrated diamond reference cell (middle column). Top/bottom time-difference spectra of cells on counter 9-0-0 (right column). Profile lines in the lower row indicate cell averages.

The first step taken to calibrate digi time stamps for offsets in time and position is independent from a geometrical matching in  $xyz$  between cell hits on different counters as individual MRPC cells are compared against diamond cells and not against each other. A hit on the diamond prior to a collision event in the target imposes no directional bias on particle trajectories in the setup. At this calibration level, only cell hits reconstructed from the earliest top/bottom digi pair on a counter cell in the respective event (a single digi in the diamond case) are considered. Noisy or dead cells are excluded from this procedure (cf. Tab. 3.4). For cell alignment on the diamond detector, residuals between diamond cells and a reference cell on counter 3-0-0 (cf. Fig. 3.15), generated from the entire event sample, are shifted to zero mean. Apart from further smoothing between neighboring diamond cells in the course of calibration, preserving the overall average,

these shifted diamond hits serve as fixed reference points in time on a continuous time axis for all hits forming the respective events. Then, time offsets between all counter cells in the setup and a reference cell on 5-1-0 are corrected for. In parallel, time-difference spectra on counter cells are centered about zero, utilizing a fit function which accounts for inhomogeneous irradiation profiles on cells,

$$f(y) = \frac{C}{s} \left[ \Phi \left( \frac{y - y_0 + s/2}{\sigma_y} \right) - \Phi \left( \frac{y - y_0 - s/2}{\sigma_y} \right) \right] \times \left( 1 + a(y - d)^2 \right), \quad (3.15)$$

noted down in position domain but equivalently applicable to time-difference domain. The function comprises—apart from a normalization constant  $C$ —two factors, the former expressing the convolution of a continuous uniform distribution  $\mathcal{U}(-s/2, s/2)$ , spanning the entire cell of length  $s$ , with a normal distribution  $\mathcal{N}(y_0, \sigma_y^2)$ , centered about  $y_0$  with a standard deviation of  $\sigma_y$  (the single-cell  $y$ -resolution). Regarding the first factor only, its full width at half maximum (FWHM) corresponds to the cell length  $s$ . As for the term on the right-hand side, the homogeneous plateau obtained for  $a = 0$  can be reshaped to assume an either convex ( $a > 0$ ) or concave ( $a < 0$ ) parabolic form originating from an adjustable vertex  $d$ . Due to the irradiation profile itself (cf. Fig. 3.9) and to signal interference pulling hit positions towards the cell center, concave  $d_t$ -distributions were measured for counters with horizontally oriented cells in the setup at CERN/SPS (cf. Fig. 3.16). The above formula facilitates extracting location and shape parameters from these distributions which are required for correcting time-difference offsets by shifting locations—not necessarily mean values—to zero and for translating between time-difference and position domains using the signal propagation velocity which is experimentally specified in this way.

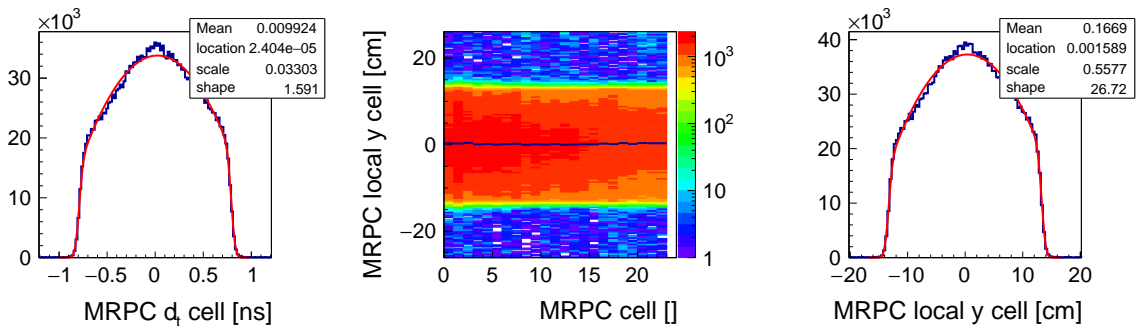


Figure 3.16: Translation of top/bottom cell time differences into local  $y$ -coordinates. The shape parameter  $s$  of Eq. (3.15) as obtained from a fit to the projection of Fig. 3.15, bottom right plot, onto the  $y$ -axis (left plot) is identified with the cell length in time-difference domain of counter 9-0-0 which is considered here. The conversion factor between time-difference and position domains (middle plot) is the signal propagation velocity (cf. Tab. 3.4) which translates the fitted shape in time-difference domain into the nominal value in position domain (cf. Tab. 3.2). An independent projection fit in position domain confirms the validity of this factor (right plot).

Table 3.4: Counter cells excluded from calibration and clustering and fitted signal propagation velocities of calibrated counters (exception: a default value of 18 cm/ns is used for the single-ended diamond cells).

counter	5-1-0	3-0-0	9-0-0	7-0-0	4-0-0
dead/disabled cells	/	0, 31	23	0, 15	0, 9
signal propagation velocity [cm/ns]	18.0	16.7	16.8	16.0	14.4

The impact of signal induction in the readout plane by a traversing charged particle which triggers an avalanche in an MRPC gas gap is not limited to a single cell. Consequently, correlations arise between reconstructed hits on adjacent cells, both in time and in position. These correlations jointly constitute the response of the counter to the particle crossing its active volume and should be treated as a whole in further calibration steps and in data analysis. In Fig. 3.17, this behavior is shown for time residuals and time differences on neighboring cells, prior to and following upon the initial round of offset corrections between cells. On the ordinates, the relations

$$\begin{aligned}\Delta d_t &:= d_t^m - d_t^n = 1/2 (t_m^- - t_m^+) - 1/2 (t_n^- - t_n^+) \quad \text{and} \\ \Delta r_t &:= r_t^m - r_t^n = 1/2 (t_m^- + t_m^+) - 1/2 (t_n^- + t_n^+)\end{aligned} \quad (3.16)$$

are plotted to quantify correlations among cells  $m$  and  $n$ , the latter being located closer to a reference cell on the counter surface which is used as a bidirectional starting point. Fitting distribution peaks with Gaussian functions yields a width for  $\Delta d_t$  which is less than half the width obtained for  $\Delta r_t$  although statistical errors on both expressions are identical according to Eq. (3.16) and can be reduced to the combined electronics resolution of discrimination and digitization processes in a single readout channel. The deviation is caused by the aforementioned dependence of measurement quality on signal amplitude, an effect which cancels out if time stamps from opposing ends of the same cell are subtracted from each other as is the case for  $\Delta d_t$  but not for  $\Delta r_t$ . Signals induced on multiple readout cells by the same avalanche vary in amplitude due to increasing distances to the response center, i.e. contributions from cells  $m$  and  $n$  to  $\Delta r_t$  do not neutralize each other in this respect. Criteria for building response clusters from individual cell hits should take this initial situation into account. Approximately oriented towards 5-sigma intervals of correlation widths obtained for different counters in the setup, distances among hits on adjacent cells are required not to exceed 0.5 ns in residual time and 0.25 ns in time difference (which translates into a position difference of 4.5 cm using a default signal velocity of 18 cm/ns). These limits are generally applied to clustering of cell hits on all counters.

A response cluster represents multiple measurements of a single physical interaction between a primary particle and the detection medium. Individual values in this ensemble are obtained with different accuracy, though, as the jitter on leading-edge discrimination is larger, on average, for smaller signals which are induced on the boundary cells of a multi-cell cluster than for bigger signals which are observed on central cells of the cluster.

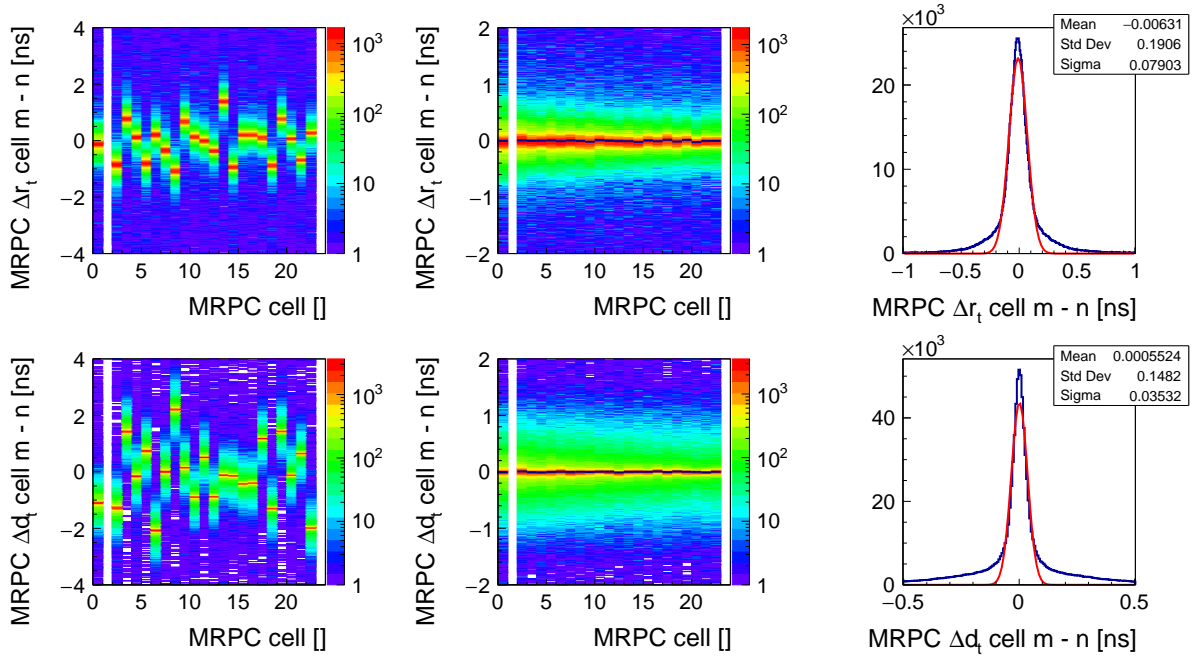


Figure 3.17: Cell time-residual (upper row) and time-difference (lower row) correlations between neighboring cells on counter 9-0-0 using cell 1 as a reference point, before (left column) and after (middle column) offset corrections (cf. Fig. 3.15). Cluster-building criteria applied to time and position differences of neighboring top/bottom digi pairs in a subsequent calibration step (cf. Fig. 3.20) are—with some safety margin—derived from  $\pm 5\text{-}\sigma$  intervals obtained from Gaussian fits to projected time-residual (upper right plot) and time-difference (lower right plot) correlation peaks. Profile lines in the middle column indicate cell averages.

Hence, an adequate weight of single cell-hit information entering calculations of mean position and time for the cluster is the sum of time-over-threshold values measured on both ends of the respective cell  $i$ ,

$$w_i = \text{ToT}_i^- + \text{ToT}_i^+. \quad (3.17)$$

Accordingly, a cluster comprising  $M$  cells on a counter with  $N$  readout cells in total is positioned in space (local  $z_{\text{cluster}}$  set to zero) and in time by

$$x_{\text{cluster}} = \left[ \frac{\sum_{i=1}^M w_i i}{\sum_{i=1}^M w_i} - 1/2 (N_{\text{cells}} - 1) \right] x_{\text{pitch}}, \quad (3.18)$$

$$y_{\text{cluster}} = 1/2 \sum_{i=1}^M w_i (t_i^- - t_i^+) / \sum_{i=1}^M w_i v_{\text{signal}}, \quad \text{and}$$

$$t_{\text{cluster}} = 1/2 \sum_{i=1}^M w_i (t_i^- + t_i^+) / \sum_{i=1}^M w_i - 1/2 s/v_{\text{signal}}.$$

Weighting contributions to the cluster with the respective ToT sum requires ToT spectra measured on all cell ends of the counter to be comparable, both in mean and in width. For two main reasons, this condition is not met prior to a dedicated alignment of these spectra: On the one hand, amplification gains of PADI channels in the setup are not uniform yielding different output amplitudes, i.e. varying ToT values, for the same input signal. On the other hand, as pointed out in Sec. 3.2, TDC input signals are stretched to digitize arrival times of both signal edges in a single delay line. This stretching offset added to the ToT varies slightly between TDC channels. To compute cluster coordinates, it is not necessary to disentangle PADI and TDC contributions to the shape of a ToT spectrum (in order to arrive at physical ToT values). Instead, ToT spectra are harmonized by linear transformations aiming at a common mean and standard deviation in arbitrary units,

$$f(\text{ToT}) = m\text{ToT} + b, \quad (3.19)$$

utilizing general rules for the expectation value and the variance of a linearly transformed random variable  $X$ ,

$$E[mX + b] = m E[X] + b \quad \text{and} \quad \text{Var}(mX + b) = m^2 \text{Var}(X). \quad (3.20)$$

ToT calibration is illustrated in Fig. 3.18. The readout cell with the highest ToT-weight contributing to the cluster—upon harmonization of ToT spectra—is considered the main cluster cell. Measured cluster sizes vary as a function of main cell across the counter surface for reasons of symmetry (cf. Fig. 3.19). Induction occurring on the central cells of the readout plane can affect adjacent cells in two directions while an avalanche triggered above a peripheral cell can geometrically only have some further impact towards the counter center. The mean cluster size measured for a counter depends both on design, in particular on the granularity of its readout cells, and on operating conditions like electric field strength in the gas gaps and discrimination threshold. With some selection bias on counter surfaces due to the mix of hardware-trigger conditions used for data taking, the following mean cluster sizes are obtained for the five counters under consideration: 1.00 on 5-1-0 (diamond), 1.59 on 3-0-0, 1.49 on 9-0-0, 1.09 on 7-0-0, and 1.23 on 4-0-0, with statistical errors on the mean of the order of  $10^{-4}$ .

Upon combining correlated cell hits to clusters by an algorithm which is visualized in Fig. 3.20, an iterative calibration procedure eliminates remaining residual offsets between clusters and the dependence of time measurements on the signal amplitude (sketched *ibid.*). Compensation values for average shifts in cluster position and time are attributed to the main cell of the respective cluster and added to  $c^-$  and  $c^+$  for this cell. While position corrections aiming at homogeneously centered  $y$ -distributions across the counter surface are performed internally, time residuals to be shifted to zero mean are formed between clusters on a counter to calibrate and—alternately—the earliest clusters in an event on either the diamond detector 5-1-0 (providing a stable overall time reference) or one of two calibration selector counters in the setup, a task assigned to counters 3-0-0 and 9-0-0 here. Thus, all counters in the setup are repeatedly calibrated against each other.

When convergence of corrections on cluster residual means is achieved after a few iterations, the time-walk effect, i.e. the dependence of the average time residual between

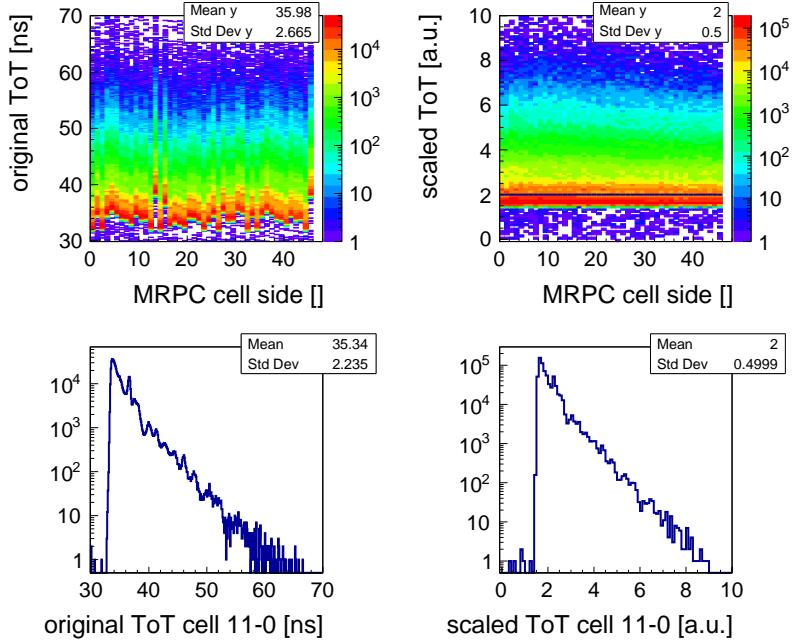


Figure 3.18: Original time-over-threshold spectra from each cell side ( $2 \cdot \text{index} + 0/1$  for bottom/top) of counter 9-0-0 as measured by the connected TDC channels which internally stretch input signals to detect both leading and trailing edge in a single delay line (upper left plot). Final ToT spectra from each cell side after individually scaling every spectrum to a common mean of 2 (cf. profile line) and a common standard deviation of 0.5 (upper right plot). Respective projections of bottom-edge ToT spectra of cell 11 are shown in the lower row.

clusters on the time over threshold of cell digis, can be mitigated. For this purpose, average deviations of cluster time residuals from the integrated residual mean in typically 0.1 or 0.2 (a.u.) wide scaled-ToT bin slices (with a sufficient number of entries) are calculated individually for each cell end contributing to a cluster on the diamond or on an MRPC, compared against a selector cluster which matches in position. In the subsequent iteration, these ToT-dependent deviations are subtracted from digi time stamps, linearly interpolating correction values between ToT bin centers. To increase the efficiency of time-walk corrections, each round is preceded by a compensation of the particle velocity spread which is inherent to the time residual between clusters due to the velocity spectrum of collision secondaries in an event. Corresponding correction values against the time difference between earliest clusters on the diamond and the active selector counter are not applied permanently to reconstructed cluster time stamps but serve the sole purpose of preparing residuals for the following evaluation of time walk. Between consecutive iterations of velocity and time-walk corrections (depicted in Fig. 3.21), cluster residual means in time and position are repeatedly realigned to compensate for possible minor shifts introduced by the former procedure. Finally, a calibrated array of clustered cell hits in each event is available for data analysis (cf. Chap. 5).

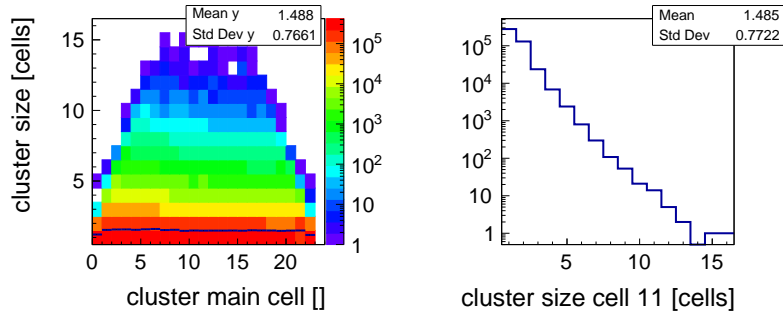


Figure 3.19: Cluster-size distribution of counter 9-0-0 as a function of the main cluster cell by ToT-weighting of contributing cells (left plot). Individual cluster-size distribution with central cell 11 as main cell (right plot).

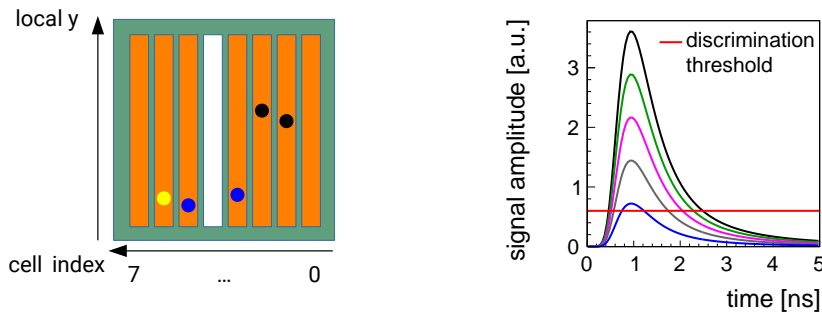


Figure 3.20: Illustration of the cluster-building criteria for time and position correlations between neighboring readout cells (left sketch). Scanning the counter surface for hits on neighboring cells starting from cell 0, the two hits marked in black on cells 1 and 2 meet both criteria while the adjacent hit on cell 3 marked in blue is too far off in position, at least, to belong to the black cluster, hence starting a new (blue) cluster. With the hit on cell 5 found to be correlated with the hit on cell 3, the blue cluster spans cell 4 which is declared dead. The hit marked in yellow on cell 6 could position-wise be integrated into the blue cluster but is not compatible in time with the average of the hits marked in blue, leaving it isolated. Illustration of the time-walk effect, an interplay between signal amplitude and discrimination threshold (right plot). Amplified MRPC signals with identical rise times but different amplitudes, i.e. charge content (demonstrated by a set of Landau functions with identical location and scale parameters but varying coefficients), cross the discrimination threshold at different points in time, larger signals earlier than smaller signals. As the ToT measurement (time difference between threshold crossing points of both signal edges) is directly linked to the signal amplitude, this systematic type of timing jitter can be corrected for.

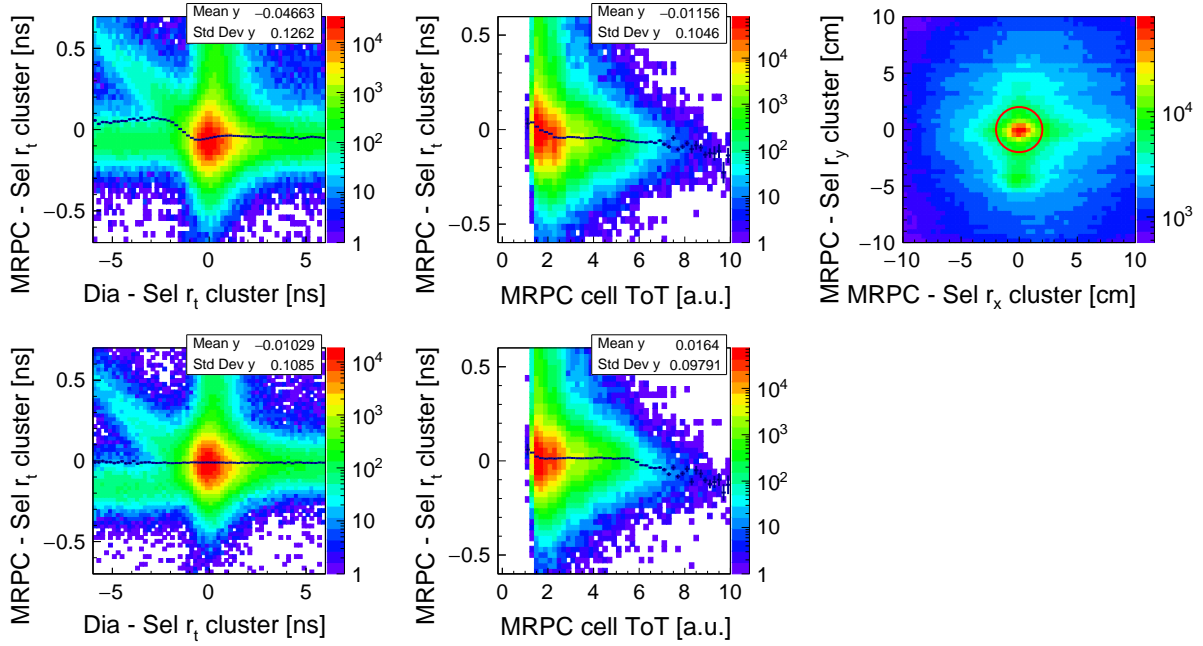


Figure 3.21: Dependence and its correction of the time residual between a cluster on 9-0-0 and the earliest cluster in an event on calibration selector (Sel) counter 3-0-0 on the time residual between the earliest clusters, respectively, on the diamond detector and on counter 3-0-0 (left column, upper and lower plot). The diagonal trend in the negative abscissa range towards the point of origin reflects increasing velocities of particles which propagate from the collision zone to both MRPCs. A significant number of random assignments under the given experimental conditions constitutes a horizontal band which reduces the effectiveness of an alignment based on bin averages. This (transient) velocity/time-of-flight correction always precedes a subsequent time-walk correction to uncover the latter effect on the ordinate residual between MRPCs. As residuals on ordinate and abscissa are directly correlated by Sel cluster times entering into both quantities, the correction is not passed on to analysis. Average time-walk dependence and its correction (if enough statistics are available in a bin slice) on the average ToT of 9-0-0 cells constituting the cluster (middle column, upper and lower plot). Correction histograms are filled if a basic matching condition in space ( $r_{xy} < 2$  cm) is met between clusters on the counter and on the selector (upper right plot).

## CHAPTER 4

### DETECTOR RESPONSE PARAMETRIZATION

Response simulations of detectors in a heavy-ion-collision scenario are an indispensable tool not only in the planning stage of an experiment like CBM but also in parallel to actual physics data taking for a comprehensive understanding of results and for proper error estimation. Experimental insights into detector behavior under specific conditions are incorporated into simulation code which allows for both reproducing and extrapolating from measured data, making response modeling a driving force for new detector developments. In CbmRoot, event-based digitization software generating a cluster of digital detector messages (“digis”) in response to a charged Monte Carlo track traversing the stack of sensitive gas gaps in an MRPC has been developed in [110]. If any gap in the glass stack crossed by the simulated particle is found—by random sampling relating to a single-gap efficiency  $\varepsilon_{\text{gap}}$  (cf. Eq. (2.10))—to trigger a response, the number of affected cells and the cumulative time over threshold (ToT) of the cluster are independently drawn—by inverse transform sampling—from measured cluster-size and cluster-ToT distributions, representing cosmic-irradiation or heavy-ion data. The microscopic calculation of avalanche dynamics is bypassed in order to save computation time. Subsequently, the sampled cluster ToT is distributed among the predetermined cluster cells according to their respective area shares of a ToT density function integrated over the counter surface, optionally a disk or a one-/two-dimensional Gaussian which is centered about the initial Monte Carlo point and constrained in radius or standard deviation, respectively, by the sampled cluster size. Resulting ToT values obtained for opposing cell ends (half the total cell ToT) which surpass an adjustable ToT threshold qualify for digi generation. Digi time stamps are derived from MC point times to which normally distributed jitter is added, based on an intrinsic MRPC resolution and a combined, i.e. signal discrimination and digitization not treated separately, electronics resolution. If two consecutive digis in the same readout channel—created from different MC tracks traversing the counter in the same event—are spaced in time by less than an adjustable TDC dead time, the latter digi is dropped.

For the purpose of this work, the existing digitization strategy for CBM TOF generates an overly idealized detector response function which does—apart from the dead-time feature—not take into account the impact of different response processes interfering in the detection medium and in the readout channel on the quality of time and position measurements in a multi-hit environment. Time-based simulations (cf. Sec. 2.3), in contrast to processing individual events independently from each other, should comprise buffering of response information for some interference interval on a continuous simulation time axis until subsequent events cannot be affected by response processes in the current event anymore. If a counter is irradiated with a continuous particle flux, its response function will exhibit degradation effects over time resulting from local breakdowns of the electric field in the gas gaps which the counter recovers from on a resistivity-dependent relaxation time scale (cf. Fig. 2.11 and Eq. (2.11)). Such behavior

can be observed as a function of event time in an accelerator spill with an event-based, i.e. conventionally hardware-triggered, data acquisition system (cf. Chap. 5) but not be described with event-based simulations in the above sense. Response observables and their respective deterioration with irradiation time are, in addition, mutually dependent which is not considered in the existing digitization code that splits the response calculation into a series of partially independent sampling processes. A geometrical ten-cell cluster created upon identification of an efficient gap, for instance, should not receive a cluster ToT drawn from the same spectrum which is accessible also to a two-cell cluster, and possibly be reduced to an effective six-cell cluster by ToT discrimination. Instead, the distribution of charge induced on individual cells in the readout plane and the discrimination of corresponding signals picked up at cell ends with a given threshold determine both efficiency and cluster size. Thus, together with a demand for rate-effect and interference handling, there was a need for a more holistic digitization approach. In this chapter, a new digitization algorithm for time-based MRPC response simulations is described which derives subsequent response observables from an initial sampling of total induced charge in the readout plane using a parametrized, i.e. not experimentally determined spectrum. Further parametrizations of functions for the distribution of induced charge onto individual readout cells and, in particular, for (amplified) signals containing half of the respective cell charge facilitate introducing amplitude-dependent discrimination jitter and time-residual means (walk) into the code. As a consequence, downscaling the original induced charge spectrum which results in—on average—smaller signal amplitudes directly impacts the response. Model parameters are constrained by a set of measured response observables. The modeling process, features, and limitations of the new approach are outlined in Sec. 4.1. An extension of the static response case towards a dynamic irradiation scenario by a particle memory which causes a scaling of the induced charge spectrum depending on the impact of previous particles hitting the counter on the current one is presented in Sec. 4.2 and used to mimic the physical breakdown and recovery of the electric field in the gaps. Lastly, the time-based handling of signal interference in the readout channels in CbmRoot is sketched in Sec. 4.3, followed by discussions on reducing execution times of the digitization code via multi-threading/parallelization and on its applicability for test-beam simulations.

## 4.1 Modeling assumptions and procedure

### 4.1.1 Signal generation and calibration of simulated data

The parametrization of the MRPC response function developed in this work is not the result of a strict theoretical derivation—as given in [74], for instance—from first principles of molecular ionization in the gas gaps, followed by avalanche formation of accelerated free electrons in the applied electric field and a simultaneous induction of signals by avalanche charges moving towards readout cells. To save computation time, microscopic processes are subsumed under a series of functions aiming at describing complex response dynamics with a concatenation of static impressions which allows for

averaging over the response development in time to a certain extent. These parametrized functions are inspired by the physical laws which govern the reaction of an MRPC to an incoming charged particle. However, a physical quantity like induced charge measured in units of coulomb is considered a dimensionless numerical quantity in the absence of explicit electrodynamic calculations in the digitization code. Position and time scales are constrained by detector geometry and by discrimination points in time of induced signals with dimensionless charge content and amplitude.

When a counter is hit by a Monte Carlo track leaving a trace of intersection points with active gas gaps in its detection volume, considering a single track at a time and ignoring descendant tracks created along the original trajectory, the average of point coordinates in space and time is identified with the induction “spot” in a virtual readout plane positioned at local  $z = 0$  in the center of the glass stack. The total charge induced in the readout plane in this response process is a sample value  $q_{\text{ind}}$  obtained from a random variable  $Q_{\text{ind}}$  which is scaled with a constant working coefficient  $c_{\text{work}}$ . Based on empirical findings regarding the tail behavior of measured cluster-size and ToT distributions (cf. Sec. 3.3) and on the theoretical description of energy-loss fluctuations of a charged particle in thin layers by ionization of atoms [111], the probability density function (PDF) of  $Q_{\text{ind}}$  is assumed to be a Landau distribution, represented by the complex integral

$$p(\lambda) = \frac{1}{\xi} \frac{1}{2\pi i} \int_{c-i\infty}^{c+i\infty} e^{\lambda s + s \log s} ds, \quad (4.1)$$

with  $\lambda = (x - x_0)/\xi$  containing a location parameter  $x_0$  and a scale parameter  $\xi$ ,  $c$  being an arbitrary positive real number needed for integration only. The implementation in ROOT follows the numerical ansatz presented in [112]. Although the Landau distribution can be normalized, qualifying it for deployment as a PDF, a mean value and a variance cannot be defined. For the cluster-size distribution to end at about half the total number of readout cells which is observed in experimental data (cf. Fig. 3.19), depending also on available statistics, a charge sampling limit of  $q_{\text{max}}$  is applied as explained further down. Then, similar to the digitization strategy developed in [110], the sampled induced charge is distributed among immediately adjacent virtual cells in the readout plane with a surface charge density centered about the induction “spot” that is borrowed from the method of image charges. The density of an electrostatically induced charge on a grounded metal plate of infinite dimensions in  $xy$  by a point charge at a distance of  $R$  carrying  $q_{\text{ind}}$  is given by

$$\sigma(x, y) = \frac{q_{\text{ind}} R}{2\pi (x^2 + y^2 + R^2)^{3/2}}, \quad (4.2)$$

yielding a total induced charge of  $q_{\text{ind}}$  if integrated over the entire surface of the metal plate. Utilizing inverse trigonometric functions, the integral of  $\sigma(x, y)$  over the rectangular area of a readout cell can be expressed analytically and corresponds to the induced cell charge half of which is attributed to signals propagating to opposing cell ends. Induced signals are again parametrized with a (normalized) Landau function that

is multiplied with the numerical charge content,

$$f(t) = \frac{q_{\text{cell}}}{2} \times \text{Landau}(t, t_0, \xi_t), \quad (4.3)$$

positioned on the time axis—for numerical reasons—with a fixed offset  $t_0$  (here: 14 ns) and scaled with a free model parameter  $\xi_t$  which is—once determined—used unalteredly for all signals generated, i.e. only the charge coefficient varies between signals (cf. Fig. 3.20 for a visualization). A Landau function was chosen primarily in view of approximately reproducing the shape of measured ToT spectra which could not be achieved with triangular or exponentially rising/falling signal functions.

Skipping the preamplification stage for simplicity which deprives the model—at the moment—of considering gain differences between PADI channels, the maximum amplitudes of parametrized signals induced on every counter cell (with varying charge content depending on the distance of the respective cell to the induction point) are checked against a numerical discrimination threshold at each cell end. This dimensionless quantity is yet another free model parameter. As the same underlying Landau parametrization is applied to all signals, the function maximum linked to the most probable value of the distribution needs to be determined by numerical minimization only once at the beginning of the digitization run. Multiplying this maximum value with the respective charge content allows for a quick assessment whether a cell signal is above threshold or can be disregarded. In the former case, leading- and trailing-edge discrimination points in time, i.e. the two intersections between the signal and a constant threshold, are evaluated numerically utilizing one-dimensional root-finding methods provided by the GNU Scientific Library (GSL). To the time difference between signal edges a free ToT offset parameter is added to give some additional flexibility to the optimization algorithm. Revisiting the aforementioned charge sampling limit of  $q_{\text{max}}$  in the light of charge spreading and signal discrimination, it is determined such that, placing the induction point in the  $xy$ -center of the counter with the aim of obtaining  $n_{\text{max}}/2$  efficient cells in both directions, the corresponding signal induced on cell  $\pm (n_{\text{max}}/2 + 1)$  counted from the center does not exceed threshold anymore. If this limit holds for an induction point in the counter center relatively yielding the largest charge shares by surface integration, then it is universally applicable to any point in the readout plane.

At this level in the simulated response process for an individual MC track, both cluster size and efficiency are known and not subject to change anymore, the former quantity counting the number of readout cells on which a measurable signal was induced, independent of matching criteria for reconstructed cell hits in time and position (cf. Sec. 3.3), and the latter value registering if any cell exhibited a signal above threshold. In the absence of gain variations between preamplifier channels (and dispersion effects which could possibly cause signals to arrive at opposing cell ends with amplitudes differing from each other), signals exceed threshold either on both cell ends or on none. An exemplary simulated cluster-size spectrum for counter 9-0-0 is shown in Fig. 4.1. Compared to the measured spectrum in Fig. 3.19, the difference in relative frequencies between two-cell and three-cell clusters is larger in the simulated case and the spectrum has a more logarithmically convex appearance.

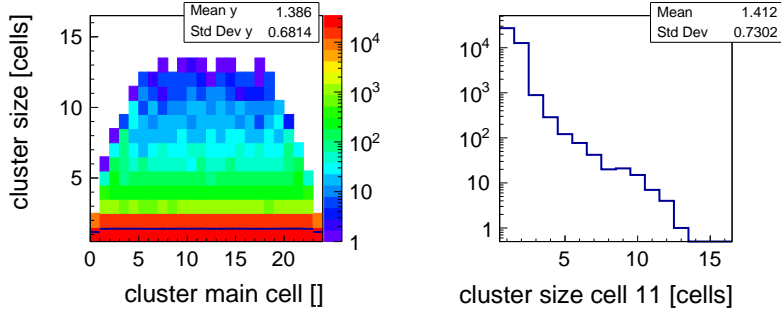


Figure 4.1: Simulated cluster-size distribution of counter 9-0-0 as a function of the main cluster cell by ToT-weighting of contributing cells (left plot). Individual cluster-size distribution with central cell 11 as main cell (right plot).

The remaining step to be taken towards digi production is the addition of timing jitter—and optionally propagation-time offsets—to the numerical positioning of signal edges on the simulation time axis. In the present approach, three sources of uncertainty affecting time measurements performed with MRPCs are taken into account, the first being an intrinsic jitter  $\sigma_{\text{RPC}}$  of the counter itself which is treated as a free model parameter. It is supposed to comprise fluctuations in the signal formation process which are not identifiable with a ToT-dependent time-walk correction, assuming a variation in signal shapes which, for instance, yields identical ToT values for threshold crossing times of leading edges which differ relatively. Also, a normally distributed MRPC jitter with a fixed standard deviation acts as a counterbalance—by preserving a Gaussian core in residual distributions, considering the present implementation—to the discrimination jitter added in the simulated readout channel. The latter uncertainty originates from noise on the signal amplitude and inversely depends on the leading-/trailing-edge slope of the signal when it crosses the threshold at time  $t_{\text{cross}}$ . The applied formula [29]

$$\sigma_{\text{PADI}} = \frac{\sigma_n}{\left. \frac{df}{dt} \right|_{t=t_{\text{cross}}}} \quad (4.4)$$

contains the Gaussian standard deviation  $\sigma_n$  of a dimensionless amplitude noise as final model parameter, amounting to eight free parameters in total. Slopes for signals above threshold are determined by numerical differentiation of Eq. (4.3) at evaluated threshold crossing times and are not confined in range, producing a significant discrimination jitter if signals barely pass threshold. While the amplitude noise itself is normally distributed, the resulting jitter distribution created from the entire spectrum of signal slopes deviates from a Gaussian shape as individual Gaussian contributions of varying widths are mixed. Finally, a fixed TDC resolution (here:  $\sigma_{\text{TDC}} = 0.02 \text{ ns}$ ) is added to simulated time stamps.

Differences in signal propagation time between readout channels of the same counter are sampled from a continuous uniform distribution on an adjustable interval with boundary values of  $\pm 3.5 \text{ ns}$  in the present case, guided by experimental findings, and used to

shift in time leading-edge measurements at the lower cell ends. Owing to an alternative FPGA-TDC design which splits incoming signals to digitize leading- and trailing-edge information in separate delay lines, routing variations between edge channels on the chip can be accounted for. Normally distributed signal propagation offsets ( $\sigma = 0.5$  ns) are generated for every pair of single-edge channels with this kind of TDC implementation in mind and added to the respective ToT measurements. The resulting displacement pattern observed in simulated ToT spectra (cf. Fig. 4.2) then resembles the experimental situation (cf. Fig. 3.18) although gain variations between PADI channels are the cause of shifts between spectra in the latter case which are not considered in the digitization code.

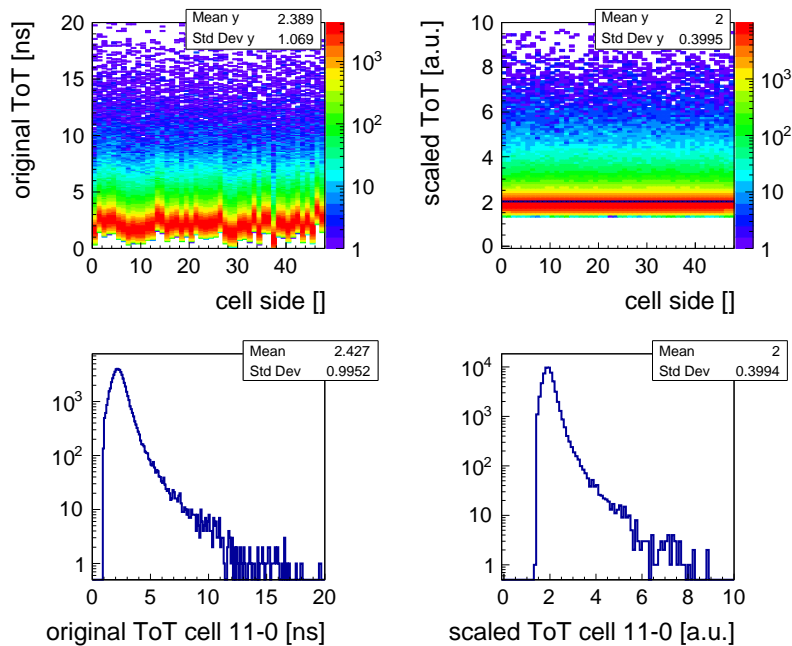


Figure 4.2: Original simulated time-over-threshold spectra from each cell side ( $2 \cdot \text{index} + 0/1$  for bottom/top) of counter 9-0-0 as modeled according to Tab. 4.1 (upper left plot). Final ToT spectra from each cell side after individually scaling every spectrum to a common mean of 2 (cf. profile line) and a common standard deviation of 0.4 (upper right plot). Respective projections of bottom-edge ToT spectra of cell 11 are shown in the lower row.

The time-walk feature which is inherent to the presented response model due to an explicit usage (and discrimination) of induced signals and the propagation-time offsets between/inside readout channels impacting both time and ToT measurements necessitate a calibration of simulated cell hits analogous to Sec. 3.3 prior to computing cluster coordinates in time and space (cf. Eq. (3.18)) and inspecting residuals. Reference values  $y_0$  and  $t_0$  to align cell hits with are—in contrast to the experimental case—known quantities corresponding to point coordinates of the Monte Carlo track which triggered the simulated response process. For this reason, a counter can be calibrated individually as

all required information is available. The alignment of ToT spectra is shown in Fig. 4.2 and the centering of position distributions on cells is visualized in Fig. 4.3. In the latter case, the geometric cell length of 26.7 cm for counter 9-0-0 cannot be reproduced exactly with the fitted scale parameter due to edge effects caused by a trend of decreasing surface integrals/signal amplitudes towards longitudinal cell edges, accompanied by a larger discrimination jitter on average. Iterative time-walk corrections are applied on the cell level as well (cf. Fig. 4.4) and need to compensate for more pronounced dependencies than observed in experimental data (cf. Fig. 3.21). However, the magnitude of the simulated time-walk effect is not constrained in the modeling process. It is interesting to note that the applied correction method, aligning at zero—within the same calibration step—mean values of the cell time residual  $r_t$  in ToT bin slices for signals from both cell ends, deteriorates the reconstruction of local  $y$  by pulling apart the position residual  $r_y$  against Monte Carlo. This behavior has been reported by other members of the CBM-TOF working group analyzing experimental data from FAIR Phase-0 activities and requires further investigation.

#### 4.1.2 Cluster residuals and resolutions

Upon calibration of cell hits response correlations on adjacent cells, i.e. clusters, can be utilized. Actually, the measurement quality of clusters is identified with the resolving power of the entire counter. Some theoretical remarks concerning the impact of cluster building on residuals in position and time are given below. Ignoring signal propagation delays, the simulated time stamps of induced signals digitized on opposing ends of a readout cell,

$$\begin{aligned} t^- &= t_0 + (s/2 + y_0) / v_{\text{signal}} + \Delta t_{\text{RPC}} + \Delta t_{\text{el}}^- \quad \text{and} \\ t^+ &= t_0 + (s/2 - y_0) / v_{\text{signal}} + \Delta t_{\text{RPC}} + \Delta t_{\text{el}}^+, \end{aligned} \quad (4.5)$$

with a cell length of  $s$  and a signal propagation velocity of  $v_{\text{signal}}$ , consist of the Monte Carlo point time  $t_0$ , the signal propagation time along the cell from the local MC point position  $y_0$  to the cell end, an uncertainty  $\Delta t_{\text{RPC}}$  attributed to the counter itself which is common to all cell hits in a possible cluster, and a summarized uncertainty  $\Delta t_{\text{el}}$  of individual signal discrimination (disregarding the amplitude dependence for simplicity) and digitization in the respective electronics channel. The  $y$ -residual for a single cell hit only depends on electronics uncertainty,

$$\begin{aligned} r_y^{(1)} &= 1/2(t^- - t^+)v_{\text{signal}} - y_0 \\ &= 1/2(\Delta t_{\text{el}}^- - \Delta t_{\text{el}}^+)v_{\text{signal}}, \end{aligned} \quad (4.6)$$

which is carried over to the residual variance,

$$\text{Var} \left( r_y^{(1)} \right) = \frac{1}{2} \sigma_{\text{el}}^2 v_{\text{signal}}^2, \quad (4.7)$$

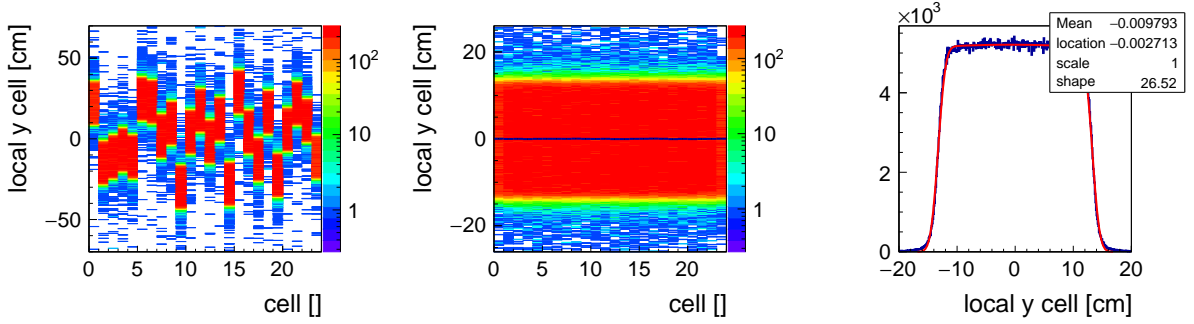


Figure 4.3: Simulated position offsets between neighboring cells on counter 9-0-0 before (left plot) and after (middle plot) applying corrections. As the irradiation of the counter surface is homogeneous in the modeling process, the parabolic factor in Eq. (3.15) is dropped for fitting the ordinate projection of the position spectra (right plot).

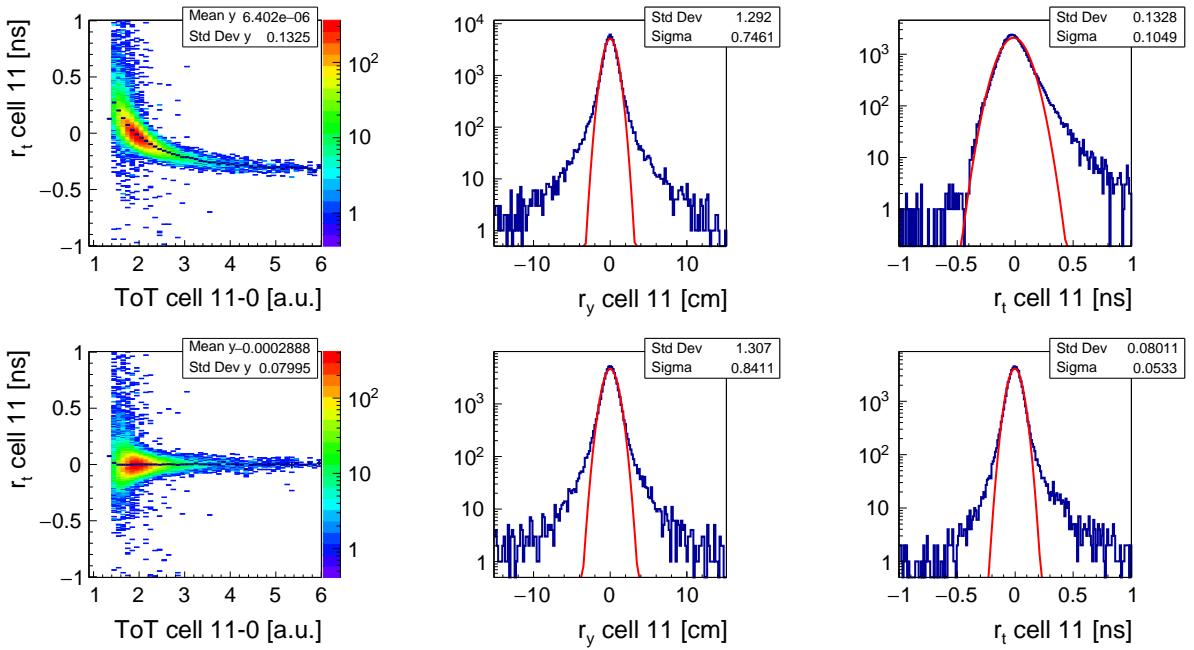


Figure 4.4: Impact of time-walk corrections on position and time residuals of hits on cell 11 of counter 9-0-0 against simulated Monte Carlo hits on this cell. The distributions in the upper row show residual widths before iteratively applying time-walk corrections the effect of which is reflected by the distributions in the lower row. While the Monte Carlo time residual—as a function of (left column) or integrated over (right column) cell-side ToT—significantly narrows, the Gaussian core of the position residual (middle column) actually widens a bit due to the time-walk corrections.

denoting equal  $\text{Var}(\Delta t_{\text{el}})$  for both readout channels with  $\sigma_{\text{el}}^2$  to indicate the link to the standard deviation. In the time residual, the intrinsic uncertainty of the MRPC does not cancel out when adding signal time stamps,

$$\begin{aligned} r_t^{(1)} &= 1/2 (t^- + t^+) - 1/2 s/v_{\text{signal}} - t_0 \\ &= \Delta t_{\text{RPC}} + 1/2 (\Delta t_{\text{el}}^- + \Delta t_{\text{el}}^+), \end{aligned} \quad (4.8)$$

and constitutes a second contribution to the residual width,

$$\text{Var}(r_t^{(1)}) = \sigma_{\text{RPC}}^2 + \frac{1}{2} \sigma_{\text{el}}^2, \quad (4.9)$$

expressing  $\text{Var}(\Delta t_{\text{RPC}})$  in terms of  $\sigma_{\text{RPC}}$ . If multiple cell hits are grouped into an  $n$ -cell response cluster, the passage of a charged particle through the detector was registered by  $n$  independent measuring devices in a way, the respective results of which are weighted with time over threshold to obtain cluster coordinates. Here, for the mathematical argument, equal weighting of cell measurements with  $w_i = 1/n$  is assumed. The position residual in local  $y$  of a cluster with  $n$  cells can be reduced to

$$r_y^{(n)} = \frac{1}{2} \frac{1}{n} \sum_{i=1}^n (\Delta t_{\text{el}}^{(i)-} - \Delta t_{\text{el}}^{(i)+}) v_{\text{signal}} \quad (4.10)$$

and has a vanishing variance in the limit  $n \rightarrow \infty$ ,

$$\text{Var}(r_y^{(n)}) = \frac{1}{2} \frac{1}{n} \sigma_{\text{el}}^2 v_{\text{signal}}^2. \quad (4.11)$$

In time, the intrinsic MRPC uncertainty is preserved,

$$r_t^{(n)} = \Delta t_{\text{RPC}} + \frac{1}{2} \frac{1}{n} \sum_{i=1}^n (\Delta t_{\text{el}}^{(i)-} + \Delta t_{\text{el}}^{(i)+}), \quad (4.12)$$

and the variance asymptotically approaches  $\sigma_{\text{RPC}}$  for increasing cluster sizes,

$$\text{Var}(r_t^{(n)}) = \sigma_{\text{RPC}}^2 + \frac{1}{2} \frac{1}{n} \sigma_{\text{el}}^2. \quad (4.13)$$

Aiming at a reduction of the statistical error of measurement, large clusters are favorable in comparison to small clusters. However, designing an MRPC with a highly granular readout electrode consisting of many small cells increases the demand for costly electronics channels. Clusters comprising a multitude of cells are also predisposed to response interference of different tracks. The fewer clean signals are required for a measurement, the better the device performs on average despite of statistical considerations.

Regarding residuals in local  $x$ , the single-cell case is equivalent to a continuous uniform distribution across the readout cell of width  $s_x$  with a variance of

$$\text{Var}(r_x^{(1)}) = \frac{s_x^2}{12}. \quad (4.14)$$

For multi-cell clusters, the  $x$ -residual is not straightforward to assess mathematically due to the dependence of cluster size on the position of the induction point relative to the cell center in transverse direction and on induced charge. Clusters with an even number of cells—for geometrical reasons—more likely originate from the boundary region between two adjacent cells while clusters with an odd number of cells tend to arise from the cell center. The weighting of constituent cell centers with ToT to obtain the cluster  $x$ -coordinate in a center-of-gravity fashion also plays an important role which additionally complicates the picture.

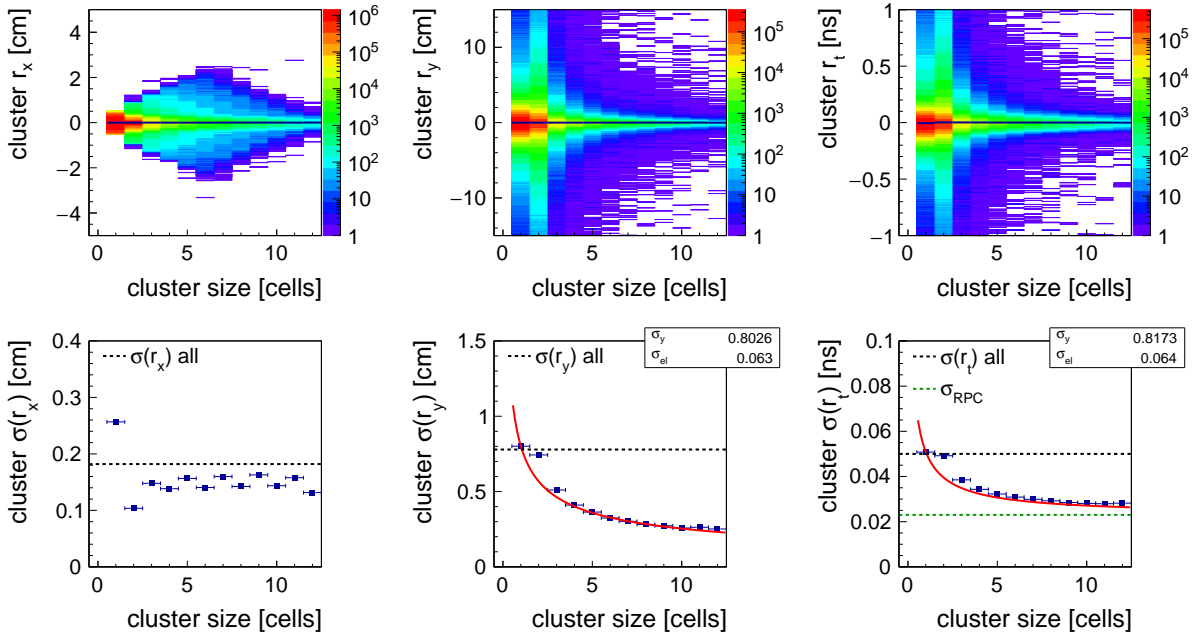


Figure 4.5: Cluster residuals of counter 9-0-0 in  $x$  (left column),  $y$  (middle column), and  $t$  (right column) as a function of cluster size (upper row). Gaussian fit sigmas obtained from cluster-residual bin slices as a function of cluster size (lower row). Profile lines in the upper row indicate histogram averages, dashed black lines in the lower row mark Gaussian fit sigmas from integrated residual distributions in Fig. 4.6, and the dashed green line in the lower right plot visualizes the modeled RPC resolution (cf. Tab. 4.1). Single-cell position ( $\sigma_y$ ) and electronics ( $\sigma_{el}$ ) resolutions given in the statistics boxes, linked by Eq. (4.7), result from a fit to the cluster-size dependence of  $\sigma(r_y)$  with the square root of Eq. (4.11) and from an analogous fit to the cluster-size dependence of  $\sigma(r_t)$  with the square root of Eq. (4.13), respectively, excluding unexpectedly large values obtained for cluster size 2.

A differential view on simulated cluster residuals in  $x$ ,  $y$ , and  $t$  as functions of cluster size is provided in Fig. 4.5. Gaussian fit widths in  $x$  show an alternating pattern with more narrow residuals for clusters which are composed of an even number of cells. A possible geometrical explanation for this behavior are position ranges across the cell from which an even-numbered cluster can emerge being smaller on average than position ranges

for generating odd-numbered clusters, reducing the uncertainty interval between Monte Carlo point and cluster position and, hence, constricting the residual. For a single-cell cluster, the fit value is below the theoretical expectation of 0.29 cm calculated with Eq. (4.14) for a 1 cm wide cell because of an increasing probability for two-cell cluster production towards the cell periphery, rounding off the edges of the originally uniform distribution, and due to fitting the latter with a Gaussian function. Residual widths in  $y$  and in  $t$  generally follow the functional relations to cluster size derived above, except for two-cell clusters owing to an extraordinarily small mean amplitude and slope (revisited below) of the four measured signals which resemble each other to a higher degree than is the case for any other cluster size, excluding single-cell clusters. Thus, four similar measurements with a relatively high discrimination uncertainty each accumulate.

The single-channel electronics resolution  $\sigma_{\text{el}}$  which is extracted from fits to residual widths in local  $y$  and in time indirectly, i.e. via the amplitude noise  $\sigma_n$  (cf. Eq. (4.4)), is a free model parameter like the intrinsic RPC resolution  $\sigma_{\text{RPC}}$ . During parameter adjustment, the relative weighting between both quantities arises from constraints put on the integrated cluster time resolution, at a nominal working coefficient of 1.5 on the one hand and in a degraded situation associated with an efficiency drop to 80% on the other hand. As the contribution of  $\sigma_{\text{RPC}}$  to residual widths remains constant, in the current implementation at least, the deterioration of the timing response with a decreasing working coefficient which translates into smaller signals on average is solely driven by a corresponding increase in discrimination jitter. Thus, an unrealistically poor electronics resolution of about 0.063 ns tied to a single-cell  $y$ -position resolution of 0.8 cm is obtained (here for counter 9-0-0) to comply with modeling constraints, while the intrinsic MRPC resolution amounts to 0.024 ns. A mitigation of this effect could be accomplished by coupling  $\sigma_{\text{RPC}}$  to  $c_{\text{work}}$ , taking load off  $\sigma_n$  concerning response deterioration. Increasing  $\sigma_{\text{RPC}}$  while keeping the cluster time resolution fixed then leads to an improved resolution in  $y$ , according to

$$\text{Var}(r_y) = \left( \text{Var}(r_t) - \sigma_{\text{RPC}}^2 \right) v_{\text{signal}}^2. \quad (4.15)$$

To estimate the average response of the counter to incoming particles, cluster residuals integrated over cluster size are considered and fitted with Gaussian functions to obtain residual widths which are identified with the resolution in the respective response dimension (cf. Fig. 4.6). By merging results for individual cluster sizes in a single histogram, however, mixture distributions are generated which are technically not Gaussian in shape although the underlying residuals for a specified cluster size are normally distributed, neglecting the amplitude dependence of the discrimination jitter. In the simplified picture described above, the theoretical mixture variances of the integrated  $y$ -residual,

$$\begin{aligned} \text{Var}(r_y) &= \sum_{n=1}^{\infty} p_n \text{Var}(r_y^{(n)}) \\ &= \frac{1}{2} \sigma_{\text{el}}^2 v_{\text{signal}}^2 \sum_{n=1}^{\infty} \frac{p_n}{n}, \end{aligned} \quad (4.16)$$

and of the integrated  $t$ -residual,

$$\begin{aligned}\text{Var}(r_t) &= \sum_{n=1}^{\infty} p_n \text{Var}(r_t^{(n)}) \\ &= \sigma_{\text{RPC}}^2 + \frac{1}{2} \sigma_{\text{el}}^2 \sum_{n=1}^{\infty} \frac{p_n}{n},\end{aligned}\quad (4.17)$$

both depend on the inverse weighted harmonic mean of the cluster-size distribution, expressed by the infinite sum over inverse cluster sizes  $n$  weighted with relative frequencies  $p_n$ .

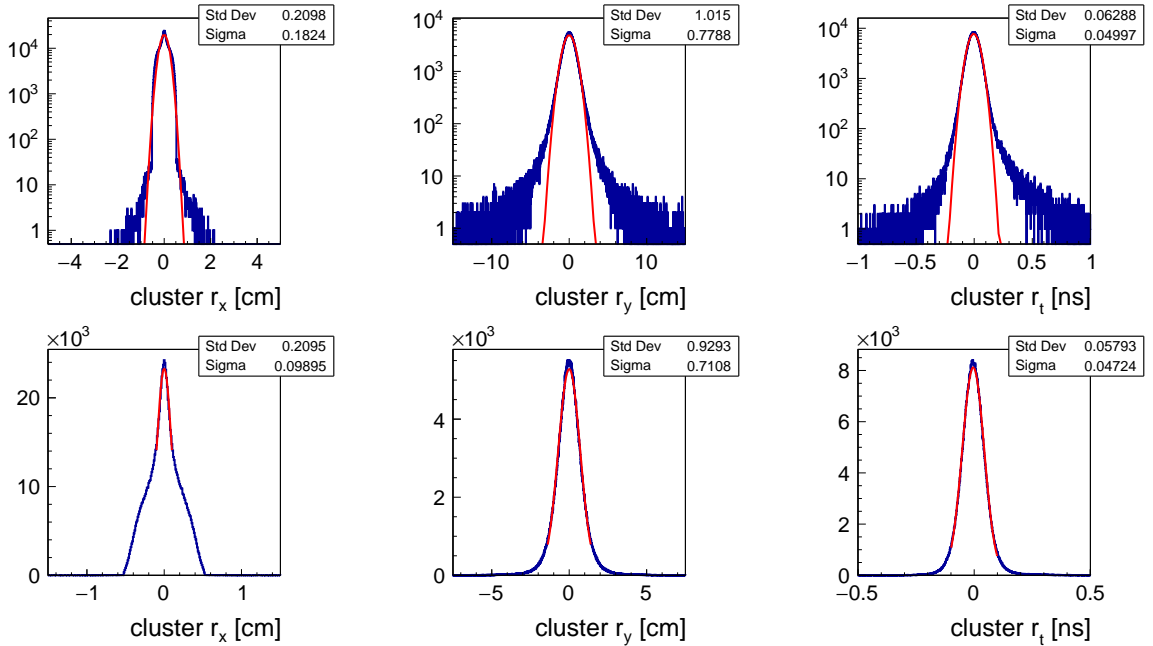


Figure 4.6: Time-walk corrected residuals in  $x$  (left column),  $y$  (middle column), and  $t$  (right column) between ideal cell clusters and the corresponding Monte Carlo points on the surface of counter 9-0-0, in logarithmic (upper row) and in linear scale (lower row). Differences between widths of Gaussian fits to the entire distribution (upper row) and widths of Gaussian fits to the distribution peaks only (lower row) cannot only be attributed to non-Gaussian tails ascribable to discrimination jitter which affects  $r_y$  and  $r_t$  but also to the inherent mixture character of distributions containing residuals from the entire spectrum of cluster sizes. The  $x$ -residual which is a simple uniform distribution for a cluster of size 1 (cf. Eq. (4.14)) and which receives its final shape from ToT-weighted centers of cells contributing to a multi-cell cluster is anyway not intrinsically Gaussian.

The corresponding standard deviations differ numerically from Gaussian sigmas obtained by fitting residuals. However, the latter values are the best estimators available for the “Gaussicity” of the response residual in each dimension and serve as weights to a  $\chi^2$ -formalism which is applied to matching residuals between counters in the final analysis

(cf. Chap. 5). In view of varying Gaussian widths of integrated cluster residuals from top to bottom, the sigma values extracted from fits to the entire distribution represent a mean Gaussian width. Comparing simulated cluster coordinates to Monte Carlo point information with a  $\chi^2$ -distribution constructed from weighted residuals in  $x$ ,  $y$ , and  $t$ , deviations visualized in Fig. 4.7 are primarily due to the shape of the  $x$ -residual and response tails in the latter dimensions. The former effect can be attenuated if position residuals are formed between two counters with perpendicular cell orientations, folding local  $x$  with local  $y$  and vice versa.

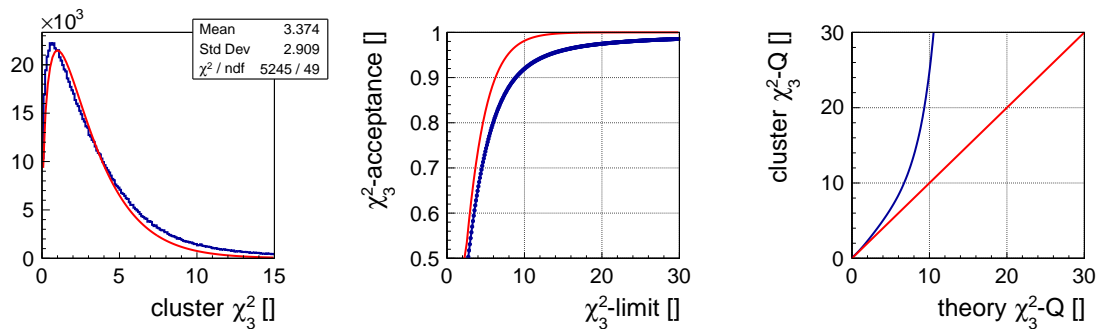


Figure 4.7: Chi-square distribution obtained from cluster residuals of counter 9-0-0 shown in Fig. 4.6, upper row, weighted in  $x$  with the histogram standard deviation and with Gaussian fit sigmas in  $y$  and in  $t$  (left plot). The distribution is fitted up to a  $\chi^2$ -limit of 5 with a normalization constant being the only free parameter. Integral share of both the simulated (in blue) and the theoretical (in red) chi-square distribution as a function of the upper  $\chi^2$ -integration limit (middle plot). Quantile–quantile (Q–Q) plot (blue curve) comparing quantiles of the simulated chi-square distribution on the ordinate with theoretical chi-square quantiles on the abscissa, against an ideal  $y = x$  line in red (right plot). Example: A theoretical  $Q_{0.9} = 6.25$  coincides with a simulated  $Q_{0.9} = 8.92$ .

### 4.1.3 Response dependence on a static working coefficient

The simulated response function of a counter is designed to change with the working coefficient  $c_{\text{work}}$  scaling the random variable  $Q_{\text{ind}}$  which represents the total induced charge. Analogous to a high-voltage scan performed for a real counter to determine optimal operating conditions, simulated response observables are dependent on the applied working coefficient, yielding—generally speaking—better results for bigger  $c_{\text{work}}$  which can even extend into a virtual region of “overvoltage”. In a dynamic scenario,  $c_{\text{work}}$  defines the starting point for the behavior of the system as a function of time. The higher its value, the more buffer is provided to compensate for irradiation-induced performance deterioration. In the modeling process, however, constraints which control the adjustment of parameters need to be evaluated at a fixed working coefficient which is set to 1.5. In Fig. 4.8, the most important response observables are shown as functions

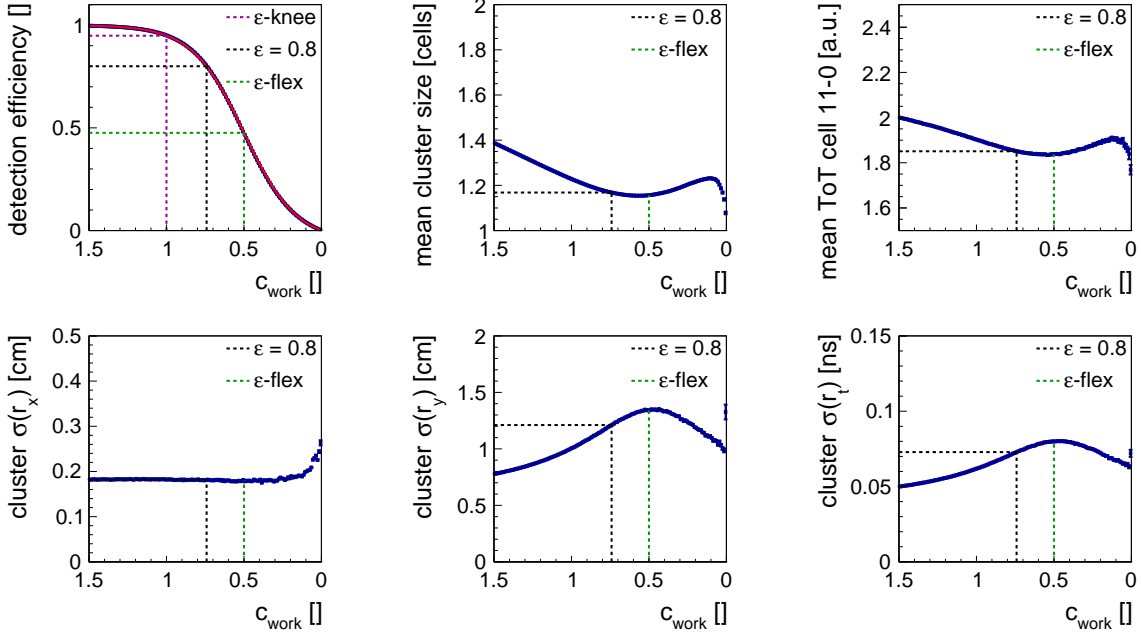


Figure 4.8: Evolution of the Monte Carlo detection efficiency (upper left plot), the mean cluster size (upper middle plot), an exemplary mean channel ToT (upper right plot), and the residual sigmas in  $x$  (lower left plot),  $y$  (lower middle plot), and  $t$  (lower right plot) on counter 9-0-0 as a function of working coefficient  $c_{\text{work}}$  which the accessible induced charge spectrum is (down-)scaled with. The efficiency evolution is fitted with the logistic sigmoid function from Eq. (4.18). As points of orientation, the efficiency-knee coefficient ( $c_{\text{work}} = 1.0$ ), the degradation coefficient ( $\varepsilon = 0.8$ ), and the sigmoidal inflection coefficient ( $c_{\text{work}} \approx 0.5$ ) are indicated by colored dashed lines. The trend reversal in observables towards smaller values of  $c_{\text{work}}$  at about the inflection coefficient is discussed in the text.

of  $c_{\text{work}}$ . Concerning detection efficiency, the idea to fit the curve with a logistic sigmoid function,

$$f(x) = a + \frac{d}{1 + e^{-\lambda(x-x_0)}}, \quad (4.18)$$

and to use the label “efficiency knee” for the point at which the efficiency reaches 95 % are taken from [113]. The S-curve formula comprises an offset  $a$ , the distance  $d$  between the two asymptotes, the mid- or inflection point  $x_0$ , and the efficiency slope at  $x_0$  multiplied by  $4/d$ , which is  $\lambda$ . Two constraints to be met by the free model parameters are derived from this function, the first one positioning the “knee” at  $c_{\text{work}} = 1.0$  and the latter one requiring  $d$  to equal 1. In addition, a reference value for the degradation of timing performance is associated with an efficiency drop to 80 % in view of a dynamic scenario discussed in Sec. 4.2. Except for efficiency and  $x$ -residual width, all curves exhibit a trend reversal with decreasing  $c_{\text{work}}$  which roughly occurs at the flex coefficient of the efficiency sigmoid. This effect is caused by the tail of the Landau distribution which the

total induced charge is sampled from. If analytic Landau approximations like Gumbel or Moyal distributions are used instead, this behavior is not observed but the shape of experimental cluster-size and ToT distributions cannot be reproduced with these substitutes due to their less pronounced tails. For this reason, the Landau solution is maintained which allows for studying the response deterioration in the efficiency range above  $\sim 50\%$  before the counterintuitive response improvement sets in. Actually, the behavior of mean cluster size in a high-voltage scan conducted with MRPCs deployed at the CMS experiment [114] suggests to experimentally investigate the region beyond efficiency inflection with sufficient statistics. When the working coefficient approaches zero, a second trend reversal reflects the rapidly decreasing probability to generate multi-cell clusters with the limited induced charge spectrum still available.

#### 4.1.4 Parameter adjustment and model limitations

To adjust the response parameters of the diamond detector and four MRPCs in the setup at CERN/SPS, five parameter sets need to be generated for five different readout-cell geometries. The reference values of the selected boundary conditions which constrain the modeling process (cf. Tab. 4.1) are deduced from experimental observations and—in this work—chosen to be identical for all counters. If special response characteristics of individual detectors need to be considered, individual values can be applied which necessitates a readjustment of model parameters. The diamond is treated as a small MRPC for simplicity. To complement information on the listed constraints, the ratio between root mean square and Gaussian sigma obtained for the  $y$ -residual is supposed to regulate the impact of discrimination jitter without directly posing a condition on the residual width in  $y$  which would conflict with the target value for  $\sigma(r_t)$  as resolutions in  $y$  and  $t$  are mutually dependent. The degraded cluster time resolution of 0.070 ns is an upper stability limit for a parametrization which bases timing deterioration on the increasing discrimination jitter for diminishing signal amplitudes only; experimental results indicate larger deteriorations at 80% detection efficiency (cf. Sec. 4.2). Parameters are optimized numerically utilizing a GSL implementation of the downhill simplex algorithm [115] by minimizing a chi-square constructed from weighted differences, depending on the desired precision, between reference values and response observables obtained with the current parameter set. As the digitization code intrinsically generates non-ideal signal time stamps and shifted ToT spectra which require offset, scaling, and time-walk corrections to be applied, the chi-square calculation in every single iteration of the simplex algorithm—upon modifying a model parameter—is preceded by five iterations of counter calibration against Monte Carlo information at the nominal working coefficient of 1.5. Moreover, concerning constraints imposed on efficiency and time-residual deterioration, the response is subsequently evaluated for a total of 15 working coefficients between 1.5 and 0, for every minimization step. The calibration of reconstructed cell hits obtained for  $c_{\text{work}} = 1.5$  can be reused throughout the entire range of working coefficients. A single response evaluation is based on one million Monte Carlo points which are uniformly distributed in the virtual readout plane of the counter. Thus, the time it takes for the

Table 4.1: Reference values and their reproduction (at  $c_{\text{work}} = 1.5$  if not stated otherwise) with the five different counter geometries in the setup (upper part) constraining the adjustment of free parameters for response modeling (middle part). The values of some observables resulting from the parametrization are given in the lower part of the table. For details see text.

	ref.	5-1-0	3-0-0	9-0-0	7-0-0	4-0-0
mean cluster size central cell [cells]	1.4	1.438	1.358	1.412	1.332	1.361
cluster-size RMS central cell [cells]	0.7	0.698	0.688	0.730	0.591	0.619
mean ToT central cell [ns]	2.5	2.553	2.586	2.427	2.685	2.550
ToT RMS central cell [ns]	1.0	1.035	0.776	0.999	0.776	0.996
cluster $\sigma(r_t)$ [ns]	0.050	0.050	0.050	0.050	0.050	0.050
cluster RMS( $r_y$ )/ $\sigma(r_y)$ ratio	0.75	0.763	0.785	0.767	0.794	0.765
sigmoidal knee efficiency ( $c_{\text{work}} = 1.0$ )	0.95	0.935	0.943	0.949	0.949	0.934
sigmoidal efficiency drop	1.0	1.028	0.993	1.047	1.004	1.053
degraded ( $\varepsilon = 0.8$ ) cluster $\sigma(r_t)$ [ns]	0.070	0.073	0.081	0.073	0.079	0.071
induced-charge Landau location [a.u.]	n/a	5.916	4.042	4.000	4.163	4.609
induced-charge Landau scale [a.u.]	n/a	1.065	0.421	0.761	0.518	0.811
surface-charge-density distance [cm]	n/a	0.027	0.226	0.184	0.387	0.170
induced-signal Landau scale [ns]	n/a	0.324	0.250	0.263	0.259	0.272
discrimination threshold [a.u.]	n/a	0.757	0.689	0.620	0.682	0.670
induced-signal ToT offset [ns]	n/a	0.877	1.412	0.966	1.402	1.079
amplitude jitter $\sigma_n$ [a.u.]	n/a	0.193	0.204	0.197	0.206	0.193
avalanche jitter $\sigma_{\text{RPC}}$ [ns]	n/a	0.020	0.024	0.023	0.023	0.025
cluster $\sigma(r_x)$ [cm]	n/a	0.019	0.169	0.182	0.348	0.166
cluster $\sigma(r_y)$ [cm]	n/a	0.805	0.765	0.779	0.772	0.751

minimization algorithm to converge to a stable solution in parameter space can amount to up to 24 hours.

Apart from the imbalance between intrinsic MRPC and discrimination types of jitter owing to the constancy of the former with decreasing working coefficients (cf. Sec. 4.1.2), the presented digitization approach is primarily subject to bias originating from a heavy-tailed Landau distribution used for induced-charge sampling (cf. Sec. 4.1.3) and from a strictly geometrical spreading of induced charge to individual readout cells. A visualization and description of corresponding effects on the counter response function is provided in Fig. 4.9.

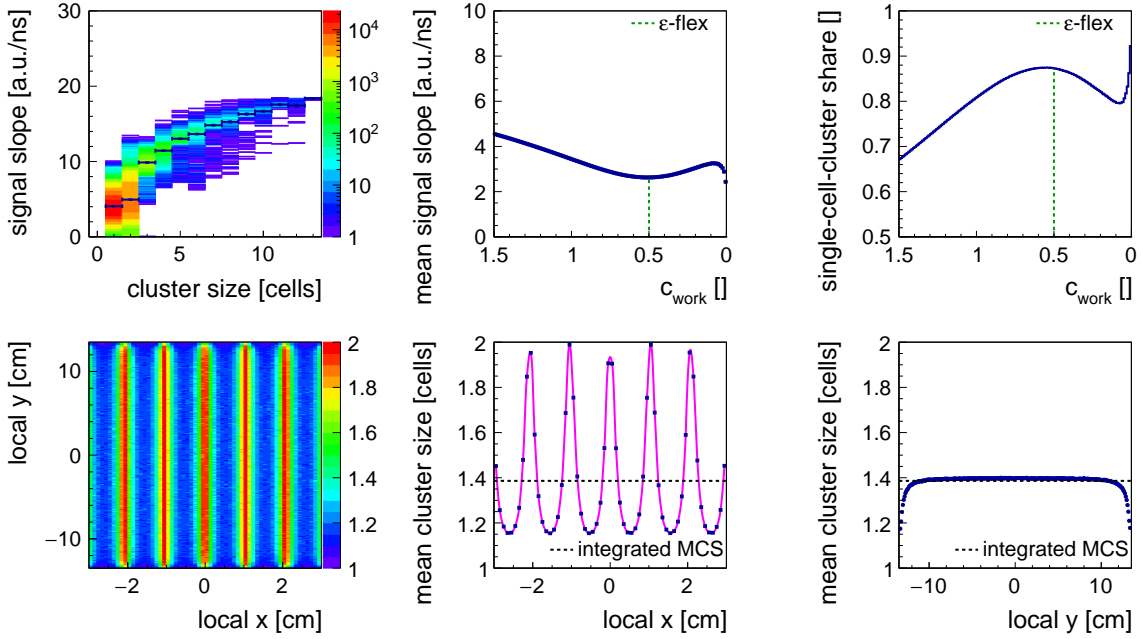


Figure 4.9: Exemplary representation of bias related to the interplay between cell geometry and induced-charge sampling on the modeled response function of counter 9-0-0. The exceptional role of clusters of size 2 (cf. Fig. 4.5) can be attributed to the corresponding mean signal slope of the—by ToT-weighting—main cluster cell not following the overall trend (profile lines in the upper left plot). Subsequent trend reversals of the mean signal slope integrated over cluster size (upper middle plot) and the single-cell share of all cluster sizes (upper right plot) around the efficiency flex as a function of working coefficient  $c_{\text{work}}$  are the basis of similar effects seen in higher-order observables (cf. Fig. 4.8). Illustrated with the example of—but not limited to—mean cluster size, the simulated response is not homogeneous across the active detection area segmented into cells (lower left plot). An abscissa projection (lower middle plot) identifies the integrated mean cluster size (MCS) with an average of position-dependent oscillations, owing to integrating the induced charge density over rectangular cells which also leads to edge effects on detector response towards cell ends as shown in an ordinate projection (lower right plot).

## 4.2 Memorization of local E-field breakdown and recovery

If an MRPC is irradiated with a flux of particles for some time, its response function will deteriorate as the electric field in the gaps locally breaks down due to avalanche charges accumulating on the glass plates (cf. Sec. 2.4.2), the extent varying with avalanche size. Many local breakdowns eventually degrade the overall performance of the detector. However, on a relaxation time scale depending—among others—on the resistivity of the glass plates (cf. Eq. (2.11)), the E-field recovers which eventually restores the original response function if irradiation ceases. Assuming a sustained particle flux instead, breakdown and recovery cancel out over time and the response function enters into equilibrium at a level determined by the ratio of incoming flux to relaxation time. To handle these effects in simulations, the impact of Monte Carlo tracks traversing the detection volume prior to the current track on the response capability of the counter needs to be memorized. With several million simulated particles required to be transported through the setup for realistic beam intensities and spill lengths, computational effort for evaluating the state of the E-field memory upon arrival of every single particle at the detector is high. The time complexity  $T(n)$  of an algorithm summing up contributions from  $n - 1$  previous tracks to the response function which is available to track number  $n$  is quadratic, i.e.  $O(n^2)$ , as—for large  $n$ —the number of arithmetic operations to perform grows like  $n^2$ . Every track which is processed increments the amount of particles in the memory by 1, resulting in

$$\sum_{i=1}^{n-1} i = (n^2 - n) / 2 \quad (4.19)$$

mathematical terms to calculate for  $n$  successively simulated tracks. Iterating over a large particle memory comprising the entire counter surface can be avoided—and execution times be reduced—by segmenting the active area into many small memory cells ( $1 \text{ cm}^2$  in size, for example) which need to store only a fraction of information compared to a single comprehensive counter memory. This would, however, introduce edge effects between adjacent memory cells. The present work focuses on implementing an unsegmented particle memory and on exploring its limits of applicability.

The starting point for parametrizing the impact in time and space of preceding tracks on simulating the counter response to the current one is the total induced charge spectrum, scaled with a constant working coefficient  $c_{\text{work}}$  so far (cf. Sec. 4.1.3). Now, a memory term is multiplied to  $c_{\text{work}}$ ,

$$Q_{\text{ind},n} = c_{\text{work}} \left[ 1 - \sum_{i=0}^{n-1} \left\{ \frac{q_{\text{ind},i}}{q_{\text{max},0}} \times \frac{1}{1 + \left( \frac{\mathbf{x}_n - \mathbf{x}_i}{r_{\text{eff}}} \right)^2} \times \exp \left( -\frac{t_n - t_i}{\tau_{\text{MRPC}}} \right) \right\} \right] Q_{\text{ind},0}, \quad (4.20)$$

translating the induced charge spectrum accessible to the first particle impinging on the counter, the product of  $c_{\text{work}}$  and random variable  $Q_{\text{ind},0}$ , into a spectrum which the induced charge for the particle of index  $n$  in the series is sampled from, expressed by random variable  $Q_{\text{ind},n}$ . The sum in the memory factor which is subtracted from 1 can by design not exceed 1 itself. For particle  $n$  hitting the counter at position  $\mathbf{x}_n$  at time

$t_n$ , induced charges  $q_{\text{ind},i}$  obtained for particles 0 to  $n - 1$  relative to the general charge sampling limit  $q_{\text{max},0}$  (cf. Sec. 4.1.1) are added up, respectively weighted with distances between  $\mathbf{x}_n$  and  $\mathbf{x}_i$  in the readout plane of the counter and between  $t_n$  and  $t_i$  on the continuous simulation time axis. The spatial distance term is maximal, i.e. equals 1, if particle positions are identical, which also holds for vanishing temporal distances between them. In fact, the impact of the electric field breaking down locally is stronger the closer in time and in space a subsequent particle arrives to a preceding one. As simulation time progresses, the earliest particles decreasingly influence the latest ones, owing to an exponential recovery of the response function on a relaxation time scale of  $\tau_{\text{MRPC}}$ . The inverse quadratic distance of particles in space which is used to describe the radial extension of a locally reduced E-field is weighted with an effective impact radius  $r_{\text{eff}}$  the size of which needs to be determined by comparison with experimental data. Concerning relaxation times, values of 100 ms and of 5000 ms are applied to low-resistive and to common glass, respectively, for qualitative demonstration purposes (cf. Sec. 2.4.2).

A flux scan of high-rate counters conducted by the Tsinghua group of the CBM-TOF collaboration at HZDR/ELBE in April 2011 [116] provides a reference measurement for adjusting the unknown memory parameter  $r_{\text{eff}}$ . More recent studies carried out at CERN/PS on the flux-dependent performance of common glass [117] and low-resistive glass [118], integrated over and as a function of irradiation time, could also be used for this purpose. At the ELBE facility, a setup consisting of an MRPC prototype with pad- or with strip-shaped readout cells, respectively, was positioned between plastic scintillators serving as hardware trigger and irradiated with a beam of single electrons of 30 MeV beam kinetic energy. The estimated Gaussian beam profile on the counter surface was about 2 cm wide in  $x$  and in  $y$ . Results obtained for the strip-MRPC are compared with simulated data to adjust the remaining free model parameter. Regarding its architecture, a double-stack configuration of low-resistive glass plates featuring  $2 \times 5$  gas gaps with a width of  $250 \mu\text{m}$  was used. Signals were picked up by three readout cells with a length of 24 cm and a pitch of 2.5 cm ( $2.2 \text{ cm} + 0.3 \text{ cm}$ ) each. In data analysis, the digitized radio frequency (RF) signal of the linear accelerator serves as a reference to the reconstructed time on the cell which relatively shows the largest signal in a trigger event. Then, the cell time resolution is obtained by subtracting quadratically the resolution of the RF measurement from the Gaussian fit sigma of the above time difference. The number of events in which any measurable signal was induced on at least a single cell of the counter divided by the total number of events corresponds to the detection efficiency.

To approach this experimental situation in a response simulation, the four different counter geometries in the upper branch of the test-beam setup at CERN/SPS are spot-illuminated in the center of their respective readout plane, irradiating a small area of  $1 \text{ cm}^2$  with a constant flux of Monte Carlo test particles which are exponentially distributed on the simulation time axis according to the inverse rate. Thus, induced signals from subsequent tracks are—like in the scenario at ELBE—not very likely to interfere in the readout channels, with rates not exceeding 100 kHz. However, preceding particles in such a single-track environment have an impact on the response function which is applied to the current track, according to Eq. (4.20). The diamond detector is generally

operated without an active particle memory in response simulations. Assuming every counter in the modeling process to be composed of low-resistive glass, ignoring—for counter 7-0-0 at least—the actual design, the respective parameter  $r_{\text{eff}}$  is constrained to achieve an efficiency drop to 80 % with a sustained particle flux of  $100 \text{ kHz/cm}^2$ , oriented towards ELBE data, over spills of 30 s. For low-resistive glass with a relatively short relaxation time, the equilibrium between local E-field breakdown and recovery sets in very fast compared to the total measurement time which allows for considering values of response observables integrated over time (as obtained from [116]) equal to equilibrium values. This identity does not hold for a common-glass parametrization, though.

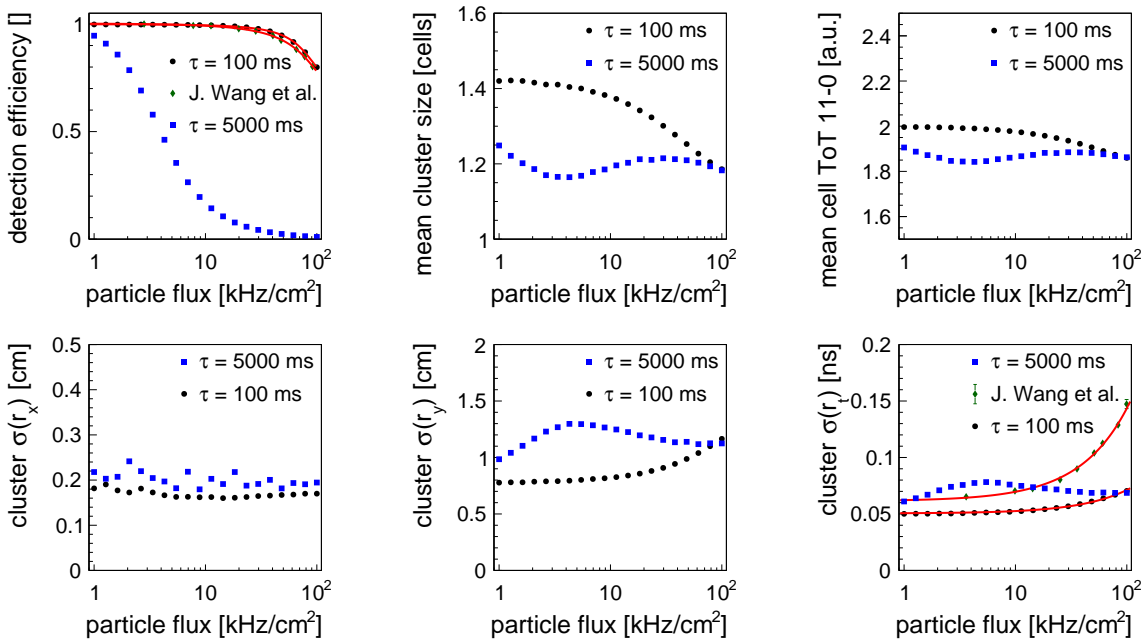


Figure 4.10: Simulated particle-flux scan of different response observables with a spot-illuminated ( $1 \text{ cm}^2$ ) counter 9-0-0. Data points correspond to equilibrium values of observables extracted from the integrated last 10 s of ten averaged 30 s spills for each flux (cf. Fig. 4.11). The effective impact radius  $r_{\text{eff}}$  is fixed at  $257 \mu\text{m}$  here (cf. Tab. 4.2) which results in an efficiency of 80 % for a flux of  $100 \text{ kHz/cm}^2$  (guided by measurements of Wang *et al.* [116]; green data points) with a low-resistive-glass time constant  $\tau$  of 100 ms (black data points) at a working coefficient  $c_{\text{work}}$  of 1.5. For the case of common glass (blue data points), only the time constant is changed to 5000 ms. As in Fig. 4.8, trend reversals of mean cluster size (upper middle plot), mean cell ToT (upper right plot),  $y$ -residual sigma (lower middle plot), and  $t$ -residual sigma (lower right plot) are observed with a common-glass parametrization as functions of particle flux beyond efficiency inflection. Efficiency curves (upper left plot) for low-resistive material are fitted with asymmetric sigmoids (cf. Eq. (4.21)) and the corresponding time-residual sigma curves (lower right plot) grow linearly (cf. Eq. (2.13)). Widths of the  $x$ -residual (lower left plot) are geometrically biased in this spot-illumination scenario.

In Fig. 4.10, the results of a simulated flux scan—upon adjusting  $r_{\text{eff}}$ —with equidistantly spaced particle fluxes on a logarithmic abscissa are depicted for counter 9-0-0, considering both low-resistive and common glass plates. Reference measurements conducted at ELBE are included where available, i.e. for efficiency and time resolution. Experimental and parametrized efficiency data obtained with low-resistive glass are fitted with a Gompertz curve,

$$f(x) = d - a \exp[-b \exp[-cx]], \quad (4.21)$$

a sigmoid function which asymmetrically approaches its asymptotes in contrast to a logistic curve (cf. Eq. (4.18)). In the case of real data, a linear fit function could also be applied, in accordance with Eq. (2.14). To further improve the agreement between experimental and simulated efficiency curves—if a linear behavior also of the latter is desired, for instance—the working coefficient needs to be fine-tuned to reduce the steepness of the efficiency drop. Concerning the linear deterioration of time resolution in both cases, the magnitude of the experimentally observed trend cannot be reproduced in response simulations without introducing an intrinsic MRPC jitter that increases when the induced charge spectrum is scaled down. The initial offset is due to the difference between a modeling constraint of 0.05 ns imposed on the cluster time resolution (cf. Tab. 4.1), which is justified by comparison of simulations to data taken at CERN/SPS (cf. Chap. 5), and an ELBE result for 2 kHz/cm<sup>2</sup> of about 0.062 ns. Again, the latter value can be matched by the present digitization approach if model parameters are redetermined with modified boundary conditions imposed on the optimization procedure. Requiring a specific cluster time resolution at 80 % detection efficiency during parameter adjustment with a static working coefficient (cf. Sec. 4.1.3) is motivated by the presented method to fix  $r_{\text{eff}}$ . As soon as an intended enhancement of the response model allows for it, the current deterioration limit of 0.07 ns on  $\sigma(r_t)$  will be extended. The trend reversal in response observables below detection efficiencies of about 50 % which is traced back to the tail behavior of the initial Landau distribution for induced-charge sampling might be more difficult to suppress. However, this efficiency range is not of any relevance in standard simulation scenarios. Memory parameters used in the following are summarized in Tab. 4.2.

Table 4.2: Parameters to control the impact of preceding particles hitting the counters in the simulated test setup on the digitization of the current particle (cf. Eq. (4.20)).

counter	5-1-0	3-0-0	9-0-0	7-0-0	4-0-0
working coefficient $c_{\text{work}}$	1.5	1.5	1.5	1.5	1.5
effective impact radius $r_{\text{eff}}$ [ $\mu\text{m}$ ]	0	338	257	155	262
relaxation time constant $\tau_{\text{MRPC}}$ [ms]	0	100	100	5000	100

The data points in Fig. 4.10 correspond to time averages of underlying dynamic processes. Using the example of detection efficiency, the associated behavior as a function of irradiation time under different particle fluxes is visualized in Fig. 4.11. The equilibration feature of the particle memory is demonstrated here. When illumination with

particles starts, the response function of the counter deteriorates until recovery effects compensate for the addition of new particles to the memory and an equilibrium efficiency is reached. At lower fluxes, the decline observed with short relaxation times, i.e. for low-resistive glass, is hardly visible. To experimentally examine the time dependence of response observables, stable beam conditions right from the beginning of accelerator spills are essential and numerous spills need to be recorded for a low statistical error in small time bins.

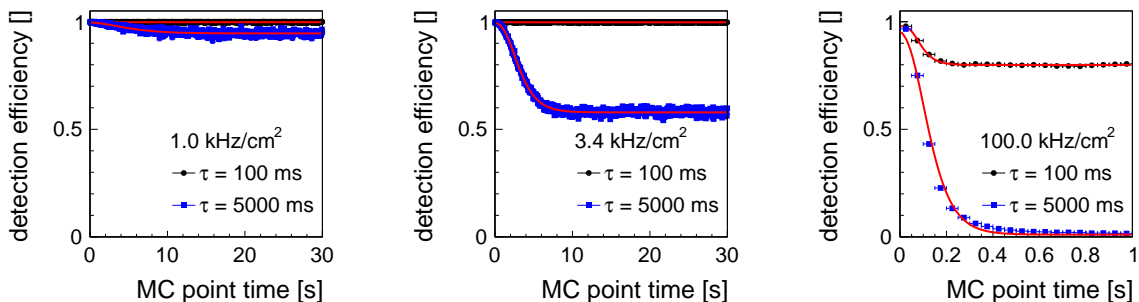


Figure 4.11: Efficiency dependence on simulated spot-illumination time for selected fluxes on counter 9-0-0, contributing to Fig. 4.10: 1.0 kHz/cm<sup>2</sup> (left plot), 3.4 kHz/cm<sup>2</sup> (middle plot), and 100.0 kHz/cm<sup>2</sup> (right plot). Black data points mark results obtained with a low-resistive glass parametrization and blue data points indicate the behavior of simulated common glass. Efficiency data generated with a rather fine time binning of 50 ms to resolve degradation effects also at 100.0 kHz/cm<sup>2</sup> are—primarily to guide the eye—fitted with asymmetric sigmoids (cf. Eq. (4.21)).

In order to compare simulated response results to experimental observations with heavy-ion collisions in the test-beam setup at CERN/SPS, the memory parametrization obtained with spot-illuminated counters needs to be employed in a corresponding flood-illumination scenario of the entire counter surface. Here, execution times of the digitization code with an active particle memory can exceed reasonable limits already at fluxes of a few kHz/cm<sup>2</sup> as the irradiated area, contrasted with a 1 cm<sup>2</sup> spot, is multiplied by a factor of up to 1000 depending on the respective counter geometry. A Monte Carlo flux estimate at the nominal beam intensity of 23.7 MHz yields values of 1.5 and 1.3 kHz/cm<sup>2</sup>, respectively, for the two detectors under test, 9-0-0 and 7-0-0, which are positioned between selector counters (cf. Tab. 3.3). With all counters included in the simulation setup and particle memories activated, this situation gets close to what is feasible with available computing resources (cf. Sec. 4.3.2). As the quantitative reproducibility of experimental results with simulated data is in any case negatively affected by the spill conditions at CERN/SPS (cf. Figs. 3.5 and 3.6), simulated fluxes are not necessarily required to exactly match with experimental conditions. For a qualitative investigation, virtual fluxes of 1.0 kHz/cm<sup>2</sup> on these counters are sufficient, also easing computational constraints.

Simulated cell hits and clusters have been compared against Monte Carlo point informa-

tion so far, unambiguously associating a response cluster with a single generating MC track. Concerning multiple heavy-ion collision secondaries impinging on the counter surface within a short time window, signal interference effects remove this clear assignment by merging several tracks into a single cluster with possibly distorted coordinates in time and space. To have a clean, i.e. practically interference-free reference scenario for flood-illuminated counters at hand which provides direct comparability to Monte Carlo, counters 9-0-0 and 7-0-0 are—in separate runs—homogeneously irradiated with single muon tracks at 3 GeV/c momentum originating from the target volume, for a sustained period of 10 s to mimic the spill length at CERN/SPS. Response observables as a function of MC point time in spill are plotted in Fig. 4.12.

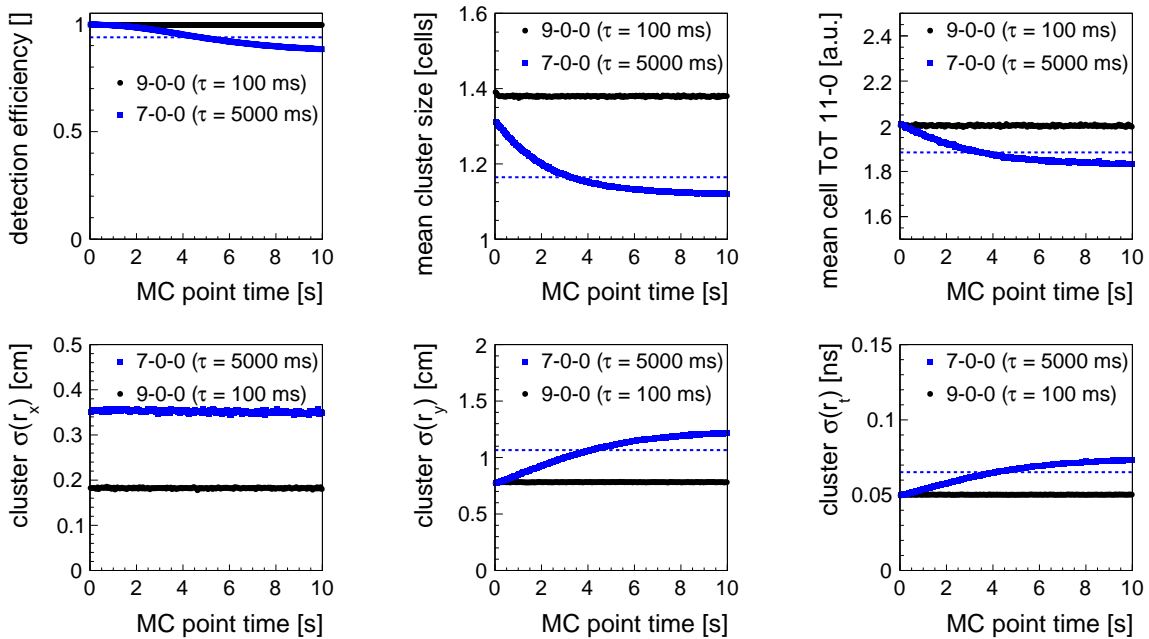


Figure 4.12: Dependence of efficiency (upper left plot), mean cluster size (upper middle plot), mean cell ToT (upper right plot), and cluster residual sigmas in  $x$  (lower left plot),  $y$  (lower middle plot), and  $t$  (lower right plot) on the illumination time of counters 9-0-0 (equipped with low-resistive glass; black data points) and 7-0-0 (equipped with common glass; blue data points). Detectors are exposed to a constant flux of single 3 GeV/c muons (no MC track interference in an event) impinging on the full counter area, respectively, at 1 kHz/cm<sup>2</sup>. Simulated muon tracks originate from the target volume of the CERN/SPS setup (cf. Fig. 3.3). Time averages of the degrading common-glass performance are indicated by dashed blue lines. Ideally reconstructed clusters on the counter surfaces, taking into account all digis originating from a muon track without applying cluster-building conditions, are unambiguously matched against MC information for residual formation.

The initial offsets between mean cluster sizes and  $x$ -residual widths are due to independent outcome of parameter optimization (cf. Tab. 4.1) and to different readout-cell

geometries (cf. Tab. 3.1), respectively. Towards the end of a spill, the onset of equilibration between breakdown and recovery of the electric field, i.e. induced charge spectrum, is visible. No trend reversals occur with the common-glass parametrization which proves the response model to be applicable in the considered efficiency range.

## 4.3 Implementation in a time-based simulation framework

### 4.3.1 Signal interference handling

Building on general remarks concerning the simulation strategy realized in CbmRoot to transform event-based input data into time-based output data given in Sec. 2.3, the peculiarities of the digitization software developed for the TOF subsystem are described hereinafter. Upon propagating collision secondaries event by event through the virtual setup with a Monte Carlo transport code, the run manager—in the subsequent digitization stage—reads prepared events from file and samples event start times from an exponential distribution of inter-event intervals, the mean length of which corresponds to the inverse product of beam intensity and interaction probability with the target. Time stamps of Monte Carlo points belonging to an event are augmented with the respective event start time placing them on a continuous simulation time axis. All MC points in an event which result from an intersection between a MC track and a TOF counter volume (averaging times and positions of entry into individual gas gaps during transport) are sorted by time and filled into a buffer. The digitization class implemented in this work reads time-sorted MC points from this buffer with time stamps smaller than the current event start time, optionally inserting MC points associated with an adjustable counter dark rate beforehand. In the first event, only a single point created in the diamond detector is extracted from the buffer which originates from a straight-line extrapolation of the collision point in the target to the diamond volume against the beam direction, yielding a time stamp prior to the collision time by subtracting the time of flight of beam particles between diamond and target from the latter. In subsequent events, MC points from the preceding one are read out unless they are positioned in time later than the current event start time which splits events for digitization and can lead to event mixing.

For every MC point which is passed to the digitization algorithm, the counter response is calculated according to Secs. 4.1 and 4.2 which comprises adding—if enabled—the corresponding tuple of induced charge  $q_{\text{ind},i}$ , spatial coordinates  $\mathbf{x}_i$ , and time  $t_i$  to the particle memory of the respective counter. If induced signals exceed discrimination threshold, transient digi objects are constructed—yet without digitization (TDC) jitter—and filled into a signal buffer which is in charge of interference handling. The output format of detector raw messages comprising a (leading-edge) time stamp and a ToT value is used for this purpose as signal interference—in the present implementation—depends on the relative positioning of leading and trailing edges (time stamp plus ToT) of subsequent signals in time only. In an iterative merging procedure, the current digi is successively checked for overlapping ToT ranges with digis from the same readout channel which

reside in the buffer. Upon a positive interference evaluation, the original pair of digis is combined into a new digi carrying the earliest leading-edge time stamp and the latest trailing-edge time stamp of the two parent digis which are deleted afterwards. As the resulting digi, in turn, might overlap with other digis in the buffer (in case of a newly arriving digi bridging the ToT gap between two detached buffered digis, for instance), interference handling continues until the buffer exclusively contains non-overlapping digis for the respective readout channel.

After treating all MC points eligible for digitization in the current round of method calls by the framework in the described manner, digi objects with a ToT interval ending prior to the current event start time are removed from the signal buffer for further processing. Detector signals generated by a MC point which is positioned on the continuous axis right after the current readout time of the signal buffer are assumed not to interfere with extracted digis anymore. This assumption is based on identical propagation times of subsequent signals in the same readout channel with a fixed time offset of 14 ns applied to the Landau parametrization (cf. Eq. (4.3)), ensuring a safe distance between Monte Carlo point times and leading-edge time stamps of corresponding digis. Under these premises, it is unlikely that a digi—due to electronics jitter and/or time walk—is positioned in time prior to the generating MC point, considering also the finite propagation time of signals along the cell if induction does not occur right at longitudinal cell ends. The opposite case would allow for the leading edge of a subsequent signal to precede the trailing edge of a signal already removed from the buffer, erroneously supposing that further interference handling was not necessary.

Upon extraction from the signal buffer, both leading- and trailing-edge time stamps of non-interfering digis are compared with the corresponding memorized values of the preceding digi in the respective readout channel. If the time difference in either case is larger than an adjustable TDC dead time, the digi object is preserved, otherwise dropped. Then, digitization jitter is added to both edge measurements. A summary sketch of interference handling for simulated counters is provided in Fig. 4.13.

Optionally, the calibration obtained with cell hits during response modeling can be applied at this stage, including the scaling of ToT spectra and time-offset and time-walk corrections (cf. Sec. 4.1.1). By the merging of digis overlapping in ToT, a bias is introduced onto the relation between leading-edge time and time over threshold. A small signal with an originally short ToT that is combined with a subsequent signal receives a larger new ToT value which is associated with a signal amplitude bigger than the original one. Consequently, performing a time-walk correction based on merged ToT ranges would yield wrong compensation values for the amplitude-dependent variation of threshold crossing times. Hence, the digitization class keeps track of the original assignment between signal time stamp and ToT to properly account for the time-walk effect. Throughout this work, simulated digis are calibrated with this method. A potential use case for non-ideal detector data obtained from simulations could be testing the calibration chain for real data (cf. Sec. 3.3).

Finally processed MRPC digis are moved to an output buffer for timeslice building which is common to all simulated CBM subsystems. To make sure that a timeslice of variable size, e.g. the mean distance between events multiplied by one thousand, is not closed

before all digis associated by time stamp have been read from the signal buffers, only digis preceding the previous event start time less an adjustable buffer time are filled into the current timeslice. Alternatively, if the latter point in time exceeds the closing time of the timeslice, the corresponding TClonesArray of digis is written to disk and the next timeslice is opened, asynchronous to the event-based procedure of the framework.

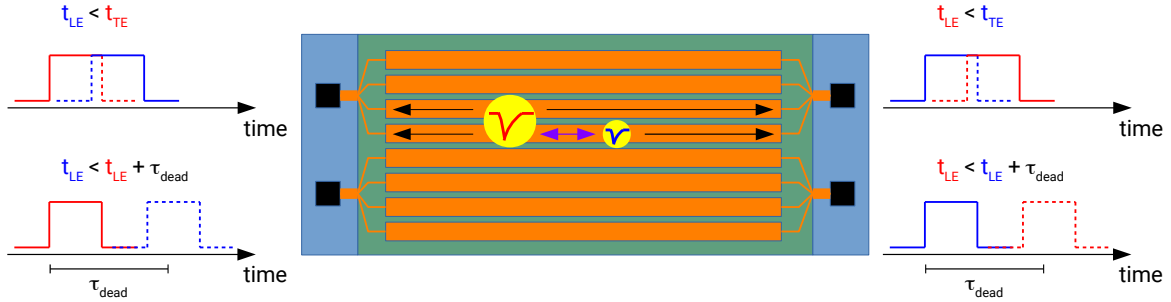


Figure 4.13: Interference handling of multiple signals induced on the same readout cell close in time. If the leading edge of a signal from the blue induction spot—which has a longer propagation time along the cell to the electronics on the left-hand side than a signal from the red induction spot—is positioned on the continuous simulation time axis ahead of the trailing edge of a signal from the red induction spot, signals get merged preserving leading-edge information of the red signal and trailing-edge information of the blue signal. If ToT ranges—which serve as interference intervals—of two consecutive signals do not overlap in time and the leading edge of the latter follows the leading edge of the former within an adjustable TDC dead-time window (here: 20 ns), the latter signal is considered lost. In all other cases, both signals are digitized not interfering with each other. Response information distorted by interference could, for instance, prevent proper reconstruction of the two-cell cluster physically emerging from the red induction spot or spoil the time-walk correction of a leading-edge time stamp to which a too large ToT is assigned by merging of ToT ranges, etc.

Following digitization, simulated cell hits can be reconstructed on counters from time-sorted digis and be grouped into clusters even prior to event building. However, with multiple Monte Carlo tracks contributing information to response clusters in a multi-hit environment, the one-to-one correspondence between MC point coordinates and cluster coordinates—the basis for residual formation in a single-track scenario—is removed. Also, if all digis which an individual MC track helped generating were (ideally) combined into a separate cluster, assuming digis to be reused, plenty of cluster duplicates would be created. Thus, to not drop an ideal cluster-building approach completely in view of interfering response processes, clusters could be formed for MC tracks/points meeting certain selection criteria only. Referring to Sec. 3.1.3, a limitation of cluster building to external tracks originating outside the respective aluminum box, ignoring descendant tracks in the module volume, or to tracks crossing all counters in line are conceivable options. While the number of duplicate clusters is reduced in this way, the impact of

signal interference, a response feature in a multi-track situation, is not.

In Fig. 4.14, cluster residuals in  $x$ ,  $y$ , and  $t$  between external MC points and the associated ideal collections of digis are depicted which exhibit interference effects. Concerning the ToT-weighted centers of cluster cells from which the  $x$ -position across the readout plane is derived, merged ToT ranges of interfering signals affect the weighting method, in particular for larger clusters. If a double hit is registered on a cell within a short time window (cf. Fig. 4.13), timing information—assuming signals on opposing cell ends to overlap in ToT—is preserved only on one side of the readout cell, respectively, one digi reflecting the arrival time of the first hit and the other digi referring to the passage of the second hit through the counter. Neither in time nor in  $y$ -position a reconstruction of actual single hit coordinates is possible in this situation. Due to allegedly shorter signal propagation times along the cell, losing information on the interval between induction points, a hit time is calculated by averaging top and bottom time stamps which precedes the MC point times of the two original tracks. The  $y$ -position along the readout plane is determined from propagation-time differences of the induced signal to opposing ends of the cell. Signal propagation times are similar for a hit in the longitudinal center of the cell and differ most if induction occurs close to a cell end. Considering interfering signals from two opposing peripheral hits, the time differences that would be obtained in separate processing balance out here, positioning the reconstructed hit in the cell center. For a central and a peripheral hit on the same cell, either originally similar propagation times become more unequal or initially asymmetric propagation times become more equal, depending on the respective point of view. In any case, the reconstructed hit is located between the two original ones, pulling the  $y$ -residual symmetrically apart. Special attention to response distortions caused by signal interference effects needs to be paid in multi-hit data analysis (cf. Sec. 5.2).

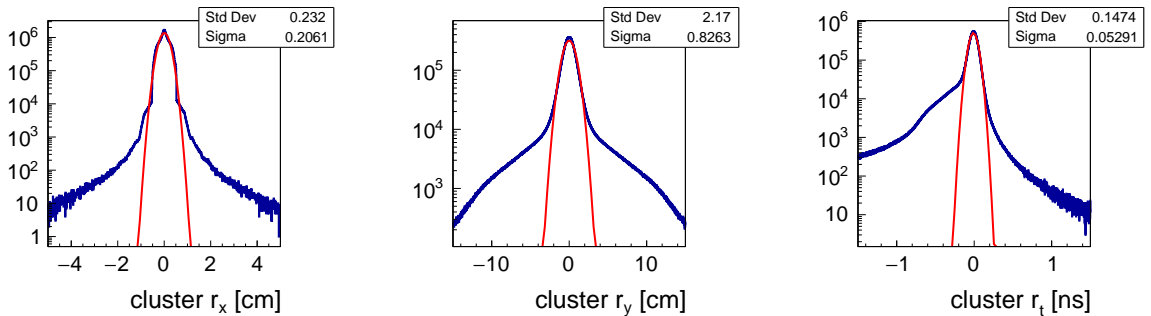


Figure 4.14: Interference effects on cluster residuals of counter 9-0-0 seen when irradiating the CERN/SPS setup with heavy-ion reaction secondaries, creating a multi-track environment. Residuals in  $x$  (left plot),  $y$  (middle plot), and  $t$  (right plot) are formed between ideally reconstructed clusters on the counter surface and contributing MC tracks. Distortions contrasting with Fig. 4.6 originate from signal merging as sketched in Fig. 4.13.

### 4.3.2 Multithreading and parallelization

An important aspect of digitization code design is the efficient implementation of an unsegmented particle memory (cf. Sec. 4.2) which stores information about the charge induced in the readout plane of a counter in time and in space by every single Monte Carlo point created in its detection volume in the course of a simulation. Given the quadratic time complexity of repeatedly summing up contributions from previous tracks to the response function of the current track (cf. Eq. (4.20)), a multithreaded computing strategy is embarked on. Concretely, the summation load is shared between  $n$  parallel threads, utilizing TThread functionality in ROOT, each handling only the  $n$ th fraction of particles in the memory. Eventually, the  $n$  partial sums are combined into the total memory coefficient of the induced charge spectrum available to the latest particle. A suitable computing infrastructure to execute intrinsically parallel programs on is provided by the Kronos cluster installed in the Green IT Cube at GSI (cf. Sec. 2.2). Job scheduling for different users on a total of 530 single computing nodes forming the main partition of the cluster which are equipped with dual-socket motherboards is carried out by the Slurm workload manager. Each node contains two identical CPUs from the Intel Xeon family, either a pair of E5-2660 v3 processors individually featuring 10 physical cores and 20 logical threads or two E5-2680 v4 units with 14 cores and 28 threads each. Altogether, the batch computing farm comprises 190 nodes with the former and 340 nodes with the latter configuration, yielding 1,060 CPUs, 13,320 cores, and 26,640 threads to be shared among users.

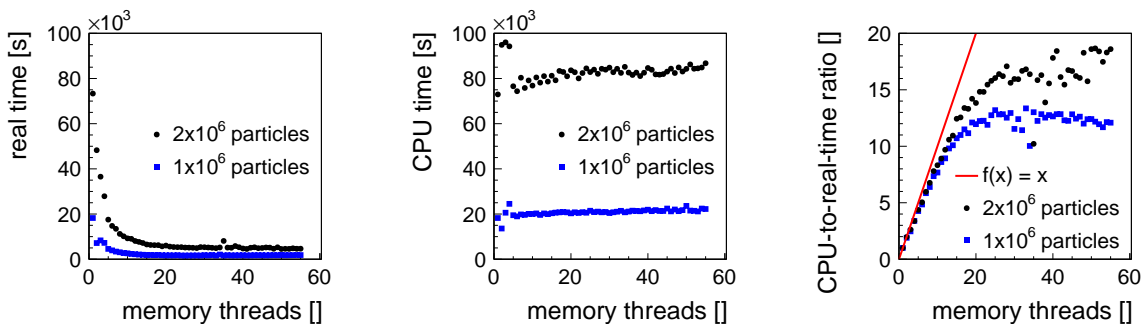


Figure 4.15: Run-time benefits of computing contributions to a particle memory comprising one (blue data points) and two (black data points) million maximum entries by multiple threads in parallel. Real execution times (left plot) of corresponding flood illuminations of a counter surface with the respective amount of test particles as a function of memory threads spawned. Total CPU time consumed by all participating threads (middle plot) indicating an increased administrative effort the more threads participate in the computation. The CPU-to-real-time ratio (right plot) visualizes the degree to which multithreading functionality is exploited by the two benchmark simulations. For simulating a large amount of particles, it proves beneficial to spread the computational load to many threads. Benchmark results shown in this figure were obtained mainly with Intel Xeon E5-2680 v4 CPUs (14 cores, 28 threads) on dual-socket motherboards.

Results of a feasibility study for a multithreaded particle memory conducted on either one or both CPUs of a node on Kronos are presented in Fig. 4.15, for two sets of 1,000,000 and 2,000,000 subsequently memorized particles that can be processed within a day of run time even by a single memory thread. Ideally, doubling the number of deployed threads would half job execution times as, when computing the memory coefficient for the current track, only half the amount of terms need to be summed up in series. Theoretically also, twice the number of particles to simulate would correspond to an increase in execution time by a factor of four, independent from the respective thread count, due to a quadratic time complexity of the summation algorithm. In reality, these expectations are not fully met. The performance gain from distributing the computational load to multiple threads is diminished, especially for smaller particle numbers, by wait conditions individual threads have to obey for reasons of thread safety. With more tracks participating in the simulation, the latter effect is increasingly outweighed by the benefit of less terms to add up in partial summation. Regarding the benchmark data in Fig. 4.15, while the CPU time—indicating a quadratic growth in computational effort between the two samples—only slightly rises as a function of deployed memory threads, the respective real execution time drops rapidly resulting in a CPU-to-real-time ratio which grows linearly, in the beginning at least. Eventually, curves level off due to an increasing computational inefficiency caused by managing more and more threads for a constant number of memory particles. The ratio between CPU and real time rises with sample size for a given thread count which implies an improved utilization of multithreading resources.

To simulate the test-beam conditions at CERN/SPS, more than 10 million (external and internal) tracks passing through a large-area prototype need to be memorized if a particle flux of  $1 \text{ kHz/cm}^2$  on the counter surface is to be sustained over a 10 s spill. Thus, regarding Fig. 4.15 and the constraint to share computing capacities at GSI with other users, a particle memory with 39 threads (plus a main thread) is used for the production of simulated data on the Kronos cluster, to allow for executing jobs on both types of computing nodes. Empirical run-time values measured under these premises suggest a maximum memory size of about 30 million particles for a simulation time of one week—without any buffer—which is the current upper limit on Kronos. Considering the illumination of a single counter, not distinguishing between external rate and internal response tracks (cf. Sec. 3.1.3), the resulting limitations on irradiation time, i.e. spill length, are given in Tab. 4.3, depending on the respective area.

Prototypical counter designs MRPC1 and MRPC2 (cf. Sec. 2.4.3), to pick an example, can be exposed to nominal particle fluxes of up to  $25 \text{ kHz/cm}^2$  for less than 5 s in simulations if the particle memory is enabled. Apart from the practical impossibility to reserve the entire Kronos cluster for TOF simulations, the available number of 530 computing nodes, provided that all counters could be processed in parallel on individual machines, would not suffice to cover the entire wall which is composed of 1376 MRPC1–4 counters. Thus, the applicability of the full response model developed in this work including the memory feature is limited to smaller setups like the one at CERN/SPS or mCBM at GSI/SIS18 (cf. Sec. 5.4) and to modest particle fluxes on counters if longer accelerator

Table 4.3: Maximum achievable particle fluxes sustained over spills of various lengths on different counter geometries with an active particle memory constrained by a run-time limit of 7 days on the Kronos computing cluster at GSI which allows for memorizing up to 30 million particles if 39 memory threads are spawned.

irradiation time/ illuminated area	1 s	2 s	5 s	10 s	unit
spot (1 cm <sup>2</sup> )	30	15	6	3	MHz/cm <sup>2</sup>
4-0-0 (60 cm <sup>2</sup> )	500	250	100	50	kHz/cm <sup>2</sup>
MRPC1 (302 cm <sup>2</sup> )	100	50	20	10	kHz/cm <sup>2</sup>
MRPC2 (604 cm <sup>2</sup> )	50	25	10	5	kHz/cm <sup>2</sup>
9-0-0 (668 cm <sup>2</sup> )	45	22.5	9	4.5	kHz/cm <sup>2</sup>
MRPC3a/b (864 cm <sup>2</sup> )	35	17.5	7	3.5	kHz/cm <sup>2</sup>
MRPC4 (1696 cm <sup>2</sup> )	18	9	3.6	1.8	kHz/cm <sup>2</sup>

spills are requested.

In Fig. 4.16, the parallelized simulation workflow from Monte Carlo transport to data analysis is summarized, pointing also at room for improvement regarding the currently sequential processing of counters in the digitization stage. Compared with the values stated in Tab. 4.3, simulating  $n$  identical counters in a row reduces the respective maximum particle flux by about a factor of  $\sqrt{n}$ . Multiple accelerator spills can be simulated in parallel only if spill breaks in between are considered long enough for the detector response function to fully recover in the absence of beam. This assumption is supposed to be valid for CERN/SPS data given a spill length of about 10 s followed by a 20 s break and, hence, applied to simulations.

### 4.3.3 Applicability for full-featured test-beam simulations

To approach test-beam results obtained with argon-on-lead collisions in simulations, conditions at the experimental site should be reflected in software. With an estimated beam intensity of 23.7 MHz (cf. Sec. 3.1.2), an interaction probability between projectile and target nuclei of 4%, and a spill duration of 10 s, about 9.5 million UrQMD collision seeds need to be propagated through the virtual setup in a single spill to generate sustained external particle fluxes ranging—in mean—from 1.8 to 1.1 kHz/cm<sup>2</sup> on the line of counters. The estimated digitization time (memory enabled) on the Kronos cluster for such a spill of beam particles leaving traces in the diamond detector and—by collision secondaries—in four differently sized MRPCs would amount to about 5 days which is feasible, in principle, but gets close to the general limit of 7 days if some safety margin for run-time variations between parallel jobs is included. As the spill structure at CERN/SPS is not uniform and shows a significant intensity spike in the beginning, a

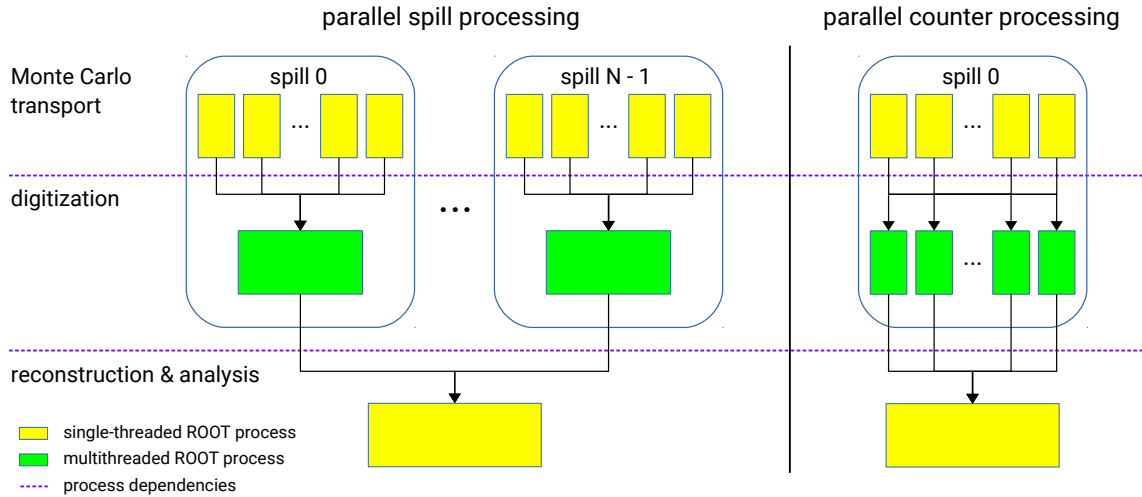


Figure 4.16: Options for parallelizing time-based MRPC simulations with a particle memory enabled during digitization. If the particle memory is supposed to be cleared between spills, multiple spills can be processed in parallel as no information needs to be exchanged between different processes. For a single spill (left part), a certain amount of Monte Carlo collision seeds—depending on the desired beam intensity and beam-target interaction probability—needs to be transported through the virtual setup event by event which happens in parallel processes (yellow boxes) which are internally single- (but potentially multi-) threaded. Digitization (green box) can start when Monte Carlo transport is finished. Intersections of tracks from transported input events with an active detector volume (MC points) are arranged on a continuous time axis and the corresponding induced charge is stored in the particle memory along with time and position coordinates. The joint impact of preceding tracks in memory on the digitization of the current one is computed in parallel by multiple threads in the single digitization process, counter by counter. As a counter operates as an independent entity concerning particle memorization, execution times for digitization could be further reduced by processing memory-active counters in parallel, not sequentially, i.e. by running a separate digitization process for every counter (right part; green boxes). This functionality is currently not implemented. Reconstruction and analysis following digitization—here depicted as a single-threaded synopsis (yellow box)—could be parallelized as well.

qualitative comprehension of trends observed in experimental data is primarily aimed at by simulating collisions in the test-beam setup rather than an exact quantitative description of effects, following an argument already given in Sec. 4.2. Hence, a reduced beam intensity of 17.6 MHz (decreasing the demand for collision seeds to 7 million per spill) is applied which generates a mean external particle flux of precisely  $1.0 \text{ kHz/cm}^2$  on the common-glass counter under test (7-0-0) and, accordingly, average fluxes of 1.348, 1.125, and  $0.830 \text{ kHz/cm}^2$  on counters 3-0-0, 9-0-0, and 4-0-0. At the end of a digitization run, i.e. a single processed spill, with an extrapolated computing time of 2 days and 20 hours on the Kronos cluster which is a more relaxed situation, particle memories comprise—in the sequence of counters—about 13.6, 8.8, 9.9, and 0.6 million entries under these conditions.

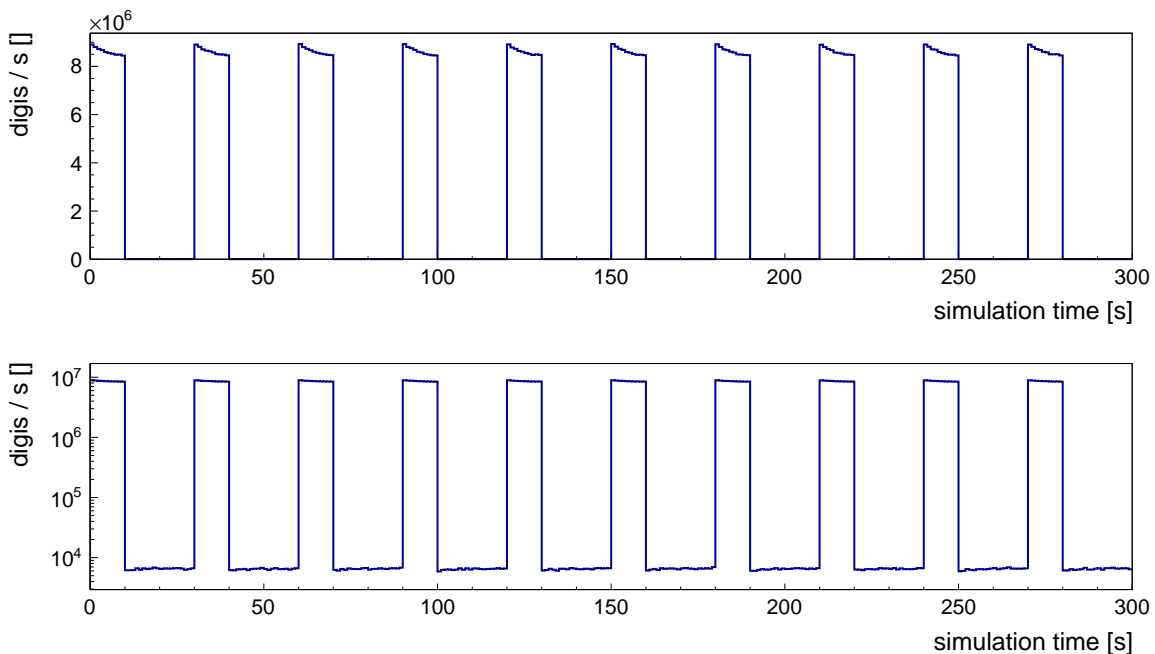


Figure 4.17: Rate effects visible in production time stamps of detector digis distributed over 10 consecutive spills of simulated heavy-ion reactions (upper plot; linear scale). A 10 s spill is always followed by a 20 s spill break—mimicking the spill length and duty cycle at CERN/SPS—which contains digis attributed to detector noise on the MRPCs of  $1 \text{ Hz/cm}^2$  (lower plot; logarithmic scale). At the beginning of a new spill, the particle memory is reset.

Actual digitization times for 10 spills of this type (cf. Fig. 4.17) are listed in Tab. 4.4, comparing computational effort for otherwise identical runs with and without an active particle memory. Execution times systematically vary between different processors but not for this reason alone. With the memory feature disabled, the digitization class can be inserted into the common simulation chain of the CBM experiment.

Following time-based digitization, detector raw messages (digis) reside in timeslices with information on the original event assignment and contributing MC points preserved in

Table 4.4: Digitization times (ddd-hh:mm:ss) of ten parallel spills of simulated heavy-ion collisions (cf. Fig. 4.17), with an active (left-hand side) and an inactive (right-hand side) particle memory, executed on members of the Intel Xeon processor family on the Kronos computing cluster at GSI. In the case of an active particle memory, the summation of contributions from preceding tracks to the current response function is performed by 39 threads in parallel.

spill	CPU time	real time	ratio	CPU time	real time	ratio	processor
	w/ particle memory			w/o particle memory			
0	112-11:52:23	03-07:39:04	33.9	00:48:01	00:51:04	0.94	E5-2660 v3
1	112-16:12:24	03-07:12:40	34.1	00:47:48	00:54:21	0.88	E5-2660 v3
2	112-22:16:45	03-06:28:56	34.5	00:47:36	00:51:17	0.93	E5-2660 v3
3	88-01:38:48	02-18:12:53	31.9	00:47:34	01:23:35	0.57	E5-2680 v4
4	87-11:08:55	02-18:08:16	31.7	00:42:47	00:46:02	0.93	E5-2680 v4
5	88-03:13:59	02-18:45:43	31.7	00:45:17	00:48:48	0.93	E5-2680 v4
6	87-17:22:18	02-19:30:21	31.2	00:45:02	00:48:19	0.93	E5-2680 v4
7	87-15:45:50	02-17:34:16	32.1	00:45:02	00:47:36	0.95	E5-2680 v4
8	88-16:00:22	03-05:17:19	27.5	00:44:18	00:47:17	0.94	E5-2680 v4
9	87-07:44:09	02-17:24:47	32.0	00:44:57	00:47:24	0.95	E5-2680 v4

dedicated backlink objects. Concerning the above heavy-ion collision simulation, a timeslice corresponds to a time interval of about 1.4 ms which contains 1000 events on average. A single spill cycle of 30 s is subdivided into 21, 120 timeslices. Prior to comparing time-based simulated to event-based experimental data in the analysis (cf. Chap. 5), events need to be recovered from timeslices, either by identifying accumulations of digis on the continuous time axis (cf. Fig. 3.11) or—in an ideal way restricted to simulated data—by recombining digis into events based on backlink information.

For event building in the latter case, an optional branch of time-sorted Monte Carlo points in the timeslice is scanned for coincident (by the original event number stored with each point) track passages on a set of trigger counters. If for a given event number a MC point is found on every required station, not necessarily originating from the same particle, the digi branch of the timeslice is looped over to collect raw messages referring to any MC point which is associated with the selected event. Then, these digis together with all MC point objects belonging to the respective event and backward/forward references providing links between the two data formats are saved to disk as reconstructed events, asynchronous to reading entire timeslices at the input stage. Restoring events in this ideal fashion only with MC point information contained in digi backlinks—in contrast to reading all MC points processed in digitization from a separate timeslice branch—would not give a complete picture as, by this means, no record is kept of tracks which did not induce a measurable signal on any readout cell. In the case of event

mixing, multiple digi backward references to points originating from different original events indicate a corresponding response interference which might affect digi properties. Timeslices are handled independently by the framework at the moment, i.e. events or points and related digis might be split across timeslice borders by any of the two event-building methods mentioned above. However, with a thousand events per timeslice this effect is statistically insignificant.

Regarding the two simulation scenarios to be compared with experimental findings at CERN/SPS—a homogeneous irradiation of counters under test with single muons (cf. Fig. 4.12) and a multi-track environment created by heavy-ion collisions—an ideal event building in the above sense is performed in both cases, using the diamond detector (5-1-0) and selector counters 3-0-0 and 4-0-0 as trigger stations. The corresponding selection bias on the different counter surfaces does not conflict with calibration routines here as simulated digis are pre-calibrated during digitization, applying correction terms to leading-edge time stamps and ToT values which were generated in the process of adjusting model parameters. Instead, considering collision simulations for a numerical example, the number of events to be handled by the analysis class is reduced from about 70.5 million in total, distributed over 10 subsequent spills, to 4.3 million relevant ones for testing the two counters in the middle with reference hits on the peripheral selector counters—in favor of shorter execution times. Clustering of simulated cell hits is based on correlations in time and space observed on adjacent readout cells, analogous to real data (cf. Sec. 3.3).

## CHAPTER 5

### RESULTS

Two principal effects influencing the performance of MRPCs—and its evaluation—in heavy-ion-collision experiments at high beam–target interaction rates are under investigation in this work. On the one hand, the response function deteriorates with irradiation time owing to a local breakdown of the electric field in the gas gaps upon avalanche formation. The observed decline in detection capability, reducing efficiency and widening time and position residuals, depends on the relation between incident particle flux and relaxation time for field recovery, the latter quantity being constrained mainly by the resistivity of the glass plates. On the other hand, multiple signals induced on the same readout cell by different collision secondaries may interfere with each other, merging response information and distorting residuals. With increasing projectile energies and growing sizes of colliding nuclei, counters are noticeably exposed to such multi-hit conditions which complicate the matching of correlated response clusters between two MRPCs or the unambiguous assignment of a cluster to an extrapolated particle trajectory which is reconstructed by a tracking system. The novel detector response parametrization described in Chap. 4 takes into account both rate and signal-interference effects. This allows for a systematic comparison of corresponding trends in the response function measured during the test beam at CERN/SPS with simulated data which is the subject of the present chapter.

Due to the lack of an ideal Monte Carlo reference for experimental clusters generated on a single counter, response observables in data analysis, concerning both simulated and real events, need to be evaluated against a matched cluster on another counter in the setup. The four counters are positioned in line (cf. Fig. 3.3) to obtain response correlations on different detectors primarily from straight particle tracks which consecutively pass through all stations. Cluster matching in time and space is realized with a conventional  $\chi^2$ -formalism on two levels. First, events comprising a sufficiently well matched cluster pair on selector counters 3-0-0 and 4-0-0 positioned in the very front and in the very back, respectively, are identified. Then, in these events, one of two detectors under test (DUT) mounted between selector counters is scanned for a cluster matching the interpolated coordinates of the selector hit on reference counter 4-0-0, against which residuals are calculated for the best match available. Not finding a match at all or only a poor one is counted towards detection inefficiency. Response characteristics differ with applied  $\chi^2$ -limits but also with MRPC design and irradiation scenario. The main distinguishing feature between DUT counters 9-0-0 and 7-0-0 is the resistivity of the glass plates, the former being constructed with low-resistive material while the latter is equipped with common glass. In simulations, this is reflected by different relaxation times of  $\tau_{\text{MRPC}} = 100 \text{ ms}$  and  $\tau_{\text{MRPC}} = 5000 \text{ ms}$ , respectively. Experimental results for these counters (labeled with “exp data”) are compared to findings with simulated heavy-ion collisions (“sim data”) and single muon tracks (“sim ST”)—providing a multi- and a single-hit scenario as points of reference—in two respects: the interference bias on

counter response as a function of hit multiplicity and the degradation of performance due to rate as a function of irradiation time.

In Sec. 5.1, the  $\chi^2$ -method for cluster selection and matching is described and limitations are discussed. Considering the cluster multiplicity on the first counter in line (3-0-0) as a measure of signal interference, multi-hit effects are studied as a function of a limit on this observable in Sec. 5.2. The impact of a sustained particle flux on counter response with progressing time in spill is examined in Sec. 5.3. Finally, an outlook is given in Sec. 5.4 on a continuation of the current research activity at the running mCBM experiment at GSI/SIS18 where rate and multi-hit conditions are even more challenging than at CERN/SPS.

## 5.1 Event selection and hit matching in data analysis

The starting point for analysis of both experimental and simulated data are arrays of calibrated hits (clusters) on counters in the setup, each representing an input event. In a physics production run, contrary to a test-beam scenario for detector prototypes, one would aim at reconstructing—from correlations on different stations—and identifying, e.g. by the TOF method, all particle trajectories in an event within the geometrical acceptance of the experiment. At CERN/SPS, full-scale PID (particle identification) instrumentation as required for this purpose was not available and is also not necessary to evaluate the mere counter performance under various aspects. The analysis strategy pursued in this work concentrates on finding the best possible hit match on a detector under test to an optimal prediction based on correlations between hits on a pair of selector counters. Thus, apart from a mandatory hit on the diamond detector, a maximum of three clusters—two on selectors Sel1 (4-0-0) and Sel2 (3-0-0) and one on DUT (9-0-0 or 7-0-0) if existing—is considered in a sample of events which is compiled according to the matching quality among selector hits. Clusters obtained for analysis from experiment and simulations represent the earliest response occurrences on contributing readout cells in the respective event, owing to a TDC channel dead time of (about) 20 ns and, in addition, to an adjustable minimum distance—here of 50 ns—between consecutive digis in a readout channel applied during cluster building. Hence, multiple signals induced by different tracks on a single cell are regarded in data analysis only insofar as they are merged by interference.

The matching algorithm is fairly straightforward and premised on assumed chi-square distributions of weighted cluster residuals in dimensions  $x$ ,  $y$ , and  $t$ . In a given event, the cluster pair with minimum residual  $\chi^2$  is identified, successively for counter combinations Sel2–Sel1 and DUT–Sel1 if a limit on selector  $\chi^2$  is not exceeded. The first selector counter provides a reference measurement for the DUT which is supported by the best matching cluster on Sel2. Concerning global position residuals, a straight-line interpolation of cluster coordinates on the counter which is installed further downstream (always Sel1) translates this information into the readout plane of the counter which is located closer to the target (either Sel2 or DUT). Due to varying readout-cell orientations across counters, the cells of counter 4-0-0 running parallel to cave- $y$  while cells on the counters

in front are oriented along cave- $x$  (cf. Tab. 3.2), local  $x$ - and  $y$ -coordinates enter into global  $x$ - and  $y$ -residuals for the counter in the back only. For the other counters, global and local coordinates are swapped which is important to note as response calculations along and across readout cells systematically differ. Upon digi calibration, time residuals in particular are not strictly centered about zero, neither for real data where small deviations can occur nor for simulated data. In the latter case, offsets corresponding to the average time of flight between stations need to be subtracted from cluster residual means, as time stamps are ideally calibrated against the actual passage of a Monte Carlo track through the detector.

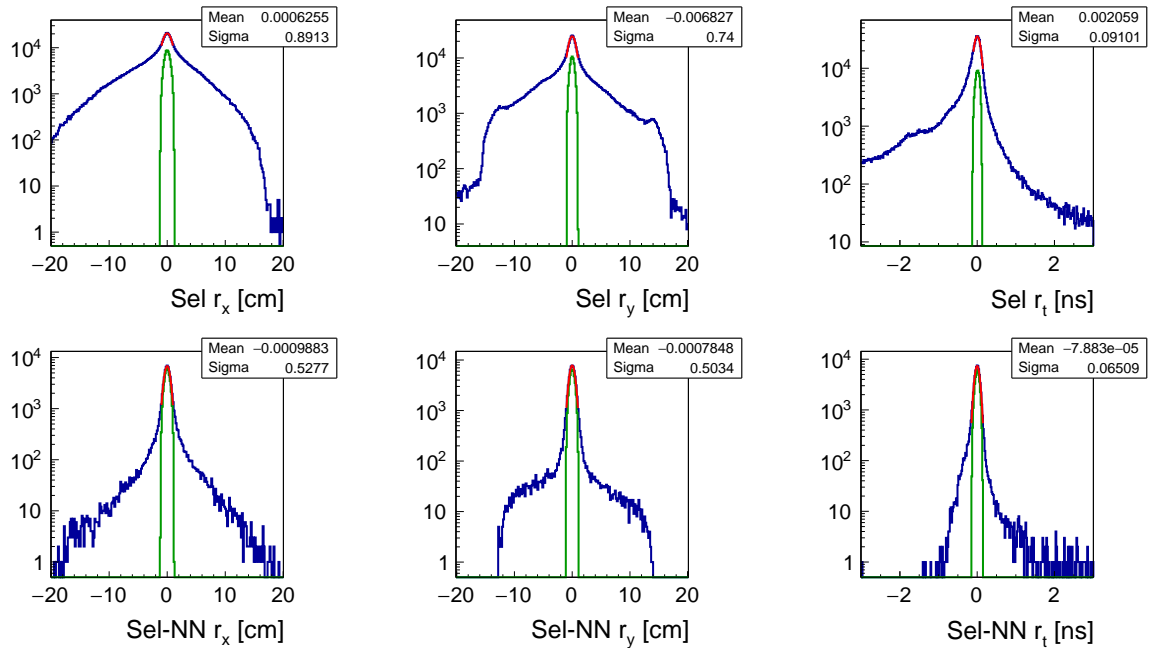


Figure 5.1: Illustration of event selection for analysis based on experimental residuals between cluster pairs on selector counters 3-0-0 (Sel2) and 4-0-0 (Sel1) with minimal residual  $\chi^2$  (cf. Eq. (5.1)) in three global dimensions  $x$  (left column),  $y$  (middle column), and  $t$  (right column) in the respective event (upper row). Peaks of the centered residual distributions are fitted with Gaussian functions (red curves) to obtain initial values for  $\chi^2$ -weight estimation (cf. Fig. 5.2). A cut on the properly weighted residual Sel  $\chi^2$  (of 2.5 if not otherwise stated) qualifies a subset of events (green distributions) for analysis of detectors under test (DUT). In these selected events, the nearest-neighbor (NN) DUT cluster to the Sel1 cluster which contributes to the selector pair is determined with an analogous Sel-NN  $\chi^2$ -mechanism. Residuals between the  $\chi^2$ -matched cluster on DUT counter 9-0-0 and the prediction from Sel1 (reference) counter 4-0-0, constrained by Sel2 counter 3-0-0, are shown in the lower row. Sel-NN residuals confined by a  $\chi^2$ -cut (of 5.0 if not otherwise stated; green distributions) are the basis for extrapolating detection efficiency.

Centering residual distributions and determining  $\chi^2$ -weights for cluster matching be-

tween selector counters (labeled with Sel) on one side and between DUT and Sel1 (labeled with Sel-NN for nearest neighbor) on the other side is a nested process owing to the dependence of the latter on the  $\chi^2$ -limit applied to the former. Prior to imposing any cut on Sel  $\chi^2$ , peaks of residual distributions of selector cluster pairs with the lowest relative  $\chi^2$ -value in the respective event, using default weights of  $w(r_x) = w(r_y) = 1$  cm and  $w(r_t) = 0.1$  ns in the three response dimensions, are fitted with Gaussian functions yielding—by extracted mean and sigma values—offsets for centering and initial estimates for actual  $\chi^2$ -weights. Fitting ranges stated in Tab. 5.1 are limited to small intervals about residual peaks due to the inherent background in Sel spectra without event filtering (cf. Fig. 5.1). For the  $\chi^2$ -method to be applicable, widths of the Gaussian core of distributions need to be considered.

Table 5.1: Ranges for Sel and Sel-NN residual peak fitting (cf. Fig. 5.1) applied to the pair of selector counters (3-0-0 and 4-0-0) and to subsequent DUT matching of counters 9-0-0 and 7-0-0 in experimental data, simulated heavy-ion reaction data, and simulated single-track (ST) muon data.

3-0-0 & 4-0-0	exp data	sim data	sim ST
Sel $r_x$ fitting range [cm]	$\pm 1.0$	$\pm 1.0$	$\pm 1.0$
Sel $r_y$ fitting range [cm]	$\pm 1.0$	$\pm 1.0$	$\pm 1.0$
Sel $r_t$ fitting range [ns]	$\pm 0.15$	$\pm 0.15$	$\pm 0.15$
9-0-0	exp data	sim data	sim ST
Sel-NN $r_x$ fitting range [cm]	$\pm 1.0$	$\pm 1.2$	$\pm 1.2$
Sel-NN $r_y$ fitting range [cm]	$\pm 1.0$	$\pm 1.0$	$\pm 1.0$
Sel-NN $r_t$ fitting range [ns]	$\pm 0.15$	$\pm 0.15$	$\pm 0.15$
7-0-0	exp data	sim data	sim ST
Sel-NN $r_x$ fitting range [cm]	$\pm 2.0$	$\pm 1.2$	$\pm 1.2$
Sel-NN $r_y$ fitting range [cm]	$\pm 1.3$	$\pm 1.2$	$\pm 1.2$
Sel-NN $r_t$ fitting range [ns]	$\pm 0.15$	$\pm 0.15$	$\pm 0.15$

Following the alignment of Sel residuals with zero, final Sel  $\chi^2$ -weights are determined by fitting the resulting distribution of a  $\chi^2$ -variable

$$\chi_3^2 = \left( \frac{r_x}{w(r_x)} \right)^2 + \left( \frac{r_y}{w(r_y)} \right)^2 + \left( \frac{r_t}{w(r_t)} \right)^2, \quad (5.1)$$

generated with Gaussian sigmas from peak fits  $w(r_i)$ , with a probability density function which comprises a free scaling factor  $a$  multiplying  $\chi^2$ -weights in all three dimensions,

$$w(r_i) = a \sigma(r_i), \quad (5.2)$$

to account for an overestimation of weights obtained from residual peak fits. The assumption of an identical scaling in  $x$ ,  $y$ , and  $t$  which can be determined by a single

fit operation is made for practical reasons as any adjustment of individual  $\chi^2$ -weights necessitates the entire analysis to be repeated in order to receive the corresponding  $\chi^2$ -distribution. Thus, the idea to reutilize multidimensional minimization (cf. Sec. 4.1.4) to determine three independent scaling values  $a_x$ ,  $a_y$ , and  $a_t$  lacks computational feasibility, in the first place. In Fig. 5.2, the fitting method is illustrated and exemplary  $\chi^2$ -weights are documented in Tab. 5.2. As the upper fitting limit is given by the respective  $\chi^2$ -cut, the procedure needs to be executed separately for different values of this variable.

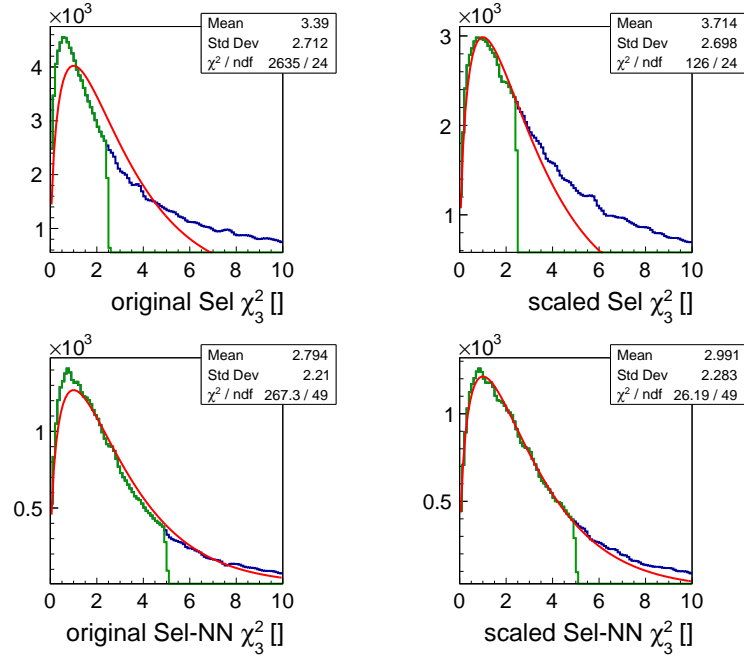


Figure 5.2: Calibration of  $\chi^2$ -distributions between selector counters (upper row) and between DUT and reference (Sel1) counter (lower row) by extracting a common scaling factor for  $\chi^2$ -weights in the three dimensions (cf. Eq. (5.2)) from a fit to the original distributions (left column) limited by the respective  $\chi^2$ -cut. Applying these weights to the (experimental) data yields the distributions in the right column. Concerning determination of Sel-NN acceptance and extrapolation of Sel-NN efficiency, the number of selector events in which any cluster is found on the DUT (entries in the blue histogram in the lower right plot) and the number of selector events in which a DUT-to-reference match meets the  $\chi^2$ -cut condition (entries in the green histogram in the lower right plot), the latter divided by the integral of the theoretical  $\chi^2$ -distribution at this limit ( $0.828$  for  $\chi^2 \leq 5.0$ ), are normalized to the total number of selector events (entries in the green histogram in the upper right plot), respectively. The extrapolation ansatz avoids counting the non-Gaussian response tail towards detection efficiency. In the case at hand, one obtains a Sel-NN acceptance of  $64,151/65,029 = 0.986$  and a Sel-NN efficiency of  $41,591/65,029/0.828 = 0.772$  for counter 9-0-0.

Upon calibrating residual and  $\chi^2$ -distributions between selector clusters, a fixed Sel  $\chi^2$ -limit is applied to select events for nearest-neighbor matching between the reference hit

Table 5.2: Numerical examples of Sel and Sel-NN  $\chi^2$ -weights  $w(r_i)$  with corresponding scaling factors obtained for the analysis of counter 9-0-0 in experimental data, simulated heavy-ion reaction data, and simulated single-track (ST) muon data. Initial weights are equivalent to sigmas of Gaussian fits to residual peaks. A larger downscaling is required in the Sel case where—in contrast to Sel-NN matching—no event selection is in place, and in a multi-hit environment.

9-0-0	exp data	sim data	sim ST
initial Sel $w(r_x)$ [cm]	0.904	0.913	0.721
initial Sel $w(r_y)$ [cm]	0.737	0.724	0.564
initial Sel $w(r_t)$ [ns]	0.092	0.096	0.071
final Sel $w(r_x)$ [cm]	0.735	0.776	0.685
final Sel $w(r_y)$ [cm]	0.599	0.616	0.536
final Sel $w(r_t)$ [ns]	0.075	0.082	0.067
Sel $\chi^2$ -weight scaling $a$	0.813	0.850	0.951
initial Sel-NN $w(r_x)$ [cm]	0.528	0.787	0.730
initial Sel-NN $w(r_y)$ [cm]	0.505	0.525	0.467
initial Sel-NN $w(r_t)$ [ns]	0.066	0.066	0.063
final Sel-NN $w(r_x)$ [cm]	0.500	0.763	0.710
final Sel-NN $w(r_y)$ [cm]	0.479	0.509	0.455
final Sel-NN $w(r_t)$ [ns]	0.062	0.064	0.061
Sel-NN $\chi^2$ -weight scaling $a$	0.947	0.969	0.973

on counter Sel1 and candidate clusters on the DUT. The approach to centering Sel-NN residuals and to finding  $\chi^2$ -weights is completely analogous to the case of Sel distributions with the exception that the event selection now visibly exerts influence on residual shapes and tails (cf. Fig. 5.1). However, Sel-NN residuals in the given experimental example are not perfectly normally distributed for three possible reasons: First of all, the cluster response itself deviates from the Gaussian ideal (cf. Figs. 4.6 and 4.7), regardless of signal interference. Second, the response function is distorted in a multi-hit irradiation scenario (cf. Fig. 4.14). And finally, if the detector under test did not respond at all to the particle track selected for analysis by the Sel2–Sel1 match, or the information got lost in the readout channels, any other hit on the counter surface in the respective event—which should almost always be available in a multi-track environment—is considered nearest neighbor and enters into residual calculations. Although the  $\chi^2$ -method which is used in this work does not provide a mathematical description of non-Gaussian effects, it allows for quantifying deviations—and their increase as a function of hit multiplicity (cf. Sec. 5.2)—from the reference case of three normally distributed cluster residuals, which is reflected in the extrapolated detection efficiency. A  $\chi^2$ -limit imposed on Sel-NN matching which necessitates an extraction of corresponding residual weights

is relevant only to the latter observable. The determination of efficiency is explained in Fig. 5.2. Position and time resolutions containing contributions from both DUT and Sel1 are identified with Gaussian sigmas of peak fits to full Sel-NN residuals (obtained with final  $\chi^2$ -weights, though). Fitting ranges which depend on the respective counter under test and on the analyzed data sample (cf. Tab. 5.1) are empirical values which are consistently applied to the listed combinations in the following. Hence, the focus of studying the behavior of residual widths (resolutions) under varying conditions is put on the approximately Gaussian core of distributions.

Finding appropriate  $\chi^2$ -limits to be imposed on Sel and Sel-NN chi-square distributions proves difficult. From a mathematical perspective, the goodness of  $\chi^2$ -fits continuously decreases with increasing fitting ranges (cf. Fig. 5.3), suggesting to use rather small values in both cases at the cost of statistics.

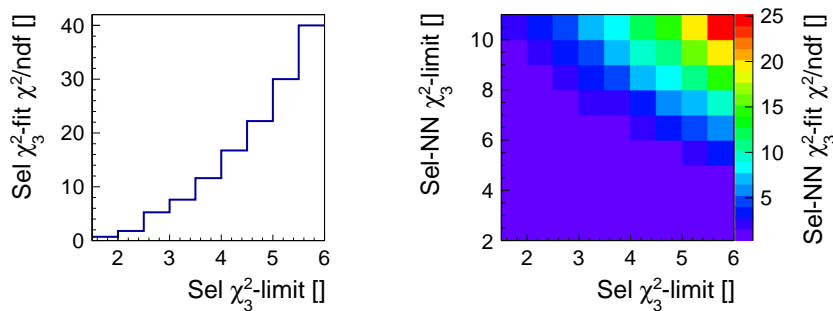


Figure 5.3: Goodness of fits to (finally weighted) Sel (left plot) and Sel-NN (right plot)  $\chi^2$ -distributions obtained from experimental data with counter 9-0-0 as DUT against upper fitting limits expressed by Sel  $\chi^2$  (left plot) and by both Sel and Sel-NN  $\chi^2$  (right plot).

Considering the behavior of fitted cluster residual widths (resolutions) as functions of the applied Sel  $\chi^2$ -cut (cf. Fig. 5.4), an expected downward trend towards vanishing limits is seen both for experimental and simulated heavy-ion collision data of the two detectors under test. If the Sel matching range is reduced, the quality of selector hits on Sel1 is improved which results in decreasing residual widths. The constraints imposed on parameter adjustment during response modeling (cf. Tab. 4.1) seemingly allow for even quantitatively reproducing measured residual sigmas between counters 4-0-0 (Sel1) and 9-0-0 in  $y$  (local  $x$  for DUT) and in  $t$  while the simulated  $\sigma(r_x)$  (local  $y$  for DUT) is too large. The latter discrepancy in absolute values is due to a preponderance of discrimination jitter in the modeled response function which is discussed in Sec. 4.1.2. Concerning deviating slopes, the diminishing contribution of the small local  $x$ -resolution by counter Sel1 at more narrow  $\chi^2$ -limits is hardly noticeable in simulations against the—generally too large—local  $y$ -resolution of the detector under test. As regards the DUT equipped with common glass (7-0-0), a numerical agreement exists for the global  $y$ -residual width only, owing to an overestimation—with the current parameter set—of the actually poor timing performance of the counter under moderate particle-flux conditions which it was

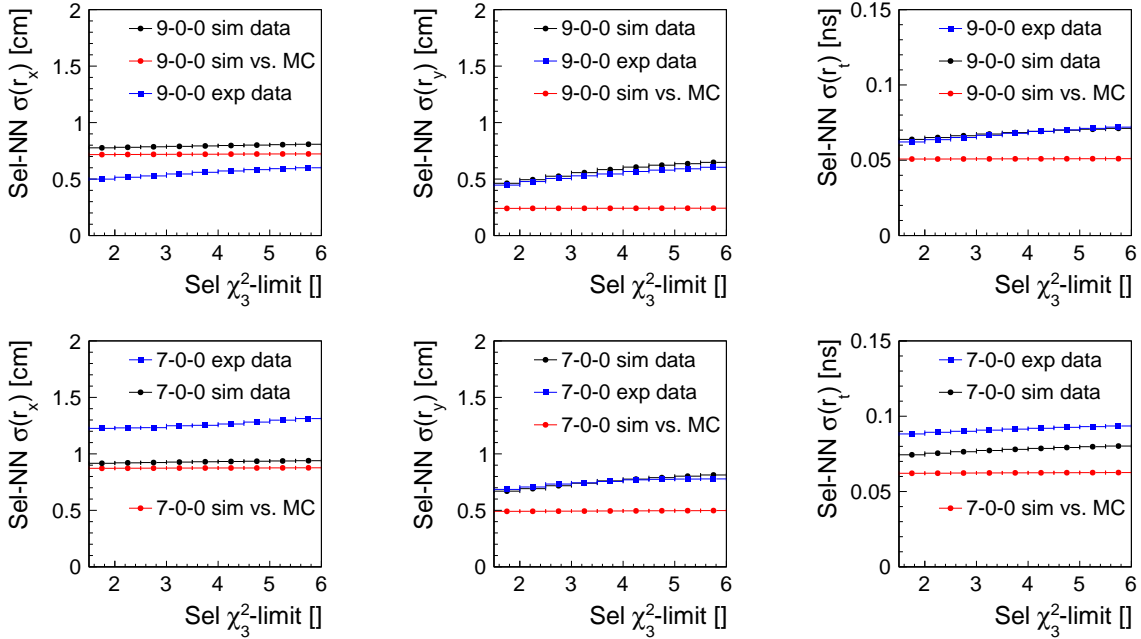


Figure 5.4: Comparison of residual sigmas in dimensions  $x$  (left column),  $y$  (middle column), and  $t$  (right column) obtained from Sel-NN residual peak fitting (cf. Tab. 5.1) for counters 9-0-0 (upper row) and 7-0-0 (lower row) in experimental (blue data points) and simulated (black data points) heavy-ion reaction data, as functions of the applied Sel  $\chi^2$ -limit. Red data points indicate Gaussian peak sigmas—extracted analogous to the Sel-NN case—of residuals between a reconstructed cluster and the main Monte Carlo track associated with it, i.e. the track which contributes to most digital detector messages forming the cluster in a track-interference scenario. The difference between black and red curves originates from the contribution of the reference (Sel1) counter to the Sel-NN residuals which decreases with stricter Sel  $\chi^2$ -cuts. Thus, the actual resolution of the physical track passage in space and time by the DUT alone would be obtained for a vanishing Sel  $\chi^2$ -limit with this method.

exposed to at CERN/SPS.

Via dedicated backlink objects, simulated clusters are affiliated to original Monte Carlo tracks passing through a counter and triggering a response process (cf. Sec. 4.3.1). If signals induced on a readout cell by multiple tracks interfere with each other, digital detector messages (digis) carry merged response information which is introduced to the cluster upon formation from correlated digis in time and space. In this case, the association between cluster and track is ambiguous. Different Monte Carlo tracks contributing to a response cluster are weighted with the number of constituents, i.e. digis, which they had an impact on. For the respective track exhibiting the highest weight, residuals are formed between cluster and Monte Carlo point coordinates and fitted about distribution peaks according to Tab. 5.1. The resulting residual widths are independent of the Sel1 counter and show an essentially constant behavior as a function of the applied

Sel  $\chi^2$ -limit (cf. Fig. 5.4). For the regular (simulated) Sel-NN resolutions, they indicate lower asymptotes reached in the limit of an infinitesimal  $\chi^2$ -cut and represent the single-counter resolutions of the DUT. The latter values cannot be inferred from dividing DUT–Sel1 residual widths by  $\sqrt{2}$  as both counters—identical performance provided—do not equally contribute to Sel-NN residuals, the Sel1 counter always being constrained by the Sel  $\chi^2$ -limit.

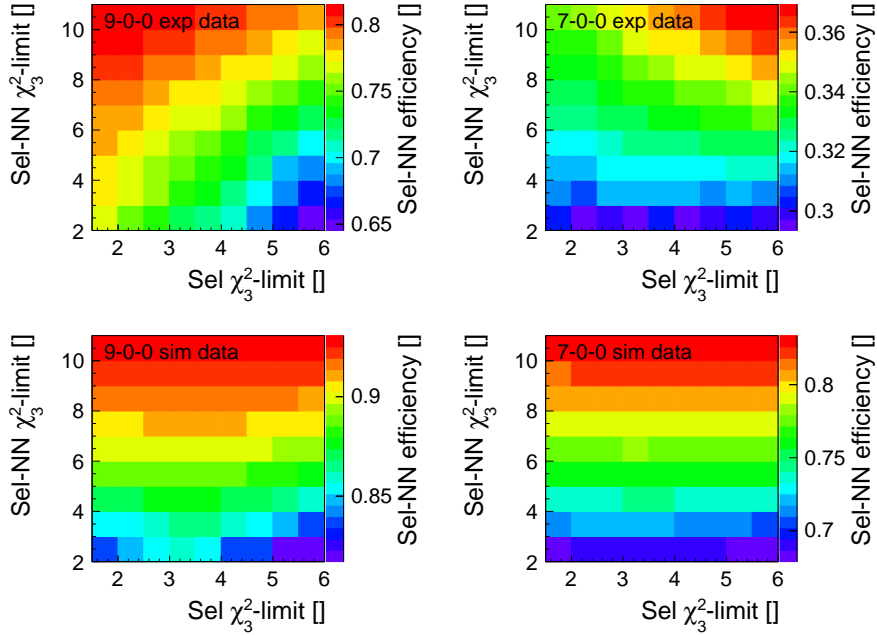


Figure 5.5: Efficiency determination of counters 9-0-0 (left column) and 7-0-0 (right column) according to Fig. 5.2 depending on Sel and Sel-NN  $\chi^2$ -limits in experimental (upper row) and in simulated (lower row) heavy-ion collision data.

The determination of detection efficiency from the extrapolated share of events within the Sel-NN  $\chi^2$ -cut region compared to the total number of selector events (cf. Fig. 5.2) is susceptible to variations in both Sel and Sel-NN cut values which is demonstrated in Fig. 5.5. In general, less restrictive Sel-NN  $\chi^2$ -limits, i.e. wider fitting ranges for the estimation of  $\chi^2$ -weight scaling factors, tend to compress the resulting  $\chi^2$ -distribution towards the ordinate, artificially increasing the integral share on the left-hand side of the respective extrapolation limit which leads to larger efficiency values. Concerning the behavior as a function of Sel  $\chi^2$ -limit, simulated efficiency values for both low-resistive- (9-0-0) and common-glass (7-0-0) detectors show a smaller sensitivity to variations than their experimental counterparts. Opposite trends observed experimentally between counters 9-0-0 and 7-0-0 indicate an exceptional behavior of the latter which is examined in more detail in Sec. 5.2. Stricter cuts on selector chi-square confine the event sample to cases of cleaner matching conditions for Sel2 and Sel1 hit pairs, e.g. due to less interference of multiple tracks, which might extend to the geometrical matching corridor for DUT clusters in these events. An increase in extrapolated  $\chi^2$ -efficiency is attributed

to a reduction of non-Gaussian tails in Sel-NN residuals which are partially caused by response interference on the DUT, assuming that any response tails on the Sel1 counter are suppressed by the cut on Sel  $\chi^2$ —at least within the considered range—and do not enter into DUT–Sel1 residuals. Possibly owing to more pronounced tails in simulated residuals even in the absence of signal interference effects (cf. Fig. 4.6), a change in selector  $\chi^2$ -limit is not coupled to a strong variation in efficiency here. Too narrow Sel  $\chi^2$ -limits, however, could introduce bias to the extrapolation method by providing an insufficiently large fitting range to account for the tail behavior of the  $\chi^2$ -distribution, both for simulated and experimental data, an argument which also holds for the Sel-NN case.

In terms of absolute efficiency scales, higher values are obtained for the virtual and real prototype equipped with low-resistive glass (9-0-0) as anticipated. The low numbers received for the measured common-glass counter (7-0-0) are surprising at moderate mean particle fluxes on the surface of about 1.3 kHz/cm<sup>2</sup> but could be explained with the spike in beam intensity preceding every recorded spill in the test beam at CERN/SPS. Regarding efficiency values in the 70 % range for counter 9-0-0, no cut on cluster multiplicity is applied in the present case yet, i.e. residual distortions due to response interference which significantly reduce  $\chi^2$ -efficiency are not suppressed. In the subsequent analysis, identical  $\chi^2$ -limits are used for all scenarios to ensure comparability. From the above discussion, cuts on Sel chi-square at 2.5 and on Sel-NN chi-square at 5.0 seem reasonable, keeping in mind the related systematic uncertainties. Assuming perfect  $\chi^2$ -distributions, about 52.4 % and 82.8 % of entries in a corresponding histogram would be located in the respective cut region while underlying response residuals—if purely Gaussian in shape—would be constrained to intervals of  $\pm\sqrt{2.5}\sigma$  and  $\pm\sqrt{5.0}\sigma$  about a mean of zero, respectively.

## 5.2 Track-interference bias on detector response

Multiple particles traversing the counter surface within a short time interval have a chance to trigger interfering response processes which influence detector performance. In principal, this phenomenon is independent of the incident particle flux on the counter and can occur also at low beam–target interaction rates. The critical factor is the mean multiplicity of reaction secondaries which the counter is exposed to in single collision events, a quantity that varies with beam kinetic energy and size of the colliding nuclei. In a Monte Carlo simulation, the number of tracks contributing to the generation of a response cluster is known and could directly be used as an indicator for signal interference. Experimentally, for the test-beam setup at CERN/SPS in particular, the measured cluster multiplicity on the large-area selector counter 3-0-0 allows for an assessment of the multi-hit conditions which the remaining counters positioned behind are confronted with in a given event. With respect to straight-line tracks originating from the target, the active area of the Sel2 counter shadows the readout planes of the two detectors under test and the Sel1 counter in the back, except for an approximately 1 cm wide vertical band on 9-0-0 in positive global  $x$ . Consequently, assuming a high

detection efficiency of the multiplicity selector, situations where two target tracks create separate single-cell clusters on adjacent readout cells of counter 3-0-0 in the projected trigger area (cf. Tab. 3.2) but get merged into a distorted multi-track cluster on a detector under test can be identified. The limit on Sel  $\chi^2$ , in addition, filters events in which interference effects are visible already in a Sel2–Sel1 cluster pair. For both experimental and simulated data, a limit on Sel2 cluster multiplicity is introduced to complement the  $\chi^2$ -criterion on event selection. As a function of this observable, multi-hit effects on the detectors under test can be studied systematically. The dependence of mean cluster multiplicities reconstructed on Sel2, DUT, and Sel1 counters in selected events on the Sel2 MUL limit is presented in Fig. 5.6. Regarding the deviations between mean multiplicity values obtained for counters 7-0-0 (DUT) and 4-0-0 (Sel1) in experiment and simulation, the former offset might result from the relatively low efficiency measured for counter 7-0-0 (cf. Fig. 5.5) and the latter difference could be due to a dead cell in the center of the real counter (cf. Tab. 3.4) which increases the chance of splitting a response cluster in two although a corresponding mitigation mechanism is implemented in the cluster-building algorithm (cf. Fig. 3.20).

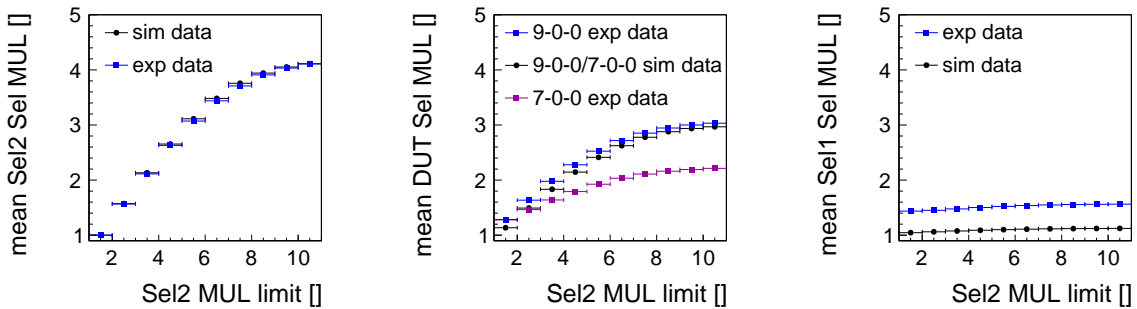


Figure 5.6: Mean cluster multiplicities in selector events on counters in experimental and simulated data analysis depending on a multiplicity limit imposed on the Sel2 counter (3-0-0). Corresponding to the positioning of counters in the setup, results for selector counter Sel2 are shown in the left plot, for both DUT counters 9-0-0 and 7-0-0 in the middle plot, and for selector counter Sel1 (4-0-0) in the right plot. Simulated DUT multiplicities are—for a better overview—given only for counter 9-0-0 as the corresponding values for counter 7-0-0 hardly differ.

With the analysis method used in this work, any change in detector behavior owing to an alteration of event-selection criteria is reflected by the shape of Sel-NN cluster residuals. In Fig. 5.7, the associated experimental and simulated distributions, choosing counter 9-0-0 as detector under test, are directly compared for an open cut on Sel2 multiplicity of 10 and for the single-cluster case. Concerning measured data, the systematic reduction of response tails by a narrow multiplicity cut originates both from a decline in signal interference and from a smaller number of possible fake matches between Sel1 and DUT clusters if the actual particle track is not recorded by the latter counter in the respective event. Simulated residuals, prior to cutting on multiplicity, al-

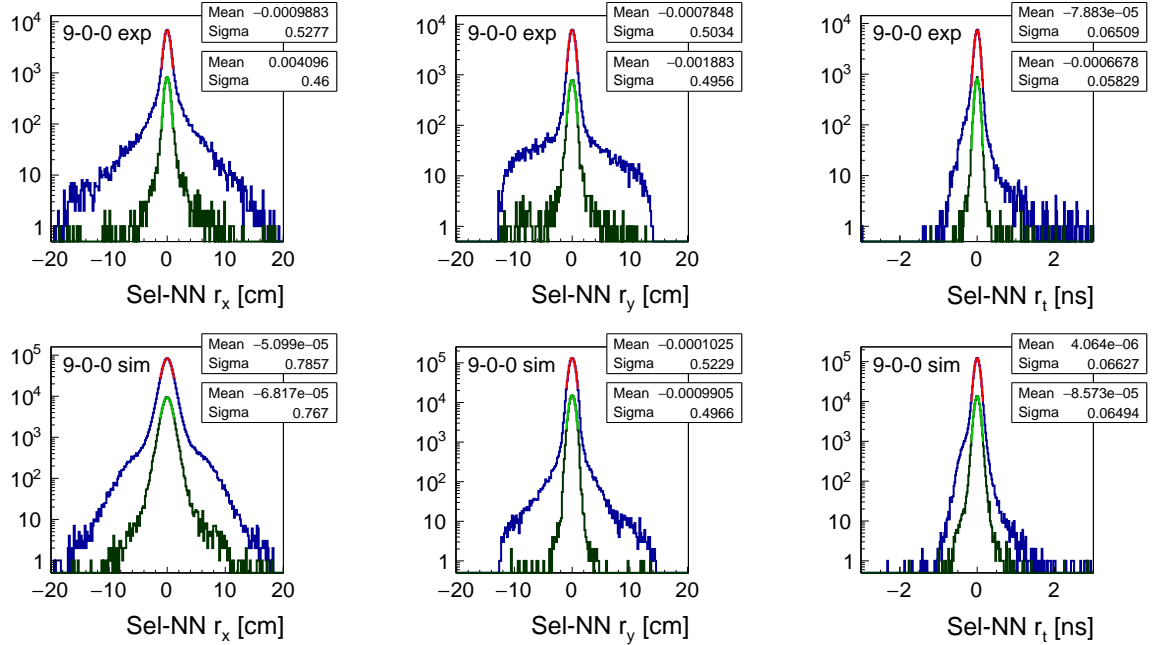


Figure 5.7: Comparison of Sel-NN residuals in  $x$  (left column),  $y$  (middle column), and  $t$  (right column) for experimental (upper row) and simulated (lower row) 9-0-0 data with a cluster-multiplicity limit on the Sel2 counter (3-0-0) of 10 (blue histograms) and of 1 (dark green histograms) in place. Statistics boxes display means and sigmas of Gaussian peak fits (cf. Tab. 5.1) for both cases. In addition to a statistical decrease in histogram entries which results from constraining event selection by a strict MUL limit, structures in the residuals attributed to track interference and—in case of local counter inefficiencies—false NN attributions of DUT clusters to a selector prediction are largely suppressed.

most exclusively comprise interference-induced tails as the counter parametrization with low-resistive glass yields a measurable detector response—not a clean one, though—for close to 100 % of incident tracks at these particle fluxes (cf. Fig. 4.10). The overestimation of local  $y$ -residual widths in simulations which—for the DUT—contributes to the global  $x$ -residual has been discussed. As regards the improvement of resolutions, i.e. the decrease of fit-extracted residual peak widths between the two cut conditions, larger differences in the timing dimensions  $y$  (global  $x$ ) and  $t$  are obtained with experimental data. While a reduction of interference effects also occurs for simulated data, primarily in distribution tails, residual centers are affected to a lesser degree. In the response model, interfering signals are treated independently up to and including signal-edge discrimination, to then be merged if ToT ranges overlap. Leading-edge information of the latter signal is lost completely. In reality, interfering response processes can influence each other already at the level of signal formation with the result that they are jointly reflected in the final leading-edge measurement, yielding smaller discrepancies between the passage of original particles through the detector and reconstructed cluster coordi-

nates. This could explain the greater susceptibility of experimental residual centers to interference suppression, apart from the presence of NN mismatches in this case.

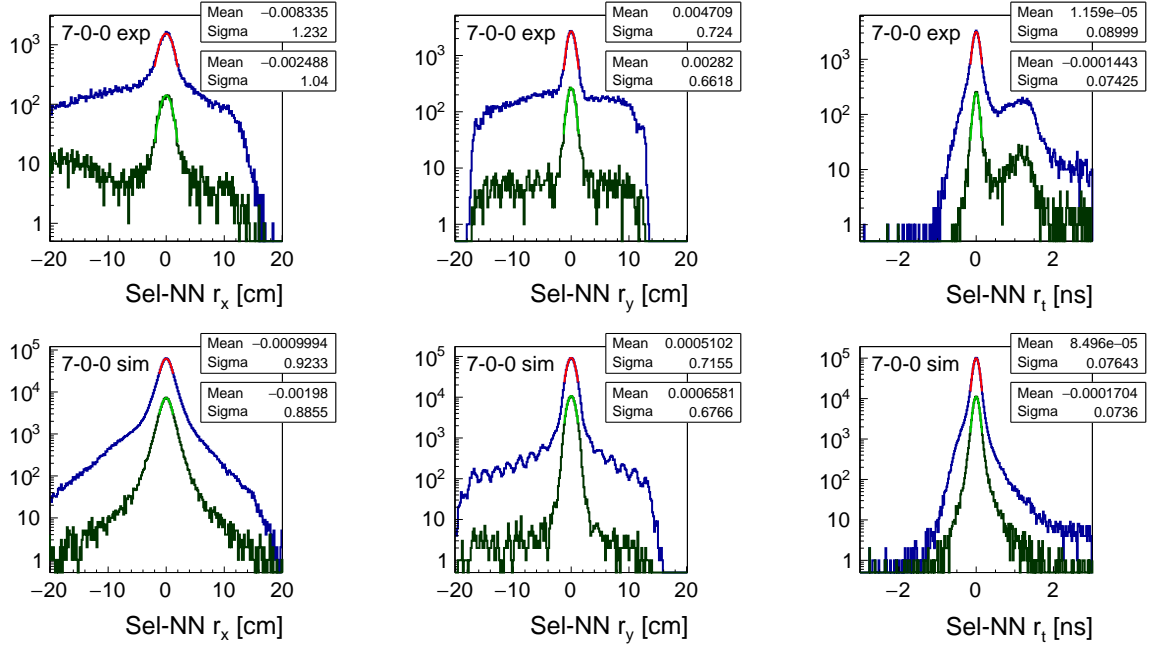


Figure 5.8: Comparison of Sel-NN residuals in  $x$  (left column),  $y$  (middle column), and  $t$  (right column) for experimental (upper row) and simulated (lower row) 7-0-0 data with a cluster-multiplicity limit on the Sel2 counter (3-0-0) of 10 (blue histograms) and of 1 (dark green histograms) in place. Statistics boxes display means and sigmas of Gaussian peak fits (cf. Tab. 5.1) for both cases. In addition to a statistical decrease in histogram entries which results from constraining event selection by a strict MUL limit, structures in the residuals attributed to track interference and—in case of local counter inefficiencies—false NN attributions of DUT clusters to a selector prediction are largely suppressed. Note the second peak in the experimental time residual (upper right plot) which is not filtered out by cutting on Sel2 multiplicity and which is assumed to originate from signal reflections at the locally positive cell end (cf. Fig. 3.4). The bump visible in the negative axis range of the low-multiplicity global  $x$ -residual (upper left plot) results from the corresponding impact of reflections on the reconstruction of local  $y$ .

The residual behavior of common-glass counters is shown in Fig. 5.8. Both the real and the simulated prototype exhibit detection inefficiencies at the given mean particle fluxes of 1.3 and 1.0 kHz/cm<sup>2</sup>, respectively, which are responsible for a prominent background from nearest-neighbor mismatches in residual spectra that also causes a broadening of distribution centers. Plateau ranges in position residuals differ as some peripheral read-out cells are declared dead in experimental data (cf. Tab. 3.4). In the simulated global  $y$ -residual, prior to applying the multiplicity cut, the discrete local  $x$ -coordinates of read-out cells are indicated on which a substitute cluster for the missing true NN match is centered. Allowing for a single cluster on selector counter 3-0-0 only does not completely

eliminate background, also due to transport physics creating secondaries in the material budget between the first (3-0-0) and the third (7-0-0) counter in line which are not registered by the multiplicity selector. Time and local  $y$ -residual peaks (global  $x$ ) are relatively wide in the experimental case and distributions are influenced by signal reflections (see caption) which cannot be counted towards  $\chi^2$ -efficiency. Further observations correspond to the case of low-resistive glass discussed above.

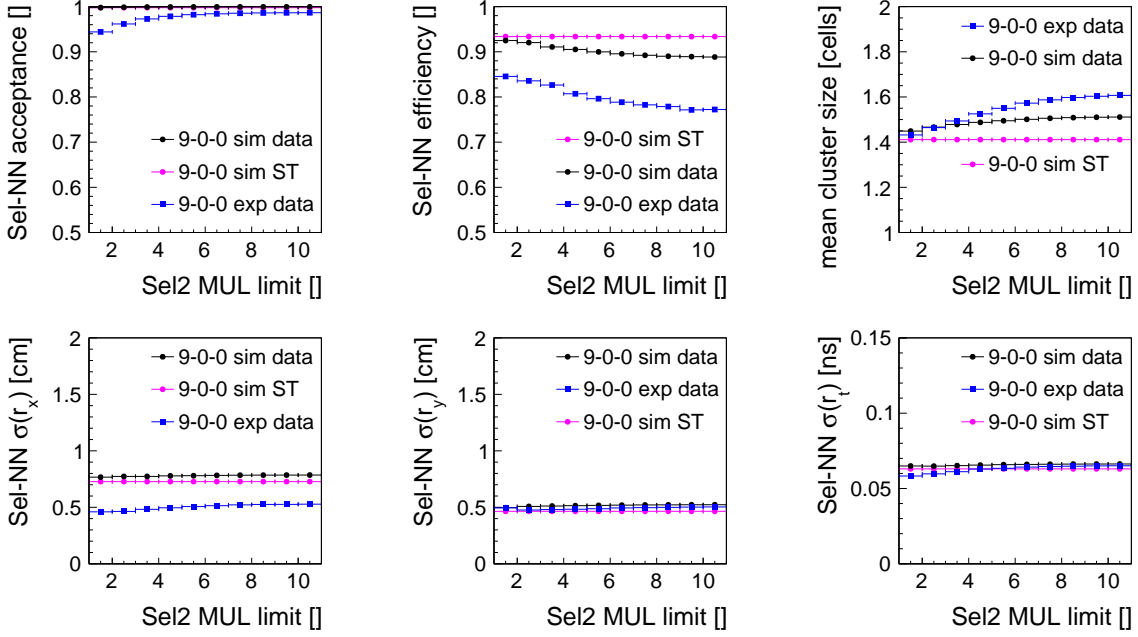


Figure 5.9: Scan of response observables for counter 9-0-0 as a function of a Sel2 multiplicity limit in experimental data (blue markers), simulated heavy-ion reaction data (black markers), and simulated single-track (ST) muon data (magenta markers). A discussion of the observed trends in Sel-NN acceptance (upper left plot), efficiency (upper middle plot), mean cluster size (upper right plot), global  $x$ -residual sigma (lower left plot), global  $y$ -residual sigma (lower middle plot), and time-residual sigma (lower right plot) is provided in the text.

A multiplicity scan for experimental and simulated versions of counter 9-0-0 interpolating results extracted from Fig. 5.7 which also comprises single-track muon data for reference is summarized in Fig. 5.9. Two response observables are considered in addition to detection efficiency and residual widths, the Sel-NN matching acceptance, i.e. the share of selector events in which any hit is found on the DUT regardless of a  $\chi^2$ -criterion, and the mean cluster size. The general availability of DUT clusters for (false) NN attributions to selector hits increases with wider cuts on Sel2 multiplicity, given the large ratio between the total active area of the detector under test—where a Sel-NN cluster match can theoretically originate from—and the projected selection area which is geometrically constrained by the relatively small size of the Sel1 counter. In experimental data, a corresponding trend in the acceptance is observed indicating a limited detection

capability of the real prototype. Towards relaxing multi-hit conditions, the number of selector events in which no cluster at all is reconstructed on the DUT rises. Regarding  $\chi^2$ -efficiency, on the other hand, a concurrent increase is observed due to diminishing interference effects which leads to a reduction of non-Gaussian tails in chi-square and residual distributions, raising extrapolated  $\chi^2$ -efficiency values. While the acceptance of 94.4% (cf. Tab. 5.3) measured with a single-cluster constraint on Sel2 represents an upper limit for the number of cases in which any response to the actually selected particle is registered on the DUT, independent of possible distortions by signal interference, the  $\chi^2$ -efficiency of 84.5% constitutes a lower boundary. Neither Sel-NN mismatches nor interfering tracks are excluded completely by the applied multiplicity cut. Thus, the expected counter behavior under single-track irradiation with cosmic rays, for instance, could be confined with observations made in a multi-hit environment up to this interval. However, some discrepancy between acceptance and  $\chi^2$ -efficiency remains even in the absence of response interference due to cluster residuals in  $x$ ,  $y$ , and  $t$  not being perfectly normally distributed.

Table 5.3: Summary of response results obtained for a low-resistive- (9-0-0; upper part) and a common-glass counter (7-0-0; lower part) with a single-cluster multiplicity limit imposed on counter Sel2 in experimental data, simulated heavy-ion reaction data, and simulated single-track (ST) muon data. Errors—if significant within the displayed precision—represent statistical uncertainties only. The systematic methodical bias is described graphically and in the text.

9-0-0	exp data	sim data	sim ST
Sel-NN acceptance []	$0.944 \pm 0.003$	$0.998 \pm 0.000$	$0.998 \pm 0.000$
Sel-NN efficiency []	$0.845 \pm 0.005$	$0.925 \pm 0.001$	$0.934 \pm 0.000$
mean cluster size [cells]	$1.43 \pm 0.01$	$1.45 \pm 0.00$	$1.41 \pm 0.00$
Sel-NN $\sigma(r_x)$ [cm]	$0.46 \pm 0.01$	$0.77 \pm 0.00$	$0.73 \pm 0.00$
Sel-NN $\sigma(r_y)$ [cm]	$0.50 \pm 0.01$	$0.50 \pm 0.00$	$0.46 \pm 0.00$
Sel-NN $\sigma(r_t)$ [ns]	$0.058 \pm 0.001$	$0.065 \pm 0.000$	$0.063 \pm 0.000$
7-0-0	exp data	sim data	sim ST
Sel-NN acceptance []	$0.527 \pm 0.006$	$0.957 \pm 0.001$	$0.945 \pm 0.000$
Sel-NN efficiency []	$0.293 \pm 0.006$	$0.815 \pm 0.001$	$0.808 \pm 0.000$
mean cluster size [cells]	$1.07 \pm 0.00$	$1.20 \pm 0.00$	$1.17 \pm 0.00$
Sel-NN $\sigma(r_x)$ [cm]	$1.04 \pm 0.03$	$0.89 \pm 0.01$	$0.87 \pm 0.00$
Sel-NN $\sigma(r_y)$ [cm]	$0.66 \pm 0.02$	$0.68 \pm 0.00$	$0.65 \pm 0.00$
Sel-NN $\sigma(r_t)$ [ns]	$0.074 \pm 0.002$	$0.074 \pm 0.000$	$0.073 \pm 0.000$

For simulated heavy-ion collision and single-muon data, the Sel-NN acceptance is virtually 1 and constant as a function of multiplicity limit according to a counter parametrization which—at moderate particle fluxes—yields a measurable signal (which is possibly

distorted by interference) for almost every incident track. Concerning efficiency, a maximum value of 93.4% can be inferred with a  $\chi^2$ -formalism in the single-track scenario which is indifferent to cuts on Sel2 multiplicity. Towards smaller MUL limits, the simulated multi-track case approaches this number as signal interference ceases. Consequently, more than 6% of simulated response processes are not accessible with the chi-square matching method in a strict sense. Experimental findings suggest that this share might be slightly higher in reality although some multi-hit bias persists even with the most narrow multiplicity cut in place. The mean size of clusters increases with harsher multi-hit conditions as simultaneous induction processes by different particles on adjacent readout cells get merged into larger response clusters. Here, simulated cell hits are grouped into clusters based on correlations in time and space, analogous to experimental data. Stronger multi-hit effects are observed in the latter case compared to simulated collision data which converge to the single-track reference line if interference is suppressed. Taking up the abovementioned argument of signal merging in reality affecting residual centers—in contrast to tails—to a larger degree than simulations allow for, a higher number of neighboring cells might be correlatable in view of intertwined response processes. This reasoning extends to the dependence of cluster residual widths on the multiplicity limit where variations in simulated data are smaller than in real data. The systematic deviation in global  $x$  is due to a known limitation concerning overlarge local  $y$ -residual widths in the response model (cf. Sec. 4.1.2).

Experimental position and time resolutions of 0.5 cm and 65 ps between the low-resistive-glass DUT and the reference counter are obtained from residual peak fits even without specifically selecting low-multiplicity events. Corresponding values further improve towards  $MUL(\text{Sel2}) = 1$  (cf. Tab. 5.3). Although the contribution of the Sel1 counter to these numbers is limited by the applied Sel  $\chi^2$ -limit, a full-system time resolution of 80 ps between a start and a stop detector as required for CBM TOF (cf. Sec. 2.4.3) is within reach also in a multi-hit environment.

As for the common-glass DUT (7-0-0), a direct comparison between experimental and simulated results is difficult owing to the unexpectedly bad performance which the prototype showed under moderate flux conditions at CERN/SPS (cf. Fig. 5.10). Probably, the registered intensity spike at the beginning of each spill corrupts the detector response function for the subsequent spill plateau. In addition, measured timing residuals exhibit a second peak due to signal reflections (cf. Fig. 5.8) which further reduces  $\chi^2$ -efficiency, to only 29.3% for a single-cluster multiplicity cut (cf. Tab. 5.3). The efficiency estimate slightly decreases towards smaller MUL limits, an exceptional behavior that is indicated also in Fig. 5.5 and currently not fully understood. For a large-area counter featuring a significant detection inefficiency, chances for a random cluster match between DUT and selector counter are still high which is reflected by the big trend upwards in acceptance. Regarding similarly pronounced tendencies in timing residuals  $x$  (local  $y$ ) and  $t$ , mismatches—besides response interference—presumably exert influence on residual peak widths as well which is reduced by applying stricter multiplicity cuts. Simulated collision results for this counter show a gradual increase in acceptance approaching 100% for wide cuts, starting from 95.7% close to the single-track reference value. By parametrization with a relaxation time constant of  $\tau = 5$  s, the virtual version of counter 7-0-0 does not

respond to all incident particles anymore at mean fluxes of  $1 \text{ kHz/cm}^2$  (cf. Fig. 4.12). The response quality in terms of residual deviations from the Gaussian ideal is worse than for low-resistive glass which does not exhibit noticeable rate effects under these conditions, indicated by an absolute discrepancy of almost 14 % between Sel-NN acceptance and  $\chi^2$ -efficiency. Due to already wider residual distributions, the growing impact of response interference on the extrapolated efficiency towards larger multiplicity limits is less distinct compared to collision simulations with counter 9-0-0 as DUT. Regarding the ensemble of response observables, values represent the mean performance drop integrated over the irradiation time in spill. A differential consideration as a function of the latter quantity is the subject of Sec. 5.3.

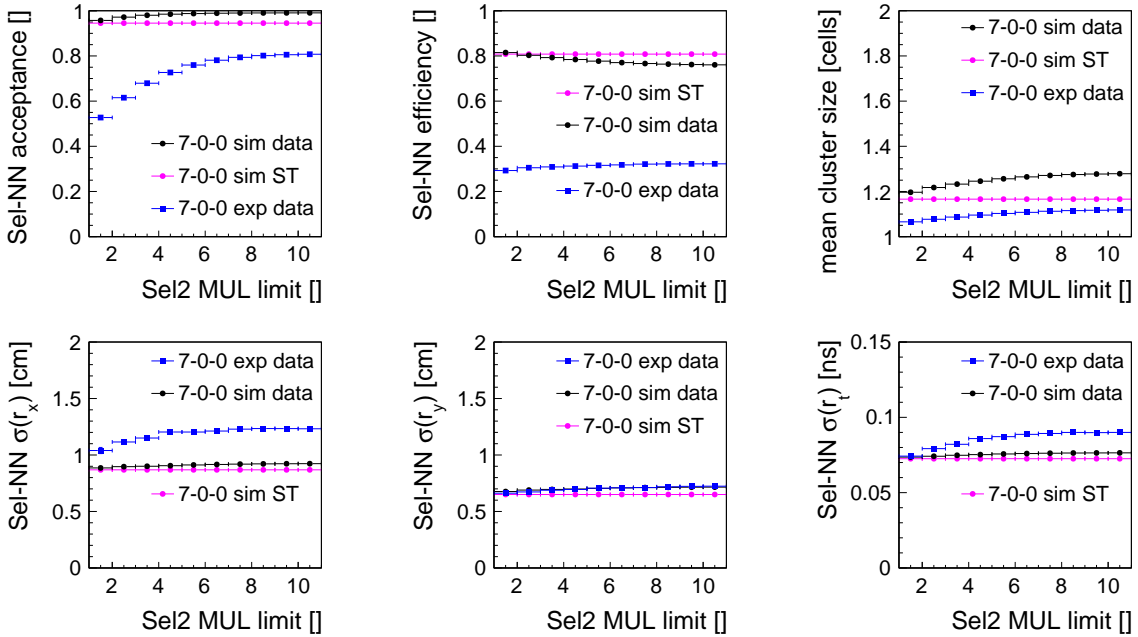


Figure 5.10: Scan of response observables for counter 7-0-0 as a function of a Sel2 multiplicity limit in experimental data (blue markers), simulated heavy-ion reaction data (black markers), and simulated single-track (ST) muon data (magenta markers). A discussion of the observed trends in Sel-NN acceptance (upper left plot), efficiency (upper middle plot), mean cluster size (upper right plot), global  $x$ -residual sigma (lower left plot), global  $y$ -residual sigma (lower middle plot), and time-residual sigma (lower right plot) is provided in the text.

In simulations, the share of true assignments between clusters on selector counters or on DUT and Sel1, respectively, can be expressed by a matching purity which is derived from information on Monte Carlo tracks participating in the formation of a cluster, provided in dedicated backlink objects. The method is explained and examples are given in Fig. 5.11. Compared to the unfiltered map of particles and underlying creation processes in the target volume which geometrically traverse all four counters in line (cf. Fig. 3.8), primary charged pions are identified as  $\chi^2$ -selector particles in pure cluster matches be-

tween Sel2 and Sel1 more frequently, their relative share increasing from 52% to 68%. At the same time, clusters created by electron–positron or proton tracks are selected less often due to trajectory deflections in the setup by multiple scattering in the former case and the comparatively low velocity of protons in the latter. The chance to trigger a clean detector response in accordance with the Sel  $\chi^2$ -criterion is highest for the earliest hits on counters in an event which are attributed to fast pions. As a function of multiplicity limit on counter Sel2, the high selector purity obtained with the default Sel  $\chi^2$ -cut (2.5) in a simulated collision scenario minimally decreases. The same applies to the Sel-NN purity—a pure Sel match provided—if counter 9-0-0 serves as detector under test. Owing to the reduced detection efficiency which a common-glass parametrization yields at the considered particle fluxes, the Sel-NN acceptance grows with more challenging multi-hit conditions (cf. Fig. 5.10) at the cost of increasingly impure cluster matches between counter 7-0-0 and selectors.

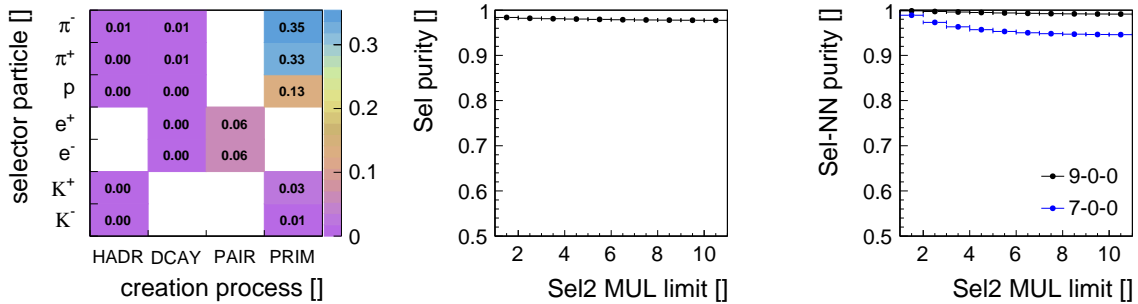


Figure 5.11: Considerations on matching purity between clusters on selector counters Sel2 and Sel1 and between the selector cluster pair and the NN cluster on DUT. If a physical Monte Carlo track (detector noise excluded) contributes to selector-cluster formation both on Sel2 and on Sel1, the selector cluster pair is considered a pure match. Creation processes of such selector particles in the high-multiplicity case of  $MUL(\text{Sel2}) \leq 10$ —here additionally constrained by requesting a track origin in the target volume (no requirement for matching purity)—are depicted in the left plot (normalized contributions up to a limit of 0.5% are not shown; cf. Fig. 3.8). If one of potentially several interfering Monte Carlo tracks contributing to both selector clusters also participates in the formation of the NN cluster on DUT, the NN matching between selector counters and DUT is considered pure as well. The dependence of selector purity (middle plot) and the dependence of DUT-matching purity (right plot) on a Sel2 multiplicity limit demonstrate higher probabilities for a mismatch the more tracks irradiate the setup simultaneously, assessed with cluster multiplicity. This effect is more pronounced for counter 7-0-0 (blue markers) which features an intrinsic inefficiency at fluxes under consideration due to its construction with common glass plates.

It should be noted that a separate alignment of residual peaks and an independent estimation of Sel and Sel-NN  $\chi^2$ -weights were conducted for every data point obtained under a different multiplicity cut in a given experimental/simulated scenario.

### 5.3 Rate effects under continuous irradiation

The detector response function of an MRPC degrades with irradiation time depending on the rate at which the electric field locally breaks down due to avalanche formation triggered by incident charged particles and on the rate at which avalanche charges accumulating on opposing glass plates dissipate (cf. Sec. 2.4.2). The latter mechanism of local field recovery via compensation currents through the external high-voltage supply occurs on a relaxation time scale  $\tau_{\text{MRPC}}$  which is characteristic of the glass plates that a counter is equipped with, varying with resistivity. Thus, the response behavior of a common-glass detector with typical recovery times of the order of seconds is expected to show a measurable degradation effect already at relatively low fluxes on the counter surface of about  $1 \text{ kHz/cm}^2$  (cf. Fig. 4.12 for a simulated projection). In fact, time averages of response observables studied under different multi-hit conditions in Sec. 5.2 indicate a significant performance drop of counter 7-0-0 in experimental results from CERN/SPS at these fluxes, exceeding quantitative expectations from simulations by far. This discrepancy is primarily attributed to the spike in beam intensity preceding accelerator spills (cf. Fig. 3.5) which causes the response function to severely deteriorate prior to recording data from the subsequent quasi-trapezoidal spill structure, under biased initial conditions. Utilizing the absence of detector noise in the diamond positioned in beam ahead of the target, alternating periods of beam on target and breaks between spills in an accelerator cycle can be easily identified. The distance of the current mean event time, obtained by averaging over reconstructed clusters on all counters, with respect to the start time of the ongoing spill, which is reset if the gap to the previous event exceeds an adjustable interval, is considered the time in spill. Regarding response observables as a function of this quantity allows for a differential examination of performance degradation in time. In the following, it is assumed that the two selector counters designed and modeled with low-resistive glass do not exhibit rate effects at the moderate particle fluxes under consideration. Concerning the necessary centering of residual distributions about zero for the  $\chi^2$ -matching method to be applicable and the estimation of  $\chi^2$ -weights in the three response dimensions, readjustments need to be executed if the response function varies with increasing time in spill. In the case of common glass, this is actually required and done for simulated data but refrained from in the analysis of the experimental sample due to statistical constraints. For the latter reason, an open multiplicity cut is used throughout this section.

The share of selector events in which any cluster is found on the detector under test, i.e. the Sel-NN acceptance, is presented in Fig. 5.12, contrasting real and virtual prototypes built with both types of glass, low-resistive (9-0-0) and common (7-0-0). Data points in single TIS (time in spill) bins are derived from averages over multiple spills. Owing to random cluster matches between a partially inefficient DUT and the Sel1 counter in a multi-hit environment (cf. Sec. 5.2), the obtained numbers are relatively high, also for common glass where clear trends are visible indicating a decreasing availability of matching candidates on the DUT surface as time in spill progresses. Given that average track multiplicities on counters per collision event are not subject to change during spill, the effect can be attributed to an increasing detection inefficiency of the common-glass

counter. The discrepancy between simulated collision and single-muon results visualizes the impact of Sel-NN mismatches on acceptance. The growth of measured common-glass acceptance within the first two seconds of the spill might reflect a transient recovery of the response function in the aftermath of the spike while the beam intensity rises to plateau level. Later in spill, an equilibrium between E-field breakdown and recovery seems to be reached which is not observed in simulated data. Due to intensity variations in spill at CERN/SPS (cf. Fig. 3.6), however, this difference in behavior must not necessarily be caused by deviating relaxation time constants.

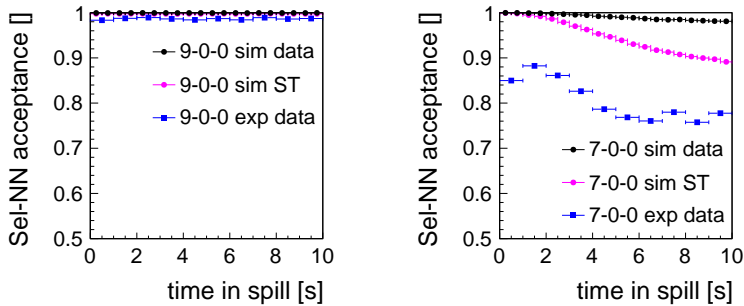


Figure 5.12: Nearest-neighbor (NN) acceptance of clusters on 9-0-0 (left plot) and 7-0-0 (right plot) with respect to the selector prediction as a function of event time in spill—an average over all associated cluster times—in experimental data (blue markers), simulated heavy-ion reaction data (black markers), and simulated single-track (ST) muon data (magenta markers) with an open  $MUL(\text{Sel}2) \leq 10$  cut. The common-glass architecture (right plot) is clearly susceptible to the incoming particle flux.

In Fig. 5.13, several response observables of the low-resistive-glass counter under test are shown in the course of an accelerator spill. Apart from minor (statistical) fluctuations which are present also in the simulated scenarios, no systematic tendencies as a function of time in spill can be recognized in real data. For this type of glass, a stable behavior is expected. Referring to Fig. 5.9 and subsequent discussions where time averages under the given multiplicity limit of  $MUL(\text{Sel}2) \leq 10$  are depicted, the deviations between collision and single-track simulations are due to response interference in the former case. Considering experimental results, the counter performance evaluated in the present multi-hit situation improves—in comparison with simulations—even more towards stricter cuts on Sel2 multiplicity. The offset between simulated and experimental  $x$ -residual widths originates from a limitation of the response model (cf. Sec. 4.1.2). Concerning  $\chi^2$ -efficiency and mean cluster size, parameters for virtual counter geometries were adjusted to comply with default constraints not tailored to the specific behavior of individual prototypes (cf. Tab. 4.1). However, the latter could be achieved in another iteration of response modeling and data analysis.

With the common-glass counter as detector under test, noticeable rate effects are obtained both in experimental and in simulated data (cf. Fig. 5.14). Corresponding trends which cannot be traced back to statistical fluctuations alone exist for all response observ-

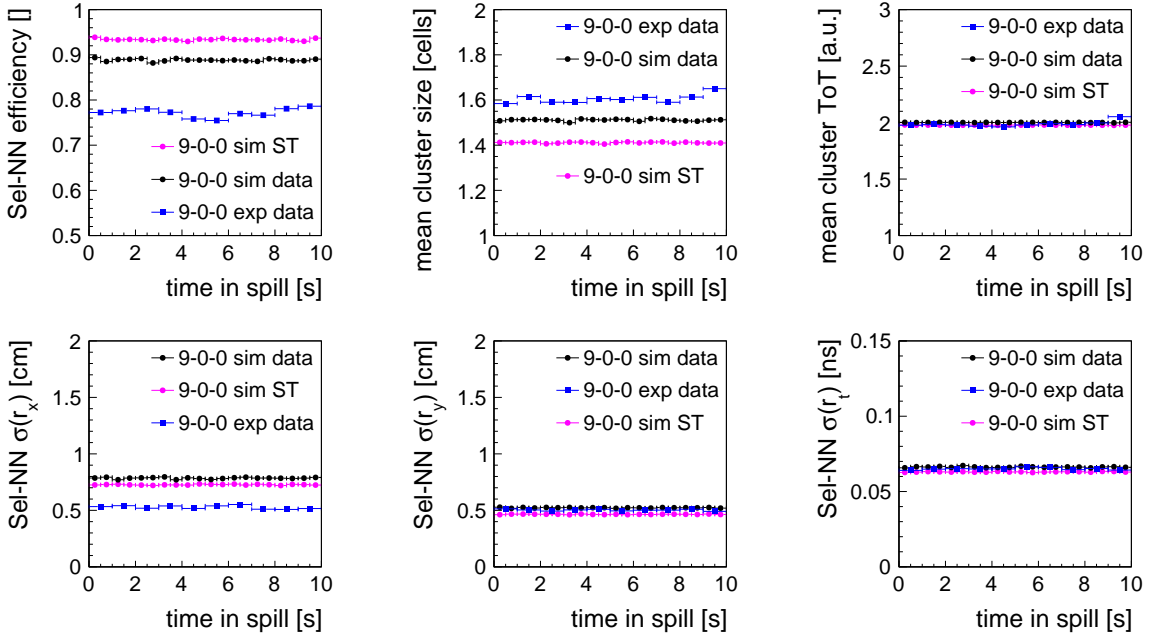


Figure 5.13: Time-in-spill (TIS) dependencies for counter 9-0-0 of extrapolated DUT efficiency (upper left plot), mean cluster size (upper middle plot), average ToT of cluster digis (upper right plot), residual sigma in  $x$  (lower left plot), residual sigma in  $y$  (lower middle plot), and residual sigma in  $t$  (lower right plot) in experimental data (blue markers), simulated heavy-ion reaction data (black markers), and simulated single-track (ST) muon data (magenta markers) with an open MUL(Sel2)  $\leq 10$  cut. Due to statistical constraints, a TIS binning of 1 s is used for experimental data while bins for simulated data cover TIS intervals of 0.5 s.

ables and are first experimental signs of an in-spill performance degradation measured with heavy-ion collision secondaries. The convergence of simulated  $\chi^2$ -efficiency curves with progressing time in spill originates from the widening of residual distributions as a consequence of decreasing signal amplitudes and increasing discrimination jitter which reduces the impact of signal interference on already larger residual tails. Thus, the multi-track scenario approaches the single-track case in this respect. In view of the other observables, the discrepancy between simulation results under different multi-hit conditions (cf. Fig. 5.10) persists and a parallel deterioration of detector performance occurs in time owing to an active particle memory which records a growing number of tracks in spill, leading to smaller values sampled from the induced charge spectrum (cf. Sec. 4.2). Regarding mean time over threshold, differences in raw-data calibration between experimental and simulated data become visible, the former being corrected on time average and the latter being aligned during memoryless parameter adjustment with a single-track irradiation of the counter surface, i.e. for TIS = 0 in the present case. The trend in experimental and simulated mean cluster ToT indicates diminishing signal amplitudes on counter 7-0-0 and is reflected by corresponding tendencies in timing-residual

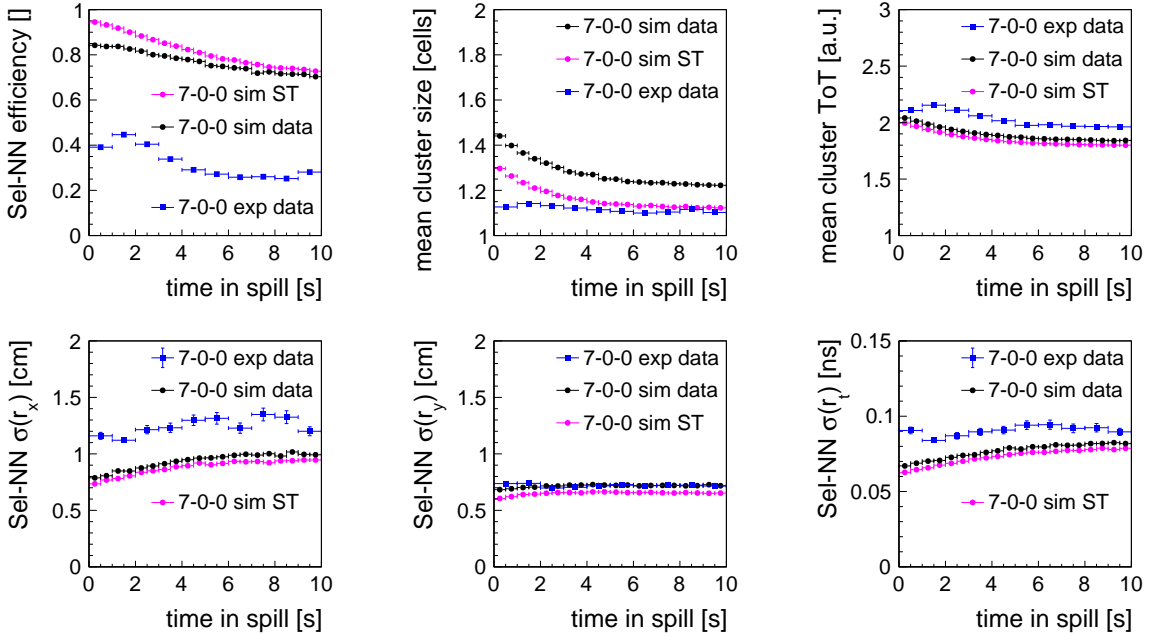


Figure 5.14: Time-in-spill (TIS) dependencies for counter 7-0-0 of extrapolated DUT efficiency (upper left plot), mean cluster size (upper middle plot), average ToT of cluster digis (upper right plot), residual sigma in  $x$  (lower left plot), residual sigma in  $y$  (lower middle plot), and residual sigma in  $t$  (lower right plot) in experimental data (blue markers), simulated heavy-ion reaction data (black markers), and simulated single-track (ST) muon data (magenta markers) with an open MUL(Sel2)  $\leq 10$  cut. Due to statistical constraints, a TIS binning of 1 s is used for experimental data while bins for simulated data cover TIS intervals of 0.5 s. A calibration of TIS-dependent Sel-NN  $\chi^2$ -weights is performed individually for each simulated bin but refrained from in the experimental case for statistical reasons.

widths of global  $r_x$  (into which local  $y$ -information enters) and  $r_t$ .

As stated before, the performance of the real prototype at CERN/SPS is found to be much worse than anticipated. In addition to a challenging spill structure, the observed signal-reflection peaks in residuals (cf. Fig. 5.8) suggest issues in the counter design, concerning the impedance matching between readout cells and front-end electronics in particular. The production architecture of common-glass counter MRPC3b [92] at the periphery of the CBM TOF wall (cf. Tab. 2.1) does not comprise a large cell width of 17 mm. Since the applicability of the response model developed in this work is constrained to an efficiency range of  $\varepsilon > 50\%$  (cf. Sec. 4.2), the comparatively poor results measured with counter 7-0-0 cannot be reproduced quantitatively. However, in a running physics experiment—in contrast to a prototype test beam—normally no MRPCs are deployed which fall below this efficiency threshold.

## 5.4 Perspectives with the mCBM experiment at GSI/SIS18

Within the scope of the intermediary FAIR Phase-0 research program towards completion of the FAIR facility in 2025, a miniature version of the future CBM setup is in operation at GSI/SIS18 since November 2018 with a dedicated physics program. Primarily, the so-called mCBM experiment [35] serves as a stationary assembly and testing site for the final configuration of the free-streaming readout concept of CBM (cf. Sec. 2.2), both in hardware concerning the transport of time-synchronized data from different subsystems to a computing farm and in software regarding the execution of efficient algorithms for online reconstruction and event selection on the latter (cf. Sec. 2.3). Efforts will culminate in a series of benchmark runs at CBM design interaction rates of 10 MHz on  $\Lambda$ -hyperon reconstruction via the decay channel  $\Lambda \rightarrow p\pi^-$  in fixed-target Ni + Ni and Au + Au collisions at  $T_{\text{lab}} = 1.93$  A GeV and 1.24 A GeV, respectively, in 2022. Along the way, pending questions on detector design, rate capability, hit matching between stations, etc. can be addressed, under conditions which are close to the final SIS100 scenario. During commissioning with  $\text{Ag}^{45+}$  ions impinging on a gold target at 1.58 A GeV beam kinetic energy in March 2019, beam intensities of up to  $10^8$  Hz were achieved in accelerator spills with a length of about 5 s, translating into particle fluxes of up to  $20 \text{ kHz/cm}^2$  on the mTOF subsystem which comprises a total of 25 MRPC3a counters, by default, and some additional prototypes (cf. Fig. 5.15). Similar conditions were available in a subsequent campaign with  $\text{Au}^{69+}$  projectiles in May 2020 and are expected to prevail also in 2021 during envisaged high-rate detector tests and commissioning of the concluding benchmark runs.

The systematic investigation of rate and multi-hit effects which the detector response model developed in this work allows for suggests applying the digitization code to simulations of the mCBM setup. The entire code is publicly available in an Apache Subversion repository [120] and requires reintegration into the main development line of CbmRoot which is primarily a matter of adapting it to modified interfaces. Due to nearly identical designs of the readout cells in MRPC3a/MRPC3b counters and in the modeled prototype 3-0-0, the set of parameter values determined for the latter under default response constraints can be directly used as a starting point for parametrizing the detector response function of mTOF counters. Studying the impact of signal interference on matching quality between counters in different mTOF modules positioned behind one another or between extrapolated target tracks reconstructed by subsystems mSTS, mMUCH, and mTRD in front and mTOF clusters is feasible without making modifications to the digitization algorithm. Regarding response deterioration by exposing a counter to sustained irradiation, the current strategy of an unsegmented particle memory retaining information on all simulated tracks which traverse the active area in a given period of measurement, e.g. an accelerator spill, can cope with particle fluxes on MRPC3a/MRPC3b counters of up to  $20 \text{ kHz/cm}^2$  for a maximum of 2 s, requiring 7 days of run time on the Kronos computing cluster at GSI (cf. Tab. 4.3). Here, the computational limit of the approach is reached owing to the inherent quadratic time complexity which outbalances any performance gain by further code optimization. Concerning a joint high-rate simulation comprising all mCBM subsystems, mTOF can—for

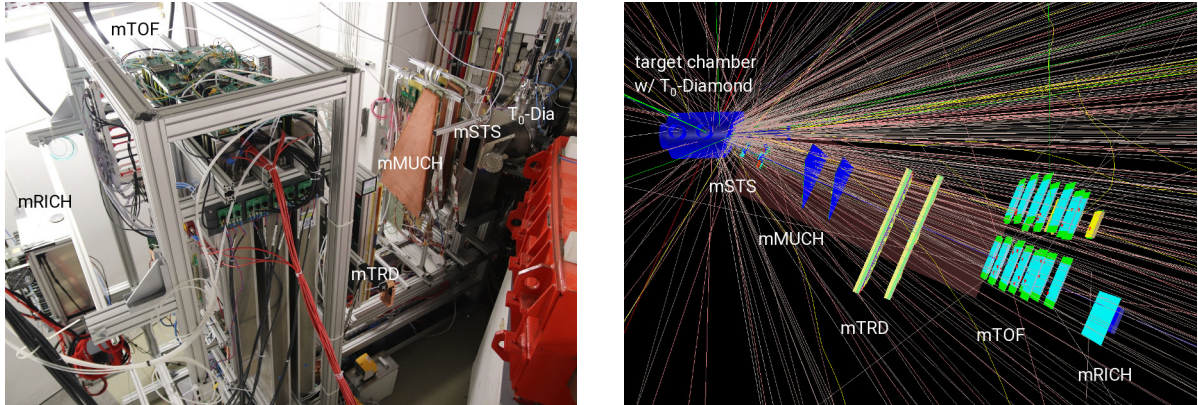


Figure 5.15: The setup of the mCBM experiment located in the HTD area of the SIS18 target hall at GSI as of March 2019 (left image), comprising—from right to left (downstream perspective)—a target chamber with a diamond detector for  $T_0$ -determination and a gold target ladder, a box with four silicon microstrip sensors mounted on carbon ladders (mSTS), two GEM (gas electron multiplier) modules of trapezoidal shape (mMUCH), two assemblies of a MWPC (multi-wire proportional chamber) with a radiator in front (mTRD), five modules (of which two and three, respectively, are positioned behind each other) containing five MRPC3a (cf. Tab. 2.1) counters each (mTOF), and a gas box with an aerogel radiator for producing Cherenkov rings on an array of multi-anode PMTs (mRICH). Some additional test modules, among them an aluminum box with two MRPC3b counters inside, equipped with common glass in contrast to MRPC3a, are included in the mTOF setup, positioned behind the left—looking downstream—double-module branch. TGeo visualization using UrQMD and GEANT 3 [119] input of an  $\text{Ag}^{45+}$  ion centrally hitting a gold nucleus in the mCBM target at 1.58 A GeV beam kinetic energy (right image). Photograph by courtesy of C. Sturm and simulation snapshot by courtesy of D. Emschermann.

the moment—be included only if the handling of rate effects is disabled, unless a significantly faster ansatz is implemented. However, distortions of response residuals due to interference are the more challenging issue to address at mCBM, for low-resistive-glass counters at least, as they necessitate a more sophisticated matching procedure to be applied in the absence of perfectly Gaussian residual shapes than a simple  $\chi^2$ -formalism. Consistently adhering to the latter method would result in renouncing a sizable amount of (true) hit-matching candidates on MRPCs which is demonstrated in Secs. 5.2 and 5.3. Aside from that, the non-ideal digital detector messages produced by the presented response model, featuring misaligned time and time-over-threshold information including a time-walk effect, can provide valuable input for testing calibration routines of raw data recorded at mCBM.

In view of the two additional common-glass counters (MRPC3b) in the mTOF setup, more reliable reference values could be obtained at lower interaction rates for the parametrization of counters with large relaxation time constants, considering the limited quality

of data measured with prototype 7-0-0 at CERN/SPS. In contrast to delicate experimental conditions at the latter accelerator in March 2015, spill structures at GSI/SIS18 during commissioning of mCBM were found to be free of intensity spikes and other confounding factors which would bias the performance evaluation of these counters.



## CHAPTER 6

### SUMMARY

Multi-gap resistive plate chambers (MRPCs) are a cost-effective solution for large-area time-of-flight (TOF) measurements in modern nuclear and particle physics experiments, combining excellent timing performance with a high detection efficiency. The 120 m<sup>2</sup> TOF wall to be constructed for the Compressed Baryonic Matter (CBM) experiment at the future FAIR facility is composed of more than 1000 single MRPC detectors varying in size and in design, depending on anticipated particle fluxes at the respective counter location. Experimental conditions in the fixed-target setup of CBM are extreme, given the unprecedented beam–target interaction rate of 10 MHz for studying rare probes in gold-on-gold collisions at beam kinetic energies of up to 11 A GeV which corresponds to the upper limit of the available SIS100 energy range for these projectiles. Closer to the beam axis, counters are exposed to higher fluxes, approaching 25 kHz/cm<sup>2</sup>, and track densities than at the periphery of the wall which is reflected by a lower resistivity  $\rho$  of the eponymous glass plates and a finer granularity of readout cells. Local breakdowns of the electric field in the gas gaps upon avalanche formation by traversing charged particles deteriorate the detector response function and are recovered on a relaxation time scale proportional to  $\rho$ . Smaller readout cells reduce the probability for signals induced by several incident tracks to interfere and generate a distorted counter response which complicates cluster matching between different stations in a tracking setup. The double burden of rate and multi-hit effects on counter performance and on its evaluation in a heavy-ion-collision scenario with high average multiplicities of reaction secondaries was systematically investigated both in experimental and in simulated data for the first time in this work.

#### **Data acquisition/calibration and Monte Carlo studies for test beams**

Two MRPC prototypes for the outer TOF wall, the former equipped with low-resistive glass and the latter built with common glass to study differences in response behavior, were tested at CERN/SPS in March 2015 with collision products of a 19 A GeV/c argon beam impinging on a lead target. According to a detailed Monte Carlo estimate based on rates measured with plastic scintillators, mean particle fluxes on the counter surfaces amounted to 1.5 and 1.3 kHz/cm<sup>2</sup>, respectively, while 3.5 and 3.9 external tracks—on average—passed through the active detection volumes in collision events selected by coincident hits in a pair of reference counters. These conditions are ideal for the purpose of this work, allowing for both rate and multi-hit aspects to be studied in a scenario which does not overstrain a common-glass detector in terms of irradiation. The data acquisition (DAQ) system based on a network of time-to-digital converters (TDCs) implemented on field-programmable gate arrays (FPGAs) which organized the readout of 512 electronics channels in the setup was configured and successfully operated as part

of this thesis project. In a reduced version, it is still in use for quality control (QC) of mass-produced final counter designs with cosmic rays, as are associated algorithms for calibrating and synchronizing TDC raw data. Regarding the free-streaming readout concept of CBM which comprises a self-triggered transport of detector raw data from the front-end electronics to a computing farm for online event reconstruction and selection, not involving a central controller or a hardware trigger derived from coincidences of detector signals, a dual readout strategy was embarked on. In addition to a conventional operation of the TrbNet communication protocol between a Central Trigger System and TDC nodes with the mentioned physics trigger, a continuous readout of front-end buffers, i.e. a free-streaming mockup, was realized by arranging data transport with a periodical pulser signal. Thus, samples of time-sorted detector messages could be recorded lacking association with a physical event to be retrieved in software by identifying accumulations of raw data in time. Results obtained for these data sets closely resemble the output of hardware-triggered runs which—for statistical reasons—were considered for comparison with simulated data. However, the handling of mockup data provided valuable guidance for the subsequent development of time-based algorithms.

### **Time-based response simulations featuring rate and multi-hit effects**

To understand experimental observations concerning detector behavior under rate and multi-hit load, a reproduction of corresponding effects in simulations is required. Prior to the present work, this functionality did not exist. The transition of the digitization software for the TOF subsystem within the CbmRoot framework from an event-based approach treating single collisions as isolated entities to a time-based scenario allowing for a continuing impact of occurrences on counters across event borders was accompanied by the introduction of a novel parametrization for the detector response function of MRPCs. The latter can be regarded the main focus of this work. Starting from a set of functions with adjustable parameters to describe signal induction on readout cells and discrimination/digitization jitter in connected readout channels, a response model was developed which realistically reproduces measured distributions of observables like cluster size and time over threshold (ToT), generates non-ideal detector raw data (“digis”) with misaligned timing and ToT information, and intrinsically features an amplitude-dependent time-walk effect. Model parameters for individual counter geometries are determined by numerical minimization respecting a number of measured constraints. Degradation effects on counter performance are a direct consequence of the inherent possibility to downscale the induced charge spectrum which is the basis of response sampling for an incident particle. A smaller mean charge content of induced signals results in lower amplitudes which less frequently exceed discrimination threshold, reducing detection efficiency and mean cluster size, and which are subject to a larger discrimination uncertainty of leading and trailing edges, deteriorating the timing response. To mimic in software the local breakdown and recovery of the electric field in the gas gaps, i.e. the physical mechanism responsible for rate effects, it therefore seemed natural to introduce a dynamic scaling factor to the random variable representing total induced

charge, reflecting the impact of previous particles traversing the counter on the response function of the current one. Individual contributions of tracks stored in this particle memory to the charge coefficient calculated for the most recent passage through the active detector volume depend on dissipation of the originally induced charge given the elapsed simulation time and on spatial distance between hits on the counter surface. The influence of preceding tracks in time decreases exponentially on an adjustable relaxation time scale which is typical for the modeled prototype. For qualitative demonstration purposes, values of 100 ms for low-resistive-glass MRPCs and of 5 s for common-glass counters are used in simulations. Concerning interference of signals induced on the same readout cell by several tracks in a multi-hit environment, consecutive digital detector messages in an electronics channel are merged if ToT ranges—on the continuous simulation time axis—overlap, causing loss of timing, i.e. leading-edge information of the subsequent digi and compromising the correction of time walk in the remaining time stamp due to an artificially increased ToT measurement. The latter digi might also be dropped completely if ToT intervals are detached but the TDC channel is still busy with processing the former object within an adjustable dead time. Residual distributions in the two spatial ( $x$  and  $y$ ) and the temporal ( $t$ ) response dimensions are distorted accordingly, deviating significantly from the ideal reference of a Gaussian shape. This complicates the matching of correlated response clusters on different counters which measure traversals of the same particle because the chi-square matching method, for instance, assumes residuals to be normally distributed.

Owing to the quadratic time complexity of the memory algorithm which repeatedly sums up the respective impact of previously digitized tracks on the current response-sampling process, the multithreaded and parallel computing infrastructure provided by the Kronos cluster at GSI was exploited to reduce execution times of full-featured test-beam simulations including rate effects to a manageable level. Within a contiguous memory period which is determined by the length of an accelerator spill (about 10 s during the campaign at CERN/SPS), the summation load is shared among a configurable number of threads assigned to computing in parallel partial sums which form the final memory coefficient. Assuming the break between subsequent spills to be sufficiently long for a complete recovery of the detector response function, multiple spills are simulated on different computing nodes simultaneously. Due to the dramatic gain in performance achieved with these measures, a maximum capacity of 30 million memory entries, considering a one-week run-time limitation for jobs on Kronos, allows for a sustained ten-second irradiation of a single large-area MRPC prototype with particle fluxes of up to  $3.5 \text{ kHz/cm}^2$ . In simulated heavy-ion collisions in contrast to an illumination scenario with single muons, however, the limit is slightly more restrictive owing to the creation of secondary tracks in the material budget of detectors which are stored in the memory in addition to external tracks that are counted towards rate. Regarding the moderate particle fluxes counters were exposed to at CERN/SPS, a reproduction of test-beam conditions in response simulations is technically feasible, unlike an extrapolation to the entire TOF wall in high-rate simulations of the full CBM setup at nominal irradiation constraints. For the latter, a segmentation of the counter surface into small independent memory cells could be an option if edge effects are properly handled.

## New insights gained from a comparative chi-square analysis

Experimental and simulated results obtained for both types of MRPCs under test, a low-resistive- and a common-glass prototype, were compared in a final analysis based on a  $\chi^2$ -formalism for event selection and matching of correlations on adjacent counters. Real data had already been associated with events by a physics-triggered data acquisition and simulated digis residing in timeslice containers of fixed length were grouped into events utilizing backlink information on original event affiliations. For performance evaluation, a subset of events with clean matching conditions is chosen, enforced by a  $\chi^2$ -cut of 2.5 on weighted response residuals in time and space between clusters on two selector counters, one of them positioned in front of and the other one installed behind detectors under test (DUT). The response cluster on the rear counter which yields the best selector match in a given event, identified by the lowest  $\chi^2$ -value, provides an interpolated reference measurement for the respective DUT. Here, an additional sorting of residual chi-squares in ascending order determines the nearest-neighbor (NN) cluster match—in position and time—between DUT and reference counter. Resolutions in  $x$ ,  $y$ , and  $t$  are derived from Gaussian peak fits to NN residual distributions while the detection efficiency is extrapolated from the integral share of the corresponding  $\chi^2$ -distribution at a limit of 5.0. The applied chi-square matching method does not allow for a comprehensive description of counter performance as residuals in the three response dimensions intrinsically differ from normal distributions particularly in the tails and deviations increase in a multi-hit environment due to signal interference. However, the method proved useful to monitor variations in detector behavior which were studied systematically as functions of both hit multiplicity in the setup and irradiation time in spill.

Concerning the real prototype equipped with low-resistive glass, the  $\chi^2$ -efficiency is found to improve by more than 7% in absolute numbers from an estimate of 77.2% without any cut on multiplicity to a value of 84.5% if only a single cluster is generated on the first selector counter in the respective event. In the same time, the general availability of any cluster on the DUT, i.e. the NN acceptance, decreases from 98.6% to 94.4% of selector events. This numerical example of a counter which did not generate a (recorded) response for every incident particle is illustrative for the growing impact of mismatches and residual distortions—due to interfering signals—on the detector response function under increasing multi-hit conditions. The remaining discrepancy between acceptance and  $\chi^2$ -efficiency at the strictest multiplicity cut indicates the limited applicability of a rigorous chi-square formalism to cluster matching between MRPCs. Within this work, light was shed on this difficulty for the first time in a methodical way. Analogous trends, albeit less pronounced, are observed for position and time resolutions owing to narrowing residual centers in the absence of the former influences. Even without restricting the analyzed event sample to cases of low hit multiplicities, Gaussian residual peak widths of 0.5 cm in  $x$  and  $y$  and of 65 ps in  $t$  are achieved with this detector, still including a contribution from the reference counter. Hence, compliance with the required system time resolution of 80 ps for CBM TOF is given.

With progressing time in spill, response observables evaluated for this prototype do not show any sign of deterioration, as expected for low-resistive glass under these moderate

particle fluxes. Experimental results for the common-glass detector, in contrast, clearly reflect a susceptibility of the counter design to rate effects at fluxes around  $1 \text{ kHz/cm}^2$ , comprising—besides efficiency—mean cluster size, mean time over threshold, and resolutions. These findings are the first evidence of in-spill response degradation of an MRPC observed in a heavy-ion-collision scenario. However, a time average obtained for the  $\chi^2$ -efficiency of only 32.2% implies biased starting conditions for performance evaluation caused by a spike in beam intensity which preceded every spill at CERN/SPS. Consequently, the detector is relatively prone to NN mismatches, given the large active area as compared to the selection zone, which add significant background to residual distributions and broaden residual peaks. The resulting poor resolutions without a cut on multiplicity considerably improve towards a single-cluster constraint.

Qualitatively, the behavior of both real prototypes was reproduced with the response model developed in this work, using different relaxation parameters for the two types of glass in a pioneering rate simulation of a full test-beam setup. Known limitations exist concerning the overlarge width of local  $y$ -residuals in simulations and a restriction to the efficiency range  $\varepsilon > 50\%$  below which counterintuitive trend reversals occur in virtual response observables. A quantitative agreement as such with individual results obtained for detectors under test at CERN/SPS was not primarily aimed at when adjusting model parameters for various counter geometries with an identical set of minimization constraints. However, it can be achieved upon redetermination of parameter values according to a particular case.

## Outlook

The interplay of rate and multi-hit effects on MRPC performance in high-intensity heavy-ion-collision experiments is a pending problem to be addressed by the CBM-TOF working group in the years ahead towards completion of the FAIR facility in 2025. This work represents a first systematic investigation of the consequences of corresponding experimental conditions for the detector response function and for hit matching between counters. An application and further development of the implemented digitization software featuring a parametrization of both degradation aspects at the running mCBM experiment is intended. Pursuing an inadequate  $\chi^2$ -matching strategy in view of response residuals which increasingly deviate from normal distributions the more likely induced signals are to interfere on a readout cell is a source of efficiency loss and requires remedial action. This refinement process of matching methods needs to be accompanied by simulations which reproduce observed behavior and provide information on matching purity. The presented response model is a suitable tool for this task.



## APPENDICES



**APPENDIX A**  
**CURRICULUM VITAE**

**Personal Information**

Name	Christian Helmut Simon
Gender	male
Date of birth	15/08/1987
Place of birth	Wiesbaden, Germany
Marital status	single
Citizenship	German

**Education**

03/2012 – present	Doctoral studies in physics at Heidelberg University, Germany
09/2011 – 02/2012	Master studies in physics at Heidelberg University, Germany
08/2011	Master of Science in physics
08/2010 – 08/2011	Master studies in physics at Michigan State University, USA
07/2010	Bachelor of Science in physics
09/2007 – 07/2010	Bachelor studies in physics at Heidelberg University, Germany
06/2007	Allgemeine Hochschulreife (general university entrance qualification)
09/1998 – 06/2007	Fürst-Johann-Ludwig-Schule in Hadamar, Germany (gymnasium)
08/1994 – 07/1998	Primary school in Dornburg-Thalheim, Germany

**Scholarships**

04/2012 – 12/2015	Helmholtz Graduate School for Hadron and Ion Research (HGS-HIRe for FAIR)
10/2007 – 03/2012	Studienstiftung des deutschen Volkes (German Academic Scholarship Foundation)

Heidelberg, November 30, 2020



## APPENDIX B

### LIST OF PUBLICATIONS

#### Refereed Journal Papers

M. Petriş, D. Bartoş, M. Petrovici, L. Rădulescu, V. Simion, J. Frühauf, M. Kiš, P.-A. Loizeau, I. Deppner, N. Herrmann, and C. Simon, “Performance of a two-dimensional position sensitive MRPC prototype with adjustable transmission line impedance,” *Nucl. Instrum. Meth. A* **920**, 100 (2019).

T. Ablyazimov *et al.* (CBM Collaboration), “Challenges in QCD matter physics – The scientific programme of the Compressed Baryonic Matter experiment at FAIR,” *Eur. Phys. J. A* **53**, 60 (2017), [arXiv:1607.01487 \[nucl-ex\]](#).

C. H. Simon and P. Danielewicz, “Interplay of anisotropies of momentum distribution and mean field in heavy-ion collisions,” *Phys. Rev. C* **87**, 054619 (2013), [arXiv:1212.4460 \[nucl-th\]](#).

#### Refereed Conference Papers

P. Lyu, D. Han, Y. Wang, Q. Zhang, B. Guo, F. Wang, Y. Yu, X. Chen, Y. Li, N. Herrmann, I. Deppner, C. Simon, P. Weidenkaff, P.-A. Loizeau, and J. Frühauf, “Study on cosmic test and QC method of high-rate MRPC for CBM-TOF,” *Proceedings, 14th Workshop on Resistive Plate Chambers and Related Detectors (RPC2018): Puerto Vallarta, Jalisco state, Mexico, February 19–23, 2018*, *J. Instrum.* **14**, C09032 (2019).

M. Petriş, D. Bartoş, M. Petrovici, L. Rădulescu, V. Simion, J. Frühauf, P.-A. Loizeau, I. Deppner, N. Herrmann, and C. Simon, “Performance tests of the MSMGRPCs using a free-streaming readout,” *Proceedings, 39th International Conference on High Energy Physics (ICHEP2018): Seoul, Korea, July 4–11, 2018*, *Proc. Sci.* **340**, 663 (2019).

D. Hu, D. Sauter, X. Wang, Y. Sun, I. Deppner, N. Herrmann, C. Simon, Ph. Weidenkaff, J. Brandt, J. Zhou, M. Shao, C. Li, H. Chen, Z. Tang, Y. Zhang, E. Lavrik, and H. Zeng, “MRPC3b mass production for CBM-TOF and eTOF at STAR,” *Proceedings, 14th Workshop on Resistive Plate Chambers and Related Detectors (RPC2018): Puerto Vallarta, Jalisco state, Mexico, February 19–23, 2018*, *J. Instrum.* **14**, C06013 (2019), [arXiv:1807.02452 \[physics.ins-det\]](#).

M. Petriş, D. Bartoş, M. Petrovici, L. Rădulescu, V. Simion, I. Deppner, N. Herrmann, C. Simon, J. Frühauf, M. Kiš, and P.-A. Loizeau, “In-beam test of the RPC architecture foreseen to be used for the CBM-TOF inner wall,” *Proceedings, 22nd International School on Nuclear Physics, Neutron Physics and Applications: Varna, Bulgaria, September 10–16, 2017*, *J. Phys. Conf. Ser.* **1023**, 012007 (2018).

C. Simon, I. Deppner, and N. Herrmann (for the CBM Collaboration), “The physics program of the CBM experiment,” *Proceedings, 11th International Workshop on Critical*

*Point and Onset of Deconfinement (CPOD2017): Stony Brook, New York, USA, August 7–11, 2017*, *Proc. Sci.* **311**, 014 (2018).

P. Lyu, Y. Wang, B. Guo, D. Han, Y. Li, N. Herrmann, I. Deppner, C. Simon, P. Weidenkaff, F. Jochen, P.-A. Loizeau, and M. Laden Kis, “Development and performance of self-sealed MRPC,” *Proceedings, 14th Topical Seminar on Innovative Particle and Radiation Detectors (IPRD16): Siena, Italy, October 3–6, 2016*, *J. Instrum.* **12**, C03055 (2017).

Y. Wang, X. J. Huang, P. F. Lyu, D. Han, B. Xie, Y. J. Li, N. Herrmann, I. Deppner, P. Loizeau, C. Simon, J. Frühauf, and M. Kiš, “A solution for the inner area of CBM-TOF with pad-MRPC,” *Proceedings, 14th Vienna Conference on Instrumentation (VCI 2016): Vienna, Austria, February 15–19, 2016*, *Nucl. Instrum. Meth. A* **845**, 318 (2017).

I. Deppner, N. Herrmann, J. Frühauf, M. Kiš, P. Lyu, P.-A. Loizeau, L. Shi, C. Simon, Y. Wang, and B. Xie, “Performance studies of MRPC prototypes for CBM,” *Proceedings, 13th Workshop on Resistive Plate Chambers and Related Detectors (RPC2016): Ghent, Belgium, February 22–26, 2016*, *J. Instrum.* **11**, C10006 (2016), [arXiv:1606.04917 \[physics.ins-det\]](https://arxiv.org/abs/1606.04917).

M. Petriș, D. Bartoș, G. Caragheorgheopol, I. Deppner, J. Frühauf, N. Herrmann, M. Kiš, P.-A. Loizeau, M. Petrovici, L. Rădulescu, V. Simion, and C. Simon, “Time and position resolution of high granularity, high counting rate MRPC for the inner zone of the CBM-TOF wall,” *Proceedings, 13th Workshop on Resistive Plate Chambers and Related Detectors (RPC2016): Ghent, Belgium, February 22–26, 2016*, *J. Instrum.* **11**, C09009 (2016), [arXiv:1605.02558 \[physics.ins-det\]](https://arxiv.org/abs/1605.02558).

Y. Wang, P. Lyu, X. Huang, D. Han, B. Xie, Y. Li, N. Herrmann, I. Deppner, C. Simon, P.-A. Loizeau, P. Weidenkaff, J. Frühauf, and M. Laden Kis, “Development and test of a real-size MRPC for CBM-TOF,” *Proceedings, 13th Workshop on Resistive Plate Chambers and Related Detectors (RPC2016): Ghent, Belgium, February 22–26, 2016*, *J. Instrum.* **11**, C08007 (2016), [arXiv:1605.02395 \[physics.ins-det\]](https://arxiv.org/abs/1605.02395).

M. Petriș, D. Bartoș, G. Caragheorgheopol, F. Constantin, M. Petrovici, L. Rădulescu, V. Simion, I. Deppner, N. Herrmann, C. Simon, J. Frühauf, M. Kiš, and P.-A. Loizeau, “Prototype with the basic architecture for the CBM-TOF inner wall tested in close to real conditions,” *Proceedings, 21st International School on Nuclear Physics, Neutron Physics and Applications & International Symposium on Exotic Nuclei (ISEN-2015): Varna, Bulgaria, September 7–12, 2015*, *J. Phys. Conf. Ser.* **724**, 012037 (2016).

I. Deppner, N. Herrmann, A. Akindinov, D. Bartos, A. Balaceanu, S. Belogurov, P. Cao, G. Caragheorgheopol, H. Chen, J. Cheng, M. Ciobanu, F. Constantin, Z. Deng, H. Deppe, V. Duta, H. Fan, H. Flemming, J. Frühauf, J. Gebelein, K. Heidel, K. Hildenbrand, U. Keschull, M. Kiš, S. Kiselev, K. Koch, P. Koczon, R. Kotte, A. Laso Garcia, J. Lehrbach, C. Li, Y. Li, P.-A. Loizeau, P. Lv, D. Malkevich, S. Manz, L. Naumann, A. Nedosekin, W. Niebur, A. Oancea, M. Petris, M. Petrovici, V. Plotnikov, M. Prokudin, L. Radulescu, M. Shao, V. Simion, C. Simon, R. Sultanov, Y. Sun, Z. Tang,

Y. Wang, J. Wüstenfeld, C. Xiang, N. Xu, Y. Zhang, D. Zhou, and X. Zhu, “The CBM Time-of-Flight wall — a conceptual design,” *Proceedings, 12th Workshop on Resistive Plate Chambers and Related Detectors (RPC2014): Beijing, China, February 23–28, 2014*, *J. Instrum.* **9**, C10014 (2014).

C. Simon, I. Deppner, N. Herrmann, P.-A. Loizeau, and J. Frühauf, “Performance test of a fully differential float-glass multi-strip MRPC prototype for the CBM ToF wall with cosmic rays,” *Proceedings, 12th Workshop on Resistive Plate Chambers and Related Detectors (RPC2014): Beijing, China, February 23–28, 2014*, *J. Instrum.* **9**, C09028 (2014).

### **Master’s Thesis**

C. H. Simon, *Interplay of anisotropy of momentum distributions and mean fields in heavy-ion collisions*, Michigan State University, East Lansing, Michigan, USA (2011).

### **Bachelor’s Thesis**

C. Simon, *An acceptance study of charged  $K$  mesons in the SIS-100 energy range for the CBM ToF wall*, Heidelberg University, Heidelberg, Germany (2010).



## REFERENCES



## REFERENCES

- [1] S. Klimt, M. Lutz, and W. Weise, “Chiral phase transition in the SU(3) Nambu and Jona-Lasinio model,” *Phys. Lett. B* **249**, 386 (1990).
- [2] D. H. Rischke, “The quark–gluon plasma in equilibrium,” *Prog. Part. Nucl. Phys.* **52**, 197 (2004), [arXiv:nucl-th/0305030](#).
- [3] L. McLerran and R. D. Pisarski, “Phases of dense quarks at large  $N_c$ ,” *Nucl. Phys. A* **796**, 83 (2007), [arXiv:0706.2191 \[hep-ph\]](#).
- [4] M. G. Alford, A. Schmitt, K. Rajagopal, and T. Schäfer, “Color superconductivity in dense quark matter,” *Rev. Mod. Phys.* **80**, 1455 (2008), [arXiv:0709.4635 \[hep-ph\]](#).
- [5] K. Fukushima and T. Hatsuda, “The phase diagram of dense QCD,” *Rep. Prog. Phys.* **74**, 014001 (2011), [arXiv:1005.4814 \[hep-ph\]](#).
- [6] K. Aamodt *et al.* (ALICE Collaboration), “The ALICE experiment at the CERN LHC,” *J. Instrum.* **3**, S08002 (2008).
- [7] J. Adams *et al.* (STAR Collaboration), “Experimental and theoretical challenges in the search for the quark–gluon plasma: The STAR Collaboration’s critical assessment of the evidence from RHIC collisions,” *Nucl. Phys. A* **757**, 102 (2005), [arXiv:nucl-ex/0501009](#).
- [8] J. M. Lattimer and M. Prakash, “The Physics of Neutron Stars,” *Science* **304**, 536 (2004), [arXiv:astro-ph/0405262](#).
- [9] H. H. Gutbrod *et al.*, eds., *FAIR Baseline Technical Report* (GSI, Darmstadt, Germany, 2006).
- [10] CBM Collaboration, *Compressed Baryonic Matter Experiment — Technical Status Report* (GSI, Darmstadt, Germany, 2005).
- [11] P. Braun-Munzinger, K. Redlich, and J. Stachel, “Particle Production in Heavy Ion Collisions,” in *Quark–Gluon Plasma 3*, edited by R. C. Hwa and X.-N. Wang (World Scientific, Singapore, 2004) p. 491, [arXiv:nucl-th/0304013](#).
- [12] A. Andronic, P. Braun-Munzinger, and J. Stachel, “The horn, the hadron mass spectrum and the QCD phase diagram – the statistical model of hadron production in central nucleus-nucleus collisions,” *Proceedings, 10th International Conference on Nucleus-Nucleus Collisions (NN2009): Beijing, China, August 16–21, 2009*, *Nucl. Phys. A* **834**, 237c (2010), [arXiv:0911.4931 \[nucl-th\]](#).

- [13] F. Li, L.-W. Chen, C. M. Ko, and S. H. Lee, “Contributions of hyperon-hyperon scattering to subthreshold cascade production in heavy ion collisions,” *Phys. Rev. C* **85**, 064902 (2012), [arXiv:1204.1327 \[nucl-th\]](#).
- [14] G. Agakishiev *et al.* (HADES Collaboration), “Statistical hadronization model analysis of hadron yields in p + Nb and Ar + KCl at SIS18 energies,” *Eur. Phys. J. A* **52**, 178 (2016), [arXiv:1512.07070 \[nucl-ex\]](#).
- [15] S. Wheaton, J. Cleymans, and M. Hauer, “THERMUS—A thermal model package for ROOT,” *Comput. Phys. Commun.* **180**, 84 (2009), [arXiv:hep-ph/0407174](#).
- [16] C. Alt *et al.* (NA49 Collaboration), “Pion and kaon production in central Pb + Pb collisions at 20 A and 30 A GeV: Evidence for the onset of deconfinement,” *Phys. Rev. C* **77**, 024903 (2008), [arXiv:0710.0118 \[nucl-ex\]](#).
- [17] A. Palmese, W. Cassing, E. Seifert, T. Steinert, P. Moreau, and E. L. Bratkovskaya, “Chiral symmetry restoration in heavy-ion collisions at intermediate energies,” *Phys. Rev. C* **94**, 044912 (2016), [arXiv:1607.04073 \[nucl-th\]](#).
- [18] W. Cassing and E. L. Bratkovskaya, “Parton transport and hadronization from the dynamical quasiparticle point of view,” *Phys. Rev. C* **78**, 034919 (2008), [arXiv:0808.0022 \[hep-ph\]](#).
- [19] W. Cassing and E. L. Bratkovskaya, “Parton–hadron–string dynamics: An off-shell transport approach for relativistic energies,” *Nucl. Phys. A* **831**, 215 (2009), [arXiv:0907.5331 \[nucl-th\]](#).
- [20] C. Blume, “Energy dependence of hadronic observables,” *Proceedings, Workshop for Young Scientists on the Physics of Ultrarelativistic Nucleus–Nucleus Collisions (Hot Quarks 2004): Taos Valley, New Mexico, USA, July 18–24, 2004*, *J. Phys. G* **31**, S57 (2005).
- [21] C. Simon, I. Deppner, and N. Herrmann (for the CBM Collaboration), “The physics program of the CBM experiment,” *Proceedings, 11th International Workshop on Critical Point and Onset of Deconfinement (CPOD2017): Stony Brook, New York, USA, August 7–11, 2017*, *Proc. Sci.* **311**, 014 (2018).
- [22] V. Friese (for the CBM Collaboration), “Strangeness Prospects with the CBM Experiment,” *Proceedings, 15th International Conference on Strangeness in Quark Matter (SQM-2015): Dubna, Russia, July 6–11, 2015*, *J. Phys. Conf. Ser.* **668**, 012014 (2016).
- [23] V. Khachatryan *et al.* (CMS Collaboration), “Measurement of the transverse momentum spectrum of the Higgs boson produced in pp collisions at  $\sqrt{s} = 8$  TeV using  $H \rightarrow WW$  decays,” *J. High Energy Phys.* **03**, 032 (2017), [arXiv:1606.01522 \[hep-ex\]](#).

- [24] J. K. Ahn *et al.* (E373 (KEK-PS) Collaboration), “Double- $\Lambda$  hypernuclei observed in a hybrid emulsion experiment,” *Phys. Rev. C* **88**, 014003 (2013).
- [25] S.-I. Maeda, Y. Akaishi, and T. Yamazaki, “ $K^-K^-pp$  - an important gateway toward multi-kaonic nuclei,” *Proceedings, 12th International Conference on Hypernuclear and Strange Particle Physics (HYP2015): Sendai, Japan, September 7–12, 2015*, *JPS Conf. Proc.* **17**, 082007 (2017), [arXiv:1610.02150 \[nucl-ex\]](#).
- [26] T. Yamazaki, A. Dote, and Y. Akaishi, “Invariant-mass spectroscopy for condensed single- and double- $\bar{K}$  nuclear clusters to be formed as residues in relativistic heavy-ion collisions,” *Phys. Lett. B* **587**, 167 (2004), [arXiv:nucl-th/0310085](#).
- [27] A. Andronic, P. Braun-Munzinger, J. Stachel, and H. Stöcker, “Production of light nuclei, hypernuclei and their antiparticles in relativistic nuclear collisions,” *Phys. Lett. B* **697**, 203 (2011), [arXiv:1010.2995 \[nucl-th\]](#).
- [28] A. Andronic, P. Braun-Munzinger, and K. Redlich, “Statistical production of antikaon nuclear bound states in heavy ion collisions,” *Nucl. Phys. A* **765**, 211 (2006), [arXiv:nucl-th/0506083](#).
- [29] P. A. Zyla *et al.* (Particle Data Group), “Review of Particle Physics,” *Prog. Theor. Exp. Phys.* **2020**, 083C01 (2020).
- [30] I. Vassiliev, private communication (2017).
- [31] T. Ablyazimov *et al.* (CBM Collaboration), “Challenges in QCD matter physics – The scientific programme of the Compressed Baryonic Matter experiment at FAIR,” *Eur. Phys. J. A* **53**, 60 (2017), [arXiv:1607.01487 \[nucl-ex\]](#).
- [32] I. Deppner, private communication (2020).
- [33] I. Deppner *et al.*, “The CBM time-of-flight wall,” *Proceedings, 10th Workshop on Resistive Plate Chambers and Related Detectors (RPC2010): Darmstadt, Germany, February 9–12, 2010*, *Nucl. Instrum. Meth. A* **661**, S121 (2012).
- [34] C. Simon, I. Deppner, N. Herrmann, P.-A. Loizeau, and J. Frühauf, “Performance test of a fully differential float-glass multi-strip MRPC prototype for the CBM ToF wall with cosmic rays,” *Proceedings, 12th Workshop on Resistive Plate Chambers and Related Detectors (RPC2014): Beijing, China, February 23–28, 2014*, *J. Instrum.* **9**, C09028 (2014).
- [35] CBM Collaboration, *mCBM@SIS18 — A CBM full system test-setup for high-rate nucleus-nucleus collisions at GSI / FAIR* (GSI, Darmstadt, Germany, 2017).
- [36] B. Friman *et al.*, eds., *The CBM Physics Book*, Lect. Notes Phys. 814 (Springer, Berlin/Heidelberg, Germany, 2011).

- [37] P. Kurilkin *et al.*, “Superconducting dipole magnet for the CBM experiment at FAIR,” *Proceedings, 23rd International Baldin Seminar on High Energy Physics Problems: Relativistic Nuclear Physics & Quantum Chromodynamics (Baldin ISHEPP XXIII): Dubna, Russia, September 19–24, 2016*, [EPJ Web Conf. \*\*138\*\*, 12001 \(2017\)](#).
- [38] CBM Collaboration, *Technical Design Report for the CBM Superconducting Dipole Magnet*, edited by A. Malakhov and A. Shabunov (GSI, Darmstadt, Germany, 2013).
- [39] M. Koziel *et al.*, “Vacuum-compatible, ultra-low material budget Micro-Vertex Detector of the compressed baryonic matter experiment at FAIR,” *Proceedings, 14th Vienna Conference on Instrumentation (VCI 2016): Vienna, Austria, February 15–19, 2016*, [Nucl. Instrum. Meth. A \*\*845\*\*, 110 \(2017\)](#).
- [40] J. M. Heuser, “The Silicon Tracking System of the CBM Experiment at FAIR,” *Proceedings, 2nd International Symposium on Science at J-PARC: Unlocking the Mysteries of Life, Matter and the Universe (J-PARC 2014): Tsukuba, Japan, July 12–15, 2014*, [JPS Conf. Proc. \*\*8\*\*, 022007 \(2015\)](#).
- [41] CBM Collaboration, *Technical Design Report for the CBM Silicon Tracking System (STS)*, edited by J. Heuser *et al.* (GSI, Darmstadt, Germany, 2013).
- [42] J. Adamczewski-Musch *et al.*, “The CBM RICH project,” *Proceedings, 14th Vienna Conference on Instrumentation (VCI 2016): Vienna, Austria, February 15–19, 2016*, [Nucl. Instrum. Meth. A \*\*845\*\*, 434 \(2017\)](#).
- [43] CBM Collaboration, *Technical Design Report for the CBM Ring Imaging Cherenkov (RICH) Detector*, edited by C. Höhne (GSI, Darmstadt, Germany, 2013).
- [44] A. K. Dubey *et al.*, “GEM based R&D for muon chambers of CBM experiment at FAIR,” *Proceedings, 3rd International Conference on Micro Pattern Gaseous Detectors (MPGD2013): Zaragoza, Spain, July 1–4, 2013*, [J. Instrum. \*\*9\*\*, C06004 \(2014\)](#).
- [45] CBM Collaboration, *Technical Design Report for the CBM Muon Chambers (MuCh)*, edited by S. Chattopadhyay, Y. P. Viyogi, P. Senger, W. F. J. Müller, and C. J. Schmidt (GSI, Darmstadt, Germany, 2015).
- [46] P. Kähler and F. Roether (for the CBM Collaboration), “The transition radiation detector in the CBM experiment at FAIR,” *Proceedings, 15th Vienna Conference on Instrumentation (VCI 2019): Vienna, Austria, February 18–22, 2019*, [Nucl. Instrum. Meth. A \*\*958\*\*, 162727 \(2020\)](#).
- [47] CBM Collaboration, *Technical Design Report for the CBM Transition Radiation Detector (TRD)*, edited by C. Blume, C. Bergmann, and D. Emschermann (GSI, Darmstadt, Germany, 2018).

- [48] I. Deppner *et al.*, “The CBM Time-of-Flight wall — a conceptual design,” *Proceedings, 12th Workshop on Resistive Plate Chambers and Related Detectors (RPC2014): Beijing, China, February 23–28, 2014*, *J. Instrum.* **9**, C10014 (2014).
- [49] CBM Collaboration, *Technical Design Report for the CBM Time-of-Flight System (TOF)*, edited by N. Herrmann (GSI, Darmstadt, Germany, 2014).
- [50] I. E. Korolko, M. S. Prokudin, and Y. M. Zaitsev, “The CBM ECAL,” *Proceedings, 2nd International Conference on Particle Physics and Astrophysics (ICPPA-2016): Moscow, Russia, October 10–14, 2016*, *J. Phys. Conf. Ser.* **798**, 012164 (2017).
- [51] V. Klochkov and I. Selyuzhenkov (for the CBM Collaboration), “Centrality determination in heavy-ion collisions with the CBM experiment,” *Proceedings, 2nd International Conference on Particle Physics and Astrophysics (ICPPA-2016): Moscow, Russia, October 10–14, 2016*, *J. Phys. Conf. Ser.* **798**, 012059 (2017).
- [52] CBM Collaboration, *Technical Design Report for the CBM Projectile Spectator Detector (PSD)*, edited by F. Guber and I. Selyuzhenkov (GSI, Darmstadt, Germany, 2015).
- [53] J. de Cuveland and V. Lindenstruth (for the CBM Collaboration), “A First-level Event Selector for the CBM Experiment at FAIR,” *Proceedings, 18th International Conference on Computing in High Energy and Nuclear Physics (CHEP 2010): Taipei, Taiwan, October 18–22, 2010*, *J. Phys. Conf. Ser.* **331**, 022006 (2011).
- [54] W. M. Zabolotny *et al.*, “Selection of hardware platform for CBM Common Read-out Interface,” *Proceedings, 40th Wilga Symposium on Photonics Applications in Astronomy, Communications, Industry, and High-Energy Physics Experiments: Wilga, Poland, May 29 – June 4, 2017*, *Proc. SPIE* **10445**, 1044549 (2017).
- [55] J. Lehnert *et al.*, “GBT based readout in the CBM experiment,” *Proceedings, Topical Workshop on Electronics for Particle Physics (TWEPP 2016): Karlsruhe, Germany, September 26–30, 2016*, *J. Instrum.* **12**, C02061 (2017).
- [56] L. Meder, J. Lebedev, and J. Becker, “A versatile small form factor twisted-pair TFC FMC for MTCA AMCs,” *Proceedings, Topical Workshop on Electronics for Particle Physics (TWEPP 2016): Karlsruhe, Germany, September 26–30, 2016*, *J. Instrum.* **12**, C03074 (2017).
- [57] J. de Cuveland, D. Hutter, and V. Lindenstruth, “CBM First-level Event Selector data management developments,” in *CBM Progress Report 2013*, edited by V. Friese and C. Sturm (GSI, Darmstadt, Germany, 2014) p. 92.
- [58] I. Kisel, “Scientific and high-performance computing at FAIR,” *Proceedings, 3rd International Conference on New Frontiers in Physics (ICNFP 2014): Kolymbari, Crete, Greece, July 28 – August 6, 2014*, *EPJ Web Conf.* **95**, 01007 (2015).

- [59] V. Akishina and I. Kisel, “4-Dimensional Event Building in the First-Level Event Selection of the CBM Experiment,” *Proceedings, 21st International Conference on Computing in High Energy and Nuclear Physics (CHEP 2015): Okinawa, Japan, April 13–17, 2015*, *J. Phys. Conf. Ser.* **664**, 072027 (2015).
- [60] I. E. Korolko, M. S. Prokudin, and Y. M. Zaitsev, “Event building for free-streaming readout in the CBM experiment,” *Proceedings, 2nd International Conference on Particle Physics and Astrophysics (ICPPA-2016): Moscow, Russia, October 10–14, 2016*, *J. Phys. Conf. Ser.* **798**, 012165 (2017).
- [61] S. Lebedev, C. Höhne, A. Lebedev, and G. Ososkov, “Selected event reconstruction algorithms for the CBM experiment at FAIR,” *Proceedings, 20th International Conference on Computing in High Energy and Nuclear Physics (CHEP 2013): Amsterdam, The Netherlands, October 14–18, 2013*, *J. Phys. Conf. Ser.* **513**, 022019 (2014).
- [62] M. Al-Turany *et al.*, “The FairRoot framework,” *Proceedings, 19th International Conference on Computing in High Energy and Nuclear Physics (CHEP 2012): New York City, USA, May 21–25, 2012*, *J. Phys. Conf. Ser.* **396**, 022001 (2012).
- [63] R. Brun and F. Rademakers, “ROOT — An object oriented data analysis framework,” *Proceedings, 5th International Workshop on New Computing Techniques in Physics Research (AIHENP’96): Lausanne, Switzerland, September 2–6, 1996*, *Nucl. Instrum. Meth. A* **389**, 81 (1997).
- [64] V. Friese (for the CBM Collaboration), “The high-rate data challenge: computing for the CBM experiment,” *Proceedings, 22nd International Conference on Computing in High Energy and Nuclear Physics (CHEP 2016): San Francisco, USA, October 10–14, 2016*, *J. Phys. Conf. Ser.* **898**, 112003 (2017).
- [65] S. A. Bass *et al.*, “Microscopic Models for Ultrarelativistic Heavy Ion Collisions,” *Prog. Part. Nucl. Phys.* **41**, 255 (1998), [arXiv:nuc-th/9803035](https://arxiv.org/abs/nuc-th/9803035).
- [66] M. Bleicher *et al.*, “Relativistic hadron–hadron collisions in the ultra-relativistic quantum molecular dynamics model,” *J. Phys. G* **25**, 1859 (1999), [arXiv:hep-ph/9909407](https://arxiv.org/abs/hep-ph/9909407).
- [67] I. Hřivnáčová *et al.* (for the ALICE Collaboration), “The Virtual Monte Carlo,” *Proceedings, 13th International Conference on Computing in High Energy and Nuclear Physics (CHEP 2003): La Jolla, California, USA, March 24–28, 2003*, eConf **C0303241**, THJT006 (2003), [arXiv:cs/0306005 \[cs.SE\]](https://arxiv.org/abs/cs/0306005).
- [68] R. Brun, A. Gheata, and M. Gheata (for the ALICE Collaboration), “A Geometrical Modeller for HEP,” *Proceedings, 13th International Conference on Computing in High Energy and Nuclear Physics (CHEP 2003): La Jolla, California, USA, March 24–28, 2003*, eConf **C0303241**, THMT001 (2003), [arXiv:physics/0306151 \[physics.comp-ph\]](https://arxiv.org/abs/physics/0306151).

- [69] V. Friese, “A cluster-finding algorithm for free-streaming data,” *Proceedings, 23rd International Conference on Computing in High Energy and Nuclear Physics (CHEP 2018): Sofia, Bulgaria, July 9–13, 2018*, [EPJ Web Conf. \*\*214\*\*, 01008 \(2019\)](#).
- [70] M. Al-Turany, D. Klein, A. Manafov, A. Rybalchenko, and F. Uhlig, “Extending the FairRoot framework to allow for simulation and reconstruction of free streaming data,” *Proceedings, 20th International Conference on Computing in High Energy and Nuclear Physics (CHEP 2013): Amsterdam, The Netherlands, October 14–18, 2013*, [J. Phys. Conf. Ser. \*\*513\*\*, 022001 \(2014\)](#).
- [71] C. Lippmann, “Particle identification,” [Nucl. Instrum. Meth. A \*\*666\*\*, 148 \(2012\)](#), [arXiv:1101.3276 \[hep-ex\]](#).
- [72] A. Akindinov *et al.*, “Performance of the ALICE Time-Of-Flight detector at the LHC,” [Eur. Phys. J. Plus \*\*128\*\*, 44 \(2013\)](#).
- [73] E. Cerron Zeballos *et al.*, “A new type of resistive plate chamber: The multigap RPC,” [Nucl. Instrum. Meth. A \*\*374\*\*, 132 \(1996\)](#).
- [74] W. Riegler, C. Lippmann, and R. Veenhof, “Detector physics and simulation of resistive plate chambers,” [Nucl. Instrum. Meth. A \*\*500\*\*, 144 \(2003\)](#).
- [75] M. Abbrescia, “Improving rate capability of Resistive Plate Chambers,” *Proceedings, 13th Workshop on Resistive Plate Chambers and Related Detectors (RPC2016): Ghent, Belgium, February 22–26, 2016*, [J. Instrum. \*\*11\*\*, C10001 \(2016\)](#).
- [76] M. C. S. Williams, “Particle identification using time of flight,” [J. Phys. G \*\*39\*\*, 123001 \(2012\)](#).
- [77] D. Gonzalez-Diaz *et al.*, “The role of the Resistive Plate response function in bringing an RPC to a stationary situation,” *Proceedings, 9th Workshop on Resistive Plate Chambers and Related Detectors (RPC2007): Mumbai, India, February 13–16, 2008*, [Nucl. Instrum. Meth. A \*\*602\*\*, 713 \(2009\)](#).
- [78] D. González-Díaz, P. Fonte, J. A. Garzón, and A. Mangiarotti, “An analytical description of rate effects in timing RPCs,” *Proceedings, 8th Workshop on Resistive Plate Chambers and Related Detectors (RPC2005): Seoul, Korea, October 10–12, 2005*, [Nucl. Phys. B Proc. Suppl. \*\*158\*\*, 111 \(2006\)](#).
- [79] J. Wang *et al.*, “Development of multi-gap resistive plate chambers with low-resistive silicate glass electrodes for operation at high particle fluxes and large transported charges,” [Nucl. Instrum. Meth. A \*\*621\*\*, 151 \(2010\)](#).
- [80] M. Ciobanu *et al.*, “PADI, an Ultrafast Preamplifier - Discriminator ASIC for Time-of-Flight Measurements,” [IEEE Trans. Nucl. Sci. \*\*61\*\*, 1015 \(2014\)](#).

- [81] H. Deppe and H. Flemming, “The GSI Event-Driven TDC with 4 Channels GET4,” *Proceedings, 2009 IEEE Nuclear Science Symposium and Medical Imaging Conference (NSS/MIC 2009): Orlando, Florida, USA, October 25–31, 2009*, [IEEE Nucl. Sci. Symp. Conf. Rec. \*\*2009\*\*, 295 \(2009\)](#).
- [82] A. Akindinov *et al.*, “Radiation-hard ceramic Resistive Plate Chambers for forward TOF and T0 systems,” *Proceedings, 14th Vienna Conference on Instrumentation (VCI 2016): Vienna, Austria, February 15–19, 2016*, [Nucl. Instrum. Meth. A \*\*845\*\*, 203 \(2017\)](#).
- [83] Y. Wang *et al.*, “Development and test of a real-size MRPC for CBM-TOF,” *Proceedings, 13th Workshop on Resistive Plate Chambers and Related Detectors (RPC2016): Ghent, Belgium, February 22–26, 2016*, [J. Instrum. \*\*11\*\*, C08007 \(2016\)](#), [arXiv:1605.02395 \[physics.ins-det\]](#).
- [84] M. Petriş *et al.*, “Time and position resolution of high granularity, high counting rate MRPC for the inner zone of the CBM-TOF wall,” *Proceedings, 13th Workshop on Resistive Plate Chambers and Related Detectors (RPC2016): Ghent, Belgium, February 22–26, 2016*, [J. Instrum. \*\*11\*\*, C09009 \(2016\)](#), [arXiv:1605.02558 \[physics.ins-det\]](#).
- [85] I. Deppner *et al.*, “Performance studies of MRPC prototypes for CBM,” *Proceedings, 13th Workshop on Resistive Plate Chambers and Related Detectors (RPC2016): Ghent, Belgium, February 22–26, 2016*, [J. Instrum. \*\*11\*\*, C10006 \(2016\)](#), [arXiv:1606.04917 \[physics.ins-det\]](#).
- [86] Y. Wang *et al.*, “A solution for the inner area of CBM-TOF with pad-MRPC,” *Proceedings, 14th Vienna Conference on Instrumentation (VCI 2016): Vienna, Austria, February 15–19, 2016*, [Nucl. Instrum. Meth. A \*\*845\*\*, 318 \(2017\)](#).
- [87] P. Lyu *et al.*, “Development and performance of self-sealed MRPC,” *Proceedings, 14th Topical Seminar on Innovative Particle and Radiation Detectors (IPRD16): Siena, Italy, October 3–6, 2016*, [J. Instrum. \*\*12\*\*, C03055 \(2017\)](#).
- [88] M. Petriş *et al.*, “In-beam test of the RPC architecture foreseen to be used for the CBM-TOF inner wall,” *Proceedings, 22nd International School on Nuclear Physics, Neutron Physics and Applications: Varna, Bulgaria, September 10–16, 2017*, [J. Phys. Conf. Ser. \*\*1023\*\*, 012007 \(2018\)](#).
- [89] M. Petriş *et al.*, “Performance of a two-dimensional position sensitive MRPC prototype with adjustable transmission line impedance,” [Nucl. Instrum. Meth. A \*\*920\*\*, 100 \(2019\)](#).
- [90] A. Neiser *et al.*, “TRB3: a 264 channel high precision TDC platform and its applications,” *Proceedings, Topical Workshop on Electronics for Particle Physics (TWEPP 2013): Perugia, Italy, September 23–27, 2013*, [J. Instrum. \*\*8\*\*, C12043 \(2013\)](#).

- [91] P. Lyu *et al.*, “Study on cosmic test and QC method of high-rate MRPC for CBM-TOF,” *Proceedings, 14th Workshop on Resistive Plate Chambers and Related Detectors (RPC2018): Puerto Vallarta, Jalisco state, Mexico, February 19–23, 2018*, *J. Instrum.* **14**, C09032 (2019).
- [92] D. Hu *et al.*, “MRPC3b mass production for CBM-TOF and eTOF at STAR,” *Proceedings, 14th Workshop on Resistive Plate Chambers and Related Detectors (RPC2018): Puerto Vallarta, Jalisco state, Mexico, February 19–23, 2018*, *J. Instrum.* **14**, C06013 (2019), [arXiv:1807.02452 \[physics.ins-det\]](https://arxiv.org/abs/1807.02452).
- [93] STAR Collaboration and CBM Collaboration eTOF Group, “Physics Program for the STAR/CBM eTOF Upgrade,” [arXiv:1609.05102 \[nucl-ex\]](https://arxiv.org/abs/1609.05102).
- [94] J. Michel *et al.*, “The HADES DAQ System: Trigger and Readout Board Network,” *Proceedings, 17th Conference on Computing Applications in Nuclear and Plasma Sciences on Real Time (RT2010): Lisbon, Portugal, May 24–28, 2010*, *IEEE Trans. Nucl. Sci.* **58**, 1745 (2011).
- [95] D. Manglunki *et al.*, “CERN’s Fixed Target Primary Ion Programme,” *Proceedings, 7th International Particle Accelerator Conference (IPAC2016): Busan, Korea, May 8–13, 2016*, *JACoW IPAC2016*, TUPMR027 (2016).
- [96] I.-M. Deppner, *Development of a fully differential Multi-gap Resistive Plate Chamber for the CBM Experiment*, PhD dissertation, Heidelberg University, Heidelberg, Germany (2013).
- [97] C. Nociforo, “Time-of-flight measurements at the Super-FRS,” *Proceedings, 13th Topical Seminar on Innovative Particle and Radiation Detectors (IPRD13): Siena, Italy, October 7–10, 2013*, *J. Instrum.* **9**, C01022 (2014).
- [98] F. Schirru *et al.*, “Development of large area diamond detectors for time-of-flight measurements of relativistic heavy ions for the super-FRS,” *J. Phys. D: Appl. Phys.* **49**, 215105 (2016).
- [99] H. G. Essel and N. Kurz, “The General Purpose Data Acquisition System MBS,” *IEEE Trans. Nucl. Sci.* **47**, 337 (2000).
- [100] F. M. Velotti *et al.*, “Characterisation of the SPS Slow-extraction Parameters,” *Proceedings, 7th International Particle Accelerator Conference (IPAC2016): Busan, Korea, May 8–13, 2016*, *JACoW IPAC2016*, THPOR055 (2016).
- [101] V. Kain, K. Cornelis, and E. Effinger, “New Spill Control for the Slow Extraction in the Multi-Cycling SPS,” *Proceedings, 7th International Particle Accelerator Conference (IPAC2016): Busan, Korea, May 8–13, 2016*, *JACoW IPAC2016*, TUPMR051 (2016).

- [102] V. Kain *et al.*, “Fixed Target Beams,” *Proceedings, Injector Machine Development (MD) Days 2017: Geneva, Switzerland, March 23–24, 2017*, [CERN Proc. \*\*2017-002\*\*, 81 \(2017\)](#).
- [103] M. A. Fraser *et al.*, “SPS Slow Extraction Losses and Activation: Update on Recent Improvements,” *Proceedings, 10th International Particle Accelerator Conference (IPAC2019): Melbourne, Australia, May 19–24, 2019*, [JACoW IPAC2019, WEPMP031 \(2019\)](#).
- [104] C. Uğur, G. Korcyl, J. Michel, M. Penschuk, and M. Traxler, “264 Channel TDC Platform Applying 65 Channel High Precision (7.2 psRMS) FPGA Based TDCs,” *Proceedings, 2013 IEEE Nordic-Mediterranean Workshop on Time-to-Digital Converters (NoMe TDC): Perugia, Italy, October 3, 2013*, [Proc. IEEE NoMe TDC \*\*2013\*\*, 26 \(2013\)](#).
- [105] K. Koch, “CLOSYP: A very Precise Clock Generation for Timing Measurements and Synchronization of the CBM ToF Wall,” *Proceedings, 2009 IEEE Nuclear Science Symposium and Medical Imaging Conference (NSS/MIC 2009): Orlando, Florida, USA, October 25–31, 2009*, [IEEE Nucl. Sci. Symp. Conf. Rec. \*\*2009\*\*, 324 \(2009\)](#).
- [106] J. Michel, *Development and Implementation of a New Trigger and Data Acquisition System for the HADES Detector*, PhD dissertation, Goethe University, Frankfurt, Germany (2012).
- [107] M. Penschuck, *Development and Implementation of a Central Trigger System for TrbNet-based systems*, Bachelor’s thesis, Goethe University, Frankfurt, Germany (2012).
- [108] J. Adamczewski-Musch, N. Kurz, and S. Linev, “Developments and applications of DAQ framework DABC v2,” *Proceedings, 21st International Conference on Computing in High Energy and Nuclear Physics (CHEP 2015): Okinawa, Japan, April 13–17, 2015*, [J. Phys. Conf. Ser. \*\*664\*\*, 082027 \(2015\)](#).
- [109] G. Korcyl, *A novel data acquisition system based on fast optical links and universal readout boards*, PhD dissertation, AGH University of Science and Technology, Krakow, Poland (2015).
- [110] P.-A. Loizeau, *Development and test of a free-streaming readout chain for the CBM Time of Flight Wall*, PhD dissertation, Heidelberg University, Heidelberg, Germany (2014).
- [111] L. Landau, “On the energy loss of fast particles by ionization,” *J. Phys. (USSR)* **8**, 201 (1944).
- [112] K. S. Kölbig and B. Schorr, “A program package for the Landau distribution,” [Comput. Phys. Commun. \*\*31\*\*, 97 \(1984\)](#).

- [113] M. Abbrescia *et al.*, “Cosmic ray tests of double-gap resistive plate chambers for the CMS experiment,” *Nucl. Instrum. Meth. A* **550**, 116 (2005).
- [114] M. Abbrescia (for the CMS Collaboration), “Operation, performance and upgrade of the CMS Resistive Plate Chamber system at LHC,” *Proceedings, 13th Vienna Conference on Instrumentation (VCI 2013): Vienna, Austria, February 11–15, 2013*, *Nucl. Instrum. Meth. A* **732**, 195 (2013).
- [115] J. A. Nelder and R. Mead, “A simplex method for function minimization,” *Comput. J.* **7**, 308 (1965).
- [116] J. Wang *et al.*, “Development of high-rate MRPCs for high resolution time-of-flight systems,” *Nucl. Instrum. Meth. A* **713**, 40 (2013).
- [117] Z. Liu *et al.*, “20 gas gaps Multigap Resistive Plate Chamber: Improved rate capability with excellent time resolution,” *Nucl. Instrum. Meth. A* **908**, 383 (2018).
- [118] Z. Liu, M. C. S. Williams, A. Zichichi, and R. Zuyeuski, “A Multigap Resistive Plate Chamber built with thin low-resistive glass: High rate capability with excellent time resolution,” *Nucl. Instrum. Meth. A* **928**, 7 (2019).
- [119] R. Brun, F. Bruyant, M. Maire, A. C. McPherson, and P. Zancarini, *GEANT 3* (CERN, Geneva, Switzerland, 1987).
- [120] C. Simon, CbmRoot SVN development branch, <https://subversion.gsi.de/cbmsoft/cbmroot/development/csimon>, [Accessed: 30/11/2020].